THE USE OF MARINE RADAR FOR INTERTIDAL AREA SURVEY AND MONITORING COASTAL MORPHOLOGICAL CHANGE

Thesis submitted in accordance with the requirements of the University of Liverpool for the degree of Doctor in Philosophy

By

Cai Bird

School of Environmental Science

Department of Geography and Planning

May 2016

DECLARATION

This thesis is the result of my own work and includes nothing which is the outcome of work done in collaboration except where specifically indicated in the text. It has not been previously submitted, in part or whole, to any university of institution for any degree, diploma, or other qualification.

In accordance with The University of Liverpool guidelines, this thesis does not exceed 100,000 words.

Signed:_____

Date:_____

Cai Bird, BSc.

Contributions by authors to manuscripts:

Chapter 5: Bell, P. S., Bird, C. O., Plater, A. J. (2016). A Temporal Waterline Approach To Mapping Intertidal Areas Using X-band Marine Radar. *Coastal Engineering.* **107**, 84-101.

P. S. Bell; research Co-I, Waterline method patent holder through *NOC* (Patent number: PCT/GB2014/050908) and tidal data processing.

C. O. Bird; algorithm development, data processing and analysis, plot creation, and principal author.

A. J. Plater; research Co-I, intellectual input, manuscript development, and advice on figure plot creation.

Chapter 6: Bird, C.O., Bell, P.S., Plater, A.J. (Submitted). Radar-derived elevation surveys for monitoring dynamic coastal geomorphology. *Geomorphology.*

C. O. Bird; principal investigator and author, data processing, analysis and plot creation.

P. S. Bell; manuscript development, and advice on figure plot creation.

A. J. Plater; manuscript development, and advice on figure plot creation.

Signed:_____

Date:_____

ABSTRACT

The Use of Marine Radar for Intertidal Area Survey and Monitoring Coastal Morphological Change.

Cai Oliver Bird.

Surveying and monitoring the dynamic morphology of intertidal areas is a logistically challenging and expensive task, due to their large area and complications associated with access. This thesis describes a contribution to the nearshore survey industry; an innovative methodology is developed and subsequently applied to marine radar image data in order to map topography within the intertidal area. This new method of intertidal topographical mapping has a reasonable spatial resolution (5 m) and operates over a large radial range (~4 km) with the required temporal resolution to observe both event-based and long-term morphological change (currently bi-weekly surveys).

This study uses nearly three years of radar image data collected during 2006-2009 from an installation on Hilbre Island at the mouth of the Dee estuary, northwest UK. The development of the novel 'radar waterline method' builds on previous waterline techniques and improves upon them by moving the analysis from the spatial to the temporal domain, making the analysis extremely robust and more resilient to poor quality image data. Results from radar topographical surveys are compared to those of a LiDAR survey during October 2006. The differences compare favourably across large areas of the intertidal zone, within the first kilometre 97% of radar-derived elevations lie within 1 m of LiDAR estimations. Concentrations of poor estimations are seen in areas that are shown to be shadowed from the radar antenna or suffering from pooling water during the ebb tide.

The full three-year dataset is used to analyse changing intertidal morphology over that time period using radar-derived surveys generated every two weeks. These surveys are used to perform an analysis of changing sediment volume and mean elevation, giving an indication of beach 'health' and revealing a seasonal trend of erosion and accretion at several sites across the Dee estuary. The ability of the developed technique to resolve morphological changes resulting from storm events is demonstrated and a quantification of that impact is provided.

The application of the technique to long-range (7.5 km) marine radar data is demonstrated in an attempt to test the spatial and operational limitations of this new method. The development of a mobile radar survey platform, the Rapidar allows remote areas to be surveyed and provides a platform for potential integration with other survey instruments. A description of the potential application to coastal management and monitoring is presented. Areas of further work intended to improve vertical elevation accuracy and robustness are proposed.

This contribution provides a useful tool for coastal scientists, engineers and decision-makers interested in the management of coastal areas that will form part of integrated coastal management and monitoring operations. This method presents several key advantages over traditional survey techniques including; the large area of operation and temporal resolution of repeat surveys, it is limited primarily by topographical shadowing and low wind conditions limiting data collection.

ACKNOWLEDGEMENTS

I would initially like to thank my superb academic supervisors, Prof. Andrew Plater and Dr. Paul Bell for their constant stream of advice, encouragement and feedback. I must also thank my colleagues Alex Sinclair, Simon Truss and Avnir Soni at *Marlan Maritime Technologies* for both the opportunity to conduct this research, and for providing the necessary training, expertise and enthusiasm, to both support and drive this project over the last three years.

This research was funded by *Marlan Maritime Technologies,* and the *Centre for Global Eco-Innovation* through the European Regional Development Fund (ERDF X02646PR). Acknowledgement must be made to the *NOC (National Oceanography Centre* funded by *NERC*) for collection of the radar dataset and the significant contribution of supervisory time.

Thanks are due to my friends and colleagues (too many to name) across the School of Environmental Sciences and within the Department of Geography and Planning, and at *NOC* for a welcoming and inclusive research environment. I would like to extend thanks to all those from the inaugural cohort of the *Centre for Global Eco-Innovation* from diverse backgrounds across Liverpool and Lancaster Universities for providing a great support network and excellent company whilst working in Shanghai and during numerous residential training events.

Primarily, I could not have done this work without the support of my better half and family, who have all shown tremendous patience and support throughout this experience. Thanks is not a great enough word to show my appreciation for their efforts - this work is dedicated to them.

"You cannot employ non-hostile, non-destructive technical skill, unless you realise, basically, that you yourself are this whole domain of nature. That's the real you. You are not in a fight against nature, you are not here to conquer nature, because there's nothing to conquer. It's all you. So when you use technology to bulldoze everything into submission… you're fighting yourself."

Alan Watts

CONTENTS

LIST OF TABLES

LIST OF FIGURES

1 INTRODUCTION

1.1 RESEARCH JUSTIFICATION

Coastal and marine environments (CMEs) are intrinsically difficult to monitor and maintain using current technologies. The highly dynamic nature of the coastline can often cause considerable problems to the human populations living nearby. Humans have always used coastal areas as a focal point for settlement and development, and this concentration of population and vital infrastructure continues to increase. The continued development of coastal areas throughout history is encouraged by the abundance of resources. These coastal resources can often be categorized in terms of ecosystem services, with fisheries (both nearshore, estuarine and access to offshore) providing provisioning ecosystem services (Barbier et al., 2011). Estuaries and coastlines often provide a regulating service in the disposal of waste, irrigation water for farmland, cooling of power stations and sites for marine renewable energy.

As service economies have developed, many of these areas also serve to provide cultural and aesthetic value to locals and tourists alike, augmenting local and national economies through the provision of recreational areas (Ghermandi and Nunes, 2013). Coastal zones also serve to accommodate large conurbations that act as focal points for economic growth, flows of migration and international trade. In order to prevent degradation of these services, the increasingly vulnerable coastal area must be carefully managed and monitored.

Advances in remote sensing, such as video camera systems and radar mounted on a variety of platforms (from satellites to scaffold towers), allow the accurate monitoring of CMEs across a range of spatial and temporal scales. There is still however a requirement for an instrument that has the capability to cost-effectively monitor large coastal areas and estuaries whilst gathering detailed data on changes in coastal morphology. The effective continued maintenance and protection of high value coastal areas such as ports, harbours, tourist and residential zones, requires a combination of engineering interventions ranging from hard emplacements, such as seawalls and breakwaters, to less intrusive solutions including wetland/dune maintenance and beach recharge (French, 2001). The effective management and placement of these defences requires long-term observation of the dynamic coastal morphological system. This thesis describes the development of a novel technique that uses standard marine radar to monitor changing intertidal morphology and perform wide area elevation surveys, with the aim of providing a significant contribution to the toolbox of techniques available to coastal scientists and stakeholders.

Marine radar is a ubiquitous tool in marine industry and a crucial tool in coastal operations, as ports are often required to operate a radar system to monitor vessel traffic and manage

navigation. Radar is also deployed during many coastal observation projects due to its established ability to measure hydrodynamics such as significant wave heights, wave spectra and surface currents in addition to nearshore subtidal bathymetric surveys (Reichert et al., 1997; Nieto-Borge and Guedes-Soares, 2000; Dankert and Rosenthal, 2004; Bell and Osler, 2011; Bell et al., 2012). The established methods of performing bathymetric surveys using marine radar do not perform well when observing areas in very shallow waters and complex intertidal zones (Serafino et al., 2010). These sub and intertidal environments are incredibility difficult to monitor cost-effectively using current technologies due to the ever-changing nature of the coast and the dangers to people and equipment this area can present. The overall aim of this research is to develop a technique that can work either alongside other remote sensing methods, or independently to fill the current gap in surveillance of the dynamic intertidal zone. With this added capability combined with existing techniques, a marine radar installation becomes effectively an 'all-in-one' solution for coastal monitoring.

The continued operation of an integrated monitoring system will provide many benefits to regulatory, management and business organisations including Port Authorities, such as: awareness of migrating sediment features that may present a navigation hazard, improved data-based decision making with regards to maintenance and construction of defences, and increased efficiency of dredging operations. In addition to these commercial benefits, widespread use of the integrated radar system could provide a comprehensive coastal network of marine environmental data. The relatively low investment cost and low maintenance requirements of radar enables long-term time series of morphological survey data to be collected remotely. These data are a valuable resource for coastal scientists and policy makers in tackling issues such as climate change, coastal erosion and adverse sedimentation. The integrated radar system

therefore presents a novel and more effective method of monitoring coastal areas whilst aiming to improve the sustainability and efficiency of critical port operations in the intertidal zone.

1.2 CHALLENGES IN COASTAL MANAGEMENT AND REQUIREMENT FOR LONG-TERM MONITORING

The global climatic system is incredibly complex and is influenced by a diverse range of variables and over many different timescales. Temporal evolution of coastal landscapes due to the effects of climate change is a subject of much research. Large-scale changes often occur over timescales larger than the human lifespan; there are problems therefore with obtaining long and reliable data sets for analysis and to validate modelling. However, significant changes to the geomorphology of coastlines and localised sea-level change do occur over relatively short geological timescales as a result of successive storms and seasonal variations in weather. An example of this case is the erosion of the south coast of England, where abrupt cliff erosion has caused loss of land and property destruction over the decadal timescale (Bray and Hooke, 1997).

Despite the fact that sea-level rise and shoreline retreat pose a threat to coastal communities from flooding and inundation of high value land (Füssel and Jol, 2012), there is little continuous large-scale scientific monitoring and observation of vulnerable coastal environments. The issue is one of critical importance for societies where significant infrastructure is concentrated in coastal zones. It is crucial for these societies to be aware of the potential risks associated with climate change, sea-level rise and excessive coastal erosion. Therefore a high quality and

comprehensive dataset must be gathered in order to make data-based decisions at these crucial coastal areas.

A major obstacle to scientific research in coastal zones is a lack of available data (Holman and Haller, 2013). The availability of high quality data can be increased by utilising existing infrastructure (such as radar installations) along industrialised coastlines and increasing cooperation between stakeholders within the area. This is a major objective of the integrated radar project, as the operators of the radar system will have a vested interest in the preservation of their operating theatre and those adjacent to them. Thus the data gathered during the operation of the radar system includes but is not limited to; intertidal bathymetric/topographic information, sediment migration and identification of areas vulnerable to coastal erosion. These data could be utilised in partnership with academic organisations and commercial entities to further increase the resilience of the coastal zone at a meso/macro-scale.

Figure 1.1 depicts an outline of the major disciplines and interactions at play in coastal management. The figure illustrates that initial conditions are determined by a combination of environmental and anthropogenic forcings that are reciprocal in their effects. The interactions between human activity and natural coastal processes are spatially and temporally variable, and both the extent and impact of these processes also varies greatly. Data on these nearshore processes can be used to supplement hydrodynamic and morphological models which, along with observational data feed directly into aids for coastal management. These aids to management take many forms, from comprehensive reports on the state and health of a

coastline to fully interactive online decision support tools where stakeholders can access relevant information. An example of one such tool was constructed during the ARCoES (Adaptation and Resilience of Coastal Energy Supply) project 2011-2016 (Knight et al., 2015; Prime et al., 2015). This tool shows information on areas vulnerable to coastal flooding over the next 500 years, with a particular focus on energy supply infrastructure. These tools and aids provide a wealth of crucial information to policy-makers, stakeholders, managers and decision-makers.

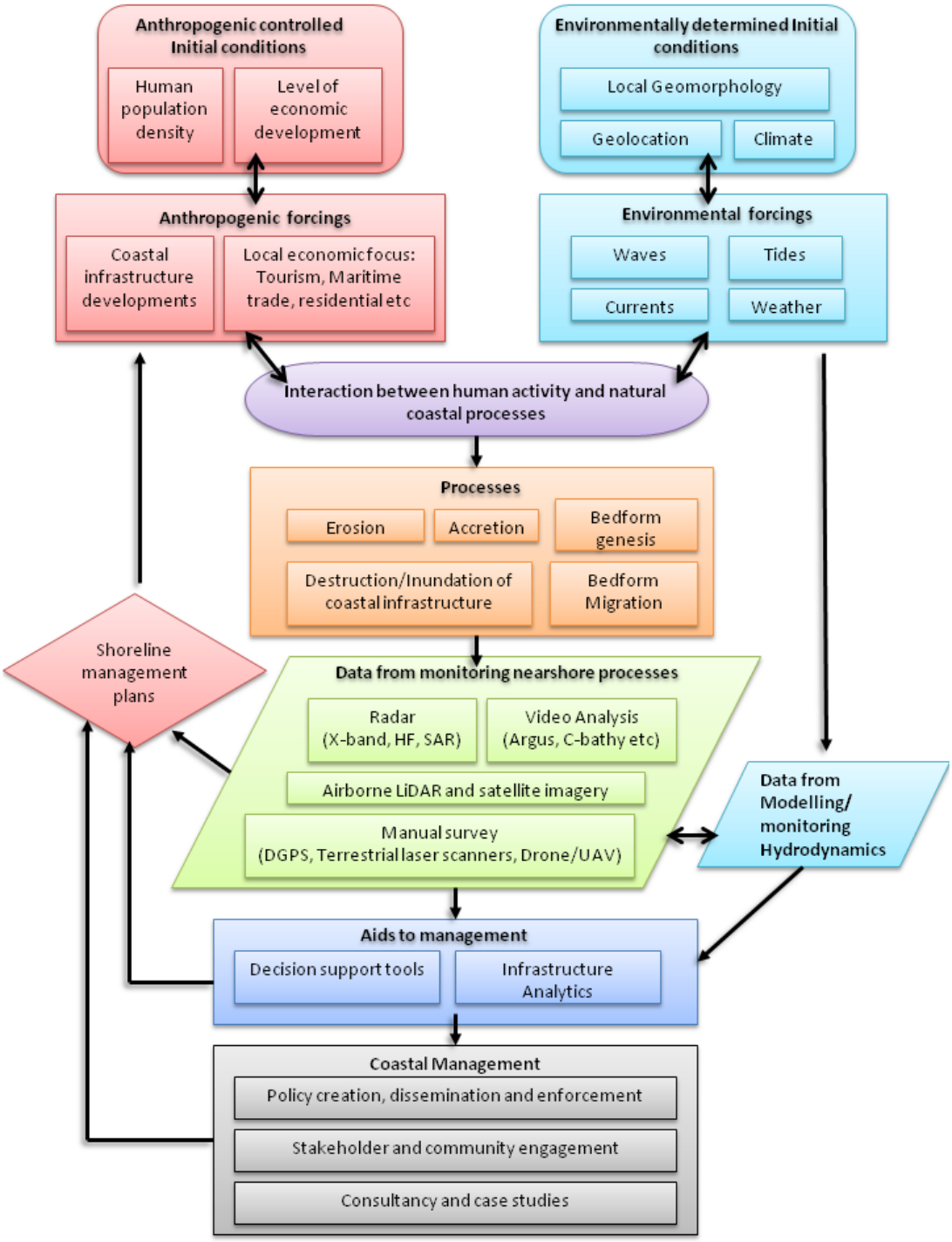

Figure 1.1: Schematic of interactions between disciplines and processes involved in coastal management.

These elements all feed (in an ideal system) into the assigned shoreline management plans. In the UK these plans take one of several forms 'hold the line', 'managed realignment', 'advance the line' and 'no active intervention'. In turn the way that human populations alter the coastline changes the scope and scale of processes affecting the coastline and the entire process forms a complex feedback loop that must be monitored carefully in vulnerable areas. This research ultimately aims to develop a tool capable of providing these long-term datasets describing coastal morphological change.

1.3 RESEARCH AIMS

The ambition of this project is to develop and test a prototype marine radar survey technique that has the ability to robustly estimate topography of an intertidal area at low tide. This technique should have the capability to operate over long periods of time with minimal manual input. It must also use data gathered by standard, 'off-the-shelf' hardware, and be efficient enough to run the analysis using standard desktop computers. By using data from standard radar and not bespoke systems, the routine ability to track vessels and observe port operations remains unimpeded. Use of standard data also enables the technique to be performed alongside other analysis methods, increasing the versatility and value of a radar deployment. In addition to describing the theoretical framework for this novel technique, this work also seeks to demonstrate its applicability to the task of monitoring coastal geomorphology. In combining these capabilities, the safety and security of port operations can be improved by observing long-term (and event-based in the case of storms) changes in coastal morphology using the radar

system, and then by tracking the implementation of remedial measures or strategic interventions and their subsequent effects on morphology.

In summary the objectives of this thesis are to:

1. Develop a unique methodology for surveying intertidal areas using standard X-band marine radar. Determine vertical and temporal resolution of the radar waterline method.
2. Test the robustness and stability of the developed method by sampling elevations over several months. Test accuracy by comparing radar-derived elevations with a LiDAR survey over the same period.
3. Demonstrate the ability of the developed technology to monitor and quantify changing coastal geomorphology and beach 'health' by measuring spatial and temporal trends of erosion and accretion over three years.
4. Assess maximum operational range of the radar waterline method using a single marine radar sensor set to short pulse by applying method to long-range dataset.
5. Explore the application of developed methodology to the nearshore survey industry, scientific projects and coastal management.
6. Identify areas for further research to improve vertical accuracies and temporal resolutions.

1.4 THESIS STRUCTURE

Following this introductory chapter, Chapter 2 provides a very broad overview of coastal environments, nearshore processes and their morphological patterns and the need for monitoring. A discussion of the primary sedimentary features that can be observed in the nearshore area is provided and an explanation of the key driving forces behind coastal morphological change. The description of critical hydrodynamic processes acting upon coastal areas follows and this feeds into an assessment of current state of the art coastal monitoring and survey techniques.

Chapter 3 is primarily a literature review and technical section focused on marine radar. The chapter describes the generation, propagation and interaction of radar-generated radio frequency electromagnetic waves with the environment. The primary equation that governs radar performance and determines a given radar system capabilities is known as the Radar Range Equation (RRE) and is described in some detail during this section. A vital aspect of marine radar in terms of coastal monitoring is the ability to image the sea surface through the interaction between electromagnetic waves and small scale ripples on a rough sea surface - this important information is described during Chapter 3. This chapter ends with a description of some of the common survey applications of radar technology.

Chapter 4 describes the study site for much of the initial research and development of this technique. Radar data were gathered from an installation on Hilbre Island in the River Dee estuary from early 2006 to December 2008; it is these data that were used to test the radar waterline survey method developed in this thesis. This section describes the morphological

evolution of the Dee estuary and its significance to the local economy. In addition, a critical data element required to perform the radar waterline survey is a reliable record of tidal elevations. In many areas (ports for example) there will already be an accurate tidal measurement device installed, but at other more remote areas, a model or temporary gauge must be deployed. This chapter describes the collection of this timeseries of tidal elevation throughout the deployment period and the required data pre-processing steps required prior to the waterline analysis. In addition the ground truth LiDAR survey data used in Chapter 5 is described here too.

The work in chapter 5 forms the basis of the paper: Bell, P.S., Bird, C.O., Plater, A.J., (2016) A temporal approach to mapping intertidal areas using X-band marine radar. *Coastal Engineering*, **107**, 84-101. This describes the overall motivation and methodologies for intertidal survey using marine radar. Using a subset of the full Hilbre Island radar dataset lasting around ten months, surveys were generated every two weeks. The accuracy of the new technique is also examined in some detail by comparison with a LiDAR survey conducted at the same time as radar data collection. Stability of the results is also analysed, using a comparison between known rock locations (expected to be stable over ten months) and other sandy regions that show absolute changes in elevation.

Chapter 6 builds upon the work presented in the previous chapter and is presented in the paper Bird, C.O., Bell, P.S., Plater, A.J., (submitted) Radar-derived elevation surveys for monitoring dynamic coastal geomorphology. *Geomorphology*. This describes the applications of the survey technique in monitoring long-term coastal evolution. Three years of radar data were used in this analysis, and morphological change was assessed both qualitatively and quantitatively at

several sites within the Dee estuary. Several methods of assessing beach 'health' were applied, and an analysis of volume change and fluctuations of mean elevations over three years showed clear seasonal fluctuations. The evolution of a series of cross-shore profiles was assessed in addition to the effects of storm events on beach morphology. The application of the technique to "Big Data" collection is also discussed.

Chapter 7 describes the application of the waterline technique to the long-range data collected from the Hilbre Island Radar. Many issues were discovered when dealing with marine radar data collected on short pulse settings at long-range and these issues are discussed. Primarily there is an issue of shadowing, where the range from the radar antenna increases such that grazing angle between projected radar waves and the topography to be surveyed becomes very shallow. As this shallow grazing angle means that small topographical features cause large areas to be shadowed by the radar. This inhibits data collected at long ranges and the results presented in Chapter 7 describe this phenomena along with methods of estimating the impact of shadowing.

Chapter 8 presents a detailed discussion section on each of the main topics discussed throughout the thesis and also presents recommended future work that has the capacity to improve results derived using the methods developed in this thesis.

Chapter 9 provides final conclusions on the work completed and reflections on the initial research objectives.

A brief Appendix is included that details several open source MATLAB functions that were used in the development of the methodology and analysis.

2 NEARSHORE PROCESSES AND MONITORING TECHNIQUES

2.1 COASTAL ZONE GEOMORPHOLOGY AND EVOLUTION

There are a wide variety of topographical and bathymetric features formed of sediment within the intertidal and nearshore zone. This section aims to outline some of the features observed using the radar technique developed, and provide a background to the processes that contribute to the formation of these features and describe their topographical distribution across shorelines.

2.1.1 Nearshore Sedimentary Bedforms and Nomenclature

The term bedform generally refers to any morphological feature that is composed of unconsolidated sediment. Details on the sedimentology of this zone can be found in Allen (1985), Pye (1994) and Hsu (2004), and the processes by which this sediment can be mobilised

will be discussed in later sections. Bedforms often exhibit quasi-regular patterns over varying timescales and are distinguishable in their appearance and behaviour, which allows some classification of sedimentary bedforms (Soulsby, 1997). The morphology of these bedforms is dependent on hydrodynamics and constituent sediment characteristics. In turn, the evolution of these bedforms effects local hydrodynamics as these features increase bed roughness which serves to reduce erosive wave energy (Masselink et al., 2014), it is therefore extremely important to monitor changes in these bedforms.

There is a wide spectrum of nomenclature involved in the description of sedimentary bedforms. Figure 2.1 illustrates the important generic terms used to describe many micro-scale and more significant meso-scale bedforms which are observed later in this work.

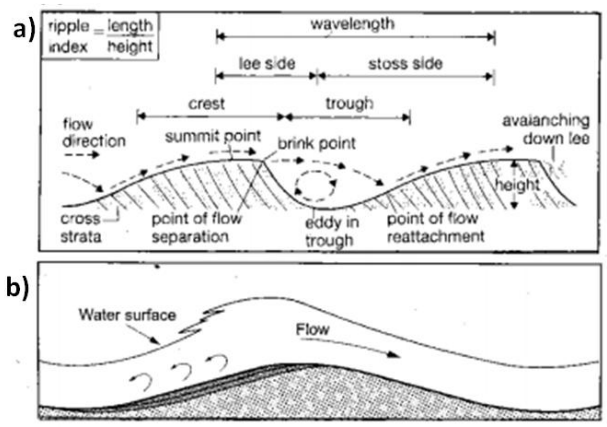

Figure 2.1: Schematics of (a) ripple and dune from Tucker (1995) and (b) antidune from Reineck and Singh (1980).

Bedforms alter the flow of water around themselves. As bedforms reduce the water depth, flow accelerates due to compression increasing the rate of transport up the shallow *stoss* slope and decelerating once over the crest into an eddy, depositing the carried sediment onto a steeper *lee* slope. When material is transported to the crest it eventually cascades downslope, and the cycle of erosion from the *stoss* slope and deposition on the *lee* slope results in the progressive migration of the bedform. Of course this pattern would require continuous unidirectional flow, which is very rare in the surf zone. Ripples that form in shallow water dominated by wave processes are therefore mostly a result of the onshore and offshore wave stroke. The offshore stroke is intuitively much weaker than the onshore, as such no eddy is formed and instead, the sediment mobilised is carried seawards by the reversed offshore wave stroke, resulting in a seaward migration of bedforms during a high energy wave event (Masselink et al., 2014). This can commonly appear as beach loss and erosion if only the intertidal area is observed in isolation.

The most common bedforms fall into one of three categories: dunes, ripples and antidunes defined in turn by their spatial dimensions. Antidunes are unique in that they form and potentially migrate against the flow, as their name implies, opposite to dunes. These antidunes only form in subcritical flow (Kennedy, 1969), which occurs in shallow water and the water surface reflects the shape of the bedforms below (this effect can sometimes be seen in radar images as shown throughout this thesis). Table 2.1 shows the physical dimensions of bedforms in relation to expected hydrodynamic parameters.

	Unidirectional Flow			Oscillatory Flow	
	Ripples	Dunes	Antidunes	Rolling Grain Ripples	Vortex Ripples
Length (Spacing)	0.1 - 0.2 m	0.6 - 30 m	0.1 - 1 m	0.02 - 1 m	0.02 - 1 m
Height	< 0.06 m	0.06 - 1.5 m	0.01 - 0.1 m	1 - 5 mm	1 - 5 cm
Typical Flow Velocity	Low	Moderate	High	Low and High	Moderate
Typical Flow Depth	> 5 cm	> 50 cm	5 cm - 50 cm	Upto 1/2 Wavelength	Upto 1/2 Wavelength
Typical Grain Size	0.03 - 0.6 mm	> 0.3 mm	Sand and Gravel	All Sand	All sand

Table 2.1: Dimensions of common bedforms with respect to dominant flow parameters from Masselink et al. (2014).

Dunes, ripples and antidunes are also distinguished by their morphodynamic qualities; their sizes increase with flow velocity and bed shear stress, but their evolution is also governed by flow depth, sediment supply and sediment characteristics. Dunes can therefore be very large in deep water on mobile sandy beds when subject to energetic flow conditions; for example dunes in the Irish Sea are much larger than those in the South China Sea (Kubicki, 2008). The stability of these bedforms is also subject to variability in flow conditions, however because bedforms take time to change their dimensions in response to flow condition change, it is very rare for bedforms to be in disequilibrium with the flow (Masselink et al., 2014).

Some observed bedforms may be termed *relicts* where the flow conditions that facilitated their evolution are different to those observed in the contemporary environment. An example of relict sand banks can be found on the continental shelf of the Celtic Sea in 180 m of water depth, well below the depth at which present day tidal currents could influence them. These features have been drowned due to sea level rise since the last deglaciation (Landeghem et al., 2009).

In addition to these meso-scale bedforms there are other significant and dynamic structures present in sedimentary environments. Tidal channels for example are deep incisions carved into beaches by currents, and are also major sediment transport pathways consisting mainly of fine sediment. Small subaqueous dunes and ripples of sand form within tidal channels, and while the ebb and flood of tidal currents are both present in estuaries, one is commonly strongest through some degree of tidal asymmetry and the nature of the channel reflects dominant current. These features are also potentially mobile and can be infilled by migrating dunes and ripples causing changes in sediment movement patterns.

Sediment deposits are usually sandy in nature and often form dunes or sand waves, these are sedimentary bedforms observed in intertidal regions by Masselink et al (2006) and in subtidal regions by Zenkovich (1967), sand waves are weakly sinuous features lying parallel to the shoreline that are relatively stable morphodynamically (Hale and McCann, 1982). The initial formation of sand waves remains unclear, potential forcings include multiple wave breaking and undertow (Dally and Dean 1984), standing infragravity waves (Bowen 1980) and shoaling waves (Boczar-Karakiewicz and Davidson-Arnott, 1987). In storm wave dominated environments (micro-tidal) sands are deposited as wave-rippled, symmetrical hummocks. Wave dominated beaches also feature beach cusps which evolve as a function of beachface morphology and swash asymmetry (Werner and Fink, 1993; Coco et al., 2000), these cusps are steep and convex at the horns and concave at the bays (Masselink et al. 1997). In macro-tidal environments, sand waves and ribbons form. Lower tidal flow conditions facilitate the formation of large-scale sand waves which are aligned perpendicular to the direction of tidal flow (Németh et al., 2002) these intertidal sand wave systems often extend offshore into the subtidal zone, merging smoothly with the subtidal bar system (Masselink et al 2006). Sand ribbons form in the higher tidal flows and align themselves parallel to the tidal flow (Harris and

Collins, 1984; Goff et al., 1999). Sediment of a fine grain tends to be deposited in water too deep to be affected by tidal currents, or it is deposited in estuaries.

2.1.2 Beach / Intertidal Morphology and Cycles of Change

Surveying the intertidal zone using standard marine radar is the particular focus of this research. This highly variable zone lies between the mean low water mark and the mean high water mark, hence it is alternately submerged and exposed repeatedly over each tidal cycle. This unique regime makes intertidal areas very complex and leads to unique bedform formations that change over varying spatial and temporal scales. The main formations commonly seen in these environments and their patterns of evolution are described in this section. Figure 2.2 shows a schematic cross-profile of the coastal environment which the developed radar technology is capable of surveying. Key intertidal regions include the backshore and foreshore, while parts of the nearshore region are subtidal, dynamics and morphology in this region are closely linked to those of the intertidal zone and are therefore included here.

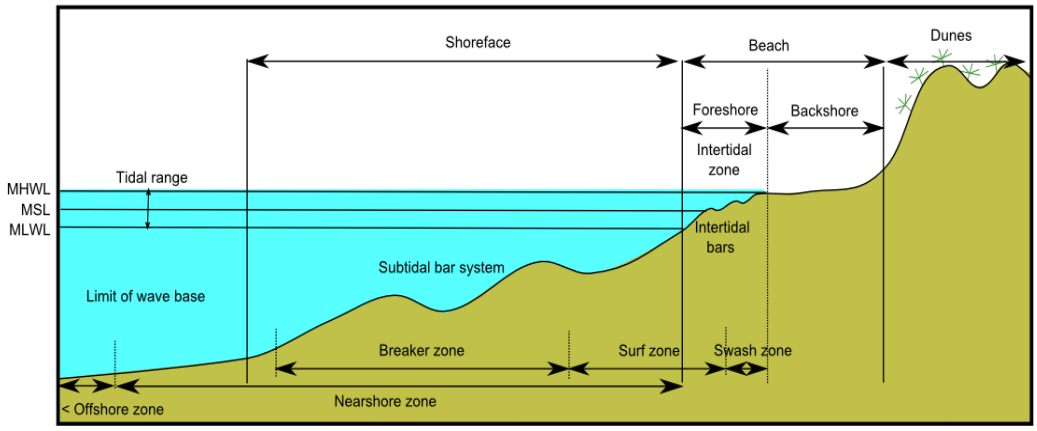

Figure 2.2: Schematic of nearshore zone showing different zones expanded upon from Davis and Fitzgerald (2009).

Sedimentation can take place along the coast as a shoreface-beach-barrier system, the primary depositional feature of wave-dominated coastlines (Roy et al., 1994; Cowell et al., 1995). The initial formation of beaches is constrained by the available sediment in a local system, a function of hydrodynamics, bathymetry, coastline geometry and sediment supply. As these variables are not constant over wide areas, the coast can be broken down into littoral cells, discrete geographical areas where sediment transport occurs to, from and within (Patsch and Griggs, 2008). Beaches are under the continuous influence of waves, winds and tides, and as such, the sediment is constantly being reworked. Some beaches are shallow and exhibit features such as dunes and ripples. Steeper beaches on the other hand may only have a small amount of low angle sediment collected. The shoreface is a general term for the upper part of a continental shelf that may be subject to wave processes (Cowell and Thom, 1994). The upper shoreface is more dynamic and seasonal changes in elevation can be observed over an annual timescale, while the lower shoreface is more established and require storms in order to significantly alter their morphology.

Beaches, which extend from the spring low tide level to the limit of landward topographical change such as a cliff or sand dune system, are classified primarily on their slope profiles. Steep (or reflective) beaches will usually not have an inner surf zone and waves break directly against the beachface, reflecting a portion of the wave energy back. These beaches generally have very poorly developed nearshore subtidal sand bars as little energy is lost as waves move across the nearshore area (Davis and Fitzgerald, 2009).

Shallower (dissipative) beaches have wide surf zones where much of the wave energy is attenuated in the breaker (outer surf) zone through breaking and within the inner surf zone as a result of turbulence. Shoreward decay of incident wave energy is often accompanied by an increase in infragravity waves and surf beat in the inner surf zone along with turbulent bores that can carry sediment onshore (Wright and Short, 1984). Beaches where both of these behaviours are evident are known as intermediate beaches; these different beach types have unique morphodynamics and patterns of morphological change. There are also more complex beach classification such as barrier islands. These are beaches that have detached from the main coast, forming a ridge of sediment running parallel to the beach and tidal inlets where a barrier beach has been breached. Many ports and harbours make use of these beach types for shelter, but they are not observed in this thesis, and their morphology and specific dynamics are outside the scope of this work. In terms of morphological features present at beaches, this section will mostly discuss those present on dissipative sandy beaches of the type observed by the radar system developed in this thesis.

The backshore area of the beach extends from the change in topographical slope which marks the foreshore in a landward direction to a cliff or sand dune system. This area is mostly supratidal and dry except during storm surge and high tide conditions. As such, it is not routinely covered by a normal tidal cycle and thus is not routinely surveyed by the developed radar technique explained in Chapter 5. An awareness of the morphology of this area is relevant however as sediment supply and morphological behaviour are intrinsically linked throughout the nearshore zone. The backshore is generally horizontal with a very gentle gradient and can be identified through the presence of a berm or multiple berm features. The width of the backshore is dependant and variable in accordance with wave energy, inundation and sediment supply. On gravel beaches the backshore appears very different and may be instead dominated by a storm ridge which can often rise several metres above high tide. As the upper intertidal zone and backshore are submerged less often it is frequently colonised by halophytic plants e.g. mangroves in sub/tropical climates and saltmarshes in temperate conditions.

The foreshore area is mostly homogenous in gradient and extends from the subtidal limit to the landward change in topography. This area also includes the swash zone, where waves uprush and backwash as they meet the shore; the wave climate at a given site is instrumental in determining the width and slope of the swash zone. Intense wave action is also able to significantly change the shape of the foreshore over relatively short timescales. The foreshore is separated from the subtidal area by a plunge step; a steep break in topography created by the coarsest sediment, this step can be relatively smooth if wave energy is high. Onshore sediment transport in this region beyond the wave breaking zone occurs through the form of turbulent bores occurring in the surf zone. These bores promote net onshore transport as they collapse in the swash zone, the spatio-temporal variability in sediment transport direction is largely determined by the influence of waves (Plater and Grenvillle, 2010).

The most seaward region of a macro-tidal beach system is characterised by a series of ridges and troughs. These ridges are symmetrical upon formation but quickly deform into asymmetrical shapes, as wave-generated currents pass over the crest. The crests, or ridges are between 0.5 m and 1 m in amplitude and have wavelengths of 100 - 500 m aligned sub-parallel to the foreshore. These intertidal bars are drained of tidal water by a series of cross-shore drainage channels that appear throughout the year and can remain quite stable despite morphological drivers in sheltered regions. Drainage also occurs via alongshore troughs between ridges. The action of these wave-generated currents cause the ridge to migrate further up the beach at a speed that is determined by the amount of time the feature is submerged by the tide. These intertidal bar features have been termed variously as swash bars, ridge and runnel topography (Wright and Short, 1984) and sand waves and there is substantial confusion in the literature where these terms are used interchangeably (Masselink et al., 2006). The large scale morphological features on beaches such as those seen at the multi-barred foreshore near Hilbre Island (see Figure 2.3), are likely a series of low amplitude ridges, as described by Masselink et al., (2006) which fit into *Group 1* bars as described by Greenwood and Davidson-Arnott (1979), these are the same as ridge and runnel topography described by King and Williams (1949). Ridge and Runnel topography can also be seen on intertidal mudflats formed from cohesive sediments (Plater and Grenvillle, 2010). These multiple intertidal bars migrate onshore during low energy conditions such as those often seen in spring or summer months (Carter and Woodroffe, 1997). Bedforms can be completely flattened by high energy waves over very short time periods or influenced by variations in fortnightly tidal current variations which can cause migration or erosion. There is some debate as to the nature of these bars with Masselink and Anthony (2001) demonstrating a case for the formation of bars around mean sea

level as the water level constantly changes. However, Houwelingen et al. (2008) argue that they are formed by a combination of processes across the whole intertidal zone and King (1972) observed ridge locations where the water level is still for the longest time.

Figure 2.3: Aerial image of Hilbre Island northwest UK, illustrating multiple swash bars (Wirral borough council).

As tidal water levels fluctuate both horizontally and vertically, the different hydrodynamic zones (swash, surf and wave shoaling zones) migrate across the intertidal zone and if the tidal range is large enough a given area can be subjected to a large variety of different processes within one tidal cycle (Masselink and Short, 1993). This is a significant morphological driver in the intertidal area as the type, intensity and duration of shallow water wave processes acting upon different regions of the cross shore profile is highly variable (King and Williams, 1949; King, 1972; Masselink and Turner, 1999; Kroon and Masselink, 2002). The sediment transport across shore resulting from wave processes is a product of wave skewness, causing onshore movement

and bed return flow promoting offshore movement. The overall trends of sediment movement are therefore determined by the balance between net onshore movement under calm conditions and net offshore movement during storm events (Sunamura and Takeda, 1984; Russell and Huntley, 1999). Masselink (2004) describes the dominant cycles of net sediment transport according to cross-shore location (shown in Figure 2.4). The illustration shows the influence of tidal rise and fall on wave-induced transport directions across the low amplitude intertidal bar morphology seen on the foreshore of many sandy beaches. The processes of wave transformation over a given tidal cycle; shoaling, breaking, surf zone bores and swash, will vary spatially and temporally depending on tidal range and wave height. This variation will determine the relative importance of each process to the forcing of intertidal (and subtidal) bar migration.

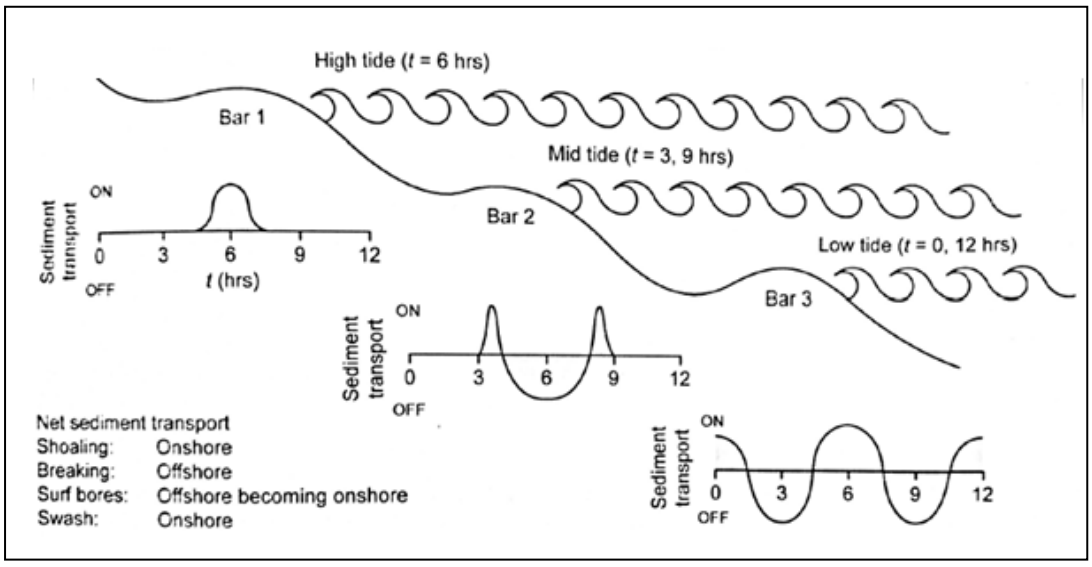

Figure 2.4: Shape function from Plater and Grenville (2010): modified from Masselink et al. (2006) modelling sediment transport at different stages of the tide.

In addition to waves, nearshore currents play a great role in the driving of low amplitude, shore-parallel intertidal bar migration patterns. Currents in this environment are driven by waves (determined by height and angle of incidence) and tidal processes. The currents travel in the longshore direction, using the troughs between bars as their main vectors of movement. It is possible that the troughs of these bars present a barrier to onshore migration of sediment as the current is fed by bores and swash (Kroon and Boer, 2001) which can be disrupted by the trough current as they cross the trough itself. This process has the potential to drive large-scale alongshore migration of the intertidal ridge and trough system (King and Barnes, 1964). These currents were observed in a typical macro-tidal, sandy beach environment in the eastern Irish Sea at Formby beach (Parker, 1975).

In addition to immediate beachface morphology, the intertidal zone also includes areas that are isolated from the beach but which also exposed at low tide. These drying areas vary greatly in their extent and relevance depending on the hydrodynamic climate, tidal range and geomorphology of the local area. They generally occur around the margins of many embayments and along some open coasts that are relatively sheltered. The surfaces of these flats consist of unconsolidated sand, mud or more commonly a mixture and are a major morphological feature of both macro and meso-tidal coasts with low, shallow gradients. Figure 2.5 shows a series of photographs from intertidal flats near Morecambe Bay and within the Mersey estuary.

Figure 2.5: Tidal flats at (a) Fleetwood, northwest UK (b) Mersey Estuary showing Eastham Sands sandbank.

Intertidal flats often have various types of bedforms and channels migrating across them, contributing to changing sediment volume fluxes within the intertidal area. The channels on tidal flats range hugely in their size and temporal behaviour, from dynamic channels that drain water to the more stable, larger channels that are major conduits for sediment movement across flood and ebb cycles of the tide (Davis and Fitzgerald, 2009). Undulations of the tidal flat surface can cause water to become constrained in low areas after emergence of the flat at low tide during an ebbing tide. The channels tend to be broad with sloping walls on sandy tidal flats and

the floors of these channels provide the ideal environment for sediment transport (McCave and Langhorne, 1982) on both ebb and flood tides. This means that areas with tidal asymmetry can be pumped with sediment in a dominant direction determined by that asymmetry (Dronkers, 1986). The primary driving force of sediment migration along these channels is wave-driven currents, where variations in radiation stress across the surf zone caused by wave breaking force long-shore currents which drive water along the channels during high tides (Masselink et al., 2006). Other types of current such as undertow (return flow under incoming waves) and rip currents can also contribute to the forcing of water along these channels. The subaqueous bedforms, such as small dunes on the channel floor can be used to empirically inform the direction of the dominant current flow that created them (Davis and Fitzgerald, 2009).

In addition to bedform evolution and migration the coastal zone is also subject to macro-scale, net changes in elevation. The rate at which these areas undergo change, depends overall on the rate of sedimentation in combination with the stability of the bed with respect to prevailing hydrodynamics. Rates of erosion and accretion are typically measured in metres per year, but many areas are much lower, and will be measured across years or decades, particularly if the area is well sheltered. These rates can be measured using a variety of techniques, primarily the regular sampling of long and cross shore profiles or semi-regular LiDAR surveys. Intertidal beach morphology also shows seasonal and cyclic variability with the profile of a beach often being different between summer and winter (Hayes and Boothroyd, 1969). While winter and summer are terms often used, the cyclicity is not strictly constrained to these seasons, and is often dependent on the wave climate of the study area (Nordstrom, 1980).

2.1.3 Nearshore Subtidal Environments

The nearshore sub-tidal environment begins at the low tide mark and extends seaward beyond the surf zone to the point at which the bed is no longer influenced by nearshore or long-shore currents seaward to the inner shelf. Beyond this point into deeper waters, sediment movement and morphology is less dependent on wave conditions. In the nearshore subtidal region sediment supply, tidal range, wave climate and shelf slope are the most common determining geomorphological factors of this area. The underlying morphology of this area determines the behaviour of waves moving across the area prior to acting on the beach and foreshore itself (Roelvink and Stive, 1989; Aagaard et al., 1998; Ruessink, 1998).

The subtidal areas in between the beach and intertidal flats isolated during low tide are often used as vessel navigation channels. Due to the mobile nature of both beach and sandbank/intertidal flat bedforms it is vital that these areas are monitored lest these bedforms begin to unpredictably infill channels (Demirbilek and Sargent, 1999). The large expanse of soft and deep mud of some intertidal flats, makes their morphology almost impossible to safely study and survey manually (Davis and Fitzgerald, 2009). The survey of these regions is ideally suited to the use of remote sensing, and potential methods of surveying these areas are described later in Chapter 2. Some examples of large intertidal flat morphology that have been monitored include the Wadden Sea (Schanz and Asmus, 2003; Schmidt and Soergel, 2013; Wiehle et al., 2015) the Wash (Blott and Pye, 2004; Pye and Blott, 2006) and the Bay of Fundy (Lambiase, 1980; Uchiyama, 2007).

The most common of morphological features in this subtidal nearshore region is the presence of a system of one to several shore-parallel sandbars. They are typically found on slopes with shallow gradients between 0.005 - 0.03 (Short and Aagaard, 1993; Ruessink and Kroon, 1994). The most landward sandbar is typically 30 - 50 m from the shoreline with the most seaward sandbar being at least twice that distance from the shoreline (Davis and Fitzgerald, 2009), whilst the inner bar is commonly dissected by perpendicular rip channels in which rip currents are drained out of the intertidal zone (Hunter et al., 1979) figure 2.6 illustrates this visually as rips drain between bars.

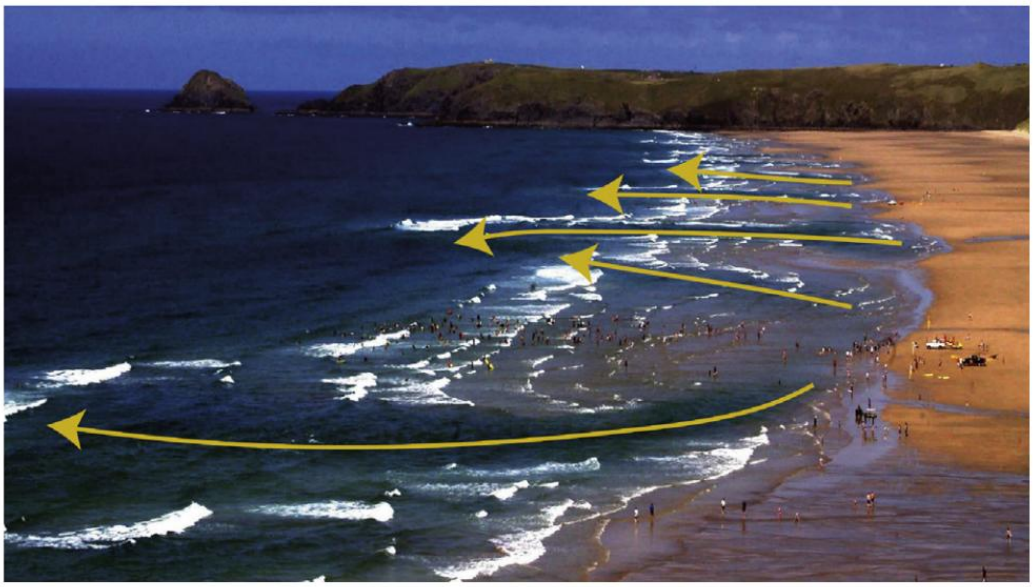

Figure 2.6: Photo showing rip currents draining between bedfroms at Perranporth Beach UK. Photo by Tim Scott taken from Gallop et al (2016).

Spacing between bars in the subtidal region are typically 10 - 100 m with heights that increase further offshore (Ruessink and Kroon, 1994) or increase inshore in multi-bar environments

(Lippmann et al., 1993). These nearshore bars are effected by complex incident wave-induced flow fields caused by breaking, refracting and reflecting processes (Covered in section 2.2) and are thus often called wave-formed bars (Greenwood and Davidson-Arnott, 1979). In a similar manner to intertidal bars, the tidal range determines the frequency and intensity of wave processes affecting the subtidal bars, though subtidal bars are immune to the effects of wave swash and currents resulting from the tidal emptying and filling of troughs.

These bars can occur on a range of different coastlines, but there is a bias in the literature towards the morphology of bars on semi-protected and open coastline rather than bar formation in highly protected or sheltered coastlines. The appearance of these bar systems varies greatly with separate categories including, two-dimensional longshore bars, and a single uniform bar, parallel to the shore (Short, 1975; Bowen, 1980). Three-dimensional longshore bars are non-straight bars where the protrusions are not attached to the shoreline, and they can be regular or very irregular in both shape and pattern (Holman and Bowen, 1982; Lippmann and Holman, 1990). Shore-attached bars are located just below the low-tide water level and are connected to the main shoreline; they are characterised by rip and feeder channels (Wijnberg and Kroon, 2002).

It is well known that these subtidal bars provide sediment pulses to the intertidal zone in the form of migrating bars moving onshore and welding to the beach. This migration generally occurs when wave energy drops to a gentle state (Wright and Short, 1984). The bars can decay in the subtidal zone (Larson and Kraus, 1992) or migration can cease under dramatically lowered wave conditions (Short and Aagaard, 1993). It should be noted that bars can also

migrate in a net offshore direction, removing sediment from the foreshore as observed by De Vroeg (1987), along the coast of Holland and in Cornwall under storm conditions by Poate et al. (2014).

2.2 NEARSHORE HYRODYNAMICS

The combination of local bathymetry, weather patterns and hydrodynamics can significantly affect the efficiency of coastal operations. Rough sea states can delay maintenance operations on defences and renewable energy platforms, while strong cross-currents at the mouth of port entrances can cause navigational hazards and slow down vessel movement or increase fuel usage (Demirbilek and Sargent, 1999). Wave processes affect the coast in a variety of ways, and knowledge of the tide is critical in coastal observation. Surface currents also play an important role in the determination of the morphology of a coastal area. This section therefore describes the basics of these hydrodynamics.

2.2.1 Shallow Water Waves

Waves are one of the primary moving forces of coastal sediment and bedforms as discussed above. They are generated primarily by wind blowing over water and they transport the energy imparted to them over very large distances, as dissipative effects during wave movement in deep water are minimal and can operate over a broad spectrum of frequencies as seen in Figure 2.7.

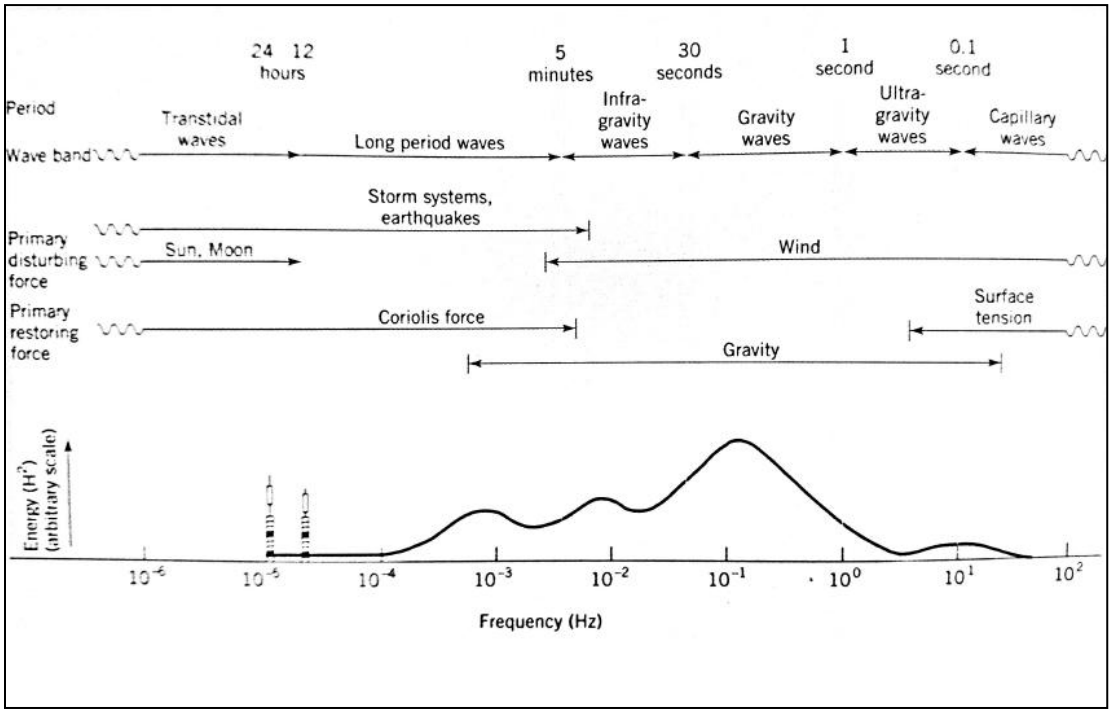

Figure 2.7: Typical frequencies and periods of ocean waves from Davis and Fitzgerald (2009).

The coastline serves as the region where waves break and that transported energy is dissipated. This dissipation of energy in the surf zone can be very high, enough to force major changes in both sandy and rocky coastline. The dynamics and mechanics of deep-water waves are covered in detail by Dalrymple and Dean (1991), Wiegel (1964), Mei (1989) and Phillips (1980); this section will primarily deal with the modification of waves within shallow water.

As waves propagate towards the shoreline, water depth begins to decrease and subsequently decreases the wavelength of the incoming wave, described by the dispersion relationship and Airy wave theory (Airy, 1845). As the wave period is fixed but the wavelength is decreasing, the wave speed decreases with progression into shallower waters. As the bottom profile over which

the wave is travelling is often irregular, a long-crested wave will slow down in different locations, causing local changes in wave direction or refraction of the water waves. The result of this refraction is that waves move away from regions of deep water and towards shallow water, potentially focussing wave energy onto headlands and shoals or sandbanks. In a simple case of waves propagating obliquely over shore-parallel, regular nearshore bathymetry *Snell's Law* can be used to model the patterns of refraction. While this law can be used to draw out predicted refracted wave vectors on bathymetric charts, modern computer models use more complex numerical methods (Thomas and Dwarakish, 2015). In addition to waves slowing down in shallow water, wave heights also increase due to a conservation of energy argument and the reduction in group velocity or celerity. This increase in wave height becomes visible as waves enter shallow water, known as wave shoaling.

Wave diffraction is also a very important aspect of shallow water wave behaviour. This process occurs where sudden changes in wave height are promoted by the wave encountering a surface penetrating object such as a rock, offshore breakwater or a semi-exposed ship wreck. Directly behind this object, waves are not present due to sheltering by the object; using light as a substitute this causes a shadow in a incoming wave field (Dalrymple et al., 1984). Changes in wave height propagate crestwise and cause waves to change direction bending in towards the shadow zone. This effect often appears as though the structure causing the effect is the source of multiple propagating waves and can be somewhat described by *Huygens Principle.* Modelling of this effect has advanced significantly from simple ray tracing models (Noda, 1974), and structured grid models (Dalrymple, 1988) through spectral and directional models (Brink-Kjær, 1984; Booij and Holthuijsen, 1987). Modern models include wave-current-bathymetry interactions, input energy from wind and estimate wave breaking such as the Simulating Waves Nearshore (SWAN) model (Holthuijsen et al., 1993). Waves can also reflect from the coastline or

interact with currents, certain coastal structures can cause these reflected waves to have damaging effects (Barnett and Wang, 1988; Dean, 1986; Santiago et al., 2013).

The wave breaking process is the point at which the greatest amount of energy is transferred onto the beach. Waves can break in both deep and shallow water, in the latter case it is caused by excessive energy input. However in shallow waters waves continue to shoal, decreasing in speed and increasing in wave height until they become so large and unstable that they collapse. Wave breaking can be related to the surf similarity parameter ζ an expression of the ratio of beach slope tan β to the square root of deep water wave steepness:

$$\zeta = \frac{\tan \beta}{\sqrt{\frac{H_0}{L_0}}} \quad \textbf{(1)}$$

where H_0 is the offshore deepwater wave height and L_0 the deepwater wavelength. Typical wave breaking characteristics are described in detail by Battjes (1974), including important breaker index figures for spilling, plunging and surging waves. For modelling of wave breaking on a simple profile Dally et al. (1985) developed a model based on a series of thresholds or breaking criteria informed by water depth where waves shoal until the highest threshold before breaking. This model was expanded to include a realistic surf zone for complicated beach profiles by using a wide distribution of wave heights to inform breaker behaviour (Dally, 1990). The detailed microscale modelling of breaking waves is difficult where non-linearities in wave behaviour and water turbulence make modelling difficult.

Waves break at the break point and progress upshore across the inner surf zone then into the swash zone. This process causes the upper part of the beach to become alternatively wet and dry due to successive incoming waves breaking. Onshore flow as the wave breaks (uprush) and resulting offshore flow (backwash) is known to be asymmetric (Hughes et al., 1997) with uprush having larger velocities and shorter durations; also when backwash interacts with the next incoming wave it forms a vortex which carves out the beach (or plunge) step. The patterns of swash flow over the beachface are shown in Figure 2.8. This asymmetry has implications for sediment transport in the swash zone (Butt and Russell, 2000; Masselink et al., 2010). A comprehensive review of swash zone hydrodynamics is given in Elfrink and Baldock (2002).

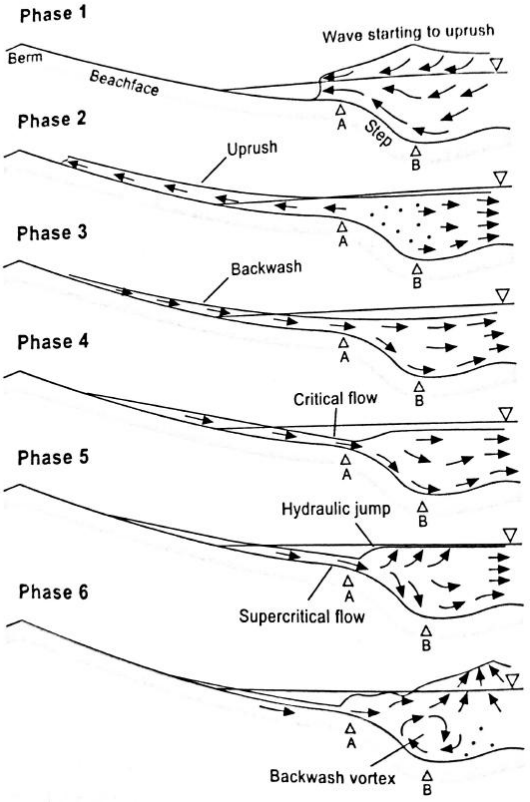

Figure 2.8: Swash patterns over beachface during uprush and backwash from Hughes and Turner (1999).

2.2.2 Coastal and Estuarine Tidal Modification and Shallow Water Currents

The behaviour of progressing tidal waves changes dramatically as the wave begins to shoal in shallow waters. In constricted areas such as inlets or estuaries, the tide can be modified significantly, Dean and Dalrymple (2004) provide an eloquent description between the difference in ocean tidal elevation and waterlevel elevation within an inlet, bay or estuary as follows. The ocean tide is characterised by a single tidal amplitude a_o equivalent to half the tidal range and with a frequency of σ which varies between semi-diurnal, diurnal or mixed. The ocean tide is simplified to:

$$\eta_o(t) = a_o \cos \sigma t \quad \textbf{(2)}$$

and the tide in the enclosed bay area is:

$$\eta_B(t) = a_B \cos(\sigma t - \in_B) \quad \textbf{(3)}$$

In this case a_B is the bay tidal amplitude and $\in_B$ is the phase lag or shift of the tide in the bay with relation to the ocean tide seen in Figure 2.9. This results in an ocean tidal amplitude greater or smaller than those of the bay at the same time as the bay tide lags by the phase angle $\in_B$. When high tide is reached in the open ocean, the water begins to flow through the constrained channel to the bay or estuary and this area is still filling with water (flood tide) until the water levels equalize. Water flow through the channel then ceases (known as slack water) and the pattern repeats as tidal levels fall (ebb tide). Sometimes the sheer inertial effect of large volumes of water entering the bay can cause the water to continue to flow after the water levels

equalize. Equations can be used to develop this crude approximation of tidal amplitude, including the conservation of mass, the momentum equation and dynamic equations, (Dean and Dalrymple, 2004); however these are beyond the scope of this work. It is significant that sometimes these phase lags can cause differences between recorded tidal elevations at the mouth of a bay or estuary and actual tidally-driven waterlevels. Tidal phase lags of nearly one hour over just several kilometres were observed in a lagoon environment (Hessner and Bell, 2009), in a macro-tidal environment like the Dee estuary, this can mean a rise of several decimeters.

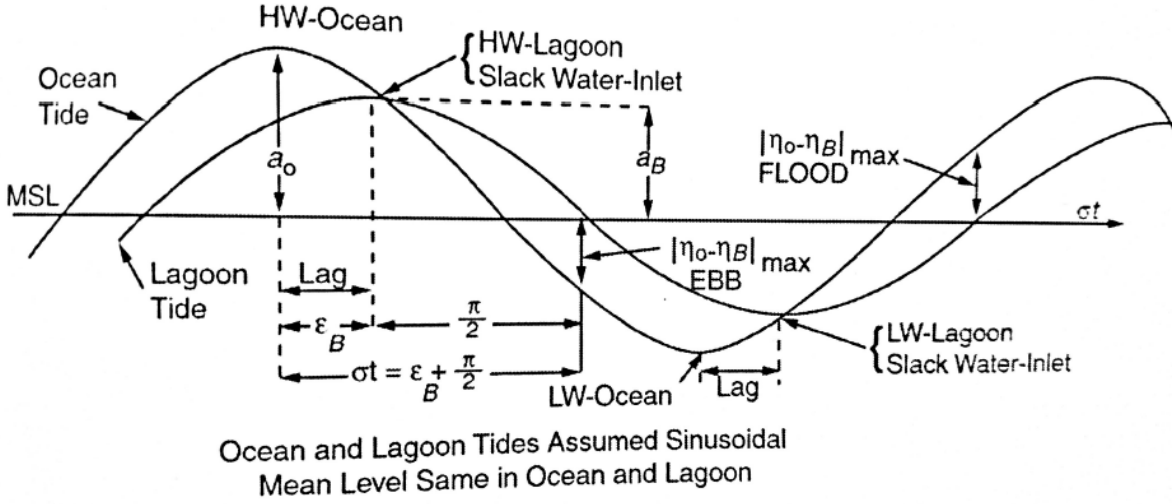

Figure 2.9: Time elevation plots of idealised ocean and bay tides from Dean and Dalrymple (2004).

An additional component in the difference between open sea tides and enclosed tides is the effect of tidal set up. This can result from strong winds, fresh water inflows from fluvial sources or frictional factors that determine flow speed (a change in bed roughness for example). In the

case of enclosed water body being more saline than the open water body, a mean set up is required to balance the salinity and net inflow to the bay will result in a greater surface elevation. Variations in the depth of channels and inlets can also cause this non-linear water set up effect (Dean and Dalrymple, 2004).

The physical shape of the morphology of many estuaries, inlets and embayments can also effect the propagation of the tide. Rotary tidal waves cannot exist in narrow areas, and therefore the tide moves in and out of estuaries constrained by the seabed which becomes (generally) shallower in the landward direction. This causes not only increase in frictional forces due to constriction but also an amplification of the tidal range from the overall steepening of the shoaling tidal wave. This effect is most common in funnel-shaped estuaries. In some very large estuaries a similar effect produces a tidal bore, where the over steepening of the tidal wave causes it to begin to break. They are often < 1 m in height but the largest in the Qiantang river reach 5 m and travel up to 20 kph (Davis and Fitzgerald, 2009).

The effects of tidal asymmetry may also cause a difference in water levels between the mouth of an estuary and those further in the estuary. When the ebb and flood of the tide show equal durations and equal velocities the tide is symmetrical. When the tidal wave is distorted on entry to the estuary, these parameters may become unequal and introduce a degree of asymmetry. A changing gradient of friction with distance from the estuary mouth (Dronkers, 1986) causes a long, weak ebb and a strong, short flood. If this flow exceeds the threshold for sediment motion then sediment transport is flood dominated. Many researchers have shown that shallow water and tidal flats promote flood asymmetry and deep channels promote ebb dominance (Aubrey

and Speer, 1985; Friedrichs and Madsen, 1992; Stanev et al., 2003). It is thought that many estuaries show alternation between flood and ebb asymmetry over timescales of more than 100 years (Pethick, 1994). Wang et al. (2002) showed that tidal asymmetry can be represented by a distortion of the M_2 (semi-diurnal) tide by higher frequency overtides, mainly the M_4 harmonic (Friedrichs and Aubrey, 1988). The dominance of one or another of these can influence net sediment flux (Brown and Davies, 2010) in addition to changing water levels.

A combination of nearshore tidal and shallow water wave processes cause currents which are created near to shorelines to have very different properties to the ocean currents. Waves are a dominant driver in the formation of nearshore currents. Longshore currents are caused by differential breaking due to refraction (Longuet-Higgins and Stewart, 1962) of incoming waves moving through the nearshore and surf zones. These incoming waves set up a steady current that flows parallel to the shore line, sometimes known as the littoral current. The velocity of this current is directly related to the size of the breaking waves and the angle of wave approach to the shore. This current is confined to the surf zone and acts like a river channel in terms of velocity distribution, they typically move at several 10's of centimetres per second, although in strong stormy conditions they can exceed 1 m/s. These currents work with the waves to transport large volumes of sediment along the shoreline. As the waves interfere with the bottom, they steepen then break, releasing large amounts of sediment. This material is then loaded into suspension and transported along the shoreline by the longshore currents. The current may flow in either direction due to these variations, meaning that there may be a large amount of sediment flux over time, but the net transport in or out of a given area may be small due to the back and forth nature of the current. "Littoral sediment transport rates" refer to the annual amount of sediment transported in a given length of coast. These currents and the associated littoral transport occur in any coastal environment where waves are refracted as

they approach the shore. They are however more common and effective on open beaches, bays, estuaries and lakes. Currents such as undertow also occur in the swash zone where the action of uprush and downrush can cause significant sediment mobilisation. Current velocities were measured in this zone to sample suspended sediment transport and it was found that although significant sediment was mobilised, frequent reversal of flow direction often limits net transport (Blenkinsopp et al., 2011).

Tides also produce and influence currents in the nearshore area, it is mainly these areas where the tidal wave becomes constricted and the currents of tides are most readily observed; these areas include harbours, tidal inlets, and rocky straits. As the tides rises faster in the ocean than it does nearshore, a slope of water is created and as water flows down a slope gradient, this is the driving force of the tidal current. As the water enters or moves through a bay or inlet, it becomes a flood-tidal current. The state known as slack water occurs when the tidal water in the bay and the ocean are in equilibrium, this can be high or low slack water if the tide is in or out respectively. The strongest of these tidal currents occur when the tidal slope is steepest, usually at or near mid-tide; they are at their highest velocities (up to 3 m/s) during spring tide when the exchange of water between ocean and bay is at maximum. These high velocities also occur along non-sandy beaches, regions with large tidal range and bay areas with narrow constrictions. An example of a strong tidal current is along the northern coast of Norway, where Vestfjord connects to the Norwegian Sea. Tidal currents flowing through this region can reach speeds of up to 4 m/s and create strong whirlpools that make travel through the region extremely dangerous during times of peak flow. They are referred to as the maelstrom and local shipping avoid these perilous eddies (Bird, 2011).

2.3 FACTORS INFLUENCING COASTAL CHANGE

The primary morphological and hydrodynamical processes that drive coastal nearshore change have been discussed in the above sections. These processes are influenced by various unique factors at the coast. The negative impacts of this coastal change manifest as erosion and adverse accretion or siltation. Storms and changing climate can be significant drivers of this coastal change, and anthropogenic developments in coastal areas also effect the morphological evolution of nearshore zones in addition to effecting hydrodynamics.

2.3.1 Impacts of Coastal Change

In coastal areas sediment is either accreted or eroded from any given location. It is extremely rare that sedimentary systems are in exact equilibrium, as even relatively stable systems change and are said to be in a state of dynamic equilibrium (Blenkinsopp et al., 2011). The rate of this sediment accretion or erosion varies drastically between location, and is dependent on many environmental variables including fluvial erosive potential, rainfall rates and biological action in estuaries, and the erosive power of waves and tides at nearshore environments. Excessive accretion or erosion of sediment in an established coastal or estuarine environment is generally considered a negative effect. For example sediment erosion at established coastal or estuarine riparian wetlands serves to remove valuable habitats, reducing ecosystem biodiversity and removing an erosion buffer zone in the process (Barbier et al., 2011). Conversely, increased sedimentation for example in a navigation channel into an estuary or harbour is detrimental to

trade and commercial shipping. In order to remediate the effects of sedimentation, heavy industrial activity such as dredging must be performed (van Rijn, 1986).

Changes in morphology can compromise navigation channels and inlets in a variety of ways (FitzGerald et al., 2000). The United States spends more than $100 million annually on Federal channel maintenance, dredging between 50 and 100 million m^3 of sand (Rosati and Kraus, 1999). At a regional level, strategic ports located in morphologically dynamic areas such as river deltas can experience significant navigation channel disruption due to sedimentation. An example of this is Port Harcourt located in the Bonny River estuary which empties into the Niger Delta region, Nigeria. This port is a crucial gateway to the oil-producing region and the complicated system of sandbars and shoals combined with dynamic bank and shoreline erosion present navigational risks to shipping operating in the vicinity of the port. Often the series of exposed jetties along the coasts and at the small estuary islands are isolated as the shoreline is eroded (Diop et al., 2014). Another example of a vulnerable area is the mouth of the Amazon River, where sandbanks are known to encroach upon the critical navigation channels. Sediment migration rates of up to 250 m/year have been observed here (Fernandes et al., 2007), causing significant disruption to the operation of the ports. At a more focused, local scale, the Port of Liverpool in the UK removed an average of 1.86 million tonnes of dredged sediment annually between 2005 - 2009. This material was extracted from the navigation channel and berthing zones, areas which are known to be significantly influenced by migrating sedimentary bed features (Bailey, 2009).

Migration of allochthonous sediment into estuaries is a prevalent problem in port management, specifically in estuaries where ports are present. The changing sediment budget combined with climate change-induced rising mean sea-level and changing bathymetry, can result in the "squeezing out" of valuable intertidal habitats which lie between hard sea defences and the shoreline (De Vriend et al., 2011). Experiments have been conducted involving the disposal of dredged material at eroding beach sites in order to supply sediment replacement (van der Wal et al., 2011). Schemes such as this, along with planned and ongoing large scale sand-scaping/ sand engine operations in the UK and Holland (see section below for more details), which seek to change the shape of a coastline in order to increase the socio-economic potential of the area, would benefit greatly from a cost effective method of long-term intertidal monitoring.

2.3.2 Morphological Change Across Temporal Scales

Beaches and the intertidal areas are subject to changes across a variety of temporal scales, from near-instantaneous event driven change, changes over individual tidal cycles (fortnightly), between seasons, and changes on an inter-annual scale. The interaction between hydrodynamic processes and beach sediment can occur under one of two general states. Most prevalent of which are *normal* conditions where wave conditions are of equal or less than average intensity (low wave heights < 1 m and 8-12 s periods), with a small addition of locally generated smaller period waves. This situation leads to an accretionary beach as the dominant processes are those of deposition, and this is the common environment of many sheltered coastlines (Davis and Fitzgerald, 2009).

Alternatively other conditions are conducive to erosion: storms are relatively short in duration but are the dominant process on many beaches. Storm conditions promote increased wind-wave heights and these steep waves entrain large volumes of sediment through longshore transport and flow motion. Swash zone energy is also greater under these conditions with uprush and backwash being more extensive (Austin and Masselink, 2006). The profile of a beach post-storm is in general flattened and relatively featureless with material having been moved offshore to the nearshore bar system which will also have been flattened to some extent and moved offshore, often by up to tens of metres (Davis and Fitzgerald, 2009). In the absence of successive storms, the beach profile begins to enter its recovery phase, whereby calm conditions again promote the onshore movement of sediment. Nearshore sandbars begin to resume their original position and as the ridges become asymmetrical they begin landward migration due to washover during flood tide. Timescales of recovery vary greatly between as little as weekly to several months depending on the strength of prevailing currents. The reoccurrence of storm conditions will interrupt recovery and as storms are frequent over winter months, beaches often do not recover and assume a winter beach profile (Thom and Hall, 1991). Other near instantaneous events may also contribute to changing beach morphology including hurricanes and tsunamis (Dawson, 1994; Tanaka et al., 2012) and high river inflow events (Maillet et al., 2006).

The alternating sequence of storm and non-storm beach conditions is the most overtly seasonal and predictable cycle of change. However changes also occur over less pronounced cycles including the (semi) diurnal and monthly lunar tidal cycles. The variations in tidal elevation allow waves to act at different regions of the foreshore. During neap tides, only a narrow range of the beach is subjected to waves compared to a larger area during spring tides causing

variations in beach profiles over tidal cycles (Miles et al., 2013). The changing tide also affects hydrodynamics by changing the way that longshore currents behave and the areas which they influence.

Variations in wider ocean atmospheric systems can also introduce a cyclicity to coastal morphological change over longer timescales. For example the El Niño Southern Oscillation (ENSO) with a periodicity of around four years (Philander, 1999) causes oscillations in the Pacific Ocean between warmer (El Niño) and colder (La Niña) conditions (Wang et al., 1999). It causes changes in precipitation and tropical storminess and this climatic variability can produce storm clusters and lead to periods of intense coastal erosion at often unexpected times (Dingler and Reiss, 2002). Severe storms were experienced during the El Niño of 1982 - 1983 in California causing significant erosion (Storlazzi and Griggs, 2000) and similar effects resulting from extreme high waterlevels were observed during 1997 - 1998 El Niño along the US West Coast (Allan and Komar, 2002). Other variational phenomena include the North Atlantic Oscillation (Perry, 2000), which causes pressure changes in the North Atlantic and leads to cycles of severe winter storms (Masselink et al., 2014) in northern and western Europe (Viles and Goudie, 2003). The Atlantic Multidecadal Oscillation (AMO), with a 65 - 80 year cycle of changing temperatures causes reduced rainfall in the USA (Enfield et al., 2001). These variations provide an additional longer term cyclicity to beach morphology that can be difficult to quantify.

2.3.3 Climate Change and Rising Mean Sea Level

Exacerbating the pressure on the coastline is sea-level-rise (SLR) (Kirshen et al., 2014). SLR has the generalised effect of reducing the amount of beach available to absorb wave energy and

allowing high energy, storm waves to attack further up beaches, transporting sand offshore. Many coasts have seen increased erosion with European coastlines losing 25 % of established sand dunes during the twentieth century and the remaining 75 % at great risk from SLR (Hanley et al., 2014).

In addition to SLR, changes in precipitation and vegetation patterns brought on by broad climate change have major impacts on sediment supply in catchment areas and associated sediment delivery to the coast. SLR has a somewhat more profound effect on sedimentation, it changes the base level of sediment systems, resulting in either the inundation of coastal environments or exposure of shallows coastal shelves depending on whether regional sea level rises or lowers. These changes are in general extremely slow, but may have profound impacts on sedimentation.

In combination with SLR and climate-induced changes in sediment regime, it is possible that broader climate change will contribute to erosion of the coast, due to a potential increase in the frequency and magnitude of high-energy storm events, which are widely recognized as some of the major driving forces of coastal morphological change (Tătui et al., 2014). Advanced models have been developed to predict beach morphological response to changing sea level and storms such as the X-Beach model (Roelvink et al., 2009). The storm season of 2013 - 2014 (Figure 2.10 shows the onset of a storm in December 2013 at New Brighton, northwest UK), saw unprecedented beach and dune erosion at several sites in Europe including the south-western coast of France (Castelle et al., 2015) and the north-western UK (Dissanayake et al., 2015). Whilst the UK experienced the largest recorded high water level, this trend of increased storminess is predicted to continue (Wadey et al., 2014; Wahl et al., 2011).

Figure 2.10: Onset of storm late afternoon in December 2013, New Brighton, northwest UK. New Brighton lighthouse and Liverpool Docks visible in the background.

2.3.4 Anthropogenic Influences on Coastal Morphodynamics

Although it is thought that present sea-level-rise due to climate change is impacting low lying coastal systems, the more important concern presently is the dramatic short-term effects of anthropogenic activities on sedimentation. Impacts on sedimentation can be a result of both direct constructions such as breakwaters, seawalls and groynes or can effect sedimentation indirectly through the building of dams (Snoussi et al., 2002), reservoirs (Xiqing et al., 2005), and changes in coastal land use. Inappropriate placement of coastal engineering, whether due to ineffective or insufficient monitoring or incompetence can exacerbate the situation and lead to

further adverse effects. It is therefore vital to be aware of the broad effects of different constructions on coastal morphology.

Construction of hard engineering is undertaken to prevent localised erosion to a beach through rock armouring, seawalls and revetments, or to restrict migration of sediment in the case of groynes, jetties and breakwaters. It is clear that unless a coastal zone is at capacity during defence construction, there will be adverse effects on adjacent areas as a result of hard engineering. Preventing longshore drift can potentially starve another area of sediment for example (Dean and Dalrymple, 2004).

Rock armour is often deployed under sand dunes so it is covered for most of the time but serves to anchor dunes during storms. A mitigative approach for rock armouring includes the placement of additional sand annually to replace that which would have entered the system had the rock armour not been there. This maintains a more natural littoral cell behaviour but requires extra costs in the form of monitoring and maintenance (Dean, 1986).

The traditional purpose of groynes is to prevent erosion in areas that experience significant longshore transport. They are usually built as a vertical barrier extending perpendicular to the shore (Nordstrom, 2014). Groynes often exhibit clear filling behaviour where the updrift side receives large accretion while the downdrift area is eroded severely. It was found that this pattern occurs even if there is no significant erosion of the overall beach system (Kamphuis, 1991). If this downdrift erosion is not managed and redistributed, significant amounts of material may be lost to the wider nearshore area as this pattern continues. To prevent this,

groynes are often built an equal distance apart along a coast to form groyne fields. This means that downdrift sediment should collect only in the furthest alongshore groyne (Dean and Dalrymple, 2004). A Detailed study of morphodynamics caused by groyne structures at a site in the northwest UK was carried out by Miles et al. (2013), who found that certain wave conditions caused extensive scour around groyne structures that was spatially variable according to the tidal conditions.

Breakwaters are built to reduce the amount of wave energy that reaches a coastline and provide a safe haven for small boats and swimmers, in addition to preventing erosion. They are often built in multiple series alongshore (Suh and Dalrymple, 1987) as a single offshore breakwater will cause localised erosion due to the focussing of wave energy. They can be fully emergent to prevent overtopping, submerged to prevent the visual impact or partially submerged. Depositional features called salients or tombolos, can often appear behind offshore breakwaters (Marc, 1954); these may present a barrier to longshore drift, potentially preventing adjacent areas being nourished. With careful construction the continued exchange of sediment from one side of the salient to the other can be maintained (Dean and Dalrymple, 2004). Significant circulatory gyres can develop in the lee of detached breakwaters, aiding salient formation (Axe et al., 1996). These breakwaters are a common sight on exposed sandy beaches; indeed there are currently over 4,000 along the Japanese Coastline (Seiji et al., 1987). The SWAN spectral wave model was used to examine the stability of breakwaters and changes in the directional wave field following the interaction with breakwaters by Ilic et al. (2007) which showed that breakwaters significantly affect wave behaviour in the nearshore, which in turn affects morphological evolution.

Revetments are shore-parallel constructions used to prevent landward beach erosion, and can be made of stone, concrete or asphalt. Their primary purpose is to stimulate wave breaking and energy loss during run up. Often they are constructed of multiple layers of specifically sorted and graded rocks (U.S. Army Corps of Engineers, 1984). They are usually high enough to prevent most wave overtopping (this overtopping can be modelled using XBeach-G (Masselink et al., 2014)), and deep enough to prevent undercutting. The usual response of a beach to storms is loss of material to the nearshore bar system, and the build-up in nearshore bars reduces future wave energy. The presence of a revetment often prevents transfer of sufficient sediment from the beach (Stive et al., 2013) to promote offshore bar build up, which can cause issues in the future.

The most common of hard engineering solutions seen on many coasts is the seawall. Construction material varies but most common is the curved concrete wall, reinforced with steel. The curved nature of the wall attempts to deflect incident waves and reduce scour at the toe (Ilic et al., 2007). The seawall aims to protect infrastructure, lives and property by minimising wave overtopping and land loss on vulnerable coasts with high erosion rates. There are areas where beaches have been significantly eroded following seawall construction or have suffered large downdrift erosion (Kraus, 1988). Wave tank experiments have shown that storm-induced erosion is only reduced to 60% with the addition of the seawalls (Barnett and Wang, 1988). Examination of shoreline erosion caused by seawalls in Monterey Bay, California where littoral drift rate is high, found that there was little to no scour and no net erosion due to the seawall even when exposed to storms (Griggs et al., 1991). Conversely in some areas prevention of seaward erosion from the shoreline by the seawall prevented the nourishment of offshore bars and the system removed extra material from adjacent beaches, to address the sediment

requirement (Walton and Sensabaugh, 1979). The length of the seawall also determines the extent to which scour occurs at the flanks of the seawall (Komar and McDougal, 1988). Seawalls are theorised to be the causes of several other erosion issues in the coastal environment, including causing steeper shore profiles and therefore greater wave heights, and the ideal placement and exposure of the seawall in the cross shore direction is still unknown owing to lack of data (Dean and Dalrymple, 2004). Figure 2.11 shows a selection of hard engineering structures from around the northwest UK coast.

Figure 2.11: Examples of hard engineering schemes in the northwest UK (a) groyne field, Cleverlys, (b) revetments, north Wirral coast, (c) Seawall at New Brighton northwest UK (Person pictured for scale), (d) rock armour exposed at New Brighton marine lake (North Liverpool visible in the background).

In addition to hard structure construction, one of the most non-intrusive methods of coastal erosion mitigation is beach nourishment, or beach fill (Hanson et al., 2002). The placement of

sand on a beach to restore or build has the objective of widening the beach to provide additional recreation area, protect against storms (Verhagen, 1996), to provide (rarely) additional environmental habitat (Leewis et al., 2012). This extra sand provides a buffer to high energy wave events; if this placed sand is eroded it prevents loss of more established sediment and protects the foreshore. Much of the sand 'eroded' from a beach nourishment scheme is often either transported offshore or redistributed through the bar system and can be returned during conditions of milder waves. One of the many reasons beach fill is popular, is that it is one of the few techniques that introduces additional sand into the systems, where other engineering techniques strive to redistribute or conserve existing sediment resources. It also has advantages in terms of public acceptance as it does not affect the visual appearance of the sea front as do other protection schemes. Once the sand is in place, usually at the steeper section of the slope beyond the equilibrium profile (Dean and Dalrymple, 2004) three stages of change occur. A cross-shore transfer of sand from the upper to lower portions of the profile occurs first, causing the appearance of beach recession but not a loss of volume. This is followed by a spreading of sediment alongshore to ameliorate ongoing shoreline erosion processes; in this way sediment is redistributed into the system (Blott and Pye, 2004). The timescales over which beach nourishment takes effect are on the order of weeks to decades, and ideally should be monitored throughout their lifecycle to justify the large costs involved in deploying a beach nourishment scheme. The empirically-based method of deploying beach nourishment described by Verhagen (1992) is described in Table 2.2.

Step Number	Processes
1	Perform coastal monitoring, regular surveys and measurements for at least 10 years
2	Calculate loss of sand in cubic metres per year per coastal section or littoral cell
3	Add 40% onto this volume loss estimate
4	Multiply this quantity by the desired lifetime of the project eg 5 year steps before reassessment
5	Place this quantity of sand on the beach between the low water - 1 m contour and the dune foot

Table 2.2: Steps to estimate requirement for estimation of sediment need prior to beach nourishment after Verhagen (1992).

The longevity of a beach nourishment scheme, ultimately depends on the wave climate to which it shall be exposed. Commonly a probabilistic approach that estimates a range of wave scenarios is used to estimate potential wave conditions (Strine and Dalrymple, 1989) and the morphological response can be predicted (Benedet et al., 2004). These schemes are also very vulnerable to SLR over longer timescales. The prediction and quantification of vulnerability to SLR is difficult and requires a combination of short-term predictive models and wide area morphological evolution modelling (Stive et al., 1991). In addition to direct placement of sediment onto an eroding beach, there is also interest in the creation of artificial subtidal berms to dampen waves in stormy conditions or be transported to the beach in calmer periods (Hands, 1991; Otay, 1994). These schemes also vary greatly in size and scope, the larger versions are also termed sand engines (Stive et al., 2013), zandmotors (Mulder and Stive, 2011) or the general process of sandscaping in the UK (Prime et al., 2015).

An additional option in coastal defence remains to "work with nature" (Cooper and McKenna, 2008) which involves the use of semi-artificial wetlands including mangrove swamps and dune systems to protect the shoreline from erosion in place of hard engineered structures. Dune

systems serve to provide a significant buffer to high energy wave, extreme storms which elevate water levels and increase erosion, possibly leading to coastal flooding. However a well developed dune system will attenuate storm energy and be eroded in place of the beach, reducing the flood risk. Sediment eroded should return to the beach and eventually the dunes (Masselink et al., 2014). Manual intervention in the stabilisation and establishment of additional dune systems has been carried out using extensive fencing and allowing for sand to stabilise (U.S. Army Corps of Engineers, 1984). The stabilisation of the vegetation on the dune system helps to stabilise the dunes and increase their resilience to erosion, Short and Hesp (1982) describe the vegetation distribution of different dune classifications. Figure 2.12 shows a stable dune system along Ainsdale Coast northwest UK.

Figure 2.12: Soft defences "working with nature" managed established sand dunes at Ainsdale northwest UK.

If there is little or no critical infrastructure on the shoreline being eroded then managed realignment of the coastline may be used instead of a strategy of protection. In the UK this decision is taken at a local - regional level and is known as a shoreline management plan (French 2004). Managed realignment involves ceding land back to the sea and is often much cheaper than defending the land, and also serves to make the coast and estuaries more 'natural' (Leafe, 1992). Managed realignment also has potential risks in the remobilisation of pollutants (Emmerson and Birkett, 2000) and eutrophication from nutrient release (Blackwell et al., 2004), but managed realignment is now being given serious consideration in the planning of shoreline management strategies (French, 2006).

Regardless of the method of beach protection implemented (or not), coastal areas must be monitored. Changes in coastal morphology may be seen over timescales as short as the hour during stormy conditions or as long as decades, as such surveys must be performed regularly and a reliable cost effective method of doing so is currently unavailable to coastal managers. The proposed radar system will allow remote sensing of intertidal sedimentary environments without the need for manual repeated surveys. Observations will be made continuously allowing potential mitigation efforts to be coordinated much more effectively and allowing better targeting of vulnerable areas which need more accurate and focused surveys, such as a terrestrial LiDAR scan (e.g. Almeida et al., 2015).

2.4 PORT AND COASTAL SURVEILLANCE SYSTEMS

Given that coastal areas cover such large areas and are regularly transited by vessels of a diverse international origin, they represent a challenging area to monitor and are a potential weak point in a nation's defence network. The United States is an interesting case in point, with a maritime industry contributing $742 billion to the GDP in 2003, 95,000 miles of shoreline and 25,000 miles of navigable waterways (Emerson and Nadeau, 2003). With a unique position in international relations, the United States must use all available resources to monitor this large area. The safety and security of private corporation assets such as oil rigs and commercial shipping operating in coastal zones must also be preserved in order to maintain a competitive international reputation for business. Therefore a method of monitoring activity over a wide area is required.

Radar is already utilised extensively in this role along industrialised coastlines and the commercial partners for this project, *Marlan Maritime Technologies,* provide comprehensive monitoring systems for ports. The product, *IRIS™* is a VTS (Vessel traffic system) combined with a network of CCTV cameras and radar to aid vessel navigation and combining this with the mapping ability of the work presented here will allow greater situational awareness of potential security threats to be gained.

A wide variety of radio and optical sensors are needed to survey coastal areas with diverse operating ranges and resolutions, an overview of which will be given in this section. These systems are a crucial part of coastal management. In addition to these high level activities they

can also be used in more routine tasks such as preventing fly tippers or illegal fishing/cockle picking for example.

There are some sensors and specific configurations of radar systems that are designed purely with both the safety and security of a ship or port in mind. For example some systems combine thermal imaging and radar with GPS satellite, the main application being in coastguard security, and search and rescue situations. *Kelvin Hughes Marine Systems* use this technique in their *MantaDigital™* product, whereby a high performance thermal imaging camera is integrated to a high performance radar system and can be set to 'man overboard' detection mode. In this mode the radar can pick up targets as small as an individual in rough water and the target can be confirmed using the thermal imaging camera. The location of the target can then be effectively relayed to coastguard and lifeguard authorities. This application is clearly superior over using only a searchlight, or traditional radar system, signals from which can be misinterpreted in bad weather situations. This system can also be helpful in identifying pirate or smuggling vessels in bad weather, as traditional radar would only indicate a target; a thermal imaging system therefore allows the target to be identified as a threat, providing greater intelligence and situational awareness.

2.5 SURVEYING AND REMOTE SENSING OF THE COAST

In order to gather data from the coastal environment, many methods have been utilised in recent years. There are a diverse range of in-situ instruments used in coastal management to precisely measure and record coastal environmental data. Water surface elevations, wave state and directionality are measured by directional waverider buoys (O'Reilly, 1996), current

velocities and directions, by the Acoustic Doppler Current Profiler (ADCP) (Geyer and Signell, 1990). Bathymetry is commonly derived using one or both of multibeam echo-sounders and sidescan sonar systems (De Moustier and Matsumoto, 1993). These methods of in-situ survey are highly accurate and provide a valuable source of validation data for remote sensing techniques and modelling, however they are extremely limited in the spatial extent of their coverage. For example the waverider buoy measures wave statistics for a single point and cannot be used in shallow areas, they are also prone to damage and can be expensive to maintain. An ADCP is either ship-mounted or tethered to the bed, thus it can either provide a long time-series of current data from one location or a wider spatial coverage which lacks long-term observation. As currents are relatively dynamic according to tides and changing morphology in nearshore areas, a combination of wide spread spatial observation and longer term observation is needed. Bathymetric surveys from aircraft or maritime vessels are also limited in spatial and temporal extent of the survey, ships are unable to access complex shallow water systems and light aircraft are unable to fly in stormy conditions. It is also not economically or environmentally viable to run these airborne or vessel-based surveys continuously given the fiscal cost of operation and maintenance along with the environmental cost of fuel use and the increased CO_2 footprint for the operating organisation. Periods of stormy weather generate large waves and strong currents, and as such they are the most energetic periods for hydrodynamic activity, and the most interesting periods for scientific observation; fortunately the basic principles of radar allow it to continue to operate to some extent under these conditions. In order to combat these issues many remote sensing techniques have been developed focussing on determining sea state parameters and the mapping of bathymetry/nearshore topography over a large area through either direct or indirect measurement methods (Holman and Haller, 2013).

Remote sensing techniques can be broadly classified into passive or active methods. Passive methods such as video cameras and infrared (IR) optics rely on electromagnetic radiation (EMR), that is reflected (in red, blue, green and near-infrared) or emitted (infrared) from the surface of the earth; they are therefore often impeded by low light conditions. Active remote sensing devices including radar, emit their own electromagnetic energy that is projected from the device, and interacting with the target environment. This typically stimulates a backscattering of energy which is subsequently detected by the device and recorded.

Most remote sensing systems seek to indirectly estimate water depth using inverse depth algorithms (IDAs), based on gathered wave parameters. Those methods which survey coastal areas vary greatly and include spectral satellite (Bierwirth et al., 1993), airborne imaging technology (El-Magd and Hillman, 2009), light detection and ranging (LiDAR) technology (Irish and Lillycrop, 1999) and Landsat technology, specifically multispectral scanners (MSS) and thematic Mappers (TM) (Benny and Dawson, 1983). Dugan et al. (2001) used airborne video footage of waves to estimate wave field parameters, tower mounted video recordings have also been used to observe sea state (Stockdon and Holman, 2000). Synthetic aperture radar (SAR) (Greidanus, 1997) and SPOT satellite data (Leu et al., 1999) have been used to image an area over a diverse range of spatial and temporal scales, however these are snapshot images as the observation device passes the target area.

Each remote sensing platform has both limitations and advantages in both practical application and underlying theory in addition to potential image resolutions, and spatiotemporal coverage. For example one of the key constraints regarding much of the imaging technology used in

remote sensing, is that it requires optical clarity to operate effectively. Thus it is difficult to extract data during stormy conditions, which are times of high interest in coastal morphology (Mason et al. 2000).

2.5.1 Video Remote Sensing

The use of various remote sensing techniques has become more popular, as technological advances have allowed greater data storage and processing power over the last decades (Holman and Stanley, 2007). They also allow data acquisition over generally larger areas and excel in providing consistent long-term monitoring within the coastal domain. The most common of passive remote sensors employed today in coastal science is the video camera. Using photogrammetric and video analysis techniques to survey the nearshore zone is now common practice in coastal science and survey/monitoring industries. The use of image-processing techniques to derive useful hydrodynamic and bathymetric information from video image sequences was pioneered in the 1970s and 1980s (Sonu, 1972; Sasaki et al., 1976; Maresca and Seibel, 1976; Wright, 1976; Katoh, 1981; Holman and Guza, 1984) where wave breaking over sand banks was observed and measured. This swiftly led to further developments of the technique where algorithms were developed and used to identify and calculate wave number components from the gradient of wave phase propagation of the recorded wave field (Stockdon and Holman, 2000). The linear dispersion relationship was utilised to determine and map water depths in nearshore areas (Aarninkhof et al., 2005); this technique was also used to map currents with aerial photographs (Dugan and Piotrowski, 2003). Furthermore, intertidal morphology was analysed by Alegria Arzaburu et al. (2007) and techniques were improved

upon to monitor changing morphology using the *cBathy* algorithm (Holman and Stanley, 2013; Morris, 2013; Wengrove et al., 2013) an example of *cBathy* survey is shown in Figure 2.13. Wave runup was analysed and quantified (Holland et al., 1995; Holland and Holman, 1999) and beach slopes mapped (Plant and Holman, 1997).

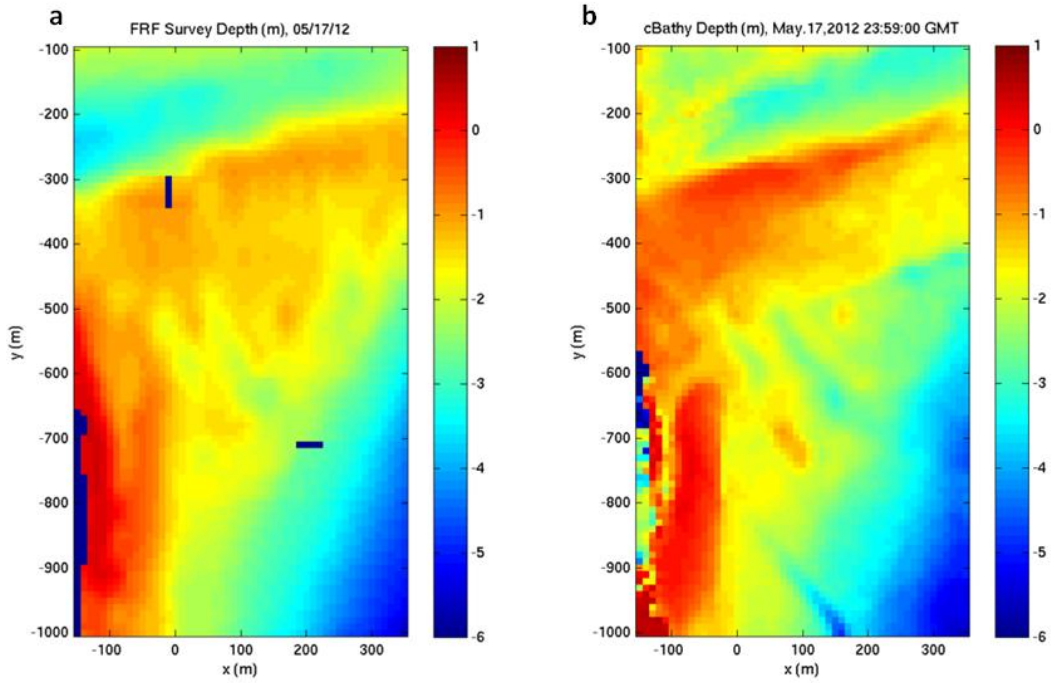

Figure 2.13: (a) Surveyed bathymetry; (b) elevation survey maps created using *cBathy* algorithm applied to Argus video data from Holman and Stanley (2013).

Measurement of submerged sand bar systems was carried out using video analysis techniques (Holman et al., 1991; van Enckevort and Ruessink, 2001; Almar et al., 2012). The impact of structures on coastal morphology have also been assessed using the Argus camera system (Ilic and Alegria, 2006; Ilic et al., 2007; Miles et al., 2013). Figure 2.14 illustrates an installation of

video cameras and an example of image data gathered, which is typical of coastal observation with video cameras.

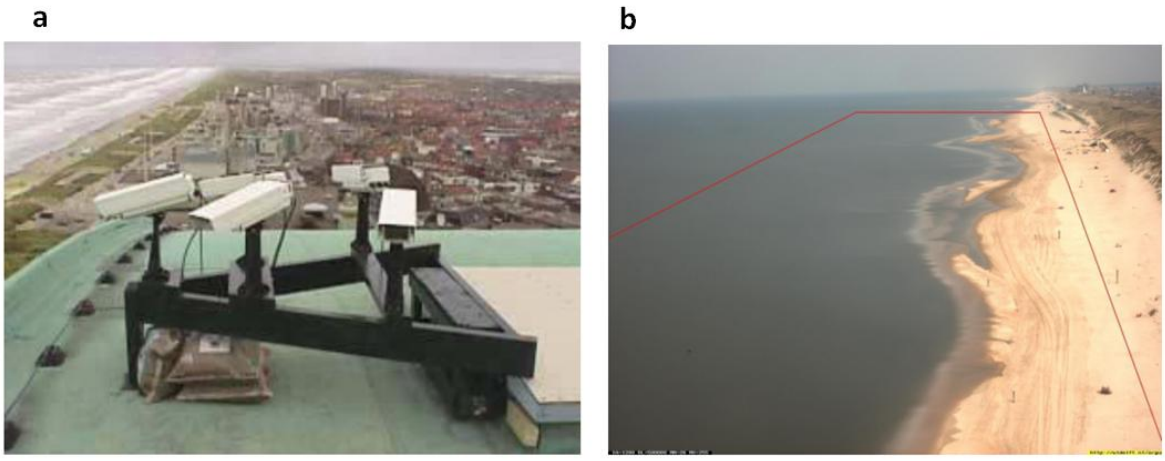

Figure 2.14: (a) Deployment of an Argus camera system at Noordwjik (b) a sample image of the coast typical of those used to derive bathymetry with video systems (Uunk 2008).

Spatial coverage is however limited to the optical range of the video camera and in widespread complex systems many video recorders would be needed; they are also limited to operation in daylight (Holland et al., 1997; Aarninkhof et al., 2003; Aarninkhof et al., 2005; Holman and Stanley, 2007; Sobral et al., 2013; Santiago et al., 2013). Video methods are now of sufficient maturity and robustness, that they are now used successfully to monitor stretches of intertidal beach during a large European research project *CoastView* (Davidson et al., 2007), and improvements continue to be made, including automated methods that are capable of updating bathymetric maps on a daily basis (Uunk, 2008). Many of the same techniques applied to video camera data can be applied to radar data with similar results (van Dongeren et al., 2008).

Due to the limitations of video monitoring, such as its reliance on clear operating conditions and its inability to gather data during low light conditions, there has been significant advances in the use of thermal infrared cameras to derive intertidal Digital Elevation Models (DEM) (Gaudin et al., 2009). IR cameras are also being used to image wave processes in the nearshore (Watanabe and Mori, 2008). IR cameras rely on energy directly emitted from the ocean and the process of evaporation alters the temperature of the sea at the surface, creating an extremely thin layer (<1 mm) skin of cooler water on the surface that is distorted with the passage of waves and by turbulence (Jessup et al., 1997). This enables IR cameras to continue imaging waves in low light conditions.

Video cameras mounted on towers along a shoreline have also been used successfully in combination with in-situ sensors to measure morphological change and sediment transport (Austin and Masselink, 2006) and along with laser-scanning systems mounted on the foreshore, they have also proved extremely useful in the remote sensing of the swash zone (Blenkinsopp et al., 2010; Brodie et al., 2012; Almeida and Masselink, 2013; Almeida et al., 2015). The laser system allows swash zone hydrodynamics and morphological bed evolution to be measured at a fine spatial and temporal resolution. These sensors have been proven to be accurate and effective in their deployment.

In addition to video camera systems mounted on towers at the coast there has been substantial development of unmanned aerial vehicles (UAV), as platforms for video observation of the coast (Rovere et al., 2014). The form of UAVs is diverse, ranging from sophisticated small unmanned light aircraft or drones used in military applications to inexpensive (<$1500) remote controlled

quadcopters available 'over the counter'. While they suffer from many of the limitations of both optical and airborne systems, they are considerably cheaper to operate and maintain. The primary usage of image data retrieved using these systems is in the reconstruction of topography using a range of techniques, including Structure from Motion (SfM) and multi-view stereopsis (MVS) in order to derive 3-D coordinates for points in the image data, that have proven to be accurate (Harwin and Lucieer, 2012). These techniques have been applied to various coastal monitoring problems including erosion, breakwater maintenance and wetland monitoring (Mancini et al., 2013; González-Jorge et al., 2014; Quater et al., 2014; Darwin et al., 2014; Wan et al., 2014; Pérez-Alberti and Trenhaile, 2015).

2.5.2 Satellite Optical and SAR Imaging

Active remote sensing has also been deployed extensively in the monitoring of coastal areas in a varied manner. Satellite or airborne mounted Synthetic Aperture Radar (SAR) is able to penetrate cloud cover with much greater reliability and alacrity, than even multispectral images and sense ground cover characteristics such as terrain type (based on scattering and roughness characteristics), in addition to ground elevation derived through measurement of electromagnetic wave return times (Dellepiane et al., 2004). SAR sensors used in coastal monitoring include ERS, ENVISAT, RADARSAT1-2, COSMO-SKYMED and TerraSAR, with differing operating frequencies and resulting spatial resolutions (Niedermeier et al., 2005). Optical instruments mounted on satellites allow for high resolution images to be taken from space, thus covering a wide area (Mason et al., 2000). Examples of satellite optical imagery can be seen to be sampled from Landsat (Bierwirth et al., 1993), SPOT satellites (White and Asmar,

1999), IRS, IKONOS and QUICKBIRD satellites are each able to sample at different resolutions and spectral bands (Niedermeier et al., 2005). Examples of images from both satellite mounted SAR (a) and optical instruments (b) can be seen in Figure 2.15**.**

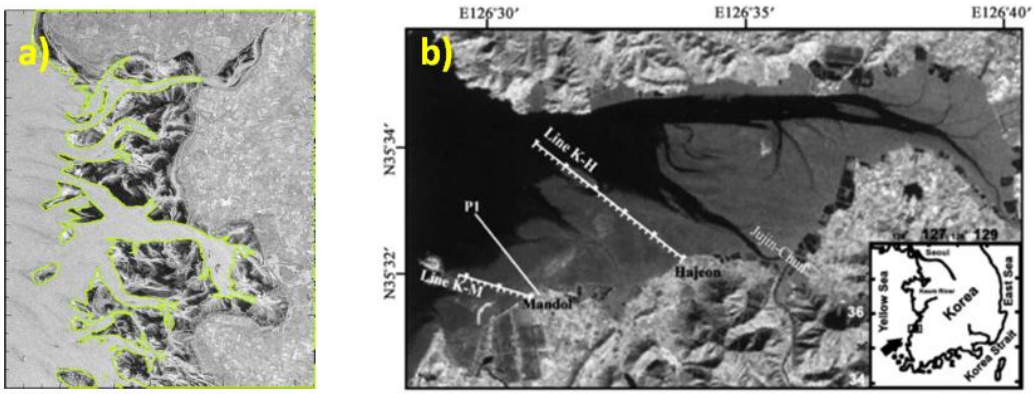

Figure 2.15: (a) Example image from a satellite mounted SAR (Niedermeier et al., 2005), (b) example image from LANDSAT thematic mapper (Ryu et al., 2002).

The primary technique for surveying coastal areas using satellite images from both optical and SAR instruments involves the construction of large area Digital Elevation Models (DEMs) using "waterline" (i.e. land-water boundaries) extraction methods that are the precursors to the method developed in this thesis. Images from several of these satellites have been used in the creation of DEMs across the intertidal area, pioneered by Koopmans and Wang (1994). With sequential images of the coastal area able to show the position of the waterline at accurate time intervals, a series of these waterline contours can be used to construct elevation maps with the aid of a tidal model (Flather and McCartney, 1995; Mason et al., 1995; Mason et al., 1999; Annan, 2001; Mason and Garg, 2001; Ryu et al., 2002; Ryu et al., 2008; Heygster et al., 2010; Liu et al., 2013a). Successive DEMs constructed using historical satellite data can be used to track long-

term macro-scale morphological change, especially shoreline retreat and advance (Niedermeier et al., 2005). Due to the often infrequent repeat image times of satellites, usually a combination of images from one or more satellites are used to create these waterline DEMs (Mason and Garg, 2001). Figure 2.16 shows a topographic DEM of the intertidal area of the tidal flats in Jiangsu constructed using LANDSAT images and tidal water elevations generated by the *Mike21* HD model.

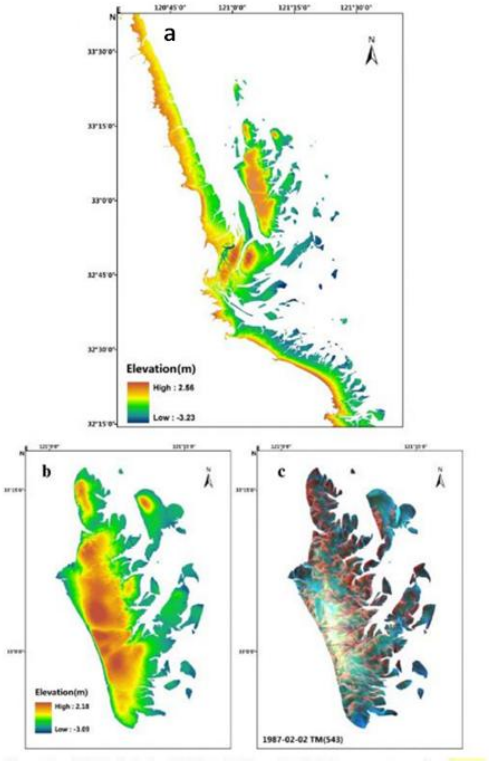

Figure 2.16: DEM of the Jiangsu coast, China (a) full intertidal area,(b) Dongsha tidal flats, (c) LANDSAT image of Dongsha, from Kang et al., (2015).

Satellite waterline elevation data are constructed using spatial image analysis techniques such as wavelet analysis (Heygster, 2010) for edge detection. These techniques rely on high image data quality to assign waterline elevation contours. In addition, the limited number of image scenes available will result in gaps, and areas of poor results which must be interpolated with some degree of spatial averaging. Holman and Bowen (1979) state that spatial interpolation over complex beach profiles can lead to serious errors when the topography is then used in further processing.

Recently this method has been used to map large areas of the coast of China with mean vertical errors in the measurements between 29 - 42 cm (Liu et al., 2013b). The technique was also applied using SAR images to map the change in topography on tidal flats along the Wadden Sea German coast between 1996 and 1999. The elevation values in this region were compared to those gathered by survey vessel; the mean error was 20 cm in 1996 and 21 cm in 1999 (Heygster et al., 2010).

2.5.3 Manual Surveys

The task of surveying intertidal areas has traditionally been the responsibility of well-established bathymetric survey methods including vessel-based echo sounders, a method able to generate accurate depth profiles along a transect. This type of swath bathymetry has been used in a variety of applications, including the surveying and detection of subtidal offshore sand waves and other bedforms with the aim of monitoring sediment transport (Duffy and Clarke, 2012) over potentially large areas; San Francisco Bay for example (Barnard et al., 2012). Recent advances in data assimilation techniques allow multibeam echosounders to gather detailed and

accurate 3-D bathymetric surveys in relatively shallow coastal waters. Vessel-based surveys are constrained by expense and inefficiency of operation over large areas and are also unable to survey very shallow waters (Gao, 2009).

Airborne LiDAR (Light detection and ranging) is a non-imaging technique using high powered laser pulses to detect water surface and sea bottoms; its use in shallow water bathymetric surveying was pioneered by Lyzenga (1985). With the introduction of GPS to airborne LiDAR, multiple surveys flown over the same area can be used to accurately monitor changes in bathymetry (Guenther et al., 2000). It has also been used to map and classify vegetation in coastal habitats (Chust et al., 2008, 2010). The spatial coverage of airborne LiDAR is limited by operating conditions for the aircraft, along with sea surface conditions and turbidity of the water (Muirhead and Cracknell, 1986).

Intertidal topography can also be surveyed using Differential Global Positioning System (DGPS) fixed to an all terrain vehicle (Osorio et al., 2012) or using a handheld device (Mohanty et al., 2012). This method is likely the cheapest but relies on continued expense of manpower and time in the field and observation times are dictated by the tide and weather conditions. It also requires extensive post-processing of the data when the desired result is a 3-D elevation map which can increase operational costs. This technique is best suited for the repeat observation of a small number of cross-shore transects or ground-truthing other topographical survey results (Plant and Holman, 1997; Aarninkhof et al., 2003; Almar et al., 2012) .

Although these techniques have improved significantly in accuracy and applicability over the last decades, they are still however expensive and relatively time consuming and must be commissioned for a specific task. Consequently surveys are not routinely performed, leading to the intertidal topographical data quickly becoming obsolete until the next survey in particularly dynamic areas. When used in this manner these methods provide only snapshots of episodic morphological change over relatively long timescales. In order to compliment these accurate and focused surveys, a method that provides constant, long-term monitoring over a wide area of the coast is needed. The following chapter will give a broad overview of radar technology and detail state-of-the-art techniques in coastal monitoring using marine radar.

3 MARINE RADAR

3.1 BASIC RADAR PRINCIPLES

3.1.1 The Radar Concept and Basic Physics

The term 'Radar' was originally an abbreviation for Radio Detection and Ranging, however these systems have evolved dramatically since their infancy when their use was limited to the detection and ranging of airborne targets. Modern evolved radar systems are capable of much more; while the basic principles remain the same, advances in computing power, signal, image and data processing have allowed the use of radar to expand into the fields of tracking, imaging, classifying and identifying targets and objects in many environments. These applications are in high demand within many industries, both civilian and military. Radar systems are used by aircraft, ships, vehicles, satellites and stationary ground-based installations. In addition to the uses defined above, radar can also be used from these platforms to pre-emptively map operational environments in 3-D, avoid collisions, and monitor resource distributions and uses.

Figure 3.1 shows a modern marine radar antenna and turning unit; the appearance of radar systems varies massively depending on their intended usage, illustrated is the type of radar used in this work.

Figure 3.1: X-band marine radar manufactured by *GEM Elettronica* deployed at Eastham Locks, River Mersey

The vast majority of radar systems use modulated waveforms and directive antennae to project and transmit radiofrequency (RF) electromagnetic (EM) waves in a specific direction or into a targeted area (there is also on-going research into the use of noise radar and light radar) in order to detect objects (targets). The targets present within the observed space should reflect back a portion of the transmitted energy which is picked up by a receiver on its return back to the radar. In principle, if an electromagnetic wave encounters sudden changes in conductivity

(σ), permittivity (ε) or permeability (μ) in the medium, a part of that energy is absorbed by the second medium inducing electrical currents on the target surface, these currents are reradiated back towards the radar (Skolnik, 2008). The nature of this re-radiated signal upon its reception at the radar antenna can tell a radar operator much about the target, including the size, shape, angular direction and speed of the target (utilising the Doppler echo effect).

Much of the returned energy may not be from the target of interest and is unwanted (or wanted for some applications) noise caused by background radiation, or from other anthropogenic sources such as engine ignitions, other radar and motor brushes, which is also known as electromagnetic interference (EMI). Noise can be introduced through the practice of jamming from electronic countermeasures systems (ECM) which are usually encountered in military hardware. Atmospheric interference (rain for example) or reflections from the sea surface are collectively known as 'Clutter' and are often filtered out to obtain a better signal to noise ratio, and thus produce a clearer image of the target. Sources and uses of this clutter signal are discussed in detail in later sections.

One of the most fundamental uses for radar is the accurate ranging of a target. This is a very simple technique and the range to a target (R) can be calculated based on the round trip time (T) it takes for the projected EM waves to reach the target and return at the speed of light (c) $c \sim 3\text{x}10^8$ m/s. Given that distance is simply speed multiplied by time, and the distance travelled by the EM wave to the target and back is $2R$:

$$\mathbf{R} = \frac{\mathbf{c\Delta T}}{\mathbf{2}} \qquad \mathbf{(4)}$$

where R is the range to target (m) and ΔT is the time taken for the round trip.

Radar is applied in many varied environments, both specific such as detection of aerial objects including missiles or warplanes, to the general monitoring of shipping in a coastal environment. Specific details about a target such as colour or exact shape cannot be resolved readily from radar signal data as it can through optical sensors, however radar is utilized primarily because it is an active device that does not rely on ambient environmental radiation (as do most optical and infrared sensors) in order to image an object; as such it is able to detect targets in adverse weather conditions and over longer ranges.

3.1.2 A Brief Description of EM Waves and Their Characteristics

The waves projected by a radar antenna are electric and magnetic field waves that oscillate at the carrier frequency that is usually defined in the radar specification. The physical nature of EM radiation is described by Maxwell's equations the details of which are outside the scope of this project. However a description of the nature of wave transmission, their frequency, wavelength and phase and their interaction with matter, is critical to gaining an intuitive understanding of radar operation which will prepare the reader for later sections and justify many choices made regarding equipment used and data processing techniques applied.

The electric field of an EM wave E lies in one plane, the magnetic field B lies in a plane orthogonal to the E field, meaning that the direction of the wave propagation is orthogonal to

the plane described by *E* and *B*. The *E* field is aligned to the y-axis and the *B* along the x, therefore the direction of propagation is along the z-axis, according to the right hand rule. The amplitude of the *E* component can be calculated given information on the peak amplitude, frequency and phase of the input signal.

$$\boldsymbol{E = E_0 cos\,(k_z - \omega t + \phi)} \quad \textbf{(5)}$$

where the initial phase is defined as ϕ and the peak amplitude is E_0. The wave number (k) and angular frequency (ω) are common units used to describe the spatial and temporal behaviour of a wave. They can be described by the elementary formula:

$$\boldsymbol{k = \frac{2\pi}{\lambda}\ \text{radians m}^{-1}} \quad \textbf{(6)}$$

and:

$$\boldsymbol{\omega = 2\pi f\ \text{radians s}^{-1}} \quad \textbf{(7)}$$

where λ is the wavelength in metres and *f* is the radar carrier frequency.

This leads us to a brief description of the roles that wavelengths and frequencies play in radar systems operation. The wavelength λ of the linearly polarised electromagnetic sinusoid is simply the distance from any point to the next corresponding point, for example from peak to peak. A standard X-band marine radar operating at around 9.4 GHz generates waves with a wavelength ~3 cm and can be calculated using:

$$\lambda = \frac{c}{f} \quad \textbf{(8)}$$

The wavelength of the projected EM waves has implications when considering the material of the target to be detected and the operating environment of the radar system. Different wavelengths react in very different ways depending on the surface characteristics of the material which they come into contact with and the environment through which they pass and image data collected may be influenced by this.

The carrier frequency of the projected waves is another simple yet vitally important concept; if the amplitude of the wave was observed at a stable point in space and allowed to fluctuate as a function of time, the wave period *(T)* is the time taken from the crest of the sinusoid to the next corresponding crest, in seconds. This can be thought of as the time taken for a wave to complete one cycle. As wave period can be expressed in seconds, the inverse of this is the number of cycles completed in a second, i.e. the frequency (*f*).

The frequency of the EM wave is measured in cycles per second (Hertz). Different types of EM wave are classified as a function of their frequency across the electromagnetic spectrum as shown in Figure 3.2 where the different operating frequencies are shown with examples of radar sets operating at those bands.

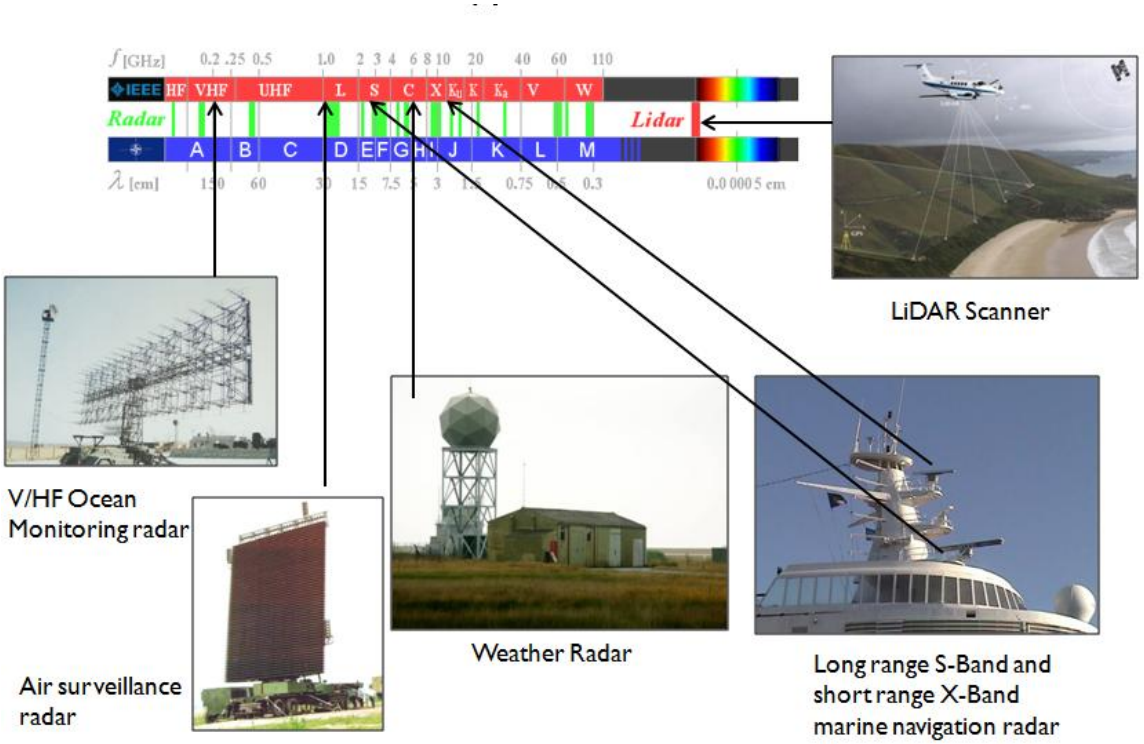

Figure 3.2: Locations of different radar operating frequencies on the electromagnetic spectrum, in relation to the visible wavelengths and LiDAR technology.

Radar operates between 3 MHz to 300 GHz, and that range is further sub-divided into named RF (Radiofrequency) bands as seen in Table 3.1. These bands are authorised for radar use by the International Telecommunications Union (ITU), a global frequency coordination organization that aims to prevent interference between devices, satellite orbits and radar operations from space. Normally permission to operate a radar must also be obtained at a national level; in the United States the Federal Communication Commission (FCC) issues permits for operation, in the UK these licenses are issued by *Ofcom* - a telecommunications regulatory body. Obtaining one of these licences from the local regulatory body will be incorporated into part of the future deployment process of the integrated radar system presented in this work.

International table				
Band designation	**Nominal frequency range**	**Specific frequency ranges for radar based on ITU assignments** (see Notes 1, 2)		
		Region 1	**Region 2**	**Region 3**
HF	3–30 MHz	(Note 3)		
VHF	30–300MHz	None	138 –144 MHz 216– 225 MHz (See Note 4)	223-230 MHz
UHF	300–1000 MHz (Note 5)	420–450 MHz (Note 4) 890–942 MHz (Note 6)		
L	1–2 GHz	1215–1400 MHz		
S	2–4 GHz	2300–2500 MHz		
		2700–3600 MHz	2700–3700 MHz	
C	4–8 GHz	4200– 4400 MHz (Note 7)		
		5250–5850 MHz	5250–5925 MHz	
X	8–12 GHz	8.5–10.68 GHz		
Ku	12–18 GHz	13.4–14 GHz		
		15.7–17.7 GHz		
K	18–27 GHz	24.05–24.25 GHz	24.05–24.25 GHz 24.65–24.75 GHz (Note 8)	24.05–24.25 GHz
Ka	27–40 GHz	33.4–36 GHz		
V	40–75 GHz	59–64 GHz		
W	75–110 GHz	76–81 GHz		
		92–100 GHz		
mm (Note 9)	110–300 GHz	126–142 GHz		
		144–149 GHz		
		231–235 GHz 238–248 GHz (Note 10)		

Table 3.1: Official operating frequencies for different radar bands (IEEE, 2003).

The phase of the projected EM waves is also an important consideration when dealing with radar. The value of φ is often known as an initial phase and is dependent on the initial conditions of the generating electric field, in particular the amplitude *E.* The resulting phase of an EM wave at a given time after generation is calculated using the cosine function of $k_z - \omega t + \varphi$ and is therefore dependant on the spatial and temporal variables of wavenumber k and angular frequency ω in addition to the initial formation conditions. Following this, the relative phase at a given time is the difference between two waves; when the relative phase is zero, two waves are in phase. Waves can become out of phase by changing the wavenumber, frequency or initial phase of either one or both of the waves. The temporal offset in seconds between two waves can be calculated by: $\Delta\varphi/\omega$.

Two waves present at the same time and space are subject to superposition, commonly known as interference. The behaviour of waves under these conditions is influenced by the amplitudes and phases of the waves; if several waves interact then the amplitude of the resulting wave will be the sum of the two respective amplitudes. This is referred to as constructive interference whereas two waves that are propagating out of phase will produce a wave that has an amplitude lower than the respective amplitudes of the two waves and is known as destructive interference. This effect can sometimes be an issue when multiple radar sensors are operating in close proximity and within the same frequency band. Waves that are 180^{o} (π) radians out of phase will cancel each other out, resulting in a null wave and no wave will be produced. In addition to the issues of interference, the importance of phase and superposition are particularly relevant to discussions of multiple object scattering, antenna beam definition, description of a radar cross-section (RCS) and the effects of multipath, which are critical in radar systems engineering (Richards, 2005).

The basic generation and propagation of EM waves have been discussed, however there remains several key aspects specific to radar operation that must also be considered. The first of which is the intensity Q of the EM wave, that is the rate of change of energy over time per unit area of the EM wave and is also equivalent to the power density in W/m^2. The intensity of an EM wave drops off with range according to the radar range equation (see section 3.3). The intensity acting on a target will inevitably affect the amount of energy reradiated back to the antenna, intuitively this often means that smaller targets at longer ranges are more difficult to detect as less energy is re-radiated. The polarisation of an EM wave describes the orientation and motion of the

electric field vector. The EM waves themselves may be polarised in several manners; linear, circular and elliptical. Marine radar systems are generally linearly polarised and project EM waves in a predefined direction, and their antennae often rotate around a vertical axis in order to cover the whole field of view. With this in mind, circular and elliptical polarisation will be left out of this discussion due to their application outside of this thesis topic, although weather radar often feature circular polarisation.

Linear polarisation is prevalent in directional antennae. In order for an EM wave to travel in the z direction along a set of Cartesian coordinates, the electric field *E* must lie along the x-y plane. The electric field has components in both the *x* and *y* direction (*Ex* and *Ey*) and the amplitude of these components will oscillate generating the sinusoidal EM wave, as described earlier in a steady direction. If the *y* component of the electric field is zero, then *E* will oscillate along only the horizontal *x* axis, thus the EM wave is said to be horizontally polarised. Conversely if *Ex* is zero then the *E* field will vary with time along the *y*-axis and the wave will be vertically polarised. The *x* and *y* components of *E* can be the same magnitude, resulting in a linearly polarised wave projecting at an angle in the *x-y* plane, the angle of this polarisation can of course be changed by varying the amplitudes of *Ex* and *Ey*. If the differences between *Ex* and *Ey* differ by an integer of π radians the polarisation will remain linear. If not the *E* field begins to trace a circle out as the wave propagates and the wave is circularly polarised (Richards, 2005). The different polarisation patterns are shown in Figure 3.3.

Antennae that transmit waves in either horizontal or vertical polarisation can generally only receive waves of the same polarisation, although multi polarisation weather radar can transmit either and receive both. Conventional marine radar use Horizontal transmit and receive (HH) transmission as it is thought to be superior in the suppression of sea clutter, allowing targets to

be acquired more effectively (Briggs, 2004; Parsa and Hansen, 2012). Recent research however has seen Vertical transmit and receive (VV) antennae being used in specialised applications such as wave spectra analysis and oil spill detection, as vertically polarised EM waves tend to interact with rough sea surfaces to a greater extent (Long, 1975; Fingas and Brown, 2014).

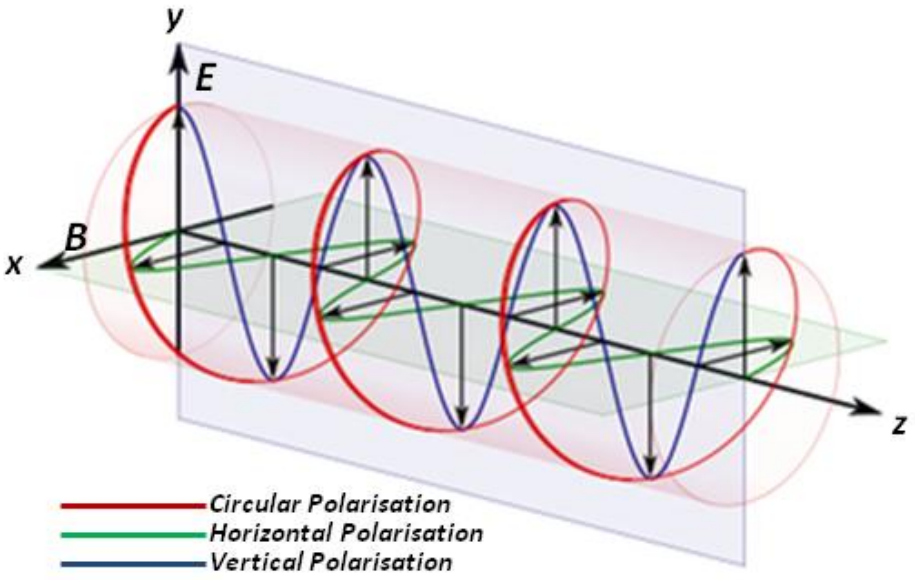

Figure 3.3: Illustration of different EM wave polarisations.

3.1.3 EM Wave Interactions With Matter

Diffraction occurs as EM waves propagate through an aperture, the waves bend by an amount dependant on the size of the antenna *a* relative to the wavelength of the wave λ. Waves exiting the antenna are governed by *Huygen's Principle* whereby waves being emitted through a slit can

be modelled as if they are being produced by many individual radiating elements which then emit waves isotropically once past the aperture (Skolnik, 2008). Due to this effect, the characteristics of the EM wave will be changed during the transition through the aperture. There can be seen a distinct radiation pattern that varies between individual radar antenna models. Radiation patterns typically have a dominant main beam and a collection of sidelobes. The width of the projected beam (antenna beam width) depends on the aperture size in relation to the wavelength. If $a >> \lambda$ there will be significant destructive interference within the sidelobes, leaving a strong main beam in the forward direction with a narrow beamwidth and few side lobes in the near field. On the other hand if $a << \lambda$ then no destructive interference will take place and EM waves will propagate over the entire exit hemisphere giving a large beam width and more disturbance.

In practical antenna applications, the radiators are arrayed across the structure of the antenna and the shape of the antenna is usually responsible for the radiation pattern and beamwidths. The waveguide serves this purpose in many marine radar systems. The advantage of having multiple radiators is that if all projected EM waves are in phase, constructive interference will occur and this will allow the resulting wave to have an amplitude N times the size of the individual waves. As range increases, the difference in angular resolution will increase and the resulting wave will be less than N times the individual. The amplitude of the EM wave will continue to drop until at maximum range (detailed in section 3.3) where the destructive interference becomes so great that a null wave is created. This effect is evident in radar images where pixel intensities drop off noticeably with range, as shown in Figure 7.4 and is a major factor in results shown in Chapter 7.

The region lying between the first null to either side of the antenna forms an angular shape which defines the main lobe. Most of the projected power is concentrated within this main beam region. The width of this region is known as the *Beamwidth* and is classified by measuring twice the angular distance from the peak of radiated power to the point at which the power has dropped to half its peak value or -3 dB. The 3 dB beamwidth is denoted by θ_3 in the radar range equations described in later sections. As the angle deviates from the normal away from the main beam, the projected energy constructively interferes and then falls back to a null in a repeating pattern of sidelobes that describe the antenna radiation pattern, the properties of which vary greatly depending on the radar set up being used (Richards, 2005). In general, larger beamwidths are desired in applications which desire to cover large spatial areas such as wide band Synthetic Aperture Radar (SAR) mapping, often mounted on satellites, whilst narrow bandwidths give better performance for tracking targets. Cross-range and azimuthal target discrimination is also improved with a narrower beamwidth. Figure 3.4 shows a typical antenna radiation pattern for a directive antenna.

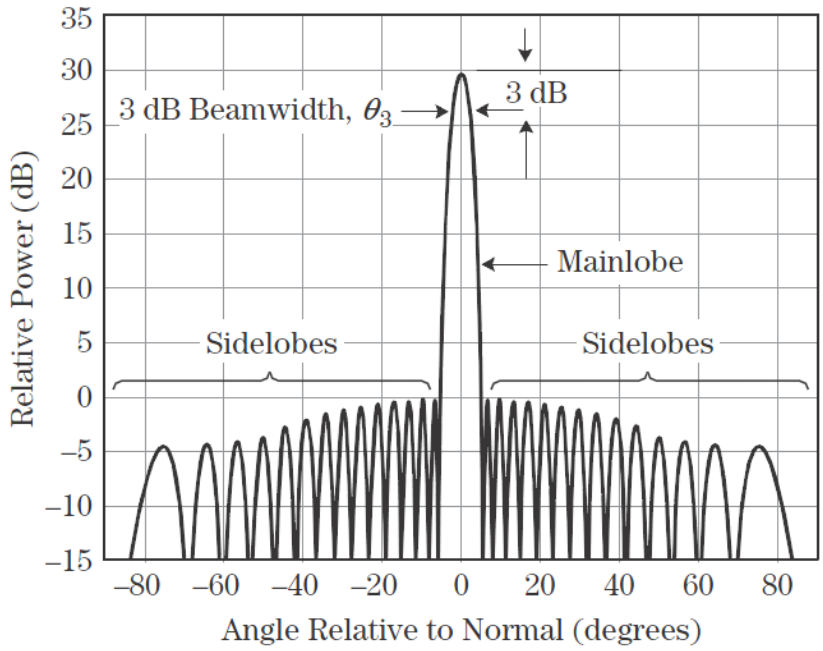

Figure 3.4: Typical directive antenna radiation pattern showing dominant main beam with sidelobes of lower power density from Richards (2005).

EM waves radiated from the radar antenna are not only subject to interaction with matter as they exit the antenna; rain, fog, clouds and dust within the atmosphere continue to attenuate projected energy as it radiates to and from a target. Attenuation also occurs within 'clear air' that is, without large amounts of fog, rain or cloud. The rate of power loss is measured in dB/km and this value is negligible at less than 1 GHz (L-band), but increases with frequency due to the decreased wavelengths, resulting in greater scattering interaction with smaller particles. Peaks in the rate of attenuation can be seen at certain frequencies where the specific distribution of certain gasses, for example water vapour and oxygen at 22 and 60 GHz influence the amount of EM energy absorbed into the atmosphere (Richards, 2005). These values of attenuation are also greater at sea level than higher altitudes. Given that marine radar operates at X-band, and much of the analysis within this work is conducted at shorter ranges, the effects of atmospheric

absorption are very small. This gives radar its reputation of an all-weather device, in contrast to IR and optical systems.

When EM waves bend at the interface of two different materials the process of refraction occurs. Speed of propagation changes depending on the optical density of the medium through which the wave travels; a denser material such as glass will reduce the wavelength and thus cause a decrease in speed as frequency remains constant. As the wave front emitted from the antenna will cover a large area, interaction between the two materials may occur at varied incident angles. In order to remain continuous, the entire wave must bend at the interface. Refraction can be advantageous in radar systems because signals projected upwards through the atmosphere will encounter thinner atmosphere as height increases, causing changes in EM wave propagation properties and an eventual deviation from a straight line back towards earth. In surface-to-surface radar systems, such as HF radar mounted on ocean going vessels, this effect can be used to project radar signals over the horizon and detect targets not visible to traditional sensors – this is known as 'Over The Horizon' radar (OTH) (Headrick and Skolnik, 1974).

3.2 RADAR FREQUENCY BANDS

Different types of radar system operate over varying frequencies across the electromagnetic spectrum, and these frequencies are designated for "radiolocation" (radar). Exact operating frequencies of radar systems are very rarely openly available, in order to prevent security threats. It is therefore convenient to assign letters to the different bands in order to differentiate

between radar systems. There are also ranges allocated to radar systems based upon the specific geographical region in which they are operating to prevent interference.

The radar system developed in this thesis operates at X-band, a frequency that is commonly used for marine navigation. However, it is important to be aware of the capabilities and limitations of this frequency band and to provide justification as to why this band is used above others. As can be seen in Table 3.1, radar operates from ~3 MHz to ~300 GHz. Applications, capabilities and technology of these radar systems vary greatly as shown:

HF (High frequency): This band of radar is usually used to detect targets at very long ranges (up to 2000 nmi). Targets include aircraft, ships and ballistic missiles, but it is also used to observe sea state, including waves and currents (Barrick, 1977).

VHF (Very High Frequency): The earliest radar technologies during the 1930s used this frequency as it represented the pinnacle of technology at that time. In a similar manner as HF radar, VHF is used for long range detection of aircraft and missiles. In spite of its low cost VHF radar also has limitations in terms of detectable target cross-section (large wavelengths have difficulty picking up small targets) and very high reflection coefficients from the earth's surface. These limitations can be overcome by higher frequency systems, thus VHF radar is seldom used.

UHF (Ultra High Frequency): Many characteristics of VHF also apply to UHF, however the limitations are somewhat mitigated. UHF is a good frequency for airborne target tracking and early warning radar. Ground-penetrating radar also uses this frequency in the detection of underground cables.

L-band: This frequency is very long ranged and is primarily used by air route surveillance radar and long-range traffic control. This frequency is the lowest at which the effects of rain are not detrimental to image quality (large wavelengths rarely pick up rain droplets).

S-band: Capable of monitoring targets to ranges of 60 nmi, this radar frequency is a good compromise between range and accuracy. The *NEXRAD* radar system (Heiss et al., 1990) detects weather patterns using this frequency as do many airport surveillance radar systems.

C-band: This is a seldom used band lying between S and X, and it is generally agreed that the applications are better suited to either S or X bands. Theoretically this band would provide a compromise between the characteristics of X and S bands. Some weather monitoring radar also operate within this band.

X-band: A very popular band used for military and civil applications. Military uses include intercepting and targeting airborne targets, detecting ground targets and missile guidance systems. Civil applications include marine navigation and imaging. The high resolution imagery is made possible by the wide range of X-band frequencies and narrow bandwidths, thus increasing accuracy. X-band will be the operating frequency used in this work, due to the flexibility of applications, and the capability for high resolution imaging.

Ku, K and Ka-band: Antenna size and transmit power decrease with an increase in frequency. There are several military applications of this band where the small antenna size is vital. An example is the system in place on the brand new (unveiled May 2015) Russian Army T-14 *Armata* main battle tank variant. This small Ka band radar allows the tank to track targets simultaneously and direct on-board weapons systems to engage targets or detect and neutralise incoming missiles or helicopters using its weapons systems; or give advance warning in order to deploy active countermeasures such as the *Shtora* system. A limitation of this band is often the echo effect from rain as the wavelength is so small; it can be a severe limitation of applications at this frequency.

MMW (Millimetre Wave Radar): Interest in this frequency band is mainly a factor of interest and expansion. Radar operating in this frequency have the potential to employ very small antenna and high resolutions with very narrow bandwidths, but have short ranges. The interest is also primarily military as frequencies in this range are very hard to counter through electronic warfare (Skolnick, 2008).

3.3 RADAR RANGE EQUATIONS

3.3.1 Introduction to The Radar Range Equation (RRE)

The radar equation can be viewed as the most useful presentation of parameters affecting radar performance. Skolnik (2008) and Richards (2010) are key texts on the basics of radar that are widely used in radar systems engineering and provide full derivations of the RRE. Selected

equations are taken from these texts in order to demonstrate variables important to this work. The radar range equation becomes more complex as its constituent components are broken down and more variables added. The following is a very basic exposition of the radar equation. A common and basic form of the equation expresses the received signal power P_r as:

$$\boldsymbol{P_r = \frac{P_t\, G_t}{4\pi R^2}\, x\, \frac{\sigma}{4\pi R^2}\, x\, A_e} \qquad \textbf{(9)}$$

The first parameter is the power density received from a target at a range *r* from a radar system that radiates a transmitted electromagnetic power of P_t watts from an antenna of gain G_t. The numerator of the second factor is the cross-sectional area of a target σ in m^2. The denominator for both factors accounts for the divergence of the electromagnetic radiation with range on both the outbound and inbound vectors, respectively. Of course only a portion of the reflected radiation is intercepted by the antenna, A_e represents the effective aperture area of the antenna - intuitively, larger A_e values are likely to lead to more returned power. Although P_t is used in the radar range equation to represent peak power, a much better measure of a radar systems ability to detect a target comes from using P_{av}, the average power. This can be derived by $P_t = P_{av}/F_{pr}\tau$, where F_{pr} is the pulse repetition frequency and τ is the pulse duration.

In order to measure a radar's maximum effective range, the maximum range R_{max} is reached when the received signal is equal to the minimum detectable signal of the radar S_{min}, given by:

$$R_{max}^4 = \frac{P_t G_t A_e \sigma}{(4\pi)^2 S_{min}} \quad (10)$$

As most radar systems use the same antenna for transmitting and receiving, there is a relation between the gain G_t on transmission and the its effective area A_e on return; $G_t = 4\pi A_e/\lambda^2$, and λ is the wavelength of the signal. In order to derive the maximum range, however, the minimum detectable signal S_{min} must be resolved.

$$S_{min} = kT_0 B F_n (S/N)_1 \quad (11)$$

In this equation, kT_0 is the thermal noise from the conductor arising from k = Boltzmanns constant, T_0 = standard temperature 290K, and B = receiver bandwidth. This function essentially accounts for the background noise produced during the operation of the radar antenna.

The radar equation can be expanded greatly to include a large number of variables, beyond the scope of this thesis. It can be used to determine the maximum range of a given radar, along with adjustments for interference of many varieties including electronic warfare, to the interference from the atmosphere (Skolnick, 2008). Although the focus of this project is not necessarily on target detection or range determination, the final product will still have to act as a navigational radar, therefore it is important to be aware of the consequences in altering power outputs and the effects on target signal return in order to retain system versatility. An awareness of the limiting factors in radar target detection is also important.

3.3.2 Power Density at Range

An important factor when considering radar systems is the density of the projected power at different ranges from the radar antenna. The radar range equation allows this quantity to be estimated effectively. This value is useful in predicting the probability of target detection at various ranges, the value also differs greatly depending on the antenna type. The system used in this work is a directive antenna which is able to project greater power per unit area than, for example an isotropic antenna with an omnidirectional radiation pattern. The key factor in this is the antenna gain (G), this variable describes the directivity, reduced by signal loss between input point to projection point. Antenna gain therefore varies between manufacturers and different radar systems. The power density at range from a directional antenna is:

$$\boldsymbol{Q_i = \frac{P_t G_t}{4\pi R^2}} \qquad \textbf{(12)}$$

where P_t is the total peak power in watts applied by the transmitter to the antenna. Note Q_i is expressed in W/m^2.

3.3.3 Received Power From a Target

With the density of projected power estimated, the amount of that energy reflected back to the antenna must also be considered (note 'reflection' is a simplification for the stimulation of electric currents on the surface of the target, such that the target becomes a source of radio waves, some of which propagate back toward the antenna, appearing to be a reflection of the

projected energy). The amount of power reflected from a target is broadly a product of the power density at target range discussed earlier, and the radar cross-section (RCS) σ of the target. The RCS is expressed in m^2 and is determined by the size, shape and material of the target. Interestingly, the sea surface has unique RCS (see section 3.5). Thus reflected power is defined by:

$$\boldsymbol{P_{reflect} = Q_i\sigma = \frac{P_t G_t \sigma}{4\pi R^2}} \quad \textbf{(13)}$$

As power projected by a radar antenna drops off with range, the same is true of energy returning from a target. The above equations must be combined to give the power density of received energy, by:

$$\boldsymbol{Q_r = \frac{Q_i\sigma}{4\pi R^2} = \frac{P_t G_t \sigma}{(4\pi)^2 R^4}} \quad \textbf{(14)}$$

The critical aspect of the above equation is the radar range *R* has been raised to the fourth power, reflecting both the outward and return journey. Essentially this means that if the range to the desired target is doubled, the power density is decreased by a factor of 16 (this will become apparent in later sections when long-range surveys (Chapter 7) are attempted and power drop off becomes evident).

The versatility of the radar range equation is demonstrated by the fact that this equation may be extended to increase the accuracy of estimated power returns by including the effective area of the antenna aperture, and by including the effective gain of the target and the antenna efficiency. For this thesis however, it is enough to understand the significance of target (sea surface) range.

3.3.4 Radar Noise

Due to the power drop off with range, the returned power usually has a very small amplitude and is thus susceptible to noise corrupting the signal. Random noise can be found in the environment due mostly to solar energy contribution. In addition, small amounts of cosmic and galactic noise originating from outer space can also be an issue in systems operating below 1 GHz. The ground is also a source of random noise. In addition to these environmental noise sources, the thermal agitation of electrons in the radar receiver generates an amount of random noise, over which the power of the returned signal from the target must exceed. The level at which the returned power must exceed the noise level varies depending on the statistical nature of the target; it can sometimes be significant when targets have low RCS (Skolnik, 1980).

Due to the nature of thermal noise, it is uniformly distributed over radio frequencies and is often known as 'white noise'. Only noise within the range of frequencies used by the radar system will impede the radar performance, therefore the amount of noise affecting a given radar system is, to a large extent, controlled by and proportional to the bandwidth of the radar system *B.* The power of this noise P_n can be derived by:

$$\boldsymbol{P_n = k\,T_s B = k\,T_0 F B} \quad \textbf{(15)}$$

where:

k = Boltzmanns constant (1.38×10^{-23} watt-sec/K) (physical constant relating particle energy to temperature)

T_0 is the "normal" temperature (290 K)

T_s is the system noise temperature ($T_s = T_0 F$)

B is the receiver bandwidth in Hz

F is the noise figure of the receiver

F can be quantified as a measure of signal degradation caused by components of the signal chain, and is specified in the hardware literature for each radar model. As the radar range equation demonstrates, the noise is linearly proportional to the receiver bandwidth. There is a delicate balance to be achieved when considering the design of a radar system, as too small a bandwidth (meaning less noise) will reduce the target signal, thus making detection less probable.

3.3.5 Quantifying SNR

With some of the major sources of noise qualified (note the above section is by no means an exhaustive list of noise sources) the signal to noise ratio (SNR) can be established. This ratio is essentially the received target signal power P_r, divided by the noise, P_n:

$$\boldsymbol{SNR = \frac{P_t G_t G_r \lambda^2 \sigma}{(4\pi)^3 R^4 k T_0 F B}} \quad \textbf{(16)}$$

SNR can be seen as an indicator of how well a radar is receiving a signal from a target. A ratio of greater than 1:1 (>0 dB) indicates more signal than noise. In addition, the signal to interference ratio can also be derived, simply through:

$$\boldsymbol{SIR = \frac{S}{N + C + J}} \quad \textbf{(17)}$$

where N is the noise (from a variety of sources including background noise, cellular services, other radar etc.), C is the clutter, a dominant source of signal interference in maritime environments and which can also be the target of a radar system; and J which quantifies the effects of jamming or electronic countermeasures, which may hamper the radar signal.

3.4 VESSEL DETECTION WITH RADAR

Detection involving a radar system involves deciding for a given beam position whether a target exists in that area. If enough energy is returned from that location in relation to its surroundings then detection has occurred. Determining whether or not that return is indeed a valid target and not a 'ghost' or external interference is a difficult task that makes use of thresholds, the value of which the return must exceed in order to be considered a valid target. There are often instances where this threshold is exceeded by a target that is not valid. In these cases radar signal processing techniques have been developed to combat false target detection. The most common technique for filtering out these false targets is maintaining a 'Constant False Alarm Rate' (CFAR). A CFAR aims to determine the validity of a target by consistent analysis of the changing

clutter reflectively and statistics in relation to its surrounding pixels. There are many variations on these algorithms, and more detail is given in Ward et al. (2013).

Although detection is often a radar system's primary purpose, the returned echo of electromagnetic radiation can provide a wealth of additional information about the target. The extraction of useful targeting information from the data in order to confirm detection of a target involves a process of matched filtering. The amount of information which can be gleaned from radar data depends on the radial and azimuthal resolution, pulse bandwidth, operating frequency and initial information received about the target (Richards, 2005).

Velocity is measured through successive measurements of range by which the changes in distance can be obtained and an approximation of velocity made. The Doppler frequency shift created by a moving target can also provide a measure of radial velocity and is widely used as the basis for sorting moving targets from unwanted stationary clutter (Skolnik, 2008); this is the principle by which Moving Target Indicator (MTI) works. The Doppler echo in this case can be written as:

$$\boldsymbol{f_d = 2v_r/\lambda = (2v\,cos\,\theta)/\lambda} \qquad \textbf{(18)}$$

where $v_r = v\,cos\,\theta$ is the relative velocity of the target, v is the absolute velocity of the target, λ is the radar wavelength and θ is the angle between the radar beam and the targets direction. This shift in frequency is used to separate and track moving targets in stationary clutter.

The angular direction of a target is found by analysis of the angle at which the returning wave front of electromagnetic radiation arrives at the antenna. This can be accomplished with a directive antenna (one with a narrow radiation pattern). The accuracy is dependent on several factors, the size extent of antenna aperture in particular; the narrower the beam width (wider antenna) the better the accuracy.

Target size can be determined only if the radar has sufficient resolution. Many targets of interest (ships) have large dimensions, often spanning tens of metres, but the resolution must of course be less than the size of the target and thus an approximation of size can be gleaned. The size of a target is a significant contributor to the RCS characteristic of a target. In addition to size, an approximate shape of a target can also be resolved if the target is large enough. In many data processing techniques, tomography is a key method in resolving shape. A two dimensional image of an object created using measurements of phase and amplitude polarization of shapes from this method theoretically allows the recognition of shapes and targets (Nicholson and Wang, 2009). This technique is more common among radar systems with a smaller wavelength and thus finer spatial resolution. The roughness of a surface is a significant characteristic of target shape. A rough target scatters energy diffusely, whilst smooth surfaced targets exhibit mostly specular reflection and this function varies according to wavelength and frequency of the observing radar.

3.5 SEA CLUTTER AS A TARGET

In addition to hard man-made objects and elements of terrain, the sea surface may also be a target of interest for marine radar systems. The principles however remain relatively similar. Rough sea surfaces stimulate large amounts of scattering due to interaction between the centimetre scale wavelength of wind-driven capillary waves on the surface of the sea and the centimetre scale wavelengths of the EM waves projected by X-band radar (Valenzuela, 1978). Many different types of radar are able to effectively image the sea surface, some more adequately than others.

In most radar system applications, the sea clutter is an unwanted nuisance and is filtered rigorously as it can obscure small targets in rough sea conditions. An example of this is the *Searchwater* radar (Watts and Gordon, 1997) in service on the UK RAF *Nimrod* MR2 aircraft, the primary role of which is long-range surveillance of maritime surface targets (ASuW anti-surface warfare) and small targets such as submarine masts (ASW anti-submarine warfare) often at ranges of over 100 nautical miles. Where it is tasked with detecting and tracking these targets in often high sea states, it becomes a significant signal processing challenge to distinguish these real targets from the sea surface. Compounding the problem, grazing angles for the above described radars, and indeed maritime radar, are often quite shallow (less than 20°) and extend to the radar horizon (when the grazing angle = zero). This means that at longer ranges the returns from the sea surface become very similar to targets and distinguishing them is difficult. Even sophisticated modern multifunction radars (MFRs), such as the *Sampson radar* used on UK RN Type 45 destroyers, must employ significant signal processing resources (mostly through modelling clutter distributions (Ward et al., 2013)) in distinguishing clutter from targets at longer ranges.

Modern radar systems generally make use of CFAR filters (Scharf, 1991) to avoid overloading the radar signal processor and aid separation of targets from clutter. In addition to CFAR filters, the Doppler profile of targets is used to pick out moving vessels from sea clutter, as targets with a high radial velocity are easier to pick out of clutter data, targets moving through clutter also leave a spectral signal and can be identified via spectral analysis (Nieto-Borge et al., 2008b).

While sea clutter may be an issue for many radar applications, in the observation of oceanographic phenomena it is actually the desired target of detection. For this thesis it is important to be aware of the various physical factors that influence the ability of the radar to observe the sea surface. If these factors are not properly understood and their effects anticipated, it can quite easily compromise the ability of the radar system to act as a remote sensor in any capacity. For example, if industry-standard filtering and sea clutter suppression methods are applied to the data, then crucial clutter data will be removed prior to analysis. It is also important to understand that radar systems will not always image the sea surface (when the sea is very calm for example), and during which conditions the radar can be expected to perform poorly in order to account for the poor quality of data during these periods.

Clutter statistics may be used to inform scientists of many hydrodynamic variables. For example, oceanographic fronts, describing regions with different temperatures, salinities or densities have been detected by analysing clutter statistics from different regions (Askari et al., 1996). Proper characterisation of sea clutter statistics requires several variables to be clearly defined, including the area reflectivity σ^o, distribution of clutter amplitudes/power across the

study area, spectrum of clutter returns, spatial variation of the clutter returns, and information on discrete clutter spikes.

The average RCS of a region of clutter is generally defined by the area reflectivity σ^o, for a given surface area A, contained within a radar resolution cell (ranging from 3-10 m for most X-band radar). The RCS can be estimated simply by $\sigma^0 A$, giving an inherently useful parameter that has been used as a crude proxy to indicate sea state (Ward et al., 2013). However, the highly complex and dynamic nature of the sea surface mean that this RCS value fluctuates wildly about the mean, and while this distribution of RCS can be extremely useful in the derivation of surface characteristics (Ward et al., 2013) supporting variables are required to properly assess the maritime environment in which the radar is operating.

Several key factors affect the reflectivity of a given area of sea surface, chiefly the roughness of the sea surface. Bragg (or resonant) scattering (Heathershaw et al., 1980) can be used to approximate the contribution to reflectivity of surface roughness. The tilting of ripples caused by long crested swell waves and interactions in complex wave fields, or waves undergoing re/diffraction changes the reflectivity of an area as the angle of incidence between radar wave and sea surface is altered. At near vertical incidence, the reflection is quasi-specular and reflection actually decreases with roughness, as a perfectly flat surface would give greatest reflection. As the incidence angle decreases, the dependence of reflectivity on grazing angle decreases slowly until a critical threshold is reached where reflectivity drops massively at low grazing angles (typically occurring at long range and in conjunction with the power drop off and serves to decrease visibility of sea clutter at long ranges) (Ward et al., 2013).

The amplitude of sea clutter returns also varies greatly, broadly as a function of sea surface reflectively. The amplitude of clutter signal returned to the radar antenna influences to a significant extent, how bright the pixel intensity of sea clutter appears on a radar image. In addition to the effects of grazing angle, ripple density and local sea surface shape, the structure of sea clutter within a radar resolution cell has many discrete structures (termed 'scatterers') which move dynamically in relation to each other and contribute to interference in the clutter signal, that is referred to as 'speckle'. This speckle is evident on many radar images and can be seen at longer ranges in the snapshot image shown in Chapter 4. The process of multiple scatterers giving rise to speckle in radar images has been studied in some detail. Ward et al., (2013) found that the speckle generally exhibits Gaussian statistics, whose PDF can be described with a Rayleigh distribution. Evidence of clutter distributions and their variance according to antenna polarisation are explored in some detail in Ward et al., (2013).

An interesting phenomena observed in sea clutter are known as sea spikes. Much of the sea clutter and speckle on radar images appears as relatively smooth, modulated features, however often there are significant points of very high intensity (Rosenberg, 2013). These spikes are non-Gaussian in nature and therefore appear distinctly on the clutter spectrum. There are two distinct classes of sea spike: the first of which appears as very short spikes that last typically less than 200 ms and show little to no modulation; the longer spikes are referred to as "Whitecaps" as they are often caused by very strong scattering from the crests of breaking waves. These sea spikes have the undesired effect of greatly increasing the probability of false target detection as they give very high returns compared to their surroundings, increasing the demand on the radar receiver dynamic range and linearity (Anderson and Morris, 2010). These sea spikes tend to be most prominent in the breaker zone as incoming waves shoal and the back-scatter from these

breaking waves is a strong mixture of both specular and non-specular reflection, thus giving a substantially higher intensity at the shoreline (Ruessink et al., 2002).

3.5.1 Search Form of The Radar Range Equation

A critical form of the radar range equation describes the ability for a radar system to search a given area. The exact location of a target is rarely known in the first instance, more often a volume of area must be scanned in order to detect targets in that location. The area to be searched is often an angular volume Ω and the time taken to search a given area T_{fs}, is determined from the product of the number of beam positions estimated to cover the area M, and the dwell time at each position T_d.

$$\boldsymbol{T_{fs} = M \cdot T_d} \tag{19}$$

The number of beam positions required can be calculated by the volume of the area to be searched, divided by the angular volume of the radar beam (which, in turn, is the product of the elevation and azimuth beamwidths).

$$\boldsymbol{M = \frac{\Omega}{\theta_3 \cdot \phi_3}} \tag{20}$$

The time required for a given radar system to search a particular area is a vital variable to estimate during radar design. Different systems have different dwell times (the amount of time an area is 'illuminated' by radar beam) and the choice of antenna will influence capabilities for target detection and imaging.

Further derivation of the radar range equation is possible such that the variables can be rearranged to derive the ideal radar requirements to search for a target of a given RCS, at range R over an area Ω and within a pre-allocated time T_{fs} (Skolnik, 1980).

It has been demonstrated that the radar range equation is one of the most critical and versatile tools at the disposal of a radar systems engineer. Its different forms allow good initial prediction of radar performance and suitability for a given task without the need for costly modelling (although models are still of course used in the development of radar systems for the testing of more experimental elements).

3.6 COMMON APPLICATIONS OF MARINE RADAR

Port operators and shipping companies must comply with strict regulations and legislation, which means that they must have the highest levels of monitoring capability in order to maintain control of vessels and activities in the port and its surrounding areas, including the monitoring of vessels, movement of ships and their containers, managing anchorages and dredging of channels. In order to effectively accomplish these tasks, port management systems are often complex integrations consisting of Radar, CCTV and telephones. State of the art systems are integrated so that an operator can view this information immediately, without the use of separate terminals. Vessel Tracking Systems (VTS) are also integral to ports, in order to

avoid collisions and subsequent environmental damage resulting from cargo discharge into the port water bodies.

3.6.1 VTS Centres

Commercial port operations often have busy schedules, with shipping arriving and departing, mooring and pilot services being carried out, and the unloading and loading of bulky or hazardous materials. The chances for accident or incidents involving large vessels with limited manoeuvring capability are high if they are not monitored and directed effectively. VTS use navigational radar, CCTV, VHF radios and Automatic Identification Systems (AIS) to monitor vessel movements, and to provide navigational safety information.

Modern VTS have the responsibility to monitor large amounts of maritime traffic. State of the art systems are designed to track multiple tracks, plot course trajectories and provide information relating to the target including speed, size and designations. In order to accomplish this task the VTS centres require integrated radar systems (to detect targets and resolves speeds utilising Doppler processing) and AIS in order to distinguish targets from each other.

3.6.2 Bridge Applications

On-board bridge radar systems must have the ability to do almost everything listed above. They must have excellent target resolution to avoid obstacles to navigation and they must have the ability to identify targets and track multiple vessels. The most advanced and state of the art of

these bridge systems will usually be found on military warships. There are regulations governing the tonnage of civilian ships and what equipment is required by law for them to carry.

3.6.3 Commercial Shipping Applications

The history of radar use within civilian merchant shipping begins shortly after WWII. The technology was developed very rapidly under the veil of wartime secrecy and was by this time a relatively mature and stable technique suitable for use in the civil maritime industry. Some of the first end-users of marine radar included ferries which were able to maintain their schedules in bad weather much more reliably and large fishing vessels operating in areas with a higher than usual shipping density. Many ports gradually began to adopt the technology for use in guiding ships to berth during bad weather. Notably the port of Liverpool installed a permanent civil radar system in 1948. As radar technology became more advanced (while the principles and basic operation remained mostly the same) the use of marine radar became more common. However, the technology was widely mistrusted by old-school mariners and in the 1950s radar had not significantly reduced the amount of collisions at sea or the frequency of accidents. The 1956 collision between the cruise ships *SS Andrea Doria* (the pride of the Italian post-war civilian fleet) and the passenger ship *MS Stockholm* (still in service today as a Portuguese cruise ship), was thought to be a result of a misinterpretation of radar data aboard the *MS Stockholm* during foggy conditions (Bell, 1971). A counter argument may be that radar greatly assisted the recovery operation in difficult conditions. Following this, regulations were introduced governing the use and interpretation of marine radar images at sea. The International Conference on the Safety of Life at Sea in 1974, made radar a mandatory requirement for all merchant ships over

300 gross tonnage (Briggs, 2004). Larger commercial vessels generally now use both an X-band scanner for shorter ranges and a larger S-band antenna for longer range detection. Smaller vessels, including leisure craft also often carry small X-band antennas as the price of the technology has steadily become more affordable since its inception.

3.6.4 Oil Spill Detection

Radar technology has many more potential applications than navigation or port management; examples such as oil spill detection indicate the varied applications of radar. Oil spill detection is increasingly being integrated into commercial radar systems. The process relies on observing the dampening effect oil has on radar backscatter from surface waves. Oil slicks in the sea smooth a significant area and appear on a radar display as a darker signature or shadow (Tennyson, 1988; 1991), which can be differentiated from its surroundings with the application of significant data processing. It works almost in the opposite manner to traditional radar detection in that it seeks the slight reductions in returned noise levels as opposed to usual data processing which picks up increased backscatter from targets (Alpers and Hühnerfuss, 1988; Tennyson, 1988). In order to separate these smoothed areas from a surrounding "noisy sea" image processing techniques are required such as those used in SAR images (Chang et al., 2008; Zhang et al., 2012).

3.6.5 Ice Detection

By using enhanced target detection methods, slow moving or stationary targets can be effectively displayed without interfering with usual radar activity which could cause over-representation of clutter and potentially obscure targets. This is useful in the detection and monitoring of ice movements as a potential way of tracking ice expansion and retreat, an alternative to aerial photography. radar could be more accurate and provide real-time updates. Modern radar systems are able to differentiate between stationary and moving targets and display them in a different colour on the display to aid interpretation. This application aids in navigation of icy waters as well as survey of ice bergs for example, which create a prominent shadow on the radar display due to their relative height (Haykin, 1994).

3.7 MARINE RADAR FOR COASTAL MONITORING

Standard marine navigation radar can also be used to create image data appropriate for use in coastal monitoring Figure 3.5 shows a marine radar in-situ. Common operating frequencies include S and X-band, which are useful for long and short-range vessel detection respectively. The fine spatial resolution (~3-10 m depending on range setting) and electromagnetic wavelengths of ~3 cm giving rise to Bragg scattering (Valenzuela, 1978) makes X-band radar the more common choice in nearshore monitoring. The strong sea clutter signal from rough sea surfaces can be used to derive useful information about hydrodynamics in the nearshore and to image the nearshore zone effectively.

Figure 3.5: Standard X-band marine radar deployed for the purpose of gathering data used during the Irish Sea Coastal Observatory Project (COBS) during 2006 on Hilbre Island (described fully in Chapter 4).

The unique advantages of radar imaging allow for numerous critical nearshore hydrodynamic phenomena to be observed and measured. Monitoring wave climate is a task often left to point measurement sensors such as waverider buoys, however over time these sensors are vulnerable to degradation in rough seas. Marine radar is ideally suited to observing wave fields and has been used extensively to derive wave spectra in offshore areas for many years (Nieto-Borge and Guedes-Soares 2000; Nieto-Borge et al., 1999). The use of marine radar in the determination of

wave statistics including significant wave heights, periods and directional spectra was pioneered by Young et al. (1985) who used sequences of radar images passed through a 3-D Fast Fourier Transform (FFT), moving the image sequence from the space-time domain to the wavenumber-frequency domain. With additional filtering to remove image artefacts and thermal noise from the radar, they were able to find the dominant wave signals within the 3-D wave spectrum, and isolate that signal from the surrounding sea clutter signal. By analysing the signal to noise ratio (SNR) between wave and clutter, the significant wave heights can be derived. By modelling the hypothetical dispersion relation using linear wave theory (Airy, 1845) and comparing its hypothetical description to the actual distribution of the wave signal, the direction and magnitude of a current influencing the waves can be detected and measured, there are a number of approaches to determining and filtering these wave spectra to extract wave and current statistics (Senet et al., 2008; Hessner and Bell, 2009; Nieto-Borge et al., 2004; 2008a; Serafino, et al., 2010; 2012b). Surface currents were successfully determined and mapped around the island of Eday, off the north eastern tip of Scotland. This area has significant potential for tidal energy production (Bell et al., 2012), and this capability serves to cement marine radar as a critical tool in coastal data collection.

With the wave behaviour observed, and the surface current-induced Doppler offset accounted for, the dispersion relation can again be used to approximate a depth value that best explains the observed wave behaviour, allowing for nearshore bathymetric maps to be created (Bell, 1999; Hessner et al., 1999; Bell et al., 2006; Hessner et al., 2008; Flampouris et al., 2009). This technique has recently been improved upon further with the ability to measure these parameters from a moving vessel overcoming the significant complication of spatial and temporal movement in the image sequences and the resulting spectra (Bell and Osler, 2011).

These applications of radar make it a well rounded and versatile tool for coastal observation that can be deployed in a wide variety of locations. Figure 3.6 shows a selection of radar data from various locations around the UK, and the work presented in this thesis adds a vital contribution to this toolbox. Current methods of depth estimation with radar begin to degrade in very shallow/intertidal regions where complex bathymetry introduces non-linearities to shoaling wave behaviour, which are difficult to account for. The method also offers a much better spatial resolution as it estimates depth on a pixel-by-pixel basis, as opposed to an area of wave field. In addition, other methods rely on the ability to image clear wave patterns which are not always visible on radar images.

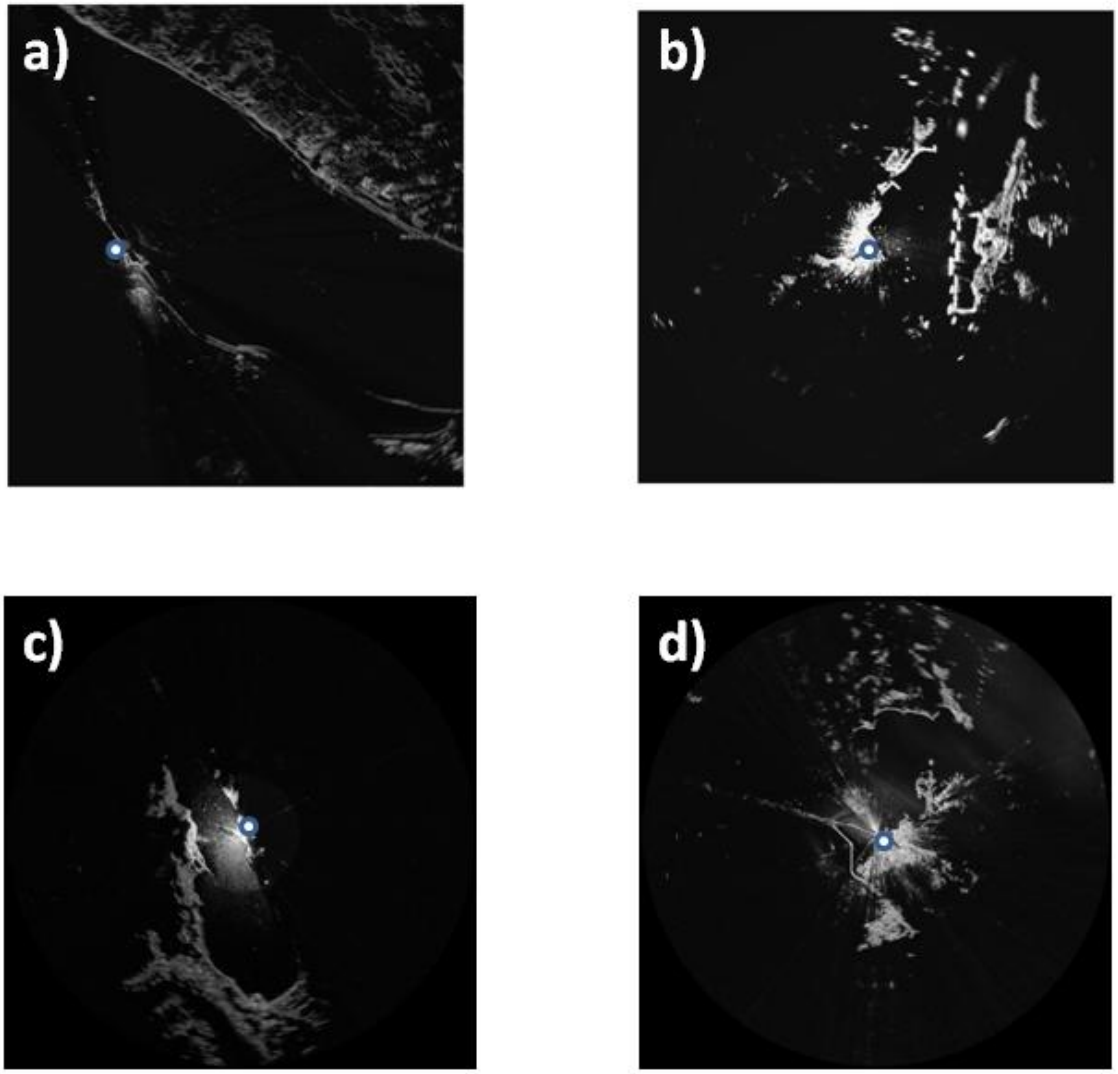

Figure 3.6: Radar image data from several locations around the UK, radar locations shown as white and blue circles in the images, (a) Port of Liverpool, (b) Milford Haven, (c) Cairn Ryan, (d) Holyhead. Note: data have been post-processed to remove much of the sea clutter as these data were collected for navigation monitoring prior to this project (Data courtesy of *Marlan Maritime Technologies*).

3.7.1 Current State-of-the-art Radar Coastal Monitoring Systems

From the analysis of current remote sensing techniques in Chapter 2, it can be seen that there are some severe limitations to the provision of cost-effective, accurate and wide reaching coastal monitoring. The use of X-band radar systems as a tool for remote sensing has many significant advantages over traditional methods (Bell et al., 2006). Radar in this capacity acts initially as a sea surface imaging tool (this imaging process is explained in more detail in Chapter 4), prior to performing more complex algorithms on the data, and is able to continue to gather data under adverse weather conditions. Radar has been used to monitor wave fields under stormy conditions (Hasan and Takewaka, 2007) including tornados (Inoue et al., 2011). Radar observation also enables continuous data collection in near real-time under these conditions. In contrast to other advanced space or airborne remote observation methods, such as satellite SAR, marine radar covers a much smaller area. However, marine radar is a fixed installation that allows the temporal evolution of the imaged area to be analysed (Nieto-Borge et al., 1999). It is also much cheaper to implement than satellite due to the ubiquitous nature of marine radar infrastructure and its low operational cost.

As radar is in continuous operation, a relatively unbroken time series of data may be gathered, this allowing for long-term trends in coastal evolution to be analysed and predicted. In addition, many in-situ measurement instruments such as wave buoys and current meters require extensive maintenance due to exposure to the sea conditions, which causes gaps in data collection while the device is repaired. This can critically affect the statistical value of a data set. The radar system is of greatest value when it is supporting other deployments for cross validation and increasing data density of the survey area.

An example of a situation where many observation techniques have been employed simultaneously alongside marine radar is the Coastal Observatory project in the Irish Sea. This project was led by the National Oceanography Centre (NOC) at Liverpool and Southampton. Figure 3.7 shows the spatial locations of observations in the Irish Sea and Liverpool Bay. X-band radar at Hilbre Island (see Chapter 4) was employed to measure waves, bathymetry and currents in the River Dee estuary (Bell, 2007). The ten-year coastal observation project has now come to an end, and with it the collection of data from many of these sources. This project demonstrated that the proper measurement and collection of data over long timescales presents a significant task.

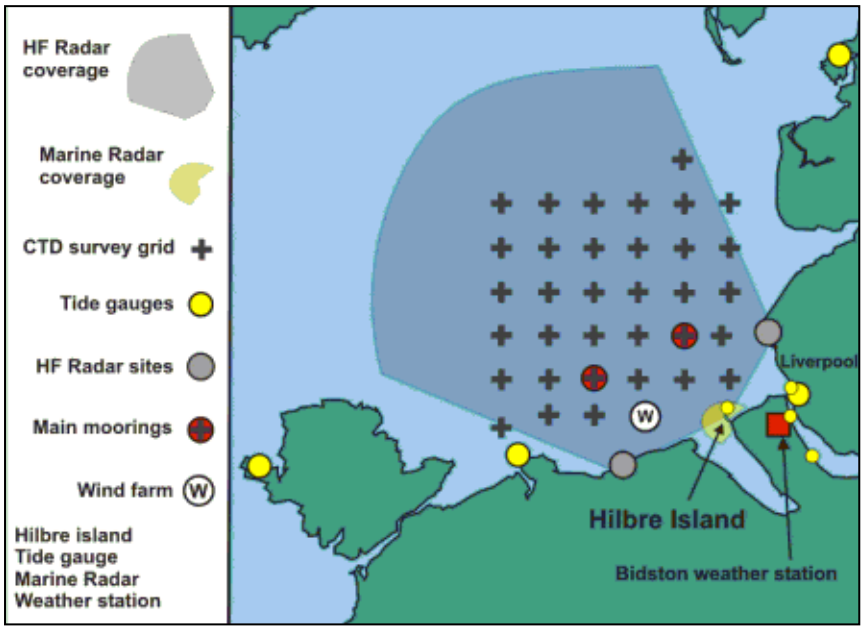

Figure 3.7: Locations of different coastal survey deployments during the Irish Sea Coastal Observatory Project (NOC, 2014).

Radar methodologies in coastal monitoring are divided into several application areas. Technology in all of these areas has advanced significantly since the inception of radar as a commercial technology. The current state-of-the-art in applications and technology will be discussed for each of the key application areas.

3.7.2 Commercial Radar Software Currently Available

Radar is used in research and commercial deployments to detect and measure wave height. *WaMosII* is a commercial software developed by *OceanWaveS GmbH*, that measures wave parameters and current information and does so effectively, especially in offshore areas (Reichert et al., 1999). *WaMos* has been commercially available since 1995. *MIROS* is a Norwegian company that produces several products for remotely monitoring wave states. Their '*SM-050* wave radar' is a microwave radar, that uses dual pulse Doppler methods for measuring waves and dual frequency analysis for measuring surface currents. It is used on fixed platforms such as oil rigs and slow moving vessels using motion compensation; it does not observe a wide area of the sea surface but is deployed in situ to measure a smaller area. The *WAVEX* product is also produced by MIROS, and this system uses an X-band scanner to measure wave states primarily using methods discussed in this section. *WAVEX* was originally used for research purposes but is now fully commercialised and lists coastal monitoring as one of its uses. However it is targeted primarily at commercial shipping operations outside of sheltered port areas.

The *SeaDarQ* system developed by *Nortek B.V.* (a Dutch subsidiary of the Norwegian Nortek AS) is a software suite that is available 'off the shelf' to interface with an X-band radar and process

the radar data. Using a fine resolution web of measurement points on radar image sequences sea state parameters are derived at a high resolution. This system also derives bathymetry and displays the results on a graphical user interface. High frequency (HF) radar systems are also used extensively to monitor waves and currents; they are also employed primarily in meteorological observation and providing data for weather prediction models (Barrick, 1977; Wyatt et al., 1999; Ohlmann et al., 2007; Barrick et al., 2012). However these large arrays are expensive and planning permission for the sites is prohibitive. They are also generally used for air surveillance, not navigation and their current use in coastal and port monitoring is limited. The following sections detail the current underlying methodologies and techniques that enable estimates of wave parameters, surface currents and bathymetry.

3.7.3 Waves Parameters Derived From Radar Data

Rough-surface microwave scattering theories can be exploited to gather information on sea state parameters; a major indicator of such is the wave power spectra (Valenzuela, 1978; Plant and Keller, 1990; Wetzel, 1990). The returned noise signal received by marine radar systems is generally a result of sea clutter including, but not limited to, the reflection of energy from sea waves. This type of clutter is usually filtered from the traditional navigational radar display and removed from subsequent data analysis (Nieto-Borge et al., 1999). However if the sea state is to be analysed with marine radar, this sea clutter will be the primary source of information. An analysis of this sea clutter can produce information on the three dimensional spatial and temporal variability of the sea surface (Young et al., 1985).

The measurement of sea state using marine radar is based on the principle backscattering of electromagnetic waves by ripples and roughness upon the sea surface. These ripples on the surface of waves are caused by local wind blowing over the surface; for this reason the presence of some amount of wind blowing is necessary to obtain information about the sea state (Nieto-Borge et al., 1999). As radar imaging relies on this minimum presence of sea surface roughness, the presence of moderate amplitude, long period swell waves may go unnoticed while small waves on a breezy day will be imaged by the radar system. In order for effective measurements to be taken, significant wave heights should be in excess of 1 m and wind speeds in excess of 3 m/s (Bell and Osler, 2011). Furthermore, Takewaka (2005) determined that Bragg scatter occurs when the wavelength of the wind driven capillary waves (roughness on the surface of a wave) is equal or in excess of half the wavelength of the radar beam. However, the pattern of detectable backscattering is modulated by larger sea surface structures such as ocean waves (Young et al, 1985; Ward et al., 2013), and surface gravity waves become visible in these radar images by hydrodynamic modulation, tilt modulation and shadowing, especially in SAR radar imaging (Alpers et al., 1981). X-band radar is ideal for this task as the relatively short electromagnetic wavelength (~3 cm) interact with the ripples and roughness caused by capillary waves with wavelengths in the order of centimetres (Bell and Osler, 2011).

Nearshore coastal zones are incredibly energetic and thus dynamic areas where waves shoal, break and interact with the morphology of the coast. As the waves approach the shore, they experience changes very different to those of waves in the open oceans. A different method to that described by Young et al. (1985) and Nieto-Borge et al. (1999) must therefore be used, however the principles of 3-D spectral analysis are still utilised. Some of the effects exerted on the incoming wave fields include refraction, non-linearity, shoaling and breaking; these

parameters influence wave properties in a variety of ways (Hasan and Takewaka, 2007) and serve to reduce the accuracy of bathymetry derived in shallow waters.

The amount of energy returned to the radar is converted to a normalised greyscale pixel intensity and sequences of radar images include sea state information in spatial (x, y) coordinates and time (t) coordinates (Nieto-Borge et al., 1999). To obtain information about the wave field from radar images, a consecutive sequence of digital radar images is stored and from the raw image data, a selection of rectangular sub-images images are extracted. The purpose of sub-sampling the data is to reduce the computational requirements of the subsequent data processing and to prepare the image for the 3-D Fourier transform to the spectral domain. Figure 3.8 from Nieto-Borge et al. (1999) shows how the images are arrayed with respect to spatial structure and time dependence; the progressing wave field is clearly visible on these images. From these images the three dimensional image power spectrum $I^3(k,\omega)$ is computed. The contributions to total spectral energy come from wave energy due to modulation of backscatter, background noise due to roughness of the sea surface, and higher harmonics of the wave energy due to radar imaging effects (Young et al., 1985).

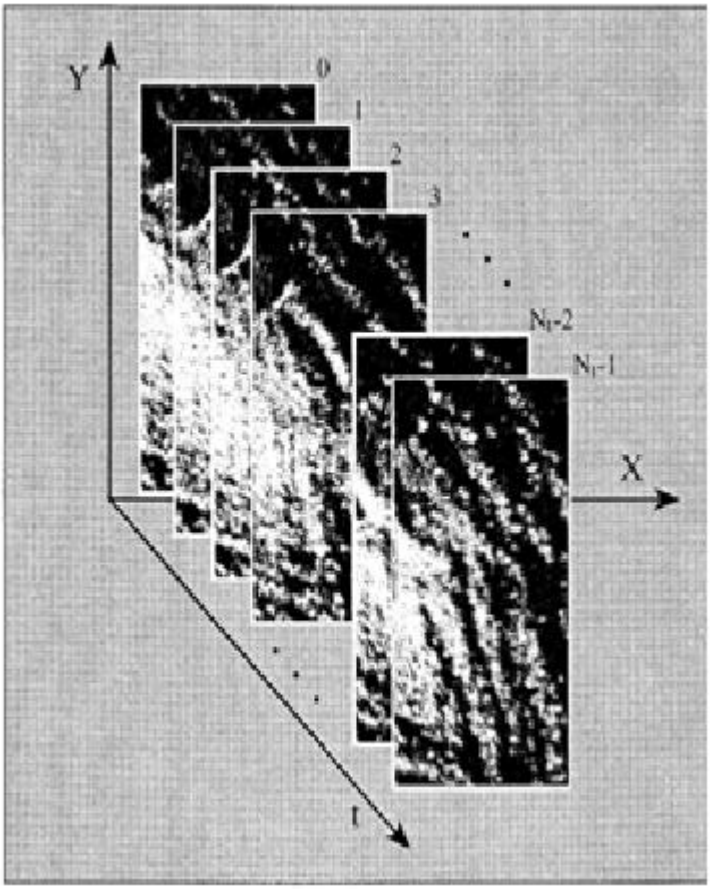

Figure 3.8: Consecutive radar snapshot images arrayed through time. From Nieto-Borge et al., (1999).

These images must also be filtered in order to remove the effects independent of the wave field, including the background noise and higher harmonics The wave energy in the three dimensional image spectrum must be located within range of the dispersion shell (Nieto-Borge et al., 1999).

The processed radar images can also be arrayed into cross-sectional image time stacks. (Hasan and Takewaka, 2007) used both cross-shore and long-shore image stacks, examples of which are shown in Figure 3.9. These images are composite images where the lateral and vertical axis

represent variations in space and time. A line of pixels is extracted from consecutive radar images and arrayed side by side to produce these images. Similar images from video cameras were used to visualise wave run-up motions and wave propagation speeds in the swash zones (Stockdon and Holman, 2000). These image time stacks contain information in the spectral domain in separate frequency components; these require frequency separation to determine and estimate the individual propagation speed of each specific wave component (Hasan and Takewaka, 2007).

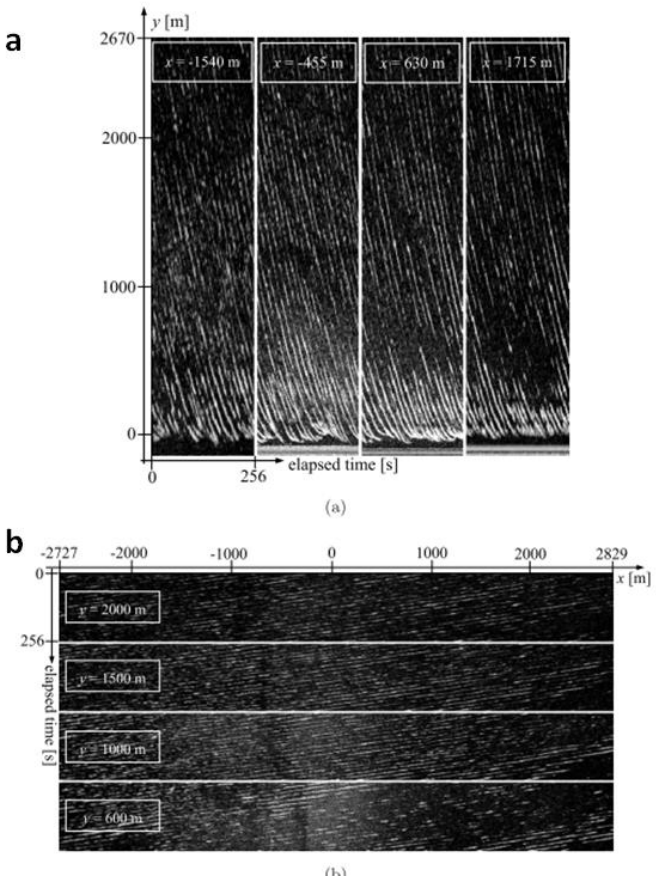

Figure 3.9: (a) Cross- and (b) long-shore image timestacks where each row represents intensities along a transect through time. From Hasan and Takewaka (2007).

Temporal variations in intensity returns shown in the time stack images are analysed with a 3-D Fast Fourier Transform (3-D FFT). The images are passed through a 3-D FFT and the peak frequency corresponding to the highest spectral density is determined. The use of FFT, and in particular 3-D FFT throughout time stacked images, is a ubiquitous practice in the observation of wave state by radar (Young et al., 1985; Nieto-Borge et al., 1999; Senet et al., 2001; Dugan et al., 2001; Bell 2001; Bell et al., 2006, 2012; Bell and Osler, 2011).

The primary function of this method is to break down the image spectrum into discrete components that can be used to determine 2-D wave spectra. Hasan and Takewaka (2007) used this technique to construct a set of frequency spectra by averaging over a transect of 128 pixels in the long-shore direction and normalising the intensity values between 0 and 1. The results from Hasan and Takewaka (2007) are shown in Figure 3.10. The higher spectral strengths are represented by brighter intensities. As the figure shows, the peak frequency (representing the wave crests on the radar image time stacks) lies around 0.067 Hz giving a wave period of ~ 15 seconds. As celerity is relatively constant from offshore to onshore (Hessner et al., 1999) and the propagation of waves is uniform across the long-shore direction. These data reflect peak wave periods from the radar images. The directional variations in onshore wave propagation can also be examined by identifying the dominant wave crests within the image and estimating the wave angle. Hasan and Takewaka (2007) propose a method to obtain such estimation which involves the temporal filtering of the image sequence. The images were filtered at the dominant Fourier component of the radar signals which correspond to the peak frequency of the averaged and normalized spectra, displayed as f_p in Figure 3.10.

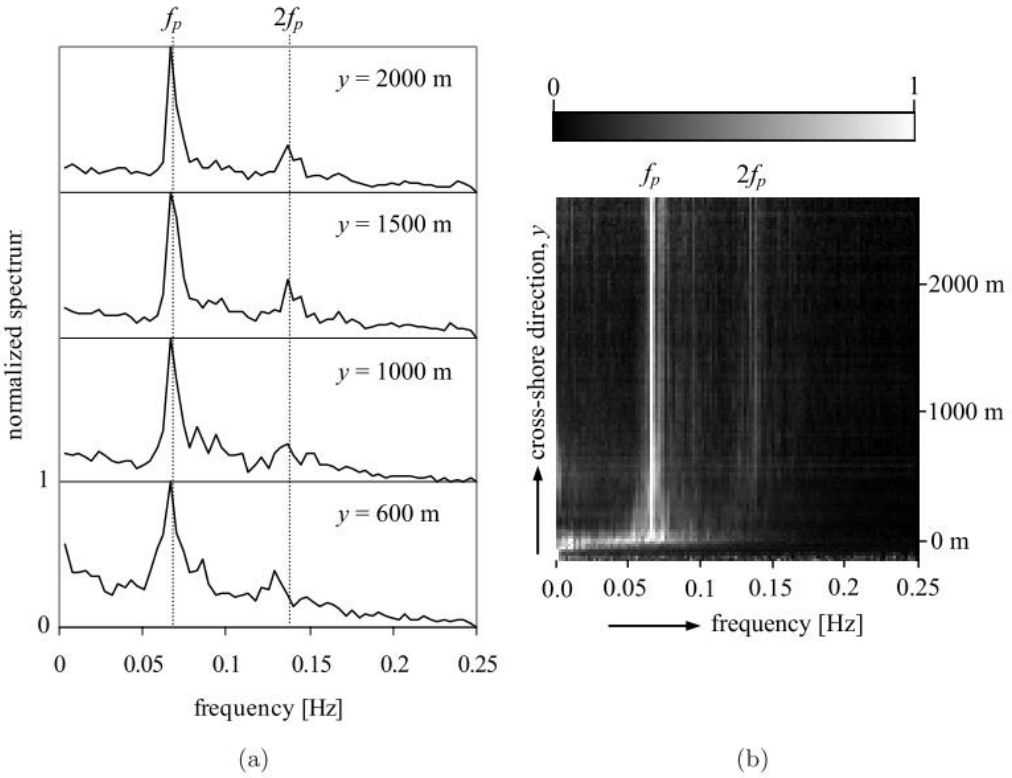

Figure 3.10: Resulting spectral analysis of cross-shore transects, illustrating peak frequency (and thus period) from Hasan and Takewaka (2007).

Figure 3.11 shows a radar image of a wave field filtered through the above process, with the dominant wave pattern clearly defined. As radar also observes this in a temporal setting, the wave speed can be determined by measuring the distance a given wave crest has travelled and dividing this value by the rotation speed of the radar. By this point the frequency, speed and period of the dominant wave crests have been determined. Using these parameters Linear wave theory (Airy, 1845) can be used to derive several other key parameters. In order to estimate the angular wave number of this field, Linear wave theory is utilised where k is angular wave number in radians per metre.

$$k = \frac{2\pi}{\lambda} \tag{21}$$

The angular frequency may also be derived with this information:

$$\omega = \frac{2\pi}{T} \tag{22}$$

These parameters form the basis of the depth inversion technique used in the derivation of bathymetry and currents.

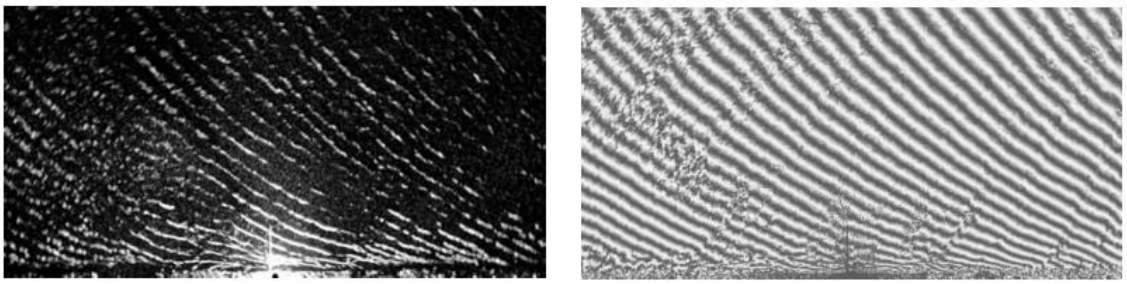

Figure 3.11: (a) Radar image (b) phase filtered around peak frequency, the wave pattern is clearly visible. From Hasan and Takewaka (2007).

In addition to directly observing wave parameters from spatial variations in an image sequence, these images can be analysed spectrally. When a stack of images is processed using a 3-D FFT, the result is a 3-D image spectrum within which energy will be distributed according to its spatial and temporal frequency. Much of this energy will be a result of radar noise and sea spike

clutter etc. However, assuming a clear and visible wave field is present in the image sequence, there will also be a prominent and clear energy distribution that represents those waves (Young et al., 1985).

3.7.4 Surface Currents Derived From Radar Data

The detectable motion of waves is seen by a radar system as a translation of the frequency echo signal from that of the transmitted frequency. This frequency translation phenomenon is called the echo Doppler shift. The radar resolves and measures the scatter velocity along the transect, between the radar transmitter and the target object (in this case an ocean wave or area of sea clutter); this measurement is known in radar nomenclature as the radial velocity (the observer in this case being the radar). The ability to detect the Doppler wave spectrum with radar has long been known Crombie (1955) and Barrick et al. (1977) used HF radar to map currents. The detection of currents via X-band radar is based on similar principles that apply to the HF radar. In the absence of currents, the sea clutter echo is seen as two symmetrical peaks around the carrier frequency and the Doppler shifts can be given by:

$$\pm f_d = 2v_{ph}/\lambda = 2(gL/2\pi)^{1/2}/\lambda = (g/\pi\lambda)^{1/2} \quad \textbf{(23)}$$

where λ is the radar wavelength, $L = \lambda/2$ is the wavelength of ocean waves (causing Bragg scattering) and v_{ph} is the phase velocity of said waves while g is the gravitational acceleration.

With the addition of a current, the two symmetrical spectral peaks scattered from the waves will be shifted from their theoretical positions by an amount proportional to the radial velocity of the current. This shift in frequency is equal to $\Delta f = 2v_{er}/\lambda$, here v_{er} is the average effective current radial velocity (Barrik et al., 1977).

The above described method applies to the derivation of surface currents using HF radar. Analysis of this phenomenon from marine radar images involves transforming the image sequence into the wavenumber - frequency domain through 3-D FFT and fitting the observed energy variance to the dispersion relation of surface gravity waves. The surface of this plot is called the dispersion shell, this shell is deformed in a predictable manner when under the influence of the Doppler shift (Young et al., 1985; Senet et al., 2001). Figure 3.12 shows the theoretical dispersion relation for linear surface gravity waves and the deformation of shape due to current influence. This shell is used as a bandpass filter to isolate wave energy 'feeling' surface currents. The shell is generated using the equation:

$$\boldsymbol{\omega = \sqrt{g\, k \tanh(k\, d) + k\, U}} \qquad \textbf{(24)}$$

where *d* is water depth and *U* is the current magnitude vector, clearly the shape varies according to both depth and current (Nieto-Borge et al., 1999)

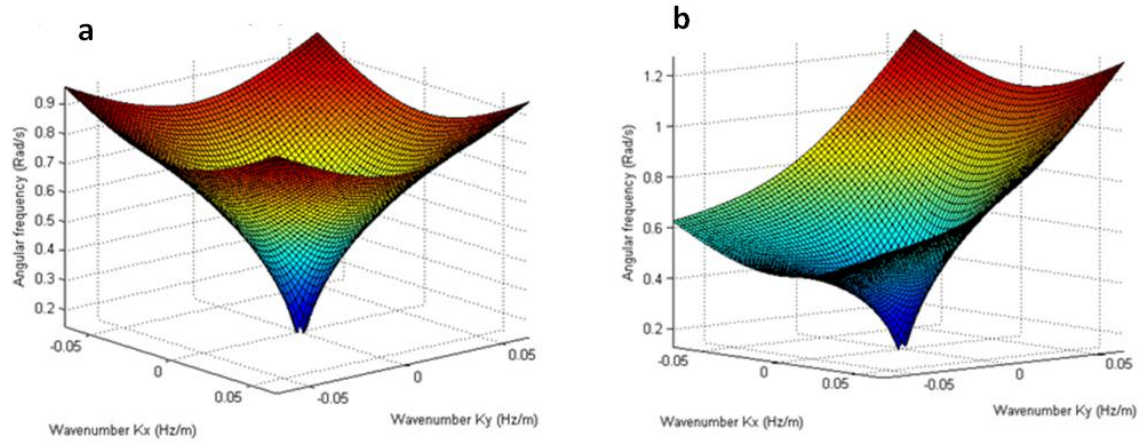

Figure 3.12: Theoretical dispersion relation for linear surface gravity waves (a), under no surface current influence (b), deformed as a result of a 5 m/s (high speed) surface current.

From the information given by the shift in frequency and the shape of the dispersion shell, the velocities and directionality of currents acting at analysis points in the radar image may be determined (Bell and Osler, 2011).

3.7.5 Bathymetry Derived From Radar Data

Marine radar generally operates well in low visibility, has excellent temporal and spatial coverage and is able to provide similar data to that of a camera at lower resolution but to a significantly greater range and regardless of light conditions. X-band radar has recently become an integral part of the nearshore remote sensing infrastructure (Holman and Haller, 2013).

Operationally, it has been used extensively to determine 2-D wave spectra in offshore areas for both commercial and scientific applications for many years now (Reichert et al., 1999; Nieto-Borge and Guedes-Soares, 2000), for the most part using techniques originally developed by Young et al. (1985). The visibility of ocean waves on the radar imagery and the ability to record sequences of these images of the waves allows their wavelength and period to be determined. If currents are neglected, various techniques can be used to fit the water depth that best explains the observed wave behaviour (Hessner et al., 1999; Bell, 1999, 2008; Bell et al., 2006; Flampouris et al., 2009).

If the data are from areas where currents cannot be neglected, it becomes necessary to find the best fit to the location of the wave dispersion surface in the full 3-D wavenumber-frequency domain, in terms of the water depth and the two components of the current vector. Again, there are various approaches to both determining (and sometimes filtering) the frequency wavenumber spectrum and also a number of approaches to finding the best fit of the current vector and depth to the observed wavenumber spectrum (Nieto-Borge et al., 2004, 2008; Senet et al., 2008; Hessner et al., 2009; Serafino et al., 2010). This technique has been used successfully to map surface currents at a tidal energy test site in Scotland UK (Bell et al., 2012). Recently, the additional complication of correcting for vessel movement has started to be addressed in order to allow bathymetry mapping using radar data from a moving vessel, and water depth maps down to approximately 50 m have been shown to be possible (Bell and Osler, 2011).

The overriding stipulation for these wave inversion techniques however, is that clear and homogeneous wave fields must be visible to the radar in order for the analysis to work

accurately. The 'waterline method' detailed in the following chapters, is much less reliant on the presence of a significant wave pattern and does not require wave inversion methods.

Traditional methods for determining the bathymetry of coastal areas include sonar scanning via periodic survey vessels; prior to this the lead line sounding method was employed to map the sea floor topography. The need to analyse bathymetry in precise detail was first fully recognised during the WWI. The British Royal Navy, in particular the Dover Patrol Command, used aerial photographs in combination with tidal levels, measured from submarines to map French and German beaches. This allowed contour maps to be constructed for potential landing sites such as the raid on Zeebrugge in 1918 (Bacon, 1932). Techniques for remote mapping of beaches were further developed in the 1940's in the process of planning amphibious landings during WWII. In the run up to D-day (06 June 1944), precisely timed aerial photographs were used to take measurements of wave velocity and wave direction and linear wave theory was used to estimate depth in preparation for landings (Hart and Miskin, 1945; Williams, 1947).

For scientific and commercial operations in coastal areas, the first necessary component is often a detailed and accurate bathymetric map. The requirement for this is to ensure effective deployment of equipment and resources to the correct areas. In addition, during coastal modelling data grids must be accurately defined and the necessary bathymetric data is often not available directly (Bell and Osler, 2011). It is extremely expensive and time consuming to commission bathymetric surveys in order to obtain this information, especially in an experimental context where available funding is often strictly limited.

Other demands for bathymetric analysis are numerous and include: quantifying seafloor textures according to different geographical regions, detecting and classifying seafloor objects (fault scarps and lava extrusions), detecting acoustic anomalies (potentially indicating the presence of natural gas or oil deposits), and detecting temporal changes in sea bed topography allowing analysis of currents and sediment movement (Vogt and Tucholke, 1986).

By using a stable, shore-based navigation radar system deployed in nearshore areas of morphological interest, wave state and sea surface (and thus depth) measurements can potentially be taken at regular intervals. The regular measurements can also allow observation of energetic events such as storms. This will allow the morphological changes brought about by the effects of a storm to be measured and future impacts mitigated. Stormy conditions will adequately exceed the minimum wind speed and wave height of 3 m/s and ~1 m, respectively, required to acquire accurate radar data on sea state (Reichert et al., 1999).

Methods of deriving bathymetric information from X-band marine radar have been developed by a number of researchers (Bell et al., 1999; 2001; 2006; 2008; 2009; 2010; 2011; 2012; Hessner et al., 1999; Serafino et al., 2010; 2012) over a number of years. These methods have used and built upon those techniques used to analyse wave parameters described in the previous section. The collection of wave state parameters and accounting for surface currents is the vital first step in estimating the bathymetry of an area.

There are a variety of different ways to indirectly estimate bathymetry using depth inversion methods. Inversions can be based on the time domain or the frequency domain, as described by (Misra et al., 2003). Temporally dense wave image data are analysed via spectral analysis and

derive the water depth from linear or non-linear wave dispersion relationships. Inversion methods performed in the time domain however, use sparse temporal wave data from few sequential images over a short time period. These images must contain wave phase or surface elevation information in order to perform the wave inversion.

Indirect inversions can be sub-divided into three groups depending on the source of information. Methods rely on either depth-induced spatial variations in water surface roughness, changes in local wavenumber or wave phase speed (celerity) in the cross-shore direction and along a varying depth profile or visible cross-shore dissipation patterns brought about by depth-induced wave breaking (Aarninkhof et al., 2005).

Data for these inversions can be provided by modelling in addition to direct observations as inputs for the linear wave dispersion relationship used to derive bathymetry (Catalan and Haller, 2005). However, if the derived information is to be used commercially or for scientific purposes, the data must be validated through direct measurement.

Regardless of the basis of the depth inversion all use the relationship between water, depth, wave period, and wavelength. The wave dispersion relationship identifies water depth given the wavelength and period. Due to the downward penetration of wave effects through a depth of water, that is proportional to their wavelength, depth can be derived from the wave dispersion relationship. Interactions of the sea bed and/or littoral currents with the wave throughout the depth profile cause noticeable changes in the propagation of a wave field. By measuring specific characteristics of the wave propagation the most likely conditions which led to the observed

wave behaviour can be inferred. In general waves slow and wavelengths decrease (attenuation) as they enter shallower water, angular frequency also decreases with depth and this causes a 'slumping' of the dispersion shell. Energy from waves propagating in shallow waters will lie at lower frequencies than those in deeper water. This method is simple in theory yet complex in application, especially in shallow water and intertidal regions where bathymetry varies greatly. Wave patterns from multiple wave fields in these areas often exhibit a broad spectrum of wave periods and angular directions caused by refraction and diffraction over varied topography and are therefore much more difficult to analyse directly. In these areas, noise from sea clutter caused by sea spikes and spray may also dominate the spectrum and make the isolation of individual wave signals and subsequent fitting of the theoretical dispersion shell in three dimensions. Detailed analysis of spectral patterns are required in order to separate and determine the isolated wave properties.

The primary technique for spectral analysis in this manner is the Fourier Transform series. This method transforms the problem from the 3-D time-space domain into the 3-D frequency-wavenumber domain. In this domain, energy of wave propagation in a given water depth is found to cluster around a 3-D surface that resembles a cone shape (Figure 3.12). This shape is defined by the wave dispersion relationship for that given water depth. Water depth can be derived from this information if enough wave components are present at the range of wave periods and directions that identify a cone shape in frequency-wavenumber space; the wave theoretical dispersion surface can then be fitted to the wave components. Sea waves often propagate in a narrow band of directions, and resonate across limited frequencies the result of this is that wave components do not outline the dispersion cone surface; they instead cluster and must be fitted to the resultant relationship in order to determine water depth. The

reliability of this procedure increases if the wave field direction spread becomes wider and frequency distribution of the wave components becomes broader (Bell and Osler, 2011).

Depth values can be determined by examining the point at which an incoming wave is affected by an interaction with the sea bed. In order to utilise this relationship a limit on which sea waves are suitable for the technique must be established. Bell et al. (2011) define waves suitable for mapping to those waves with wavelengths less than 90% of the wavelength in deep water. Although the effects of sea bed interaction can be seen earlier, a 90% mark gives enough certainty that the reduction in wavelength is caused by the transition from deeper to shallower waters and not other factors.

Deep water wavelength can be described by the Airy wave theory equation:

$$L_0 = \frac{gT^2}{2\pi} \quad (25)$$

Whereas the wavelength when under influence from sea bed is given by:

$$L = L_0 \tanh kd \quad (26)$$

utilising wavenumber and depth derived from linear wave theory in order to determine the wavelength as the wave is being effected by water depth, as shown in Figure 3.13.

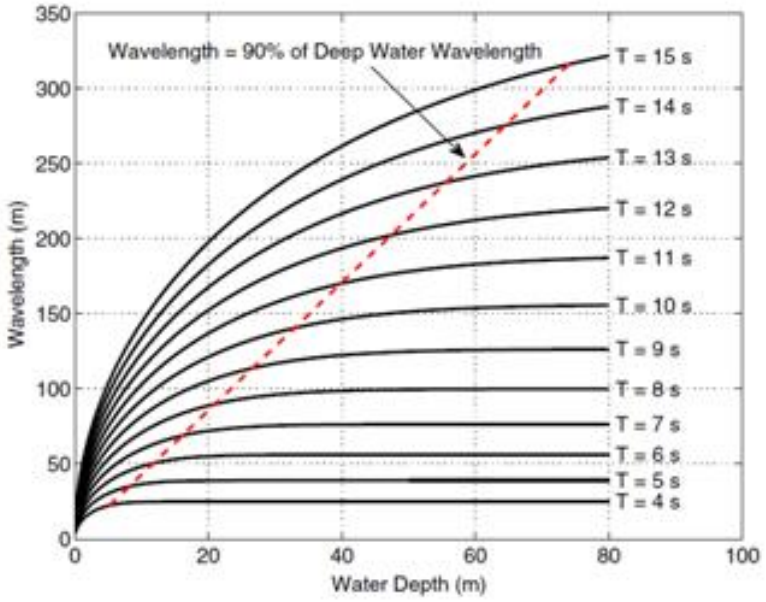

Figure 3.13: The relationships between wavelength, water depth and wave period according to linear wave theory from Bell and Osler (2011).

This phenomena is illustrated in Liverpool Bay by Bell (2007), where fetch (length of water over which wind has blown) is limited in the sheltered Irish Sea, resulting in wave periods of between 7-8 s. Following linear wave theory, such wave periods would suggest water depths of 15-20 m. This is confirmed in the Liverpool Bay area, however beyond the shallow water depth limit (~50 m) into deeper waters the depth inversion analysis will not be effective as waves show very little increase in wavelength or speed regardless of the increase in depth. Results of the depth inversion analysis by Bell (2007) are seen in Figure 3.14.

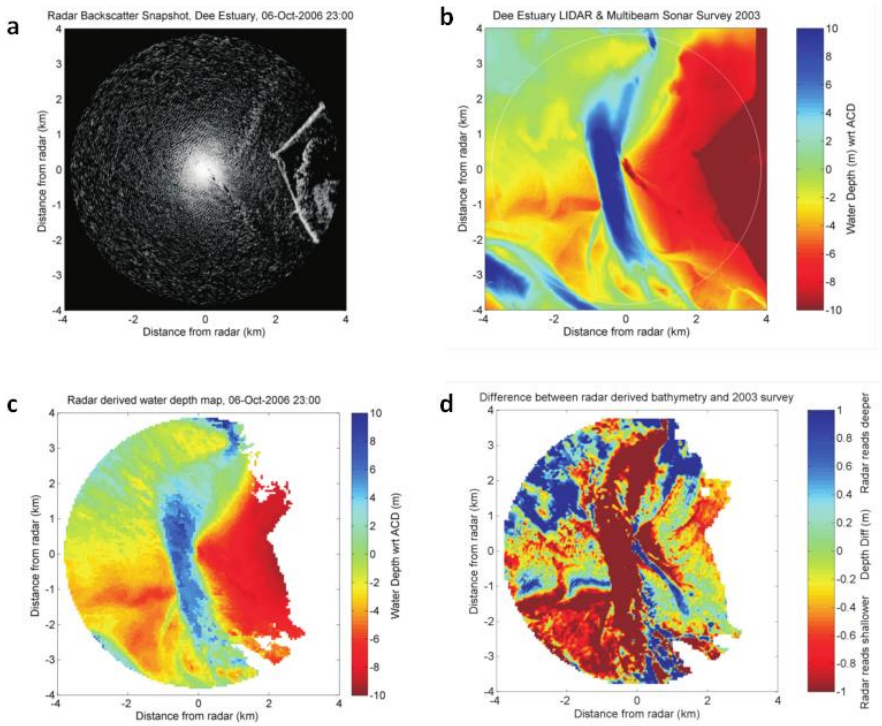

Figure 3.14: Results of a wave inversion bathymetric analysis from Bell (2007). (a) Radar snapshot from Hilbre Island (b), LiDAR and multibeam sonar survey of Dee Bathymetry. (c) Radar-derived bathymetry, (d) residuals between radar and LiDAR derived bathymetries.

Wave celerity and wavelengths are overestimated to some extent using linear wave theory, therefore errors are introduced in the depth determination. This error is most pronounced in very shallow, nearshore waters. A dispersion equation that has the capability to approximate higher order wave theories is used. This equation is based on linear theory, however the amplitude dispersion caused by the non-linear behaviour of waves in shallow water is corrected for (Hedges, 1976) which allows a better estimate of depth in shallower areas.

The used equation must also account for the temporal and spatial variability introduced through the Doppler effect as a result of nearshore currents. Hedges, (1976) describes wavelength under the influence of a current as:

$$\boldsymbol{L = \frac{2\pi\, g\, tanh\, k\,(d + Z)}{(\omega - k.U)^2}} \qquad \textbf{(27)}$$

In this equation, angular frequency $\omega = 2\pi f$ and U is the vector of the current (which can be determined with marine radar, see previous sections) and Z is the amplitude dispersion correction factor. Booij (1981) values this as Z = 0.5H (H= wave height) or Z = 0.35Hs (Hs = Significant wave height) when dealing with spectral waves. In order to derive water depth under these conditions, the equations must be re-evaluated in terms of d (Bell and Osler, 2011):

$$\boldsymbol{d = \frac{1}{k}\left(\tanh^{-1}\frac{(\omega - k.U)^2}{gk}\right) - Z} \qquad \textbf{(28)}$$

It is this process that is applied to create a map of bathymetry from marine radar image sequences. There are other ways to approximate the higher order wave activity (Kirby and Dalrymple, 1986). Regardless of the specific method used however, most errors induced during the depth inversion originate from inaccurate inputs to the equation, including wavelength, period and wave height (Catalan and Haller, 2008). These inaccuracies can result from poor or noisy image data, causing a lack of clear wave signal in the spectrum or incorrectly associating clutter or noise with valid wave signals. This technique has also been performed from a radar on a moving vessel, allowing a large area of offshore bathymetry to be mapped remotely (Bell and Osler, 2011).

A combination of these analysis techniques have been used to map bathymetry and surface currents at complex coastal areas. Figure 3.15a shows results from New Zealand from Hessner et al. (2014) and Figure 3.15b shows results from a site in the North Sea (Hessner and Bell, 2009). Note that in both examples, the intertidal region immediately adjacent to the land mass is not well resolved, a combination of current, bathymetric and intertidal mapping (Chapter 5) is now possible using a single radar system.

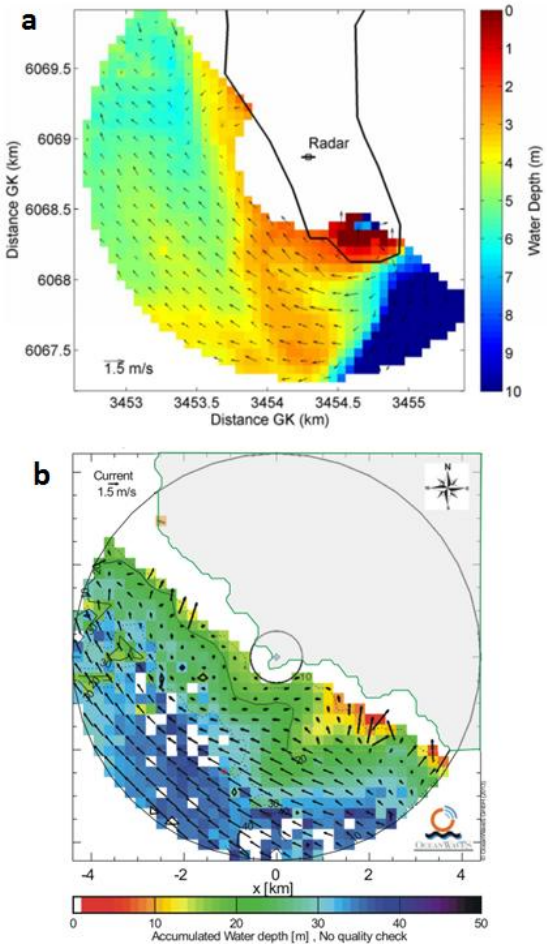

Figure 3.15: Subtidal bathymetric mapping combined with surface current analysis, (a) from Bell and Hessner 2009, (b) from Hessner et al 2014.

It is clear from this description of state-of-the-art radar coastal monitoring techniques that there is good coverage within the nearshore, subtidal area for both bathymetry and surface current derivation. There remains however, a significant gap in the available tools with the dedicated role of surveying intertidal areas. In providing this capability, the technique presented in this thesis aims to fill this role and compliment other radar survey techniques. The development of radar as a semi-mobile survey platform described in Chapter 7 also broadens the capability of radar to survey remote coastal areas.

4 DATA COLLECTION

4.1 STUDY SITE OVERVIEW

This chapter will detail the study site and data collection techniques for both the radar image data, the record of tidal elevations and an airborne LiDAR survey that will be used to ground truth the radar survey results. These data were used in the development of a radar waterline survey technique that builds on the principles of other waterline methods described in Chapter 2 in order to survey intertidal areas thereby filling a significant gap in survey capability of marine radar technology. Initial research and development of the radar waterline method was carried out using marine radar image data collected from Hilbre Island during March 2006 to January 2009. Data were collected during the Irish Sea Coastal Observatory project that ran from 2001 - 2010. The radar images were initially collected to derive sea surface currents and nearshore bathymetry, using wave inversion techniques described in Chapter 3.

4.1.1 Liverpool Bay and Irish Sea

The Northwest UK has a strong industrial and maritime heritage, and at the height of the Industrial Revolution, products were processed and manufactured at mills and factories at inland locations, such as Lancashire and Manchester. These goods and raw materials were then transported along extensive canal networks to and from ports including the Port of Liverpool, a significant site of international trade and of vital importance to the national and local economy. The Port of Liverpool has long maintained the Mersey estuary and its navigation channels, giving trade and military ships access to the Irish Sea and the wider North Atlantic.

In terms of the present-day hydrodynamics of the Irish Sea, many researchers have undertaken studies in Liverpool Bay due to the comprehensive range of processes in operation (Holt and Proctor, 2003). The eastern Irish Sea coast is dominated by a macrotidal regime, with a mean tidal range of 8.22 m at Liverpool (Admiralty, 2000). Tidal currents can reach speeds of 1 m/s on spring tides (Krivtsov et al., 2008) and exceed 1.5 m/s during stormy conditions (Jones and Davies, 1996). Wave heights in the Irish Sea are mostly determined by fetch and directional variability, whereas heights in shallower waters are attenuated and refracted in the nearshore zone (Short and Hesp, 1982). The prevailing winds and waves approach Liverpool Bay from the northwest (Sly, 1966), with the wind conditions most commonly exhibiting significant wave heights of 0.6 – 1 m with periods of 4 - 4.5 s (Parker, 1975). During the autumn and winter months, the wave heights are generally higher and the largest recorded waves were 9.4 m with an 8.7 s period (Draper, 1966), while the typical storm conditions show significant wave heights of ~5 m and periods of 8 s (Pye, 1990).

4.1.2 River Dee and River Mersey Estuary

The Port of Liverpool has been in operation since 1715 and remains a critical part of the local economy. The continued operation of the port is reliant on the maintenance of the navigation channel, and as the morphology of nearshore Liverpool Bay is also relatively dynamic, several large sediment sources currently supply sediment to the Mersey estuary (Plater and Grenvillle, 2010). This has necessitated the construction of a large training wall, beginning in 1909 and completed during the 1960s, in order to aid maintenance of the navigation channel and reduce the sediment influx to the main deepwater channel. Prior to the construction of the Crosby channel training wall, Liverpool Port was also accessible through two smaller channels, the Rock Channel to the southwest along the Wirral coastline and Formby Channel to the north. These channels have since accreted, demonstrating the dynamic nature of this region, and are now closed to commercial shipping. Shallow water fishing vessels, wind turbine maintenance vessels serving the Burbo Bank site, and leisure craft continue to use the very shallow Rock Channel.

The evolution of the Mersey estuary over time is covered in significant detail by van der Wal et al. (2002). The revetments have helped to maintain the current navigation channel position, however significant dredging and repeated sub-tidal bathymetric surveys are required in a constant maintenance cycle. Also, the margins of the current channel frequently shift position as the training wall is overtopped with sediment. There has been significant study on the morphodynamics (Thomas et al., 2002) of the Mersey Estuary and the wider Liverpool Bay area, and there has been a significant increase in sediment supply to the Mersey Estuary over the last century as a result of revetment construction and continued dredging.

The morphology of the Dee and nearby Mersey estuaries have changed significantly over the last centuries. Chester was once a thriving port area, however the canalisation and resulting continued accretion and siltation of the Dee estuary has rendered the port defunct. Much of the Dee estuary is now occupied by extensive and well-established salt marsh (Marker, 1967). A single deepwater channel is now maintained from the *Airbus* factory at Broughton, to the port of Mostyn and the Welsh channel leading to the Irish Sea, which is significant to the local economy. It is evident from the chart in Figure 4.1, that where a navigation channel cuts through Mostyn bank, regular maintenance dredging is performed to sustain the depth of the navigation channel into Mostyn port.

The Dee estuary exhibits flood dominated tidal asymmetry, and is a mature infilled estuary approaching morphological equilibrium (little net sediment flux) (Moore et al., 2009). This equilibrium suggests that the sediment infilling the navigation channel channel is likely autochthonous. The Dee estuary is a funnel-shaped, macrotidal estuary with a maximum spring tidal range of >10 m. The site features particularly interesting geomorphology, with a progressively accreting saltmarsh to the south-east, migrating tidal channels within the central sandbanks, and shifting intertidal bed features along the beach. The waves within Liverpool Bay and the mouth of the Dee estuary are locally generated and fetch-limited within the eastern Irish Sea, such that significant wave height (H_s) is less than 5.5 m, the peak wave period (T_p) is less than 12 s, and the mean period is less than 8 s (Wolf et al., 2011).

4.1.3 Hilbre Island and Radar Deployment

Data used in this contribution were gathered using a standard *Kelvin Hughes* marine radar operating at X-band, 9.4 GHz located in an elevated position (~25 m AMSL) on Hilbre Island (53.381465°N, -3.226751°W) in the mouth of the Dee estuary, UK. These data were gathered over several years during the *Liverpool Bay Coastal Observatory* project**,** and the primary purpose of data collection at this location was to derive bathymetric maps of the estuary, using well established techniques (Bell, 2007). The method used here is described fully in Bell et al. (2016) and are given in the following Chapter. The increased resolution and accuracy of this new method, in comparison to previous radar depth mapping techniques, and in addition to the robustness and temporal resolution, allows trends in morphology to be identified along the Wirral coastline and within the sandbanks of the Dee estuary itself. Figure 4.1 shows a nautical chart of the Dee estuary and the concentric rings demark the radar range of the two datasets collected.

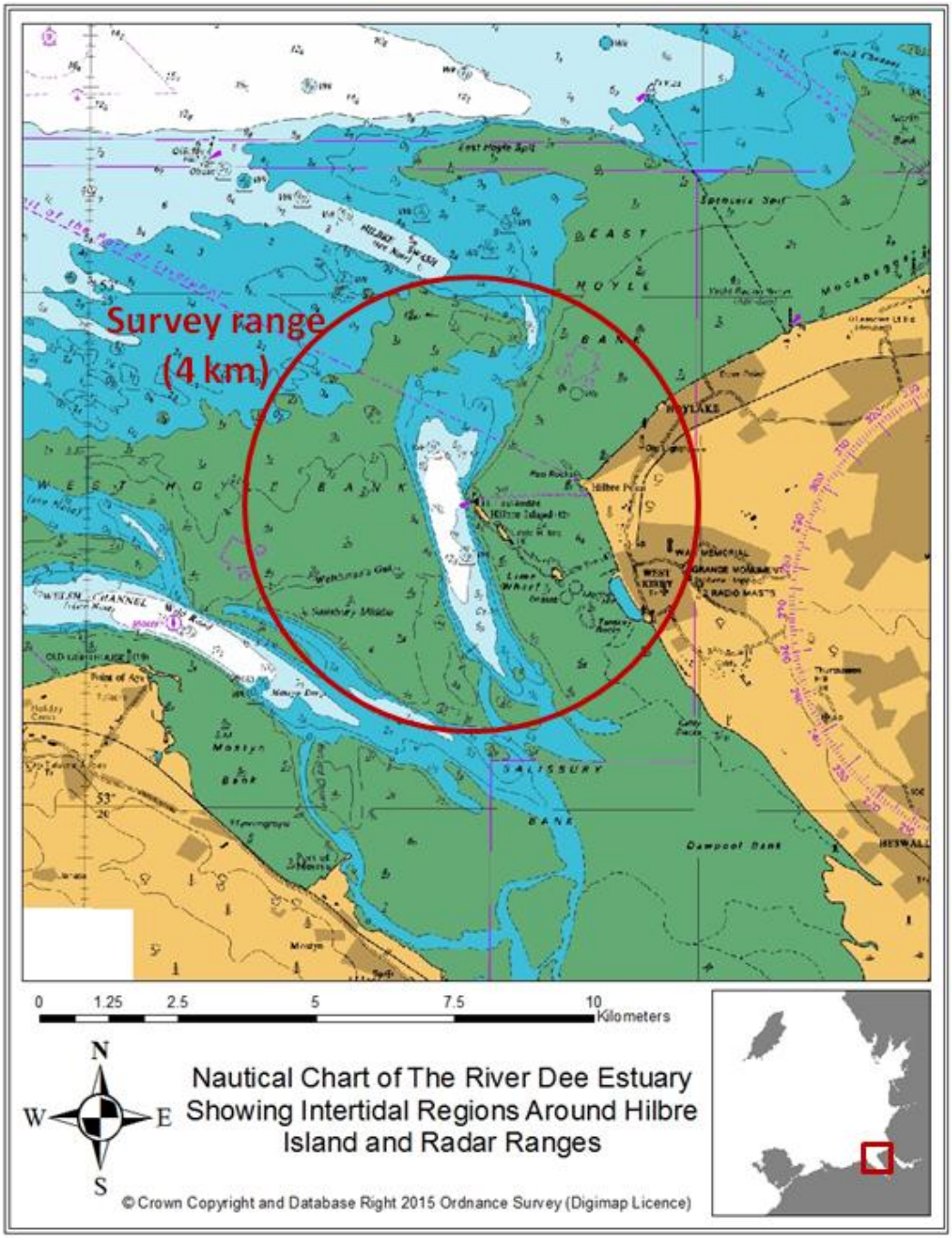

Figure 4.1: Nautical chart of the Dee estuary showing radar survey range extent from Hilbre Island (SeaZone Solutions ltd, 2015).

4.2 RADAR DATA COLLECTION AND PROCESSING

Hilbre Island at the mouth of the Dee estuary (Figure 4.2) offers clear visibility of the estuary and the north western beach of the Wirral peninsula.

Figure 4.2: Hilbre Island at mid-tide with Wirral Peninsula in the background and extensive intertidal area exposure evident.

Hilbre Island is cut off from the mainland for the upper half of every tidal cycle. In order to provide power to the site, a 2 kW wind turbine and off-grid battery storage system with a diesel generator back-up was installed by Wirral Borough Council, which provided power for the majority of the time. The remote nature of the site caused both the maintenance and monitoring of both the power systems and the radar system a challenge, and as such, numerous gaps exist in the dataset covered in Chapter 6. Despite these challenges, several years of radar data were collected before a number of factors made the collection of data impossible to continue.

The radar data used in the initial R&D work were gathered over a period of 10 months from March 2006 to January 2007. Further archives of radar data up to 2009 exist but have not been included in the initial study in Chapter 5. However, these additional data were used to analyse long-term trends in coastal morphology in Chapter 6. The antenna was set to short pulse (~60 ns), in order to cover ~4 km range radius. The data were then sampled at 40 MHz with a radial resolution of ~3.5 m, the antenna has an rpm of ~25, yielding an image every 2.4 s. The raw data were converted from polar coordinates onto a Cartesian grid, through the process of *scan conversion* to enable georeferencing and proper visualisation of the results as shown in Figure 4.3. The raw polar data can be directly converted to Cartesian with simple trigonometry, however this creates holes and spokes in the final image where data points are missing. To avoid this, the data are instead 'reverse scan converted', whereby every pixel in a pre-defined Cartesian grid with a variable cell size (in this case 5 m) is populated with the closest appropriate pixel from the B-Scan data using the following equation:

$$\boldsymbol{r = \sqrt{(x^2 + y^2)}\ and\ \theta = tan^{-1}\frac{y}{x}} \qquad \textbf{(29)}$$

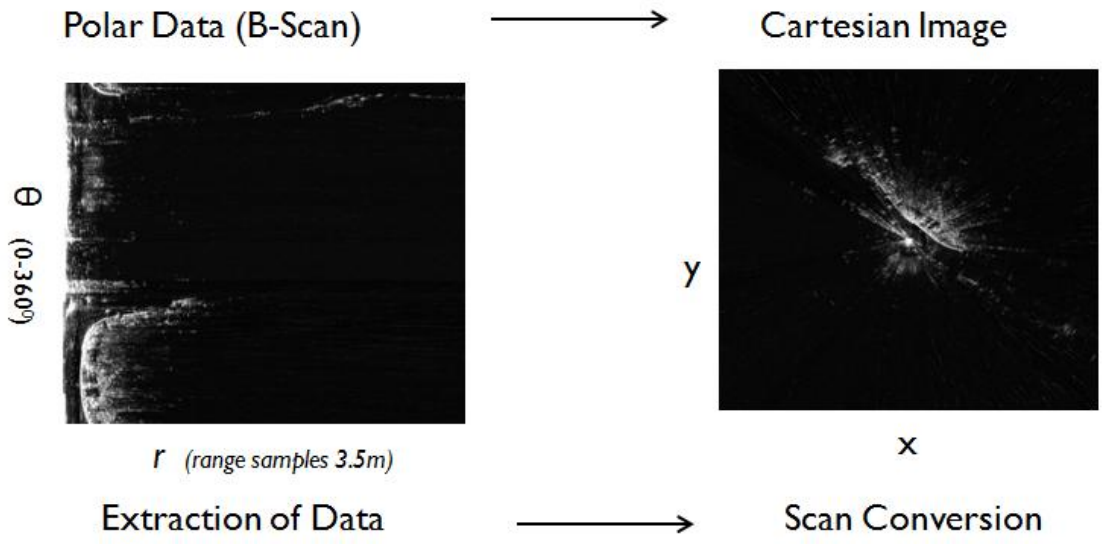

Figure 4.3: Radar snapshot image from a site at Birkenhead on the Mersey Estuary being reverse scan-converted from Polar coordinates (B-scan) (a), to Cartesian coordinates (b), with the radar location at the centre of the image.

Images produced from the radar data show not only detected hard targets such as ships and land, but also many reflections from the sea surface. This is known generally as 'sea clutter' and sea spikes, a scattering phenomena occurring when radar waves interact with steep or breaking waves at low grazing angles (Coakley et al., 2001; Fuchs et al., 1999; Ja et al., 2001; Trizna et al., 1991). This sea clutter is inconsequential for the most part if wind speed is low (<3 m/s). As the sea surface is not roughened sufficiently, significant wave heights less than 1 m are also difficult to detect with radar. Heavy rainfall is also visible on X-band radar and can potentially obscure the sea clutter (Bell et al., 2012). In most navigational radar applications, the sea clutter is considered a nuisance and is extensively filtered, in order to prevent the brightness of clutter obscuring small targets. This filtering is often performed using Constant False Alarm Rate

(CFAR) matched filter algorithms (Scharf, 1991). However, in the practice of using X-band radar as a tool for oceanographic observation, a clear image of sea clutter is strongly desired as hydrodynamic information can be derived from detailed analysis of the clutter data. Figure 4.4 shows a series of snapshot radar image data collected from Hilbre Island under different conditions. The hard coast of the Wirral is clearly defined to the east and sea clutter is also detected, particularly along the shoreline to the northeast where breaking waves give higher radar returns.

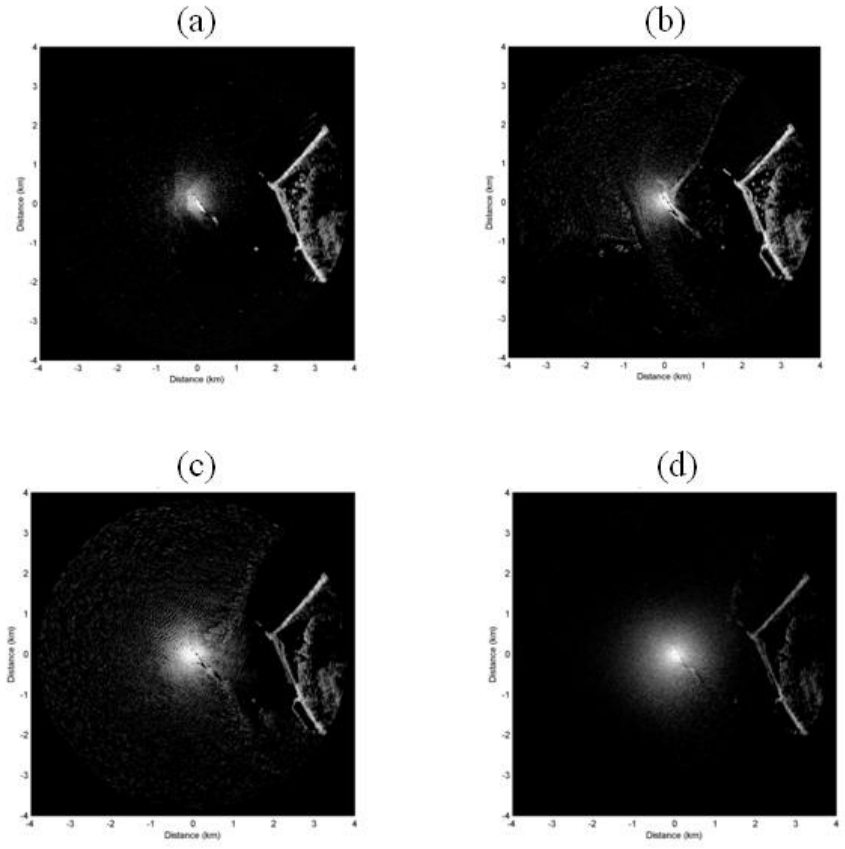

Figure 4.4: Snapshot radar image from Hilbre Island showing high returns from coastline and breaking waves along the waterline (a) calm sea state. (b) Normal sea surface conditions, (c) storm wave conditions and (d) heavy rainfall obscuring some radar data.

The conditions during which radar data are collected can dictate to some extent the quality of data retrieved. Good quality radar data have been collected during extreme storm events by Hasan and Takewaka (2007) and have been used to observe tornado dynamics by Inoue et al (2011) showing the ability of X-band radar to operate in adverse conditions. However the presence of significant rainfall can obscure the returns from the sea surface if wind speeds are also simultaneously low, this can make the detection of a waterline difficult. This aspect of data collection is somewhat alleviated by the use of time exposure images, over the course of 256 images (explained below), the stronger signal from repeated wave breaking at the waterline will be reinforced in relation to the more spatially distributed clutter signal from the rain. The more difficult issue to overcome in this application is the poor data quality during periods of low wind speed. Extremely low wind speeds (< 3m/s) will not produce significant roughening of the sea surface such to allow detection by an X-band radar. Little can done immediately to alleviate this issue, it is possible that taking time exposure images over longer time periods (e.g. 15 minutes of data) will serve to increase the detection probability of smaller returns. It should also be noted that despite a lack of sea surface clutter returns during calm weather, weakly breaking waves at the waterline should still be detected by the radar. If this methodology relied on this analysis of snapshot image data, these limitations would be significant and would introduce similar issues to those experienced in the use of video camera image analysis. However as this analysis takes place over longer time periods, it is significantly more robust when faced with periods of poor data.

Individual radar images give good temporal resolution, however for the technique presented here it is preferable to use time-averaged images to reduce the computational requirements of the method allowing for a better indication of clutter activity over a period of time; these timelapse images (also known as 'time-exposure' or 'timex' images) are effective for long-term analysis techniques. The time exposure radar images used in this paper represent just over 10 minutes of data (256 images) that were gathered either every hour or every 30 minutes depending on the operating conditions. The difference in tidal elevation between collected time exposure images can be on the order of more than one metre in the macro tidal Dee estuary. This potentially limits the vertical resolution of derived topographical elevations, this aspect of the work is explored in greater detail in section 5.3.2. At this temporal scale, individual wave fields are lost but overall patterns of breaking waves and rough sea surfaces can be seen with better clarity. Figure 4.5 shows a sample time exposure image used in this method. This image represents a period at low tide, and so a great deal of beach is exposed between the shoreline and the seawalls, along the peninsula to the east of Hilbre Island. The tidal sandbanks to the west are also exposed at low tide, and the repeated wave breaking along the margins of the Hilbre channel picks out the general shape of the sandbank margins.

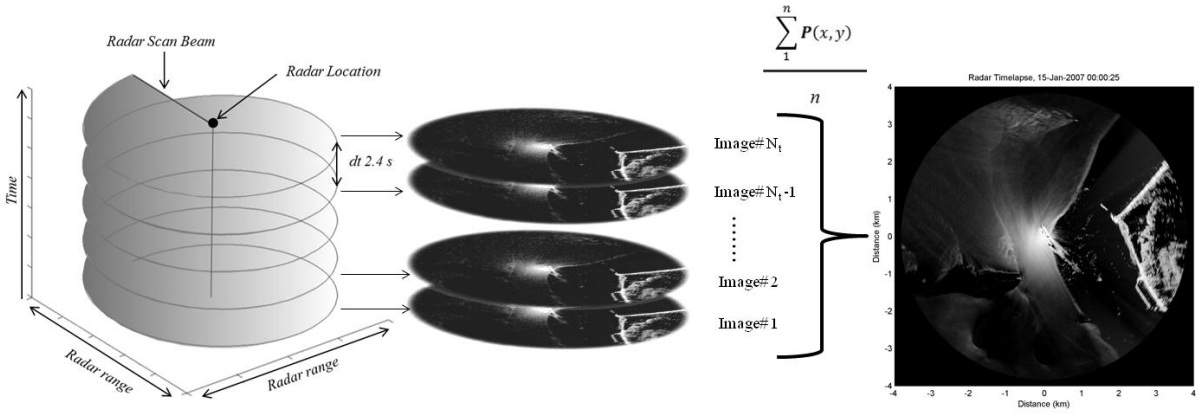

Figure 4.5: Schematic describing radar data collection, a sequence of snapshots collected every 2.4 seconds are averaged over ten minutes (~256 images), creating time exposure images highlighting areas of high pixel intensities.

4.3 TIDAL DATA COLLECTION AND PROCESSING

Figures and some text used in this section are taken from Bell et al. (2016) and the synthetic tide was generated by Dr. Paul Bell using the POLTIPS model at the National Oceanography Centre.

The aim of the presented radar method is to map the intertidal area, which follows a cycle of wetting and drying governed primarily by the tides and varied local beach morphology. A partial record of tidal elevation was available from a formerly operational tide gauge located on the northernmost tip of Hilbre Island close to where the radar was located. This tide gauge, which is thought to have existed in various forms for up to 130 years, was refurbished in its present form by the Mersey Docks and Harbour Corporation (now Peel Ports) during the 1970s. It consisted

of an obsolete float gauge with a chart plotter. The stilling well for the float was cut into the sandstone bedrock of the island, and connected to a subtidal location off the northern end of the island via a lead pipe. A pressure sensor was also located in the stilling well coupled to a VHF transmitter, from which data were automatically relayed to both the Mersey Docks and Harbour Corporation, and to the Proudman Oceanographic Laboratory (now the National Oceanography Centre). When the Proudman Oceanographic Laboratory moved from its original site at Bidston Observatory to Liverpool in 2004, the range became too great for line of sight reception of the VHF signal. As a result, a VHF receiver was connected directly to the radar digitiser PC on Hilbre Island, in order to pick up the tide gauge data from then on, whenever the radar was operating. Unfortunately the inlet pipe had degraded and became increasingly prone to blockages and siltation in recent years, compromising data quality. It was finally discontinued by Peel Ports in favour of an offshore radar level gauge in 2010.

The available Hilbre Island tide gauge data is shown in Figure 4.7 with the period that overlaps, and the study period of the present work shown in blue. Figure 4.7b shows the residual when the tidal prediction for Hilbre Island is removed from the tide gauge record. There are clear anomalies in various parts of the record that become obvious in the residuals, notably in spring 2007, towards the end of 2007 and finally showing an almost complete blockage of the system in mid-2008.

The incomplete and, at times, unreliable nature of this record therefore made it unsuitable for use in the waterline application, where a robust and continuous time series of water levels is required. An alternative approach was therefore adopted, taking advantage of the nearest UK National Tide Gauge Network class ‘A’ tide gauge outside Gladstone Dock, Liverpool. The residual meteorological contribution to the tide at Liverpool was determined by subtracting the

predicted tide from the measured tide. This is shown in Figure 4.7c with the period corresponding to the present study highlighted in blue. The assumption was made that this meteorological component of the water level was a geographically wide area effect, that could also be used as an approximation for the meteorological component of the water level at Hilbre Island, 15 km to the southwest. This was then added to the predicted tide for Hilbre Island to provide the required water level for the radar waterline analysis, shown in Figure 4.7d with the study period again highlighted in blue. In order to verify that this "synthetic tide" was a better representation of the water elevation than tide predictions alone, tidal records from mid-September 2006 to mid-February 2007 were selected subjectively as a period when the Hilbre Island tide gauge was not suffering from significant issues with pipe blockages – i.e. when obvious anomalies in the tide gauge data and residuals were not evident. It should be noted that the author cannot be certain that even this section of the data was not contaminated by pipe blockages, only that any such effects were small.

The tidal residuals for both Liverpool Gladstone Dock and Hilbre Island were calculated by subtracting the tidal predictions from the measured water levels. As expected, a scatter plot of the residuals from one gauge compared with the other (Figure 4.6) shows a strong linear relationship between the residuals from the two tide gauges, with an R^2 correlation of 0.9, a standard deviation of less than 0.10 m and a Root Mean Square (RMS) difference of 0.10 m.

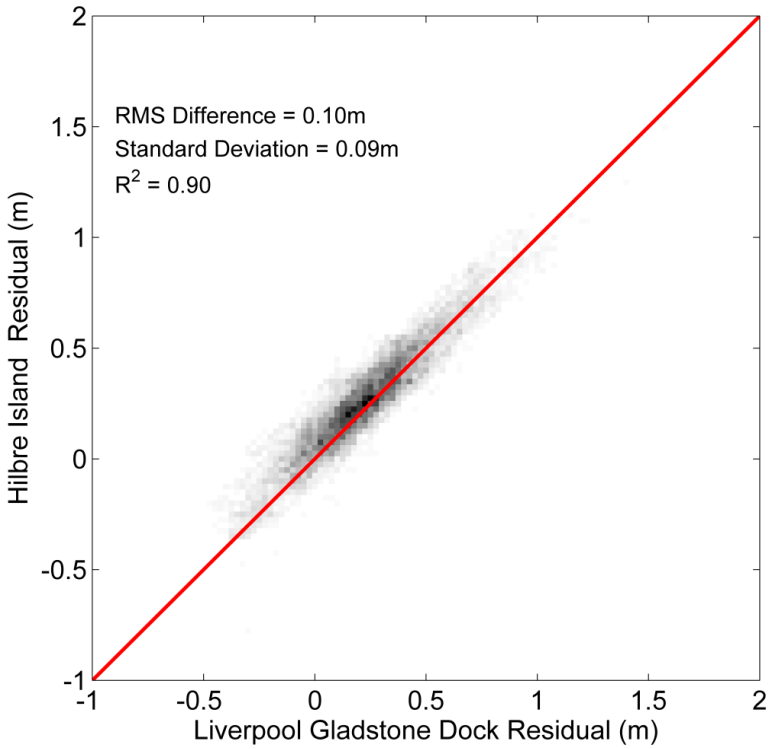

Figure 4.6: The tidal residuals (measured minus predicted) for Hilbre Island compared with Liverpool Gladstone Lock showing a strong R^2 of 0.9 from Bell et al. (2016).

Over the same period, the RMS tidal residual of the Gladstone Dock data was 0.37 m, suggesting that a similar residual was present on the Hilbre water levels, therefore through applying the tidal residual from Gladstone Dock to the tidal prediction for Hilbre Island should provide a significantly more accurate water level than using predictions alone. The residuals from the Hilbre tide gauge data with respect to the tidal predictions alone, were compared with the remaining signal when the synthetic tide (comprising the Hilbre tidal prediction plus the Gladstone Dock residual) was subtracted Figure 4.7e.

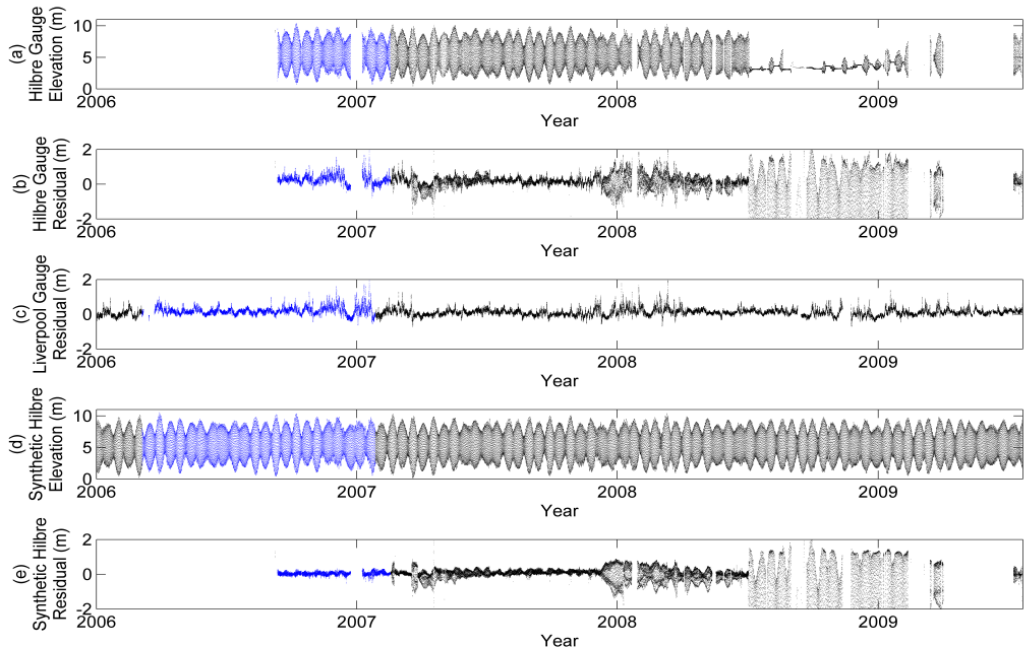

Figure 4.7: (a) The Hilbre Island tide gauge data from September 2006 to summer 2009. The region plotted in blue is the only region considered of sufficient quality to be used for the comparison of residuals illustrated in the previous figure. The gauge can be seen to become almost completely blocked in summer 2008. (b) The tidal residual calculated with respect to a POLTIPS tidal prediction. (c) The class 'A' Liverpool Gladstone Lock Tide Gauge Residual. (d) The synthetic tide constructed from the POLTIPS prediction + the Gladstone Lock residual. (e) The Hilbre Island residual with respect to the synthetic tide. From Bell et al. (2016).

With predictions alone, the Hilbre Island RMS residual for the test period of September 2006 – February 2007 was found to be 0.38 m, while the use of the synthetic tide was found to reduce this to 0.1 m. This represents a reduction in the difference of almost a factor of 4, confirming that this approach of adding the residual from the Liverpool tide gauge to that of the Hilbre

Island tidal predictions yields a significantly more accurate representation of the water levels at that site than predictions alone. A subsection of the tidal data are shown in Figure 4.8, with the tide prediction marked as the red dotted line, the Hilbre tide gauge data which was considered valid during that period marked in blue, and the synthetic tide is marked with black dots. The points marking the synthetic tide can be seen to overlay the tide gauge data (cyan line) almost perfectly.

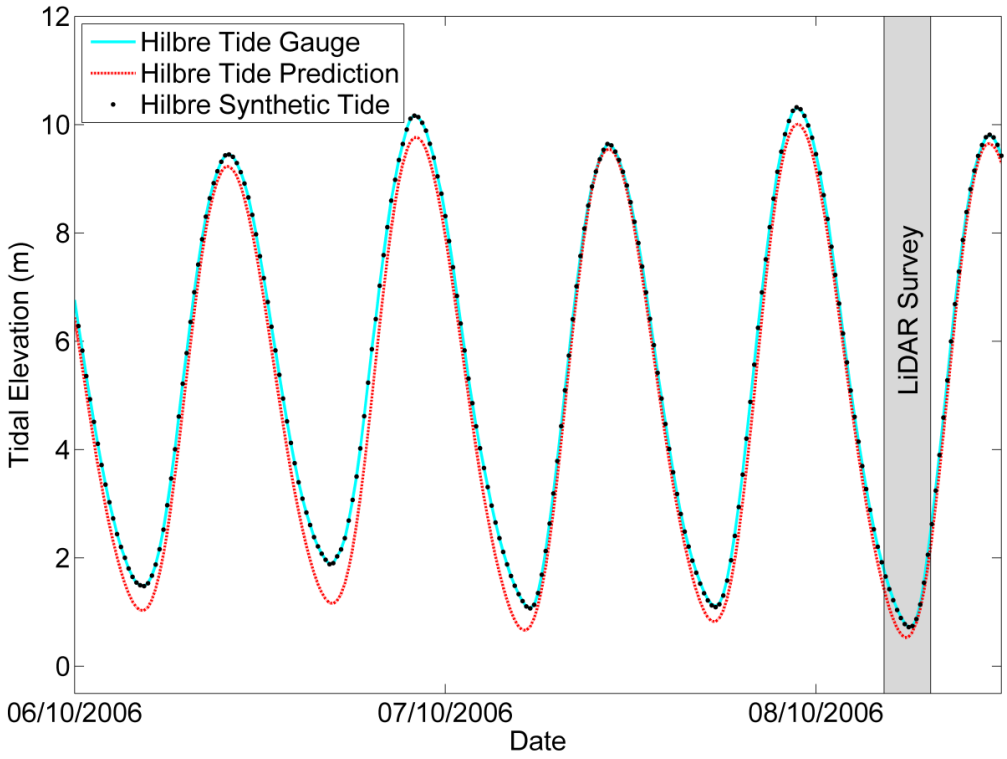

Figure 4.8: A subsection of the tidal data for Hilbre Island, with the tide prediction marked as the red dotted line, the Hilbre tide gauge data which was considered valid during that period, marked in cyan, and the synthetic tide marked as the black dots. The highlighted grey area corresponds to the period during which the LiDAR survey was flown from Bell et al. (2016).

4.4 DEE ESTUARY AERIAL LiDAR SURVEY DATA

An aerial LiDAR survey of the majority of the Dee Estuary was conducted by the UK Environment Agency on the 8th October 2006, shortly after a significant wave event. The survey was conducted using an *Optech* ALTM 3100 LiDAR system, flown by a dedicated survey aircraft at an altitude of approximately 900 m. A total of 20 flight lines were flown to cover the estuary between 04:25 and 07:26 GMT, during which the tidal elevations ranged from 0.72 to 2.47 m, shown as the region shaded in grey on Figure 4.8. Calibration flights were carried out at regular intervals by the system operators, and the last calibration flight prior to this survey was reported to be in June 2006. The accuracy of this instrument at altitudes of up to 1200 m is quoted by the manufacturer as 0.15 m or better (1 x standard deviation), with a range resolution of 0.01 m. A ground truth survey conducted by the Environment Agency as part of this survey, showed a root mean square error of 0.071 m between the LiDAR survey and a GPS ground survey, comprising a systematic error (bias) by the LiDAR data of -0.052 m and a random error of 0.097 m. These comparisons were within acceptable accuracy tolerance levels for that instrument.

The LiDAR elevation data was supplied as a gridded dataset with a 1 m horizontal pixel size. Reflectivity data were also supplied in a similar format. In order to more closely match the resolution of the radar data, the 1 m gridded elevation data from the LiDAR were mean gridded on a 5 m grid. Elevations were adjusted from Ordinance Datum Newlyn (ODN) to Admiralty Chart Datum (ACD), corresponding approximately to Lowest Astronomical Tide by adding 4.93 m to the ODN values for the comparisons presented here.

Examination of the original 1 m gridded data demonstrated clear evidence of elevations related to the water surface in wet areas, thus elevation values below 2.5 m relative to chart datum were eliminated from the comparison as potentially contaminated data points. Examination of the reflectivity values in these wet areas, showed high reflectivity when the laser beam was pointing near vertical and very low reflectivity data at lower grazing angles. Features with similar reflectivity signatures could be identified by eye, in the bottom of channels in the sand flats and sand banks, indicating a strong likelihood that such areas contained pooling water, even near low tide when the survey was conducted. Filtering out such areas from the LiDAR survey was not attempted, as no unique criteria could be determined for that purpose. Figure 4.9 shows a selection of LiDAR elevations at the same survey resolution (5 m grid) and within range of the radar. The initial radar elevation surveys are capable of observing a greater area, however the method must be validated by comparing the two methods, as shown in the next chapter.

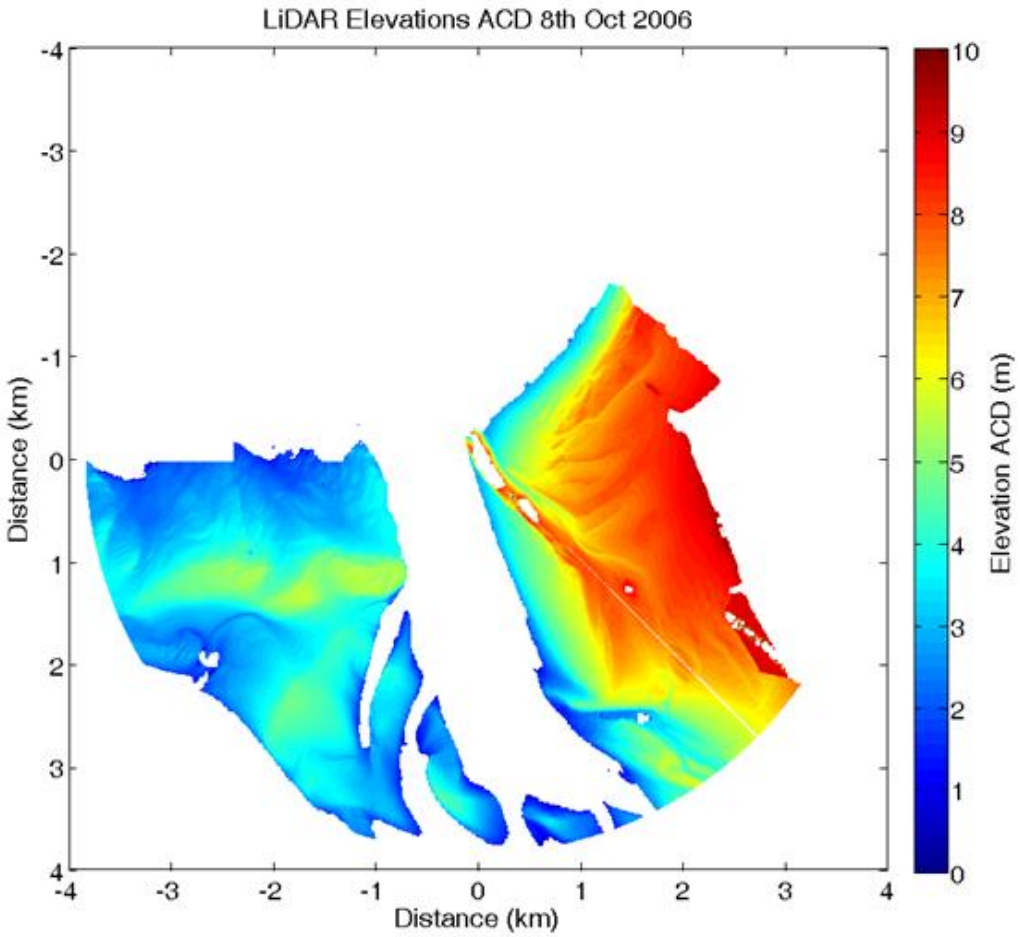

Figure 4.9: Gridded LiDAR data at 5 m spatial resolution showing elevations Above Chart Datum (ACD) at points matching those derived by the radar waterline method described in Chapter 5.

5 A TEMPORAL WATERLINE APPROACH TO MAPPING INTERTIDAL AREAS USING X-BAND MARINE RADAR

This chapter is the methodology and results section from the following publication: Bell, P.S., Bird, C.O., and Plater, A.J. (2016). A Temporal Waterline Approach to Mapping Intertidal Areas Using X-band Marine Radar. *Coastal Engineering* **107**, 84-101.

Abstract

Mapping the morphology of intertidal areas is a logistically challenging, time consuming and expensive task due to their large expanse and difficulties associated with access. A technique is presented here that uses standard marine navigational radar operating at X-band frequency. The method uses a series of time-exposure radar images over the course of a two-week tidal cycle, to identify the elevation of the wetting and drying transitions at

each pixel in the radar images, thereby building up a morphological map of the target intertidal area. This "Temporal Waterline" method is applied to a dataset acquired from Hilbre Island at the mouth of the Dee Estuary, UK, spanning March 2006 to January 2007. The radar gathered data with a radial range of ~4 km and the resulting elevation maps describe the intertidal regions of that area. The results are compared with airborne LiDAR data surveyed over the same area and within the radar survey time period. The residual differences show good agreement across large areas of beach and sandbanks, with concentrations of poor estimations around points that are shadowed from the radar or likely to suffer from pooling water. This paper presents the theoretical framework of the method and demonstrates its stability and accuracy. The Temporal Waterline radar method is aimed at providing a useful tool for the monitoring and operational management of coastlines.

5.1 RADAR DATA UTILISED

Hilbre Island, where the radar was located, is cut off from the mainland for the upper half of every tidal cycle and has no grid-connected electricity supply. In order to provide power to the ranger station on the island, a 2 kW wind turbine and off-grid battery storage system with a diesel generator back-up was installed by Wirral Borough Council, which provided power most of the time. Both the maintenance and monitoring of the power systems and radar system was a challenging process due to the remote nature of the site, and as a result numerous gaps exist in the dataset. Despite these challenges, several years of radar data were collected before a number of factors made the collection of data impractical to continue.

The radar data used in the present work were gathered over ten months from March 2006 to January 2007. Further archives of radar data up to 2009 exist and will form the basis of future work investigating episodic, seasonal and interannual changes within the estuary. The 2.4 m radar antenna was mounted approximately 30 m above chart datum and set to short pulse (~60 ns pulse length), in order to cover a ~4 km range radius. The data were then sampled at 40 MHz with a radial resolution of 3.75 m using an *OceanWaves GmbH WamosII* system linked to the internet, via a long range wi-fi link to the mainland. The antenna rotated at 25 rpm yielding an image every 2.4 s. The raw data were then interpolated from polar coordinates onto a Cartesian grid, to enable georeferencing and proper visualisation of the results. This process includes the removal of small variations in antenna rotation rate, that would otherwise cause an azimuthal error of several degrees in the location of nominally static targets, if a uniform antenna rotation rate was assumed. Strictly speaking, the polar to Cartesian conversion should also account for the slant range associated with the elevation of the radar antenna above ground level, a simple calculation using Pythagoras' theorem. However, as the ground level is the unknown quantity in this analysis, one can either assume an approximate elevation that accounts for the majority of the slant range error, or include no correction. The option of no correction was chosen in this case, as an antenna elevation of approximately 25-30 m coupled with a Cartesian pixel size of 5 m. means that the slant range error only becomes greater than the pixel size for points within approximately 100 m of the radar, in a region where data is being recorded to a range of almost 4 km.

If precision in the nearest 100 m was of principle concern, the simplest method would be to perform the waterline method with no slant range correction, and once the elevation of each pixel had been identified, to apply a correction to the radial range of each pixel based on the

slant range appropriate to that elevation and range. A detailed correction for this effect was considered an unnecessary over complication in the present work, considering the likely marginal gains in positional accuracy. It may however be implemented as a refinement in future work if necessary.

Images produced from radar data show not only detected hard targets such as ships and land, but also many reflections from the sea surface. This is known generally as ”sea clutter” and is a product of Bragg scattering from centimetre-scale capillary waves on the sea surface, interacting with the projected electromagnetic energy (Valenzuela, 1978) and sea spikes, a scattering phenomenon occurring when radar waves interact with steep or breaking waves at low grazing angles (Coakley et al., 2001; Fuchs et al., 1999; Ja et al., 2001; Trizna and Hansen, 1991). This sea clutter is inconsequential for the most part if wind speed is low (<3 m/s). As the sea surface is not roughened sufficiently, significant wave heights less than 1 m are also difficult to detect with radar. This radar frequency is also used by weather radars and thus rainfall is also visible on marine X-band radar, and can potentially obscure the sea clutter (Bell et al., 2012). The intensity of a pixel in a radar image is dependent on the strength of the radar returns from that location (Richards, 2005) and in marine radars, is uncalibrated and usually logarithmically amplified. The raw value of the returned signal is stored as an unsigned 12-bit integer by the particular digitisation system used here.

Sequential radar images recorded once per antenna rotation provide movies of waves (when visible) propagating up to the shore, and the interface between wet areas and dry areas varies from wave to wave. In order to stabilise this fluctuating signal and define a “waterline”

representative enough for this analysis, the radar images from each ten minute burst (of 256 images) are temporally averaged, smoothing the wave signatures and yielding an image that is analogous to a time-exposure in photography, in which the limit of the interface between land and ocean is more easily distinguished (Figure 5.1). The time exposure radar images used in this work represent just over ten minutes of data that were sampled either every hour or every 30 minutes, depending on the operating regime. Figure 5.1 shows a sample time exposure image used in this method.

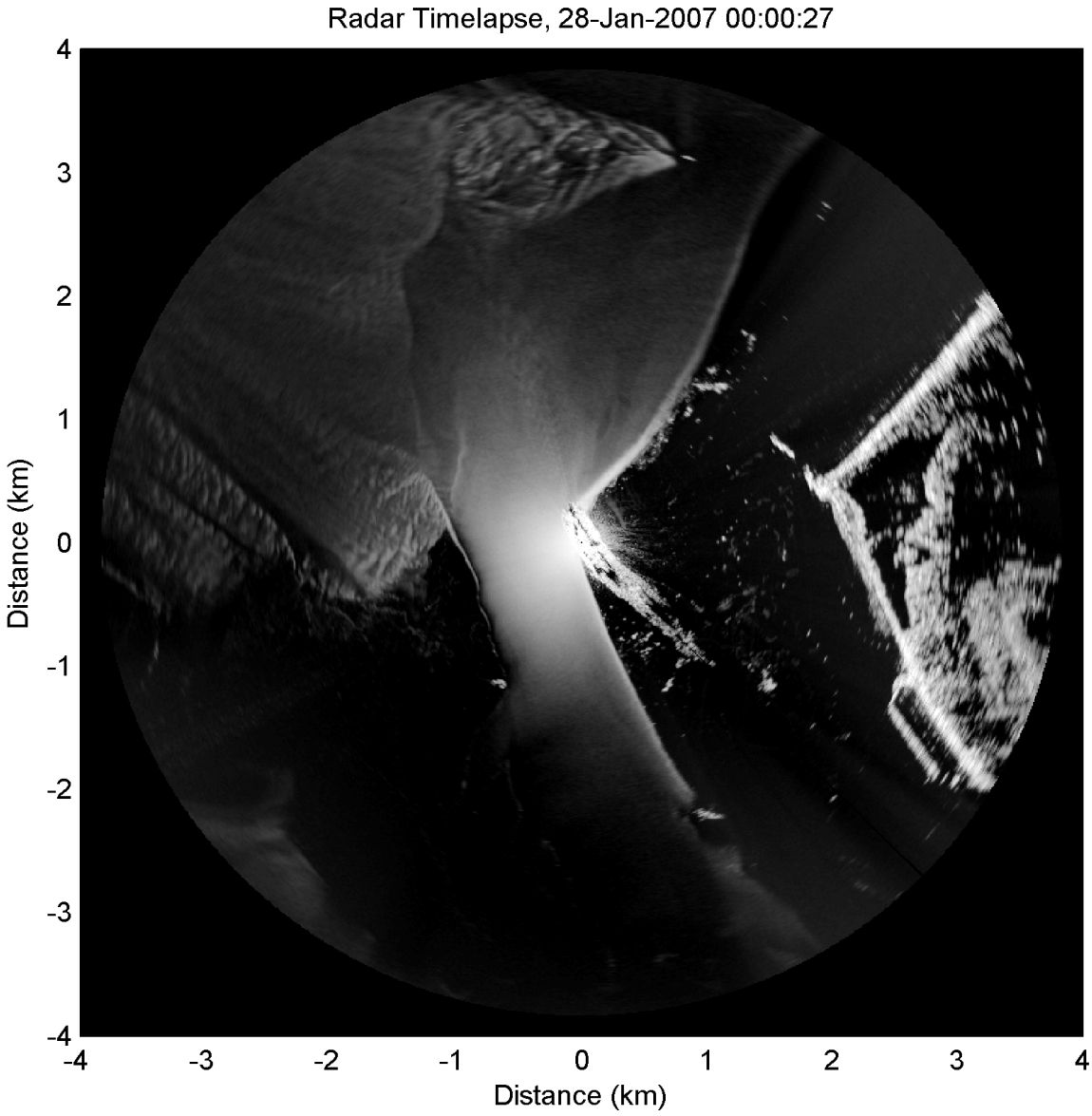

Figure 5.1: Time exposure radar image representing ten minutes of data showing general patterns of wave breaking and sea clutter.

This image represents a period at low tide and so a great deal of beach is exposed between the shoreline and the seawalls and dunes lying along the peninsula to the east of Hilbre Island. The

tidal sandbanks to the west are also exposed at low tide, and the repeated wave breaking along the margins of the Hilbre channel picks out the general shape of the sandbank margins.

5.2 THE TEMPORAL WATERLINE METHOD

The initial step in this method is to gather time series of individual radar pixel intensities from each time exposure image, across the chosen timescale, in this case two weeks as shown in Figure 5.2. For each x and y coordinate of the time exposure image ($\bar{I}$), the (mean) pixel intensity (P) is retrieved from that location; this is then repeated for each time exposure image, with the values being separated by Δt - in this case either 30 or 60 minutes.

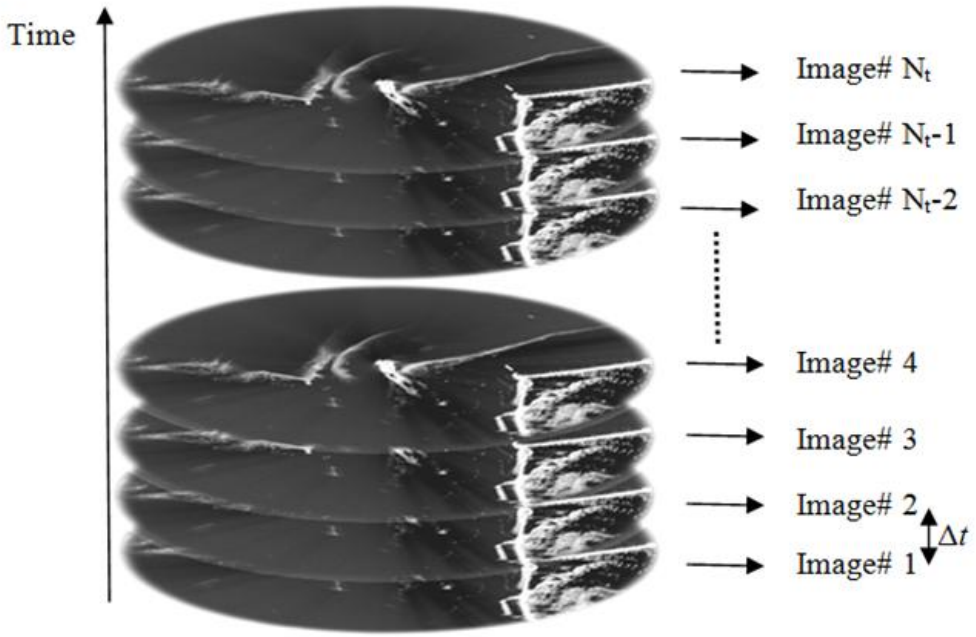

Figure 5.2: Time-exposure image timestack used to form 3D matrix from which pixel intensities are extracted at each time step and location.

The resulting plot (Figure 5.3d) shows the raw pixel intensities throughout a two week period, where periodic episodes of high and low intensities generally indicate tidal cycles of wetting and drying. The value of the radar pixel intensity at the peaks will not be regular, as it is a function of local weather and surface conditions. These include wind speed (which roughens the sea surface), wave height and wave direction relative to the radar antenna location, which contribute to varied backscatter of radar energy from the sea surface.

The two week length of the analysis period was chosen to include a full spring-neap cycle, thus maximising the vertical intertidal range able to be detected by this method, whilst maintaining a reasonable temporal resolution through a year. It would be possible to reduce the analysis period to approximately a week and still maximise the intertidal range experienced at a site, providing that the analysis period was precisely half the exact spring-neap cycle length and synchronised such, that each analysis period covered either the interval from neap to spring or from spring to neap. Periods less than this could also be used, perhaps even a single tidal cycle, however there would be times when the analysis period would be focused only on the smaller intertidal range at neaps, which does not make best use of this overall approach.

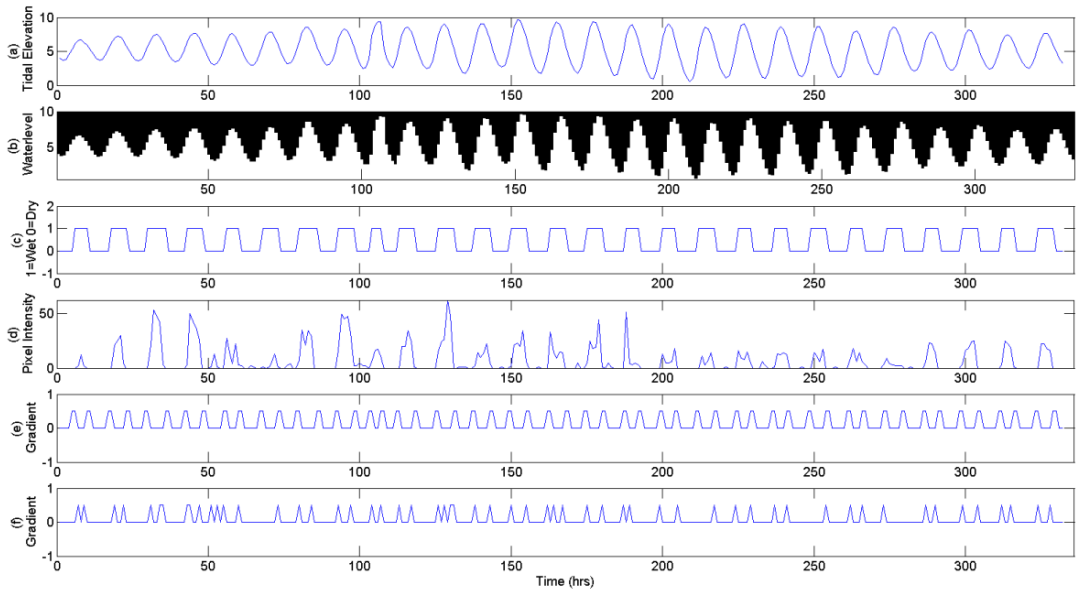

Figure 5.3: (a) Tidal elevations over two weeks sampled concurrently with the radar time-exposure image; (b) Matrix of binary wet-dry values based on tidal elevation; (c) Example row extracted from b showing the tidal square wave indicating wet or dry at a water level of 5 m ACD; (d) Raw pixel intensities over two weeks extracted from a single location; (e) Absolute gradient of the tidal square wave showing transition times from wet to dry; (f) Processed gradient of the raw pixel time series, approximating the transition times from wet to dry at a given location.

In order to relate the tidal variation in pixel intensity at a given location to an elevation, a set of water levels was chosen to reflect the potential tidal range of the deployment area; for Hilbre Island this was 0.5-10 m in 10 cm increments. For each of these elevations, the synthetic tidal record was used to determine whether a pixel at that elevation would be either covered by the tide, or exposed at the times corresponding to each radar record. This yielded a binary pulse

sequence unique to each elevation, illustrated in Figure 5.3b. Peaks in the absolute gradient of that binary pulse sequence (Figure 5.3e) represent the points of transition between wet and dry at a given elevation.

The example pixel intensity time series shown in Figure 5.3d, is not a clean binary pulse sequence like the one generated by the tidal record in Figure 5.3c, due to changing weather and surface conditions over the two week analysis period. Furthermore, the presence of strong radar reflectors such as rocks in some pixels, can exhibit a high radar cross section that is then reduced by inundation with water, thus inverting the expected pulse sequence.

In order to allow a more like-for-like comparison between the binary sequences of Figure 5.3c and the analogue time series in Figure 5.3d, we attempt to normalise the analogue time series. The absolute gradient of the time series is calculated and the gradient peaks selected (representing sharp changes in intensity), using a robust peak-finding algorithm described by Yoder (2009); these peak values were then normalised and other non-peak values reduced to zero (Figure 5.3f). Similarly, the absolute gradient is also taken of the binary wet-dry pulse sequences, illustrated in Figure 5.3e.

It is then a straightforward matter to step through each possible elevation and determine a measure of similarity between the theoretical and measured pulse sequences. In this case we use the normalised cross correlation to calculate R, the correlation coefficient at each elevation being:

$$\boldsymbol{R_N = \left\{ \frac{(P - \overline{P})(T_N - \overline{T}_N)}{\sigma_P \, \sigma_{T_N}} \right\}} \qquad \textbf{(30)}$$

The normalised correlation coefficient (R) for each water-level number (N) is calculated using the above equation, where P is the pixel intensity gradient record and T is the record of tidal state change gradients, and σ_P and σ_T indicate the standard deviation of P and T, respectively.

Each tidal elevation value now has a correlation coefficient (R) value, defining the strength of the relationship between the record of pixel intensity gradients, and the expected wetting and drying pattern at a given individual pixel location (Figure 5.4).

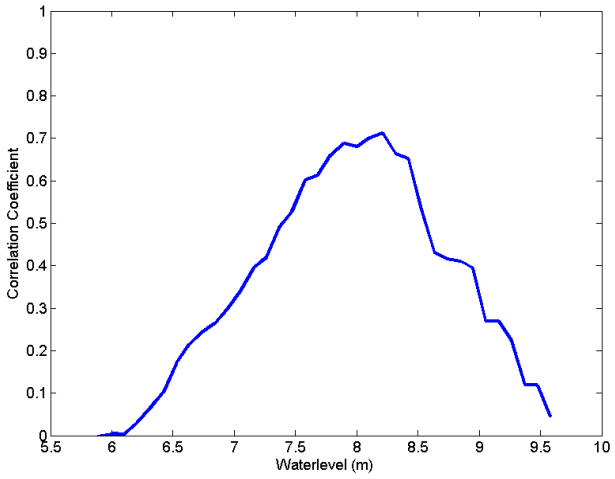

Figure 5.4: Correlation coefficients for a given pixel record at water levels within the tidal range.

The maximum coefficient is used to indicate the tidal elevation of the waterline, and the process is repeated for all pixel intensity records from every pixel location in the input image sequence. The results are then used to populate a matrix which builds up a map of intertidal pixel elevations above chart datum.

It can be seen from Figure 5.3d and the derived pulse sequence in Figure 5.3f that there are times when the transition between wet and dry is not evident in the data, probably due to very calm weather conditions. If one attempted to apply the conventional approach of identifying a physical waterline in the radar images from records around that time, it would not be possible because that information is not contained within the data. However, by taking the temporal approach to the problem, provided there are at least some measurable wet-dry transitions during the two-week time period, the absence of even days of wetting and drying transitions can be tolerated, as can the occasional erroneous identification of a transition caused by heavy rain for example.

Pixel records from areas which are submerged even at low tide (subtidal areas), generally yield low correlation coefficients with the predicted wetting and drying pulse sequences. These areas are filtered out by setting a simple threshold in the correlation coefficient as a quality control. The resulting maps can be used to visualise the mean elevations over a single spring neap cycle.

5.3 RESULTS: HILBRE ISLAND SURVEY

The Temporal Waterline method described above was used to process radar data from March 2006 – January 2007. For each two-week period during that time, the analysis yielded both an elevation map corresponding to the wetting and drying transitions, and also a corresponding correlation coefficient map reflecting the confidence level of the estimated elevations at each pixel location.

An example of a correlation map from April 2006 is shown in Figure 5.5. Pixels with higher correlation values should provide a more reliable elevation estimate, whilst lower correlation points should potentially be removed as a quality control measure. Generally, the non-mobile areas generate very strong correlations, for example the rock armouring and sea wall of a recreational marine lake to the south-east is picked out clearly on the image with high correlation values of approximately 0.8, along with the well-established sandbanks and isolated rocks across the estuary. Lower correlation values of 0.3 or less are seen in the areas which are still submerged at low tide, as these areas should not exhibit a tidal fluctuation that corresponds with wetting-and-drying.

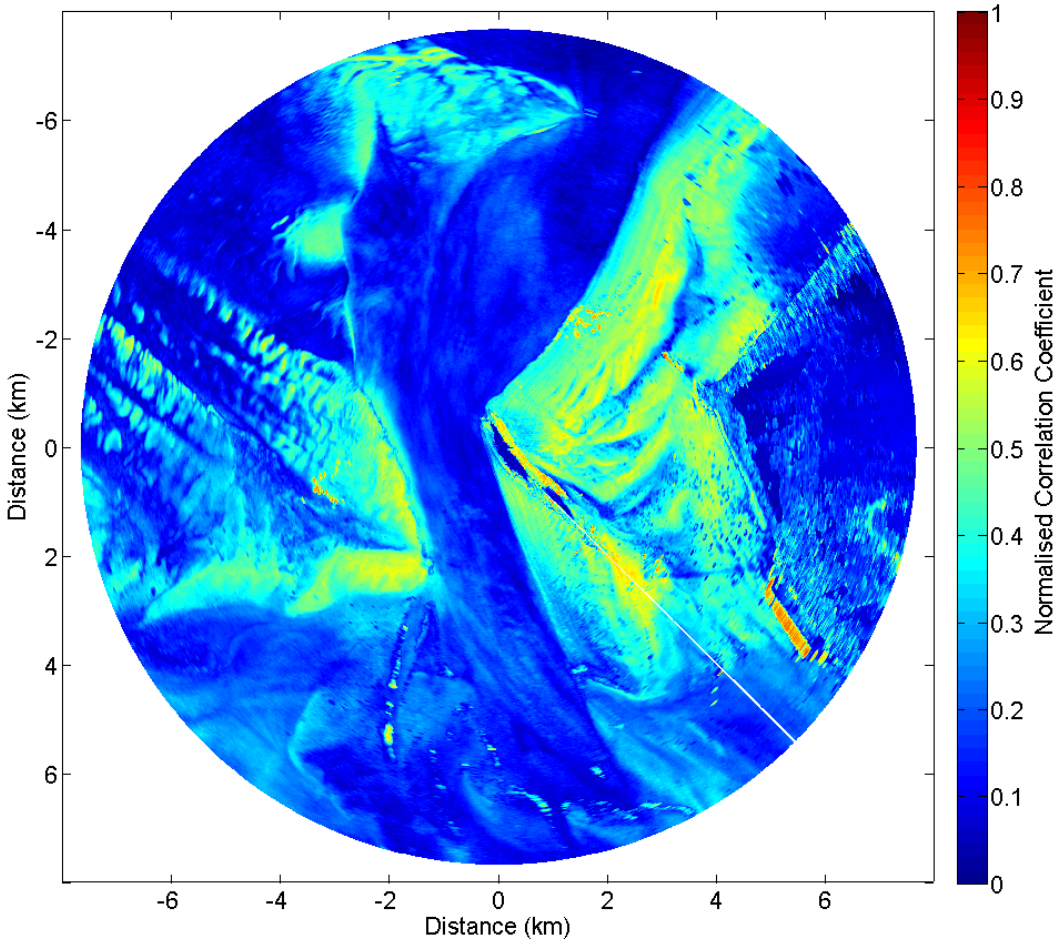

Figure 5.5: Maximum correlation values at every location across the survey area. The correlation coefficient at each point has been matched to a specific tidal water elevation above chart datum. The strength indicates the confidence of the derived elevation.

Radar data collection is inhibited through shadowing, a phenomenon common in the analysis of ocean waves with low-grazing angle radar (Lynch and Wagner, 1970; Mattie and Harris, 1978). Even with the radar being sited on a tower, the large radial range over which data has been

recorded means that some intertidal areas will still be shadowed from the radar signal, with these areas also exhibiting low correlations. Clear, unobstructed line of sight to the intertidal area of interest is therefore an important consideration when selecting a deployment site. A subjectively chosen correlation threshold of 0.3 was used to filter out the values generally corresponding to subtidal and shadowed areas as a quality control process. This threshold was chosen by qualitatively observing the areas that appear to be subtidal and inspecting the typical correlation coefficients of these locations. Lower thresholds fail to remove pixels lying in clearly subtidal areas and higher thresholds eliminate potentially valid elevation results from intertidal regions, leading to severe gaps in the data and noisy areas. The optimal threshold will likely vary between sites and will depend on a variety of factors. Collection of a further dataset is required to validate the applicability of a subjective threshold, for this deployment a threshold of 0.3 is sufficient to remove most of the elevations from the subtidal areas. Figure 5.6 shows the effects of filtering at different coefficient thresholds, on the percentage of pixels remaining following the filter. Following filtering at a threshold of 0.3, 30.51 % of pixels remain associated with an elevation value. This percentage rapidly decreases as the threshold increases. Land areas and the islands have been masked out and set to an arbitrary elevation above the maximum tide.

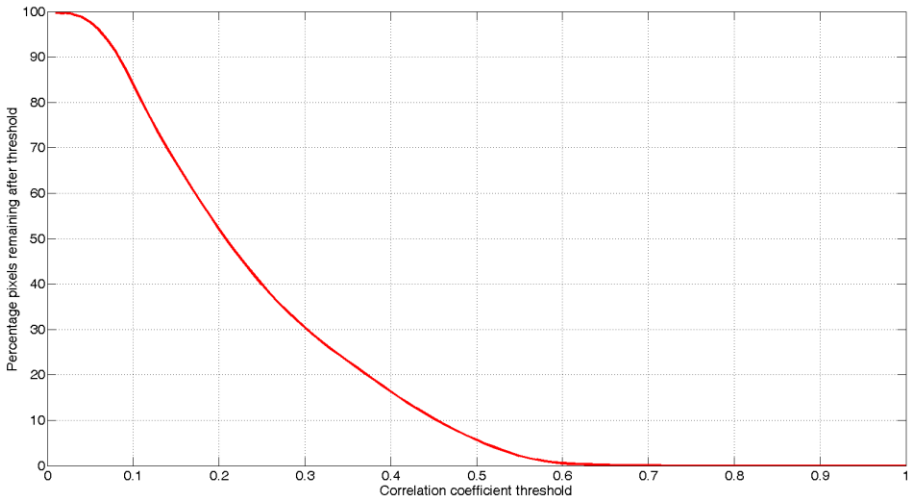

Figure 5.6: Percentage of derived elevation results remaining following correlation coefficient filters at different thresholds.

A single waterline map is shown in Figure 5.7, illustrating the mean intertidal bathymetry over a two-week period. Successive analyses over a longer time period will be useful in isolating and monitoring the movement of bed features over different timescales. The intertidal sand flats of West and East Hoyle Banks (i and v) are clear in Figure 5.7, as are the banks of the large central channel. This is one of two channels into the Dee estuary which connect to the canalised River Dee and the city of Chester, 20 km higher up the estuary.

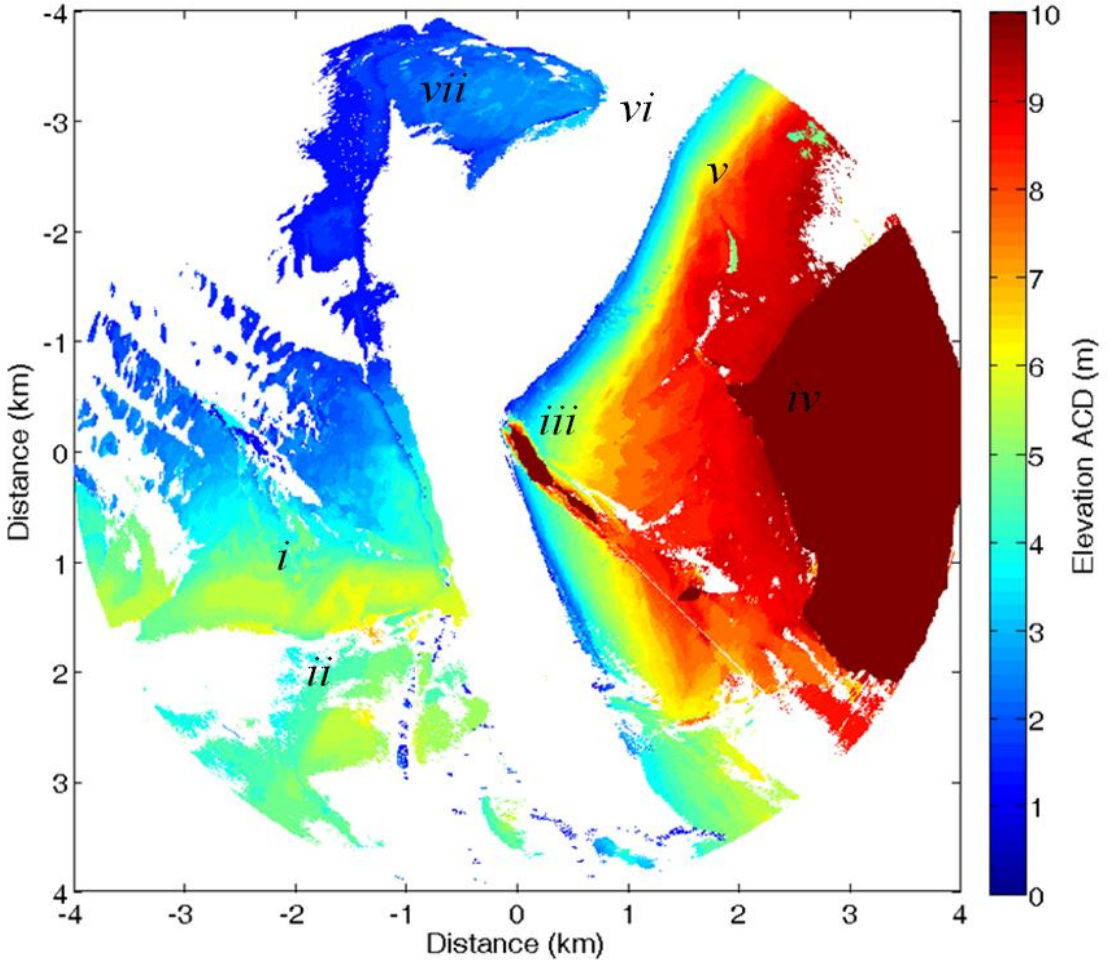

Figure 5.7: Radar-derived elevations across the survey area showing beach profile and sandbanks in addition to the Hilbre channel and subtidal zone. Regions of interest include; (i) West Hoyle Sandbanks; (ii) The Welshman's Gut (ephemeral channel linking the two main channels of the Dee estuary); (iii) Hilbre Island; (iv) The Wirral Peninsula; (v) East Hoyle Bank; (vi) Hilbre Swash; (vii) Sandbank with wrecked vessel (see Figure 5.8).

A striking result is that the wreck of the Greek cargo ship SS Nestos displayed in Figure 5.8, stranded and sunk on the sandbank in 1941, can be seen clearly to the north (vii), with an elevation of ~3.5 m at low tide.

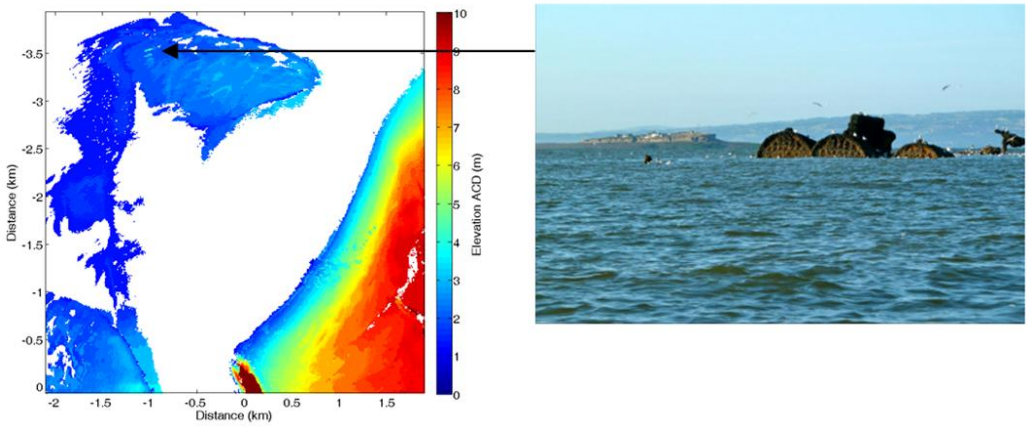

Figure 5.8: Location of the wrecked cargo ship SS Nestos. Photo courtesy of John M.X. Hughes.

5.3.1 Temporal Filtering and Smoothing of Elevation Values

The elimination of pixels by any quality control process would lead to unwanted gaps in individual elevation maps. It would not be appropriate to spatially interpolate the missing values as the gradient of complex beach profiles is rarely linear, and assuming such could lead to significant errors in further processing (Holman and Bowen, 1979). However, the existence of multiple sequential records allows an alternative approach to be taken to mitigate and filter points with intermittent poor correlations. A weighted temporal smoothing of the time series of each pixel was applied to the ten months of results. The square of the correlation coefficients was used to weight each elevation at each two-week time step, in a five-point running smoothed fit using a robust smoothing algorithm by Garcia (2010). This has the effect of strongly

smoothing the resulting time series of elevations, while emphasising points with good correlations and de-emphasising those with weak correlations. An example of the results of smoothing the data in this way can be seen later in Figure 5.12.

5.3.2 Physical Meaning of The Waterline

The algorithm described here operates in the time domain rather than the spatial domain, hence it is not immediately obvious how the derived waterline relates to an individual record. Figure 5.9 gives an example of how the derived waterline relates to both the LiDAR survey and the wave signatures on an individual radar record, along a cross-shore transect. The record started at 06:00 on 6 October 2006 and finished at around 06:10, after recording 256 images under relatively low wave conditions, just before a significant wave event. A cross-shore transect from the radar backscatter time series, and corresponding to transect 2 in Figure 5.11, is shown in the plot as it progresses through just over 10 minutes of data. The left-hand side of the plot corresponds to the onshore (dry) sand flats, while the right hand side has the sea clutter of the waves approaching from right to left. The tidal elevations at the start, middle and end of the record were 2.97 m, 3.11 m and 3.29 m respectively.

Figure 5.9 shows how the radar backscatter profile evolves over the ten minutes, with the wave breaker line clearly evident around x = 550 m. Also, the change in water level on the location of the breaking waves on the beach profile is immediately evident, with the breaker line having moved approximately 25 m as the water level rose by over 30 cm during that time. Shoreward of the breaker line to the left, there are some strong backscatter targets that appear to move around, and inspection of the full radar image sequence verified that these are almost certainly

sea birds, moving around either singly or in groups on the sands. Figure 5.9b shows the temporal mean of that backscatter profile. The cyan line marked on both plots indicates the location where the still water level, with respect to the LiDAR survey in the middle (at 06:05) of the radar record would lie. The red, green and blue lines mark the corresponding derived average waterlines from the two-week period ending on the 8 October 2006, and at the start, middle and end of the 06:00 - 06:10 6 October 2006 record respectively. The line corresponding to the middle of the radar record in time (green line) is close to the peak of the backscatter associated with the breaker line, which corresponds well with the peak of the breaker backscatter, used as the criterion for defining the water line used by Takewaka (2005).

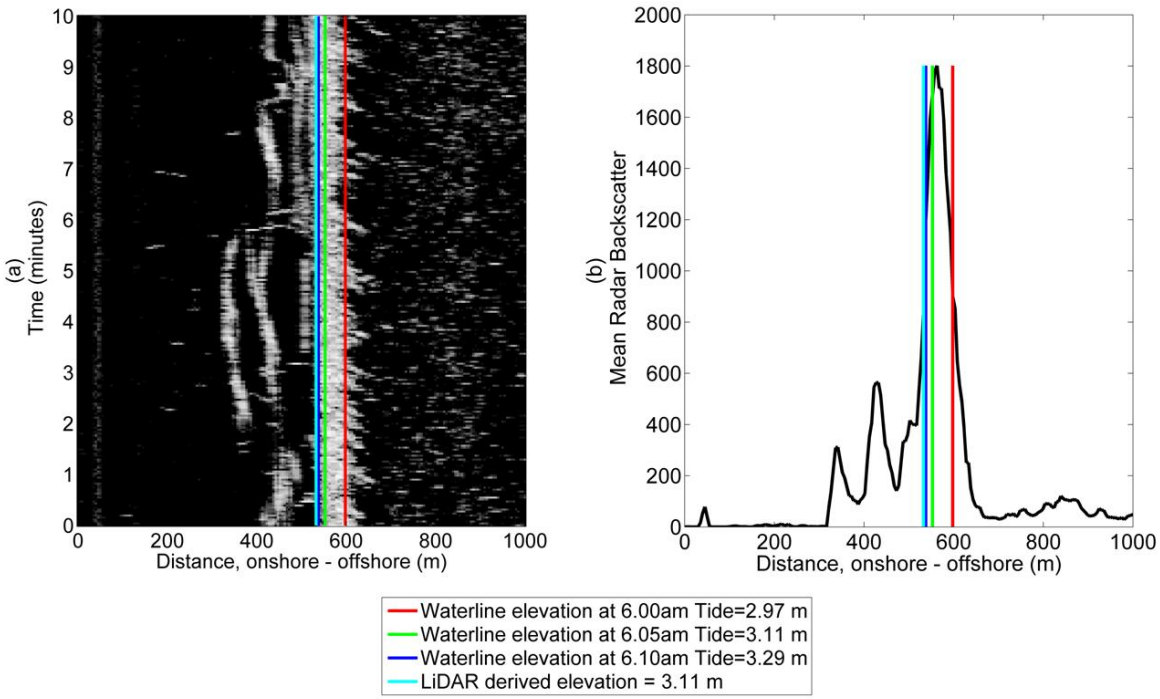

Figure 5.9: (a) The evolution of a radar backscatter cross-shore profile over ten minutes for the record starting 06:00 6 October 2006, with the wave breaker line clearly evident around x = 550

m. (b) The temporal mean of that backscatter profile (uncalibrated intensity scale). The cyan line marked on both plots indicates the location of the still water level with respect to the LiDAR survey in the middle (at 06:05 am) of the radar record. The red, green and blue lines mark the corresponding derived average waterlines from the two week period ending on 8 October 2006 at the start, middle and end of the record respectively.

Since the waterline derived here relates to the peak in the shore breaker zone, it is slightly offshore of that which might be expected from the LiDAR elevation, plus still water level at that time. This is a significant factor in generating the slight overestimate in overall beach elevations described by Figure 5.10**:** Radar (green) and LiDAR (blue) elevations along a cross shore profile taken from transect 5 (shown in Figure 5.11) demonstrating consistent overestimation of results by the radar technique.. Topographical elevations are consistently overestimated along the cross shore profile shown. It is evident that this trend is consistent and is likely caused by assigning the elevation result to the breaker location rather than the LiDAR derived waterline location. The area showing significant overestimations around 300 m on the transect is also likely subject to issues with pooling tidal water described later.

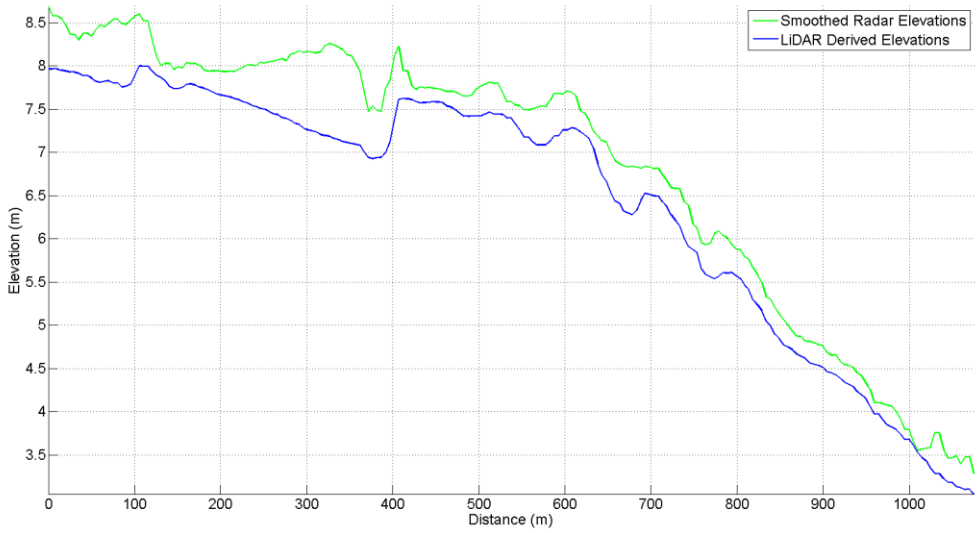

Figure 5.10: Radar (green) and LiDAR (blue) elevations along a cross shore profile taken from transect 5 (shown in Figure 5.11) demonstrating consistent overestimation of results by the radar technique.

5.3.3 Changes in Cross-shore Beach Transects

Figure 5.11 shows the location of five cross-shore transects extracted from the processed dataset. These transects capture most of the foreshore beach extending from the subtidal boundary to the backshore where the gradient decreases. Transect 5 is the northernmost, with transect 1 being closest to the Island.

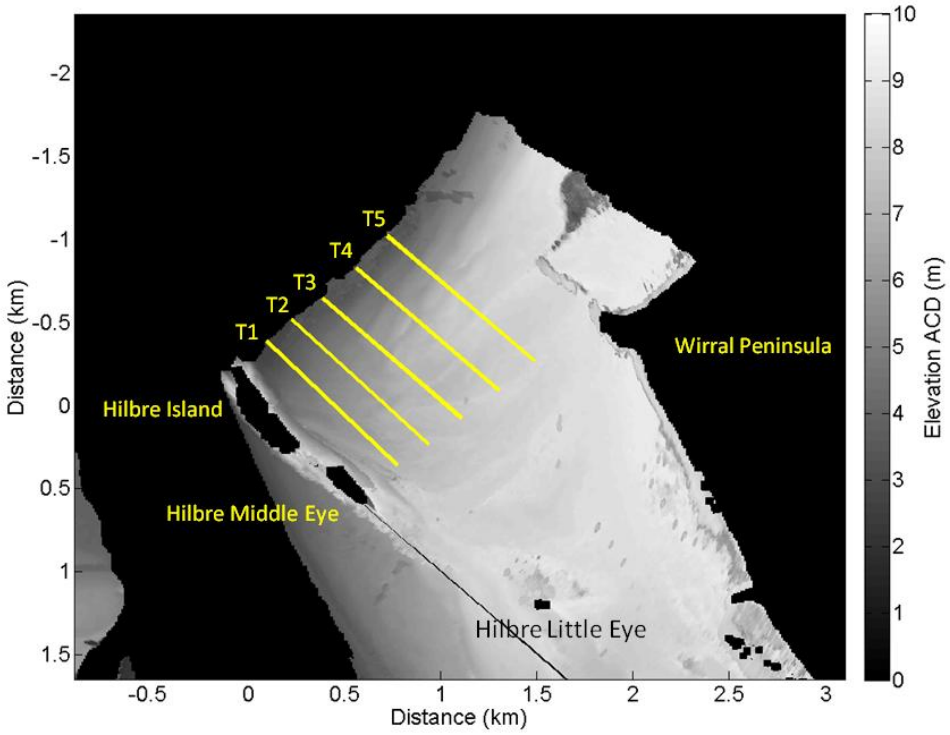

Figure 5.11: Locations of cross-shore transects extracted and analysed over a ten month period.

Figure 5.12 shows the results of extracting these transects every two weeks from 10 months of data, with each row representing the elevations along the transect from on to offshore. Noisy data appears most prominently across all transects around time step 10 and 17 (starting 29 July 2006 and 4 November 2006). This could be the result of very calm weather during the two-week sample periods, resulting in a smoother sea surface (i.e. less sea clutter) and lower correlation coefficients. The mean offshore significant wave heights for these time steps were 0.66 m and 0.82 m according to the CEFAS Wavenet buoy (WMO ID:62287) in Liverpool Bay, compared to a mean of 0.92 m and a maximum of 4.89 m seen in January 2007 (these wave data are accessible from http://www.cefas.defra.gov.uk). Waves of this height (<1 m) are difficult to detect with marine radar (although the wave heights will have increased as the waves shoal), and therefore

it is unsurprising that the data are poor for these periods. It is also clear that transect 5 runs close to a channel in the sand flats where shadowing inhibits the radar line of sight.

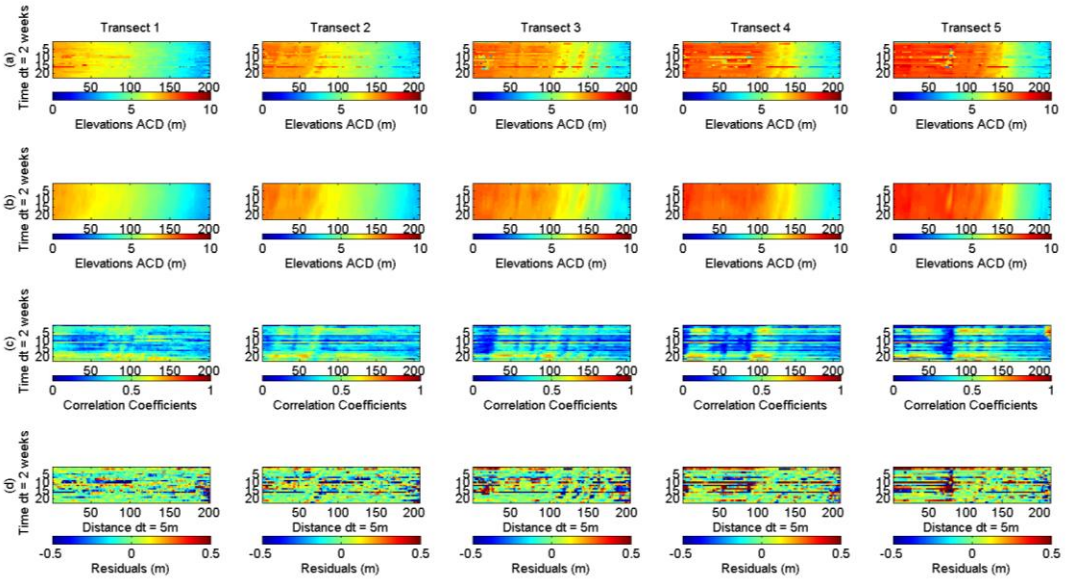

Figure 5.12: (a) Raw radar-derived elevations extracted along each cross-shore transect through time. Each row shows mean elevations over a two-week period. (b) Elevation transects from the same locations taken from data smoothed using a weighted linear filter. (c) Correlation coefficients at each point along extracted transects. (d) Differences between raw data and the filtered data, ensuring the introduction of smoothing artefacts is minimal.

It is clear from figure 5.12b that the process of temporal smoothing serves to greatly improve the results of the topographical survey along all five profiles. The overall shape of the profiles and the patterns of change are maintained whilst gaps in the data evident in figure 5.12a are filled according to the relative weightings of nearby correlation coefficients. This method of

smoothing can also be applied over various timescales, in the case of figure 5.12 the results have been smoothed using ten months of data, figure 5.13 shows the effect of filtering over various timescales. The cross shore profile from transect three during March 2006 is shown, raw elevations are traced by the red line, it is clear that elevations from the upper regions of the profile are not captured well during that period. The temporal smoothing algorithm fills these regions utilising as little as four weeks of data. The remaining elevations are not adversely altered and the integrity of the profile is preserved during the smoothing process. It is also evident that longer periods of smoothing do not greatly change elevations derived suggesting that this smoothing process could be applied during relatively short survey deployments of at least four weeks.

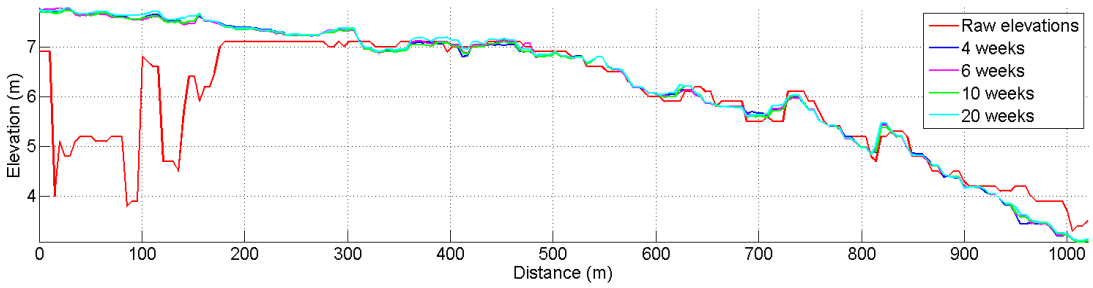

Figure 5.13: Results of temporal smoothing of elevations along the cross shore profile from transect three over different timescales.

Figure 5.14 shows the start and end transects from the ten months of data, which demonstrate that there is evidence of changes to the beach level during that time, and that those changes in beach profile are quantifiable from the waterline derived topographic maps. Although there are small sections of the beach that move seawards and that appear to be associated with the crests

of large bedforms, the overall pattern of change is a mean shorewards migration of the beach profile, which may be a seasonal effect rather than a long term-trend of erosion.

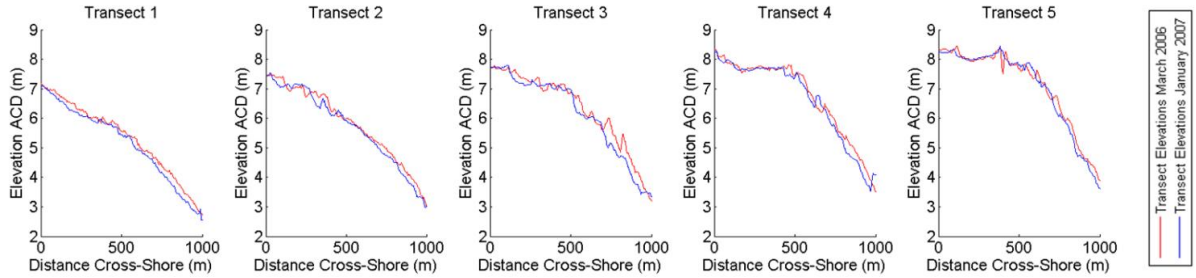

Figure 5.14: Waterline Transects at the start (red) and end (blue) of the ten-month study period. All transects show overall erosion and setback of the beach foreshore.

Table 5.1 below lists the mean changes both in elevation along the transects and horizontally, in terms of the cross-shore translation of the beach profile from the beginning to the end of the ten-month period. Vertical elevation changes averaged over each profile, range from an erosion of 0.05 m at the transect furthest from the radar, to an erosion of 0.17 m at the transect nearest to the radar. Whilst these are relatively small overall changes in the bed level, due to the shallow profile of the beach, these translate to considerable shorewards translation of the beach profile by between 25 m (furthest) and 40 m (nearest). The vertical variations are well within subjective observations by the authors, of considerable variations in beach level relative to the rocks adjacent to Hilbre Island of significant fractions of a metre. Future work will use a larger 3 year dataset in order to investigate seasonal and inter-annual variations in the beach elevations, and to track large sediment waves/dunes as they evolve and migrate.

Transect	Mean Vertical change (m) from March 2006 to January 2007	Mean Horizontal change (m)
1 (nearest to radar)	-0.17	-37.7
2	-0.1	-30.3
3	-0.16	-39.6
4	-0.1	-30.8
5 (furthest from radar)	-0.05	-24.9

Table 5.1: Mean beach profile changes for profiles 1-5 in terms of elevation and cross-shore horizontal translation. All transects show a small (<0.2 m) mean reduction in elevation over the ten months, with corresponding mean values for the cross-shore translation of the beach profile that are large due to the shallow (approximately 1 in 250) nature of the beach gradient.

It is further noted that the changes in the transects over time, strongly suggest the presence of migrating intertidal sand bars or waves, the dimensions and movements of which could be quantified with this technique. Studies by McCann (2007) and Way (2013) have previously documented the length and migration rates of these sedimentary bedforms, but the profiles could not be remotely determined with the earlier approach. These features have wavelengths of the order of 100 m - 200 m and have been observed to migrate in excess of 100 m per year landwards, using the radar signatures of breaking waves over the waves as a proxy indicator for their position. It is hoped that the ability to measure sediment volume changes cost effectively over long time periods, will allow variations in sediment fluxes within the surveyed area to be quantified effectively. This idea will be explored in further work.

Figure 5.15 shows the confidence levels of the derived transects from March 2006 and January 2007. Error bars for each point along the transect are derived from the absolute differences in elevation between stable rock locations and the elevations from these locations derived by a

LiDAR. The dominant trends in setback and accretion along these transects are maintained despite potential differences in absolute elevation. It should be noted that most differences in derived elevations are positive, representing an overestimation of elevations, the potential underestimation shown by the error bars are therefore less likely to be representative. Although they have been included as there is a possibility of underestimation.

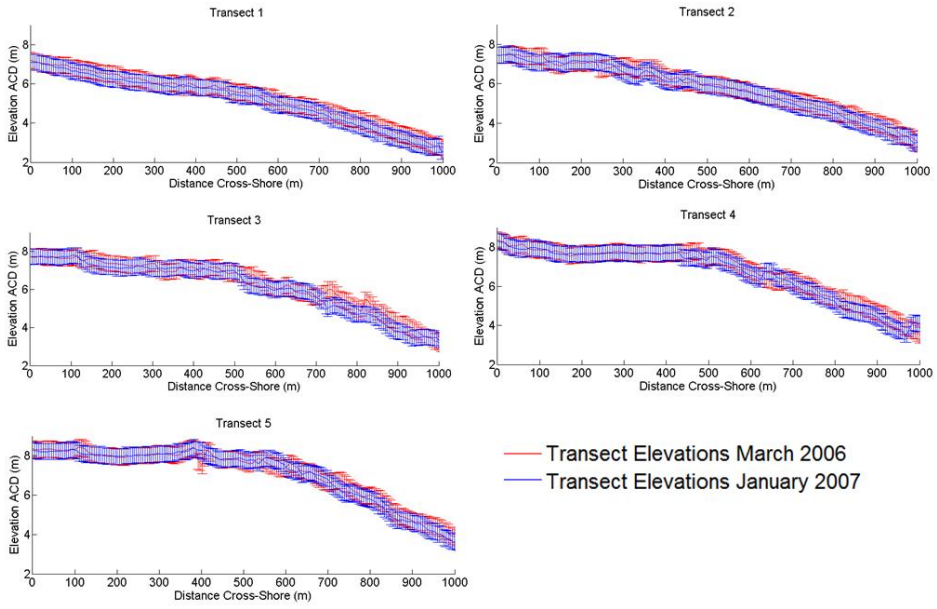

Figure 5.15: Confidence levels of radar derived elevations along a set of cross-shore transects showing change in profiles over 10 months.

5.3.4 Fixed Elevation Control Points

The changes observed in these transects demonstrate that the method is capable of determining surprisingly small changes in beach elevations, provided the changes are real and not artefacts of seasonal changes in wave height. To investigate this possibility, a number of rocky outcrops in the intertidal zone were chosen as control points that should not vary in elevation. If the results showed that that these targets did not vary in elevation through the ten months of the study period, then it would be reasonable to assume that changes in the elevations of potentially mobile sandy areas nearby, during the same period are genuine.

The locations of these control points are shown in Figure 5.16. One site is located on Hilbre Island itself, another on a rock platform close to the Island, a third from Hilbre Middle Eye, and the final site from the rock armour protecting the recreational marine lake at West Kirby.

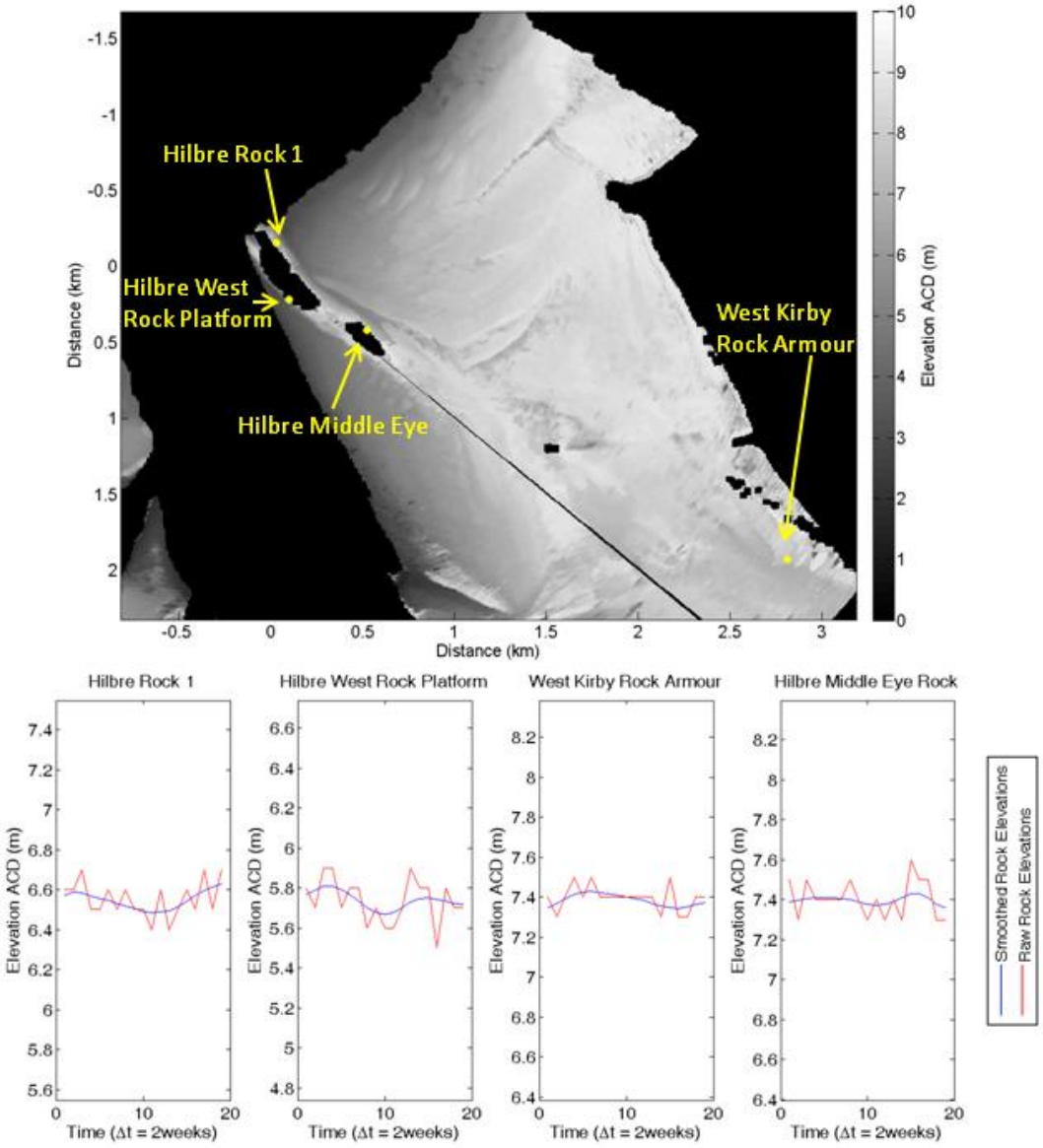

Figure 5.16: Locations of rock control points and resulting elevations throughout the ten-month analysis period, elevation records from the four sites, along with both raw (red) and smoothed (blue) elevations from each rock location.

The time series of waterline-derived elevations for each control point are displayed, with waterline elevation relative to Admiralty Chart Datum (m) on the y axis and time in two-week intervals along the x axis. The plots indicate that radar derived elevations at these control points are relatively stable across 10 months, and thus it is concluded that the elevation changes observed in the sandy areas are almost certainly genuine.

5.3.5 Relationship Between the Waterline Elevation and Absolute Intertidal Elevation

It should be emphasised that the elevations determined by this method are those of the waterline relative to the tidal water level. This is not the same as the absolute elevation that might be surveyed by LiDAR or other survey methods. However, the purpose of beach transects and surveys themselves should be considered, prior to discussing the relative accuracies of one method against another. The purpose of many beach transect monitoring campaigns is to determine to what position the combination of waves and tides might reach, damage sea defences, and potentially overtop beaches and sea walls. Conventional surveys are carried out to absolute elevation datums, which allow for tidal elevations to be combined with models of wave setup and runup, to estimate how high up the beach the water would reach under various conditions. Waterline methods potentially supply this information directly, without the need for the modelling step, meaning that absolute accuracy of the waterline derived elevations relative to a survey, may be less important than the long term stability of the technique and observation of changing trends. This is particularly the case in dynamic coastal areas which require long-term monitoring over a wide area such as a steadily eroding beach where knowledge of areas experiencing the greatest erosion and loss of material can be gained with the higher temporal resolution of radar survey. In areas where a specific area has been identified and study of micro-

scale processes is required, then other survey techniques are likely more appropriate. However these techniques will still not be able to identify critical aspects of the coastal geomorphology such as patterns of intertidal sediment migration in the same manner as the survey technique presented in this work.

Figure 5.17a displays the elevations determined by the Temporal Waterline method, cropped to the areas covered by the October 2006 LiDAR survey, and Figure 5.17b shows the LiDAR survey itself. The general shape, location and elevations of the coastline and sandbanks detected by the waterline method, are in relatively good agreement with the LiDAR survey. There is an area of particularly poor results to the southwest of the study area in Figure 5.17a, where the radar method overestimates bed elevation by >5 m in places. These areas were therefore removed in order to prevent contamination of further analysis. A combination of the shadowing effect of the sandbanks at mid to low-tide and the increasing lack of sea clutter at locations further into the sheltered estuary, is thought to be the cause of the concentrated area of poor results. It is however, significant that the present processing and filtering techniques do not remove these poor elevations, and the pixel records in these areas often have seemingly valid matches with a given tidal elevation. Identifying the reason for this and addressing the issue is a priority for future work.

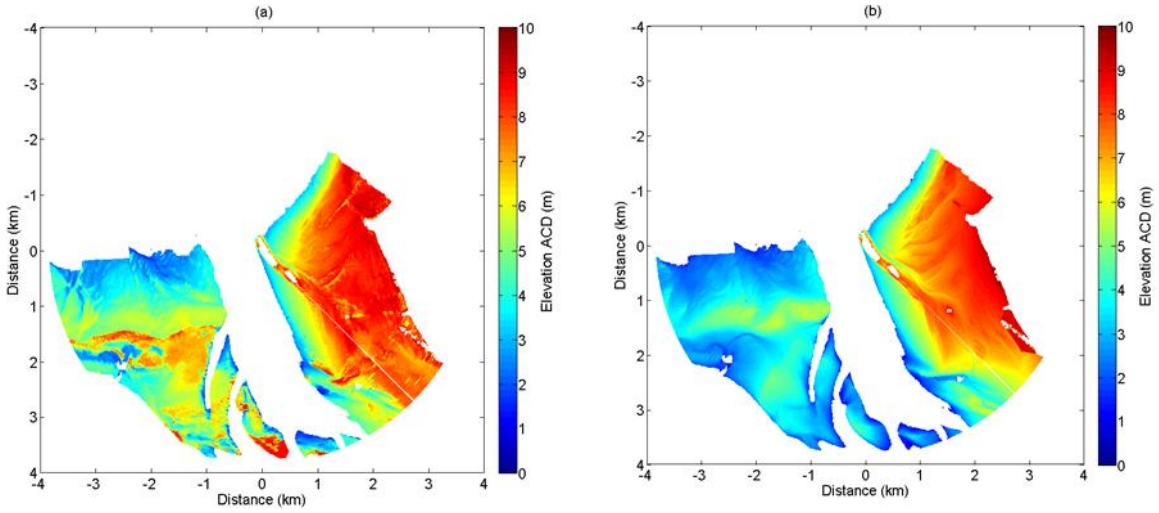

Figure 5.17: Radar (a) and LiDAR- (b) derived elevations during October 2006.

In order to quantify the differences between the LiDAR and radar elevation plots, the LiDAR values at each point were subtracted from the radar derived values. Figure 5.18 shows these residuals. The majority of the radar-derived elevations lie within ±1 m of the corresponding LiDAR elevations, with the overall pattern indicating that the waterline derived elevations are slightly higher than the survey elevations. Intuitively this might be expected, due to contributions from wave setup and runup. However, the steeper beachfaces within 2 km of the island show surprisingly good agreement with the LiDAR survey, which may indicate that the wave runup and setup may not be the only factors involved in the differences. Consistent differences between survey and waterline elevations with strong correlation values are evident over the flatter areas of the sand banks. This suggests there may be additional effects that add to the elevation of the water, such as pooling of the water between sediment features.

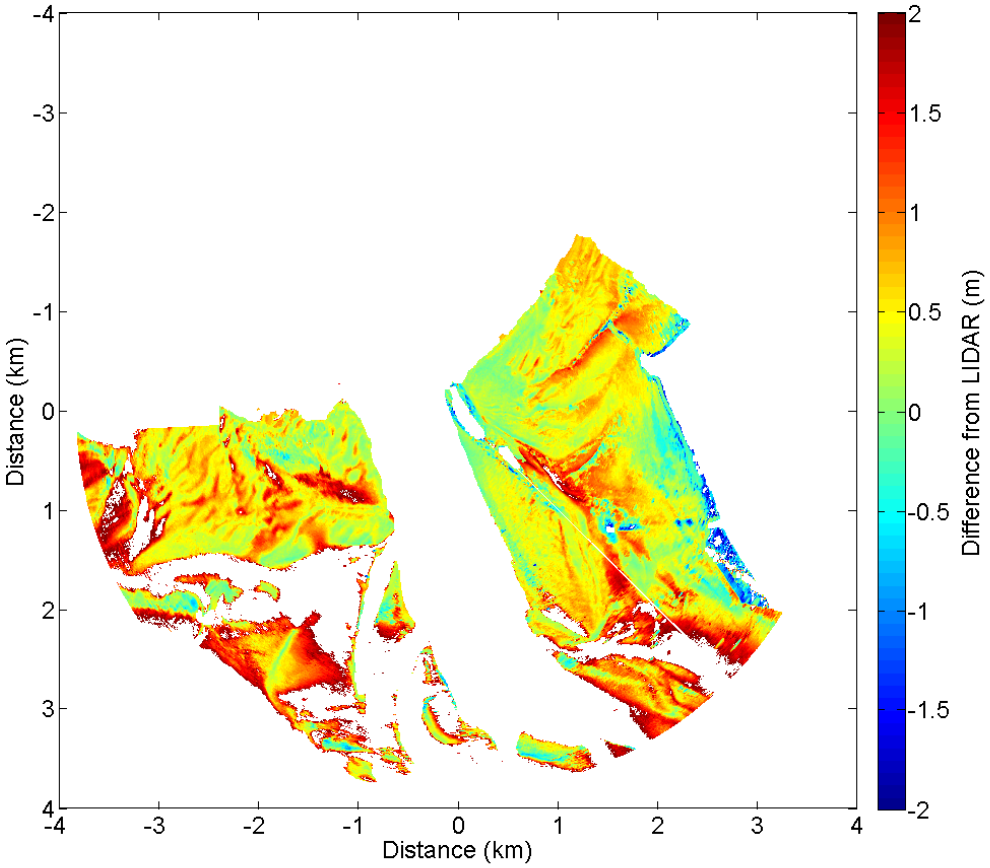

Figure 5.18: Residuals between LiDAR and radar-derived elevations.

Figure 5.19 shows a comparison between the waterline-derived elevations and the corresponding LiDAR transects. These reveal that the sloping parts of the transects leading down to the low water mark are relatively well matched between LiDAR and waterline. However, the flatter areas bounded by sediment bars or sand waves appear to have water trapped behind the bedforms, supporting the idea that water is pooling on the sand flats and creating some of the differences between LiDAR and waterline maps. As has already been noted,

the reflectivity data associated with the LiDAR elevations also indicates pooling of water in these areas, even at low water.

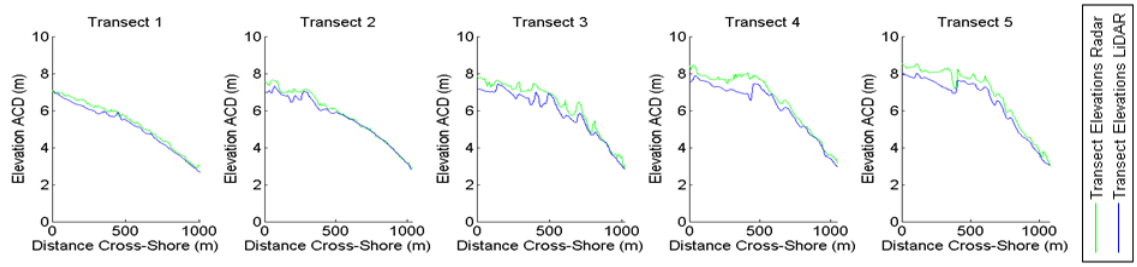

Figure 5.19: Elevations along each transect from Figure 5.11 with smoothed radar–derived (green) and LiDAR (blue) elevations.

This is an effect known to exist by the authors, based on numerous trips walking to the island. As the tide goes out, it takes a considerable time for the water to drain off the flatter areas, and it is often advisable to wait an hour or two beyond the time when the tide has nominally gone out, to allow for sufficient water to drain off the sand flats before setting off for the island on foot. These factors indicate that the simplification of applying the water level associated with the tide gauge location on Hilbre Island across the whole domain, is probably an over-simplification.

5.3.6 Close Range (< 3 km range) Accuracy

In order to better compare the features present in the LiDAR and radar-derived elevations and the spatial distribution of differences at the closer range, Figure 5.20 shows a subsection of the data covering the area of the northeastern beach in more detail. Figure 5.20a shows the radar-

derived waterline results; Figure 5.20b shows the LiDAR survey; Figure 5.20c, the difference between the waterline and LiDAR elevations and Figure 5.20d the areas likely to be shadowed based on ray tracing and the LiDAR survey. It is clear from the difference plot in Figure 5.20c that the waterline method determines absolute elevations along the immediate eastern and southern beach very well. Areas further from the radar and thus also further from the location relating to the water level data, show an increasing over estimate in the elevations compared with the LiDAR survey. Some areas of the sand flats are shadowed from the radar, as illustrated by the shadow plot in Figure 5.20d, calculated from the LiDAR survey using a simple ray tracing approach. Thus elevations calculated for these areas are unlikely to be accurate.

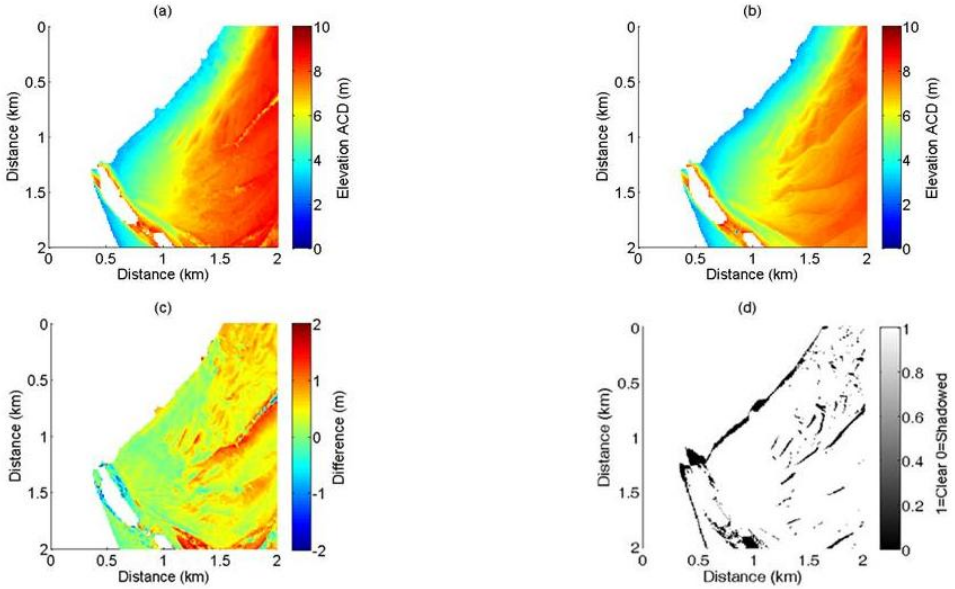

Figure 5.20: (a) Extracted subsection of radar-derived elevations (b) LiDAR elevations, and (c) residuals between radar-derived and LiDAR elevation data. (d) An artificial line of sight shadow

map, illustrating the radar line of sight based on the LiDAR observations, constructed using a simple ray tracing algorithm.

Figure 5.21 shows a series of error histograms comparing the LiDAR elevations with those of the Temporal Waterline, at different ranges from the radar. The region within 0.75 km of the radar location (Figure 5.21a) exhibits a mean bias of 0.12 m higher than the LiDAR survey, while the regions from 0.75 km range to 1.5 km range (Figure 5.21b); from 1.5 km - 2.25 km (Figure 5.21c) and from 2.25 km – 3 km (Figure 5.21d) exhibit a greater bias of 0.52 m. The 0.48 m and 0.59 m respectively. These regions encompass more of the flatter areas of sand flats. This reinforces the conclusions from Figure 5.18, suggesting that the flatter areas consistently experience pooling water, and also include larger areas shadowed from the view of the radar, which are likley to have erroneous values.

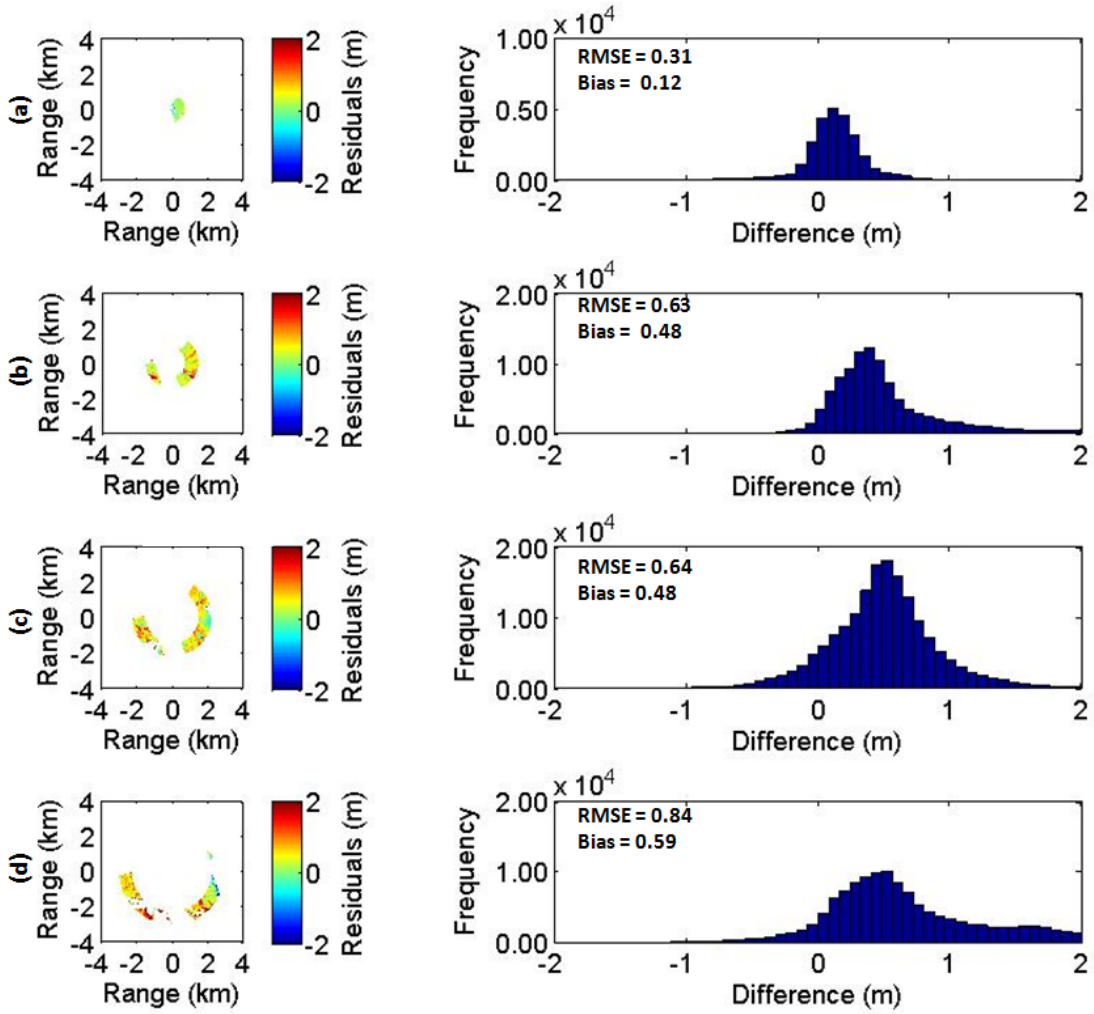

Figure 5.21: Differences between the LiDAR and radar-derived waterline elevations at different ranges from the radar (left) and corresponding error histograms (right): (a), the region within 0.75 km of the radar location; (b), the region from 0.75 km range to 1.5 km range; (c), the region from 1.5 km - 2.25 km; and (d), the region from 2.25 km – 3 km.

Further errors might be expected due to the simplification that the tidal elevation relating to the location of the Hilbre Island tide gauge, defines the water level across the entire analysis area. The true pattern of water elevation across this complex macro-tidal environment must be

expected to degrade with range from the measurement location. Moore et al. (2009) explored the differences in tidal asymmetry across the estuary via a numerical modelling study, showing stronger asymmetry over the sand banks compared with the channels, which confirms that our assumption of a uniform tidal elevation across the site at any particular moment is almost certainly an over-simplification. Attempts to apply a more realistic 2-D tidal elevation pattern, either using a tidal propagation model or empirically may be explored in future work. In particular, the issue of pooling water taking time to drain off the sand flats may suggest that, although the transition time of the rising tide may be relatively accurate across the study site, that of the falling tide may be delayed reltive to the tide gauge location.

Some differences between the radar-derived elevations and the survey are also to be expected due to the different temporal scales of the two surveys. LiDAR is a near instantaneous snapshot in time, whereas radar-derived elevations represent the mean conditions over a two-week period in this case. Thus numerical comparisons must be considered in light of this and a perfect match should not be expected. Significant changes to the shape and location of the sedimentary features have been observed to occur overnight by the authors, so the superficial features of the intertidal sand flats must be assumed to be varying slightly, even from tide to tide under dynamic conditions. Such observations reinforce the value of what could be considered a more representative average measure of intertidal elevations than the snapshots provided by surveys such as LiDAR.

5.3.7 Cumulative Changes in Elevation

Figure 5.22 shows the cumulative variations in radar-derived waterline elevations at each point in the sand flats region of the domain, over the course of ten months, with the green areas showing a high degree of stability. The most stable areas located around the landmass of Hilbre Island and the Peninsula represent concentrations of rocks. In addition, large swathes of the beach are clearly stable, suggesting a lack of medium-term sediment mobility over those regions. Regions with higher values of maximum difference in elevation through time are indicative of erosion or deposition. For example, the linear features seen across the beach face potentially mark out the migration of sand bar features, while areas of high change that are less linear may highlight areas subject to spatially discrete erosion or accretion. Overall, the plot illustrates that the majority of the area exhibits relatively little change over the ten months, with isolated areas of mobile features representing largely superficial changes to that part of the estuary.

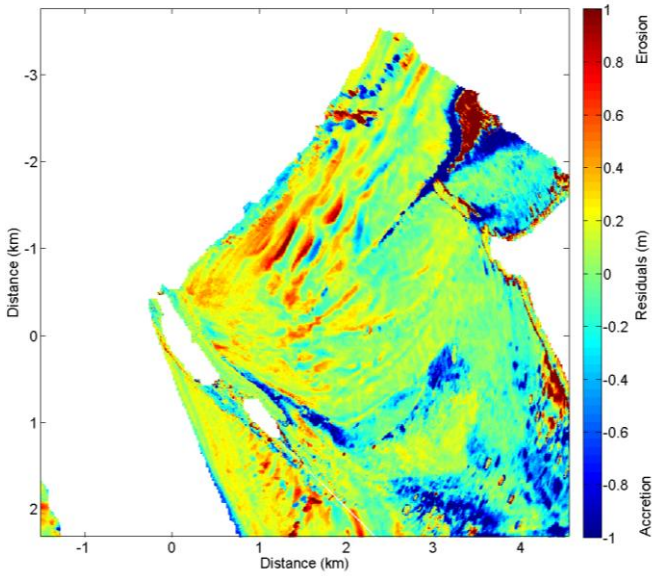

Figure 5.22: Changes in waterline elevation from March 2006 to January 2007. Red indicates erosion while blue indicates accretion.

5.3.8 Distribution of Shoreline Contours

Traditional waterline methods (discussed in Chapter 2) make use of image processing techniques, to identify a shoreline in an image and assign a tidal elevation contour based on the timestamp of the image. While this method is very different, Figure 5.23 shows that given an image taken at a specific time, it is possible to extract the dry area and superimpose that area onto the time exposure images. This demonstrates that the method accurately delineates the correct areas, according to the rise and fall of the tide. The shoreline is clearly located along the north-eastern beach and more of the sandbanks become visible as the tidal elevation falls.

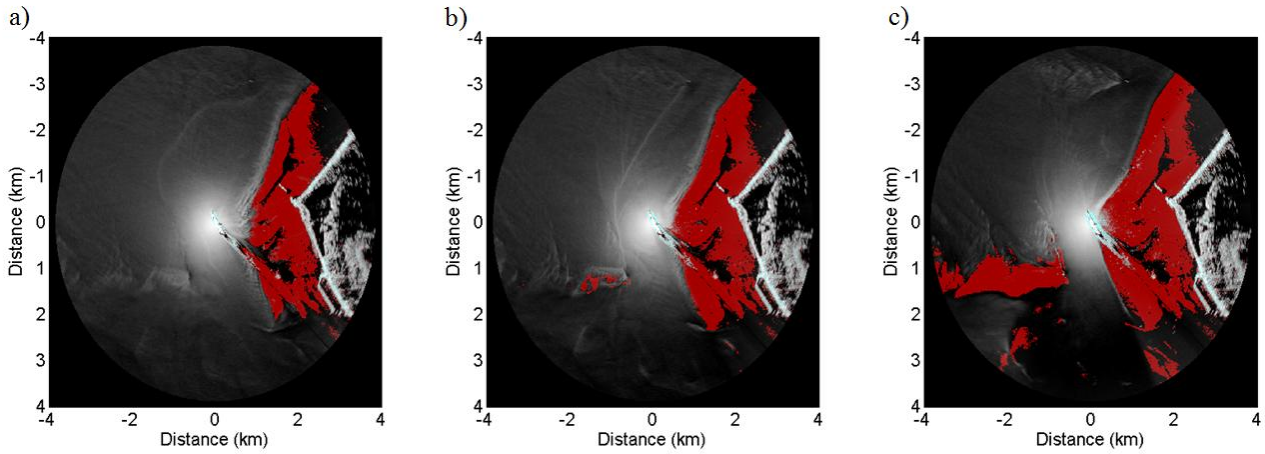

Figure 5.23: Distribution of shorelines extracted for 08/04/06 at high tide (a), mid tide (b), and low tide (c), showing increased exposure of the beach and sandbanks (red) as the tidal elevation falls.

5.4 DISCUSSION

This new method of deriving maps of the intertidal zone, although relatively effective and simple in concept, relies on a number of assumptions that are probably over-simplifications at present.

The use of a single instantaneous tidal elevation across a complex estuarine environment is acknowledged by the authors to be a simplification of reality, and appropriate tidal propagation models may in future, provide a more realistic, spatially varying water level distribution across

large areas. In particular, increasing tidal asymmetry across the sand flats and sand banks may be adversely affecting results in this complex area as a result of this assumption.

The present study was conducted in a macro-tidal estuary, in which there are extensive intertidal areas. At sites where a more modest intertidal zone is expected, consideration must be given to the expected width of the intertidal zone, relative to the radar pixel size. If the intertidal beach width is narrow relative to the radar pixel size of 5-10 m, then the X-band radar may not possess the appropriate horizontal resolution for the task. Instead, millimetre wave radar such as the 77 GHz version used by Bell et al., (2006) may be more appropriate, as such systems are capable of sub-metre range resolution and have been demonstrated to respond well to the breaking waves and beach run-up that categorises the water line. Optical camera systems are also likely to work well with this technique and can provide similar sub-metre resolution within a reasonable range of the camera, albeit in daylight and good visibility.

Further, if the vertical tidal range is narrow, the elevation intervals used in the analysis could be made finer than the 0.1 m intervals used here. Even in micro-tidal areas, meteorological effects can introduce significant water level changes in excess of the astronomical tides, and the additional contribution of these would undoubtedly assist the success of the technique at such sites.

The accuracy of the method at the limits of the tidal range also requires further consideration. This is because the number of waterline transitions close to the water level limits of the spring-neap cycle will reduce, from the peak of a uniform two transitions per tidal cycle, i.e. over 50 transitions in 14 days, down to single figures, and then zero transitions as the water level

approaches and goes beyond the limits. Looking for a correlation between the radar-derived signatures and a tidally derived signal with only a few transitions, will inevitably result in a less reliable match, and it would be prudent to implement a threshold in the number of wet-dry transitions below which any derived elevations are considered at least suspect if not invalid, regardless of the quality of the numerical match achieved. It may be that the mean low and mean high water levels would provide standardised thresholds for this application in the future.

The temporal update rate was set to two-week intervals corresponding to a single spring-neap cycle, and chosen to maximise the tidal range during each temporal analysis window. Further work may investigate reducing this interval to approximately a week or even less, but this should be synchronised to span neaps to springs, or springs to neaps to ensure the maximum tidal ranges were experienced during each analysis period.

5.5 CONCLUSIONS

A new method of analysing the location of waterlines in remotely sensed data has been presented. The method differs from established methods by moving the problem from the spatial domain to the time domain, and looking for matches in the expected temporal pattern of transitions between wet and dry areas over a spring-neap cycle. This is inherently more robust and easier to implement automatically, rather than attempting to identify the precise physical waterline in individual remotely sensed images. The accuracy relative to a LiDAR survey varies from an overestimate of 0.12 m within the first 0.75 km from the radar, to an approximate 0.5 m

overestimate further from the radar, although these comparisons are complicated by the complex nature of the macro-tidal estuary used as the test case.

The tidal water level used for the analysis is assumed to be flat across the study area at any instant in time, which is almost certainly an over-simplification, and the application of a modelled 2-D water level that took into account the tidal asymmetry over sand flats and sand banks, may improve the absolute accuracy in future.

The method provides a map of the elevation of the waterlines relative to the tidal reference, rather than the absolute elevation of the bed. The analysis of pixels corresponding to a number of rocks, demonstrated that elevations of the derived waterlines relating to those rocks are relatively stable through the ten months of processed data. In contrast, inspection of a number of beach transects showed gradual evolution of those transects during the study period, with all beach transects exhibiting a slight lowering of the beach face during the ten months from March 2006 to January 2007. Hence, the waterline elevations can therefore be viewed as a very effective measure of intertidal change, yielding volumetric changes that could be used in conjunction with a single validation survey to relate such changes to absolute elevations if necessary.

Despite these simplifications, the results are remarkably stable through time, suggesting that the method would be suitable for the autonomous monitoring of changes to large intertidal areas over sustained periods of months to years.

In commercial operation, the results from this method could be coupled with bathymetric survey data of navigation channels to create an integrated chart system, which would populate sub-tidal areas using data from conventional survey methods, and intertidal zones with waterline derived information. This would potentially provide regularly updated reports on sediment flux and channel migration. That said, the waterline method is also effective as a stand-alone tool for monitoring changes in the inter-tidal channel margins. This combined mapping strategy may be a vital source of data for coastal stakeholders and port authorities operating in areas where sedimentary features are mobile across the intertidal area, and also those areas where sediment accretion or erosion in between cycles of commissioned surveys and maintenance, is causing problems in the management of the coast.

5.6 ACKNOWLEDGEMENTS FOR CHAPTER 5

The authors would like to thank Wirral Borough Council's Ranger Service and in particular the (then) Hilbre Island Ranger - Mr David Cavanagh, for many years of enthusiastic help with numerous aspects of installing and maintaining a remote system in such a challenging location. Thanks are due to Mr John M. X. Hughes for the photograph of the SS. Nestos exposed at low tide used in Figure 5.8 and a set of insightful pilotage notes for the Dee Estuary. The radar data were collected by the *National Oceanography Centre (NOC) Liverpool* under the umbrella of the *Liverpool Bay Coastal Observatory* and was funded by the *UK Natural Environment Research Council.* Cai Bird's PhD study was funded by the *Centre for Global Eco-Innovation (CGE)* through the *European Regional Development Fund (ERDF)* and *Marlan Maritime Technologies*. The

authors would also like to thank the anonymous reviewers, whose comments were extremely helpful in improving the content of this paper.

6 RADAR-DERIVED ELEVATIONS FOR MONITORING DYNAMIC COASTAL GEOMORPHOLOGY

This chapter is based on the publication Bird, C.O., Bell, P.S., Plater, A.J., (submitted) Radar-derived elevation maps for monitoring dynamic coastal morphology. *Geomorphology.*

The contents of this paper are currently in the final stages of pre-submission revision and are thus subject to change.

Abstract

Monitoring morphological change in the dynamic intertidal region is an extremely difficult task, relying on many different sensor platforms and survey techniques. This contribution aims to demonstrate the application of marine radar and a newly developed waterline mapping technique, to the continued surveillance and monitoring of inter-annual intertidal morphological change. Marine radar data from 2006 - 2009 are used to

create a sequence of waterline elevation surveys that show clear morphological evolution of two different sites in the Dee estuary, UK. An estimate of the total volumetric change was made at two locations. West Hoyle sandbank and the NW Wirral beach. Both sites exhibited a similar cyclic pattern of volumetric change, with lowest volumes in autumn and winter, respectively. The average beach elevations above Admiralty Chart Datum of these two areas clearly reflect the change in sediment volume, with reduced elevations in winter and increased elevations observed in summer, suggesting a trend of high energy storm waves in the autumn and winter removing sediment and simultaneously flattening bedforms in the intertidal area. These data at this temporal and spatial scale are not easily obtainable by other current remote sensing techniques. The use of marine radar as an integrated tool for quantifying coastal change over seasonal and event timescales at in complex hydrodynamic settings is therefore illustrated. Specifically its unique application to monitoring areas with dynamic morphology or that are vulnerable to erosion and/or degradation by storm events is demonstrated to good effect.

6.1 SUMMARY OF CONSTRUCTION OF INTERTIDAL ELEVATION MAPS

Marine radar creates images via the rotation of a directive antenna (at ~25 rpm) projecting radiofrequency electromagnetic waves around 360° and listening for the re-radiated energy at each azimuth and range. The magnitude of returned energy is then translated into pixel intensity and the polar data converted to a Cartesian image. It should be noted that while individual radar images appear to be snapshots of the surrounding area taken synoptically, they are actually captured progressively over a 2.4 s period, giving an image sampling frequency of just 0.416 Hz. While that is less than the period of most nearshore waves, allowing the

progression of wave fields to imaged effectively, there are some minor inherent inaccuracies in spatial and temporal image analysis if the images are assumed to be true snapshots. Figure 6.1 depicts a schematic of radar data collection at this scale; it can be thought of as a helix describing the transgression of the radar scan through time and space. These 'snapshot' images are temporally averaged over ten minutes, creating a series of time exposure images taken every hour throughout 2006 - 2008.

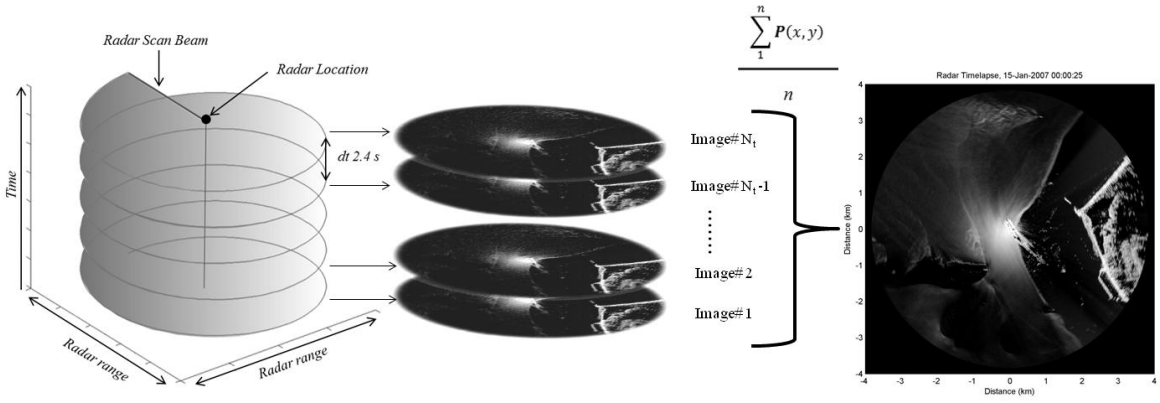

Figure 6.1: Schematic describing radar data collection, a sequence of snapshots collected every 2.4 seconds are averaged over ten minutes (~256 images) creating time exposure images highlighting areas of high pixel intensities.

When these images are viewed in sequence, the spatial location of the waterline can clearly be seen migrating across the image according to the rise and fall of the tide. The the high image intensity results from higher radar returns from the breaking waves in the surf zone. Surface roughness, and therefore image pixel intensity turbulence within the water column caused by the sandbanks and tidal flats further out in the estuary. By extracting a given image pixel

intensity at each time step over two weeks, the temporal signal of a spatially transgressing waterline can be obtained. Each tidal elevation within a given tidal range 0-10 m with 10 cm vertical resolution in this case, has a unique temporal signal indicating the times of transition from wet to dry at a given location according to the tidal cycle. The pixel signal from every point in the input image sequence is matched to a unique tidal elevation above ACD using the method detailed in Bell et al. (2016). Figure 6.2 shows a schematic of the technique used to derive intertidal elevations.

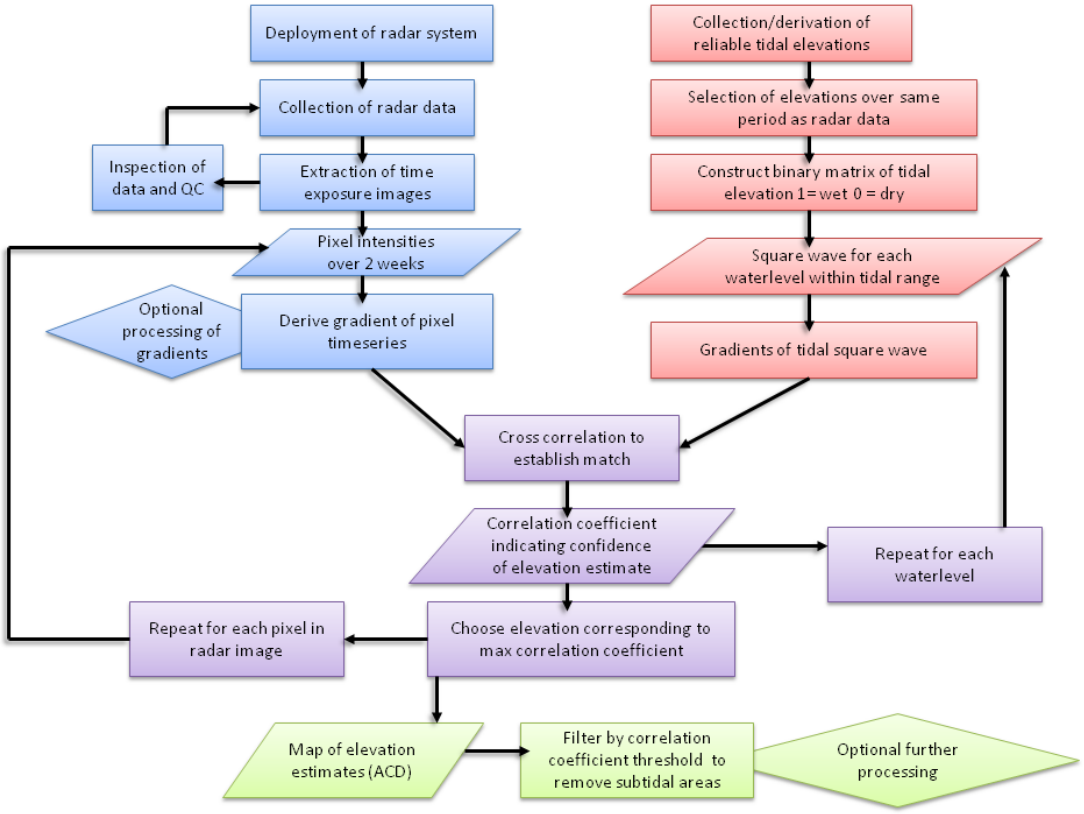

Figure 6.2: Schematic overview of radar waterline survey method developed by Bell et al. (2016).

The resulting maps of elevation reflect the mean elevation of the waterline over the two-week analysis period, giving a good approximation of the intertidal morphology at that time. The algorithm can make use of data collected over a shorter time period, however the full tidal range between a given spring and neap tide will not be observed. Therefore the elevations outside of the tidal range would not be resolved. The maps are filtered according to correlation coefficient derived by the waterline algorithm, with low correlations representing areas of low accuracy. Typically these zones reflect areas that are shadowed from the radar antenna, or subtidal zones where there are less obvious cycle of tidal wetting and drying for the algorithm to detect.

6.2 ANALYSIS OF ELEVATIONS OVER LONG TIMESCALES

The derivation of single elevation plots as a product of several weeks of data is a useful tool, however the true strength of the developed radar waterline method lies in the ability to monitor the same area for an extended period of time in a robust and cost-effective manner. Given the dynamic nature of intertidal regions, snapshot surveys may quickly become obsolete. Using repeated surveys of the same region, it is possible to improve the estimations of elevation and alleviate potential noise or missing data points caused by lower correlations at certain points in time. The cause of these lower correlations can often be attributed to calmer sea state conditions over the two-week period, as smoother sea surfaces return reduced amounts of radar energy and therefore result in a more unstable pixel intensity signal.

Elevation results can be filtered in the following manner to improve their stability. The signal of elevations over time denoted by $\eta_{(t)} = I_{(x,y,t)}$, where I is the sequence of intertidal elevation plots,

is passed through a robust smoothing algorithm based on a least squares regression method (Garcia, 2010). This smoothing function is weighted by the signal of maximum correlation coefficients corresponding to the input elevations. The result is that outlying data and missing values that have low correlation coefficients are less able to negatively influence the smoothed elevations. This method enables missing data to be filled with an approximate elevation whilst still retaining the overall trend of the signal, giving an unbroken record of elevations over long time periods which allows for the evolution of a given intertidal area to be tracked effectively.

In addition to the two-week plot cycle, it is also possible to increase the temporal resolution by using a moving window analysis. In this case, two weeks of data are used in the analysis, then the following week is appended to the data, dropping the first week and generating weekly updates of mean waterline elevations. It is possible even to reduce the time between surveys to daily resolution, depending on the processing capabilities available to perform the research. It is crucial that the analysis runs over the period from spring to neap or neap to spring to ensure that the maximum tidal range over each period is exploited. This technique was not applied to the data used in this paper due to the computational requirements of performing this analysis on three years of data. Here, a temporal resolution of two weeks was deemed suitable for analysis over sub and inter-annual timescales.

6.3 RESULTS

Figure 6.3 shows the results of two weeks of radar data (26 March 2006 - 8 April 2006) analysed using the radar waterline method. The noise in this plot at longer ranges is indicative of the increased area lying in shadow and the drop off in radar power, resulting in lower

intensities and more unstable pixel signals at longer ranges. Figure 6.3 is colour-coded according to waterline elevation above ACD and illustrates two sites; Site A is the West Hoyle sandbank and B is a section of the NW Wirral beach, the morphology of these areas will be examined in more detail in following sections.

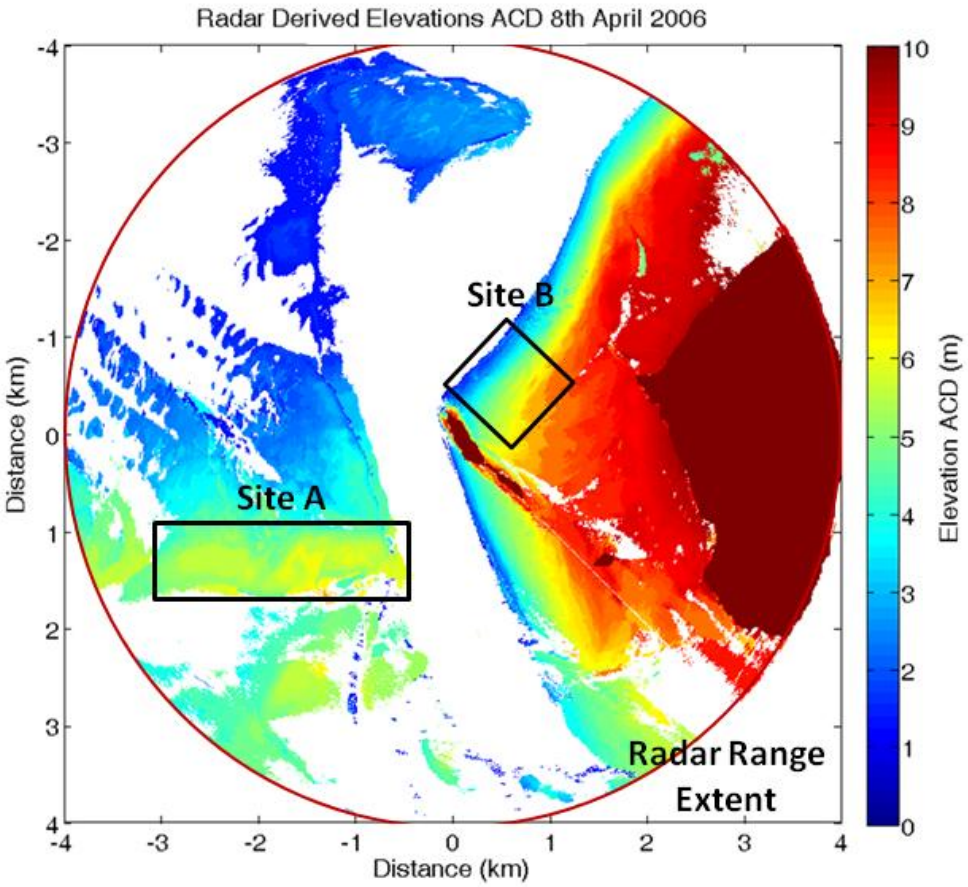

Figure 6.3: Radar-derived waterline elevations surveyed during April 2006 showing Site A, the West Hoyle sandbank and Site B, the NW Wirral beach to the east of Hilbre Island.

A waterline survey in the form of Figure 6.3 was completed for every two-week period from the beginning of 2006 to the end of 2008, however there were some periods where surveys could not be produced due to inadequate radar data or failing power supply; these gaps in the dataset are detailed in Table 6.1.

2006			2007			2008		
Month	Day	Survey Completed?	Month	Day	Survey Completed?	Month	Day	Survey Completed?
1	1	×	1	1	×	1	15	✓
1	14	×	1	13	✓	1	29	×
1	28	×	1	27	✓	2	9	✓
2	12	×	2	10	✓	2	23	✓
2	26	×	2	24	✓	3	7	×
3	11	✓	3	10	✓	3	21	×
3	25	✓	3	24	✓	4	4	×
4	8	✓	4	7	✓	4	18	✓
4	22	✓	4	21	✓	5	6	×
5	6	×	5	5	✓	5	20	✓
5	20	✓	5	19	✓	6	5	✓
6	3	✓	6	2	✓	6	19	✓
6	17	✓	6	16	✓	7	1	×
7	1	✓	6	30	✓	7	12	✓
7	15	✓	7	14	✓	7	26	✓
7	29	✓	7	28	✓	8	9	✓
8	12	✓	8	11	✓	8	23	✓
8	26	✓	8	25	✓	9	7	×
9	9	✓	9	15	✓	9	21	×
9	23	✓	9	29	✓	10	4	✓
10	7	✓	10	13	✓	10	18	✓
10	21	✓	10	27	✓	11	1	✓
11	4	✓	11	15	✓	11	15	✓
11	18	✓	11	29	✓	11	29	✓
12	2	✓	12	13	✓	12	13	✓
12	16	✓	12	27	✓	12	27	×

Table 6.1: Documented dates of completed surveys and missing data throughout the three year deployment at Hilbre Island.

6.4 MONITORING MORPHOLOGICAL CHANGE

In order to explore changes in intertidal morphology, several sites have been chosen to highlight the spatial variability over a relatively small area. The Dee estuary is a very complex macro-tidal estuary (Moore et al., 2009) and each of the selected sites has very different characteristics, including environmental forcings, levels of exposure, underlying geology, beach gradients and orientations.

6.4.1 Accuracy of Elevations at Site A (West Hoyle Sand Bank)

Site A, the location of which is shown in Figure 6.3, is a section of the West Hoyle sandbank. This feature is known from local anecdotal evidence to be quite mobile. Figure 6.4a shows this area cropped out of the radar waterline data, and Figure 6.4b shows the same area extracted from a LiDAR survey flown at the same time period (October 2006).

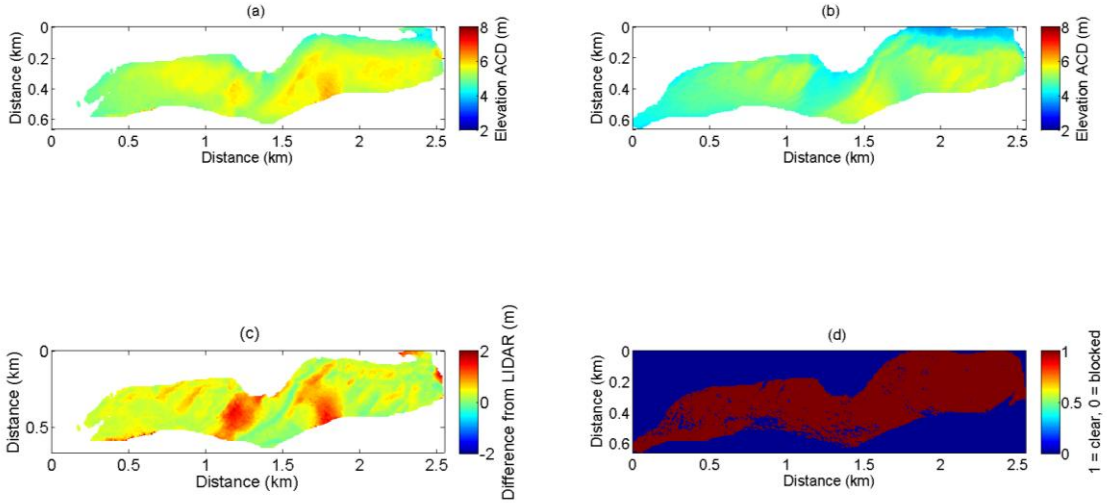

Figure 6.4: Comparison of (a), radar-derived waterline elevations and (b), LiDAR-observed bed elevations. (c) Residuals between (a) and (b). (d) Areas in shadow from the radar antenna defined by a simple ray tracing method based on the LiDAR elevations, 1 = clear, 0 = shadowed.

The overall accuracy of this technique has been explored in some depth in Bell et al. (2016), however it is useful to re-examine the accuracy of the method for West Hoyle sandbank. It is important to set the differences between radar-derived elevations and the LiDAR elevations in context with regards to the different physical phenomena being observed. Figure 6.5c shows the residual differences between the radar waterline elevations and the LiDAR bed elevation measurements, in which the majority of the area of West Hoyle sandbank is well defined with elevation differences of 0 - 50 cm (green and yellow areas) with two main concentrations of larger differences > 50 cm. Figure 6.4d shows the areas shadowed from line of sight of the radar by intervening topography. It is clear that most of the survey area is unobstructed to the radar antenna and therefore shadowing is likely not the cause of the larger elevation differences

which occur in areas not shadowed. The issue of pooling water was briefly considered in Bell et al. (2016) and it is likely that residual tidal water resident on the ebb tide is causing the general over-estimation of elevations across the surveyed area. In this case where tidal elevation falls, water remains pooled in situ and its wind-roughened surface is being imaged by the radar until it drains off, causing the matching algorithm to incorrectly associate a higher waterline elevation. Figure 6.5 shows a comparison between the radar and LiDAR values at site A, highlighting the distinct over-estimation in several areas. Methods of identifying stationary water bodies and compensating for their presence are currently being developed and it is hoped that these amendments will significantly reduce the localised over-estimation of elevation significantly.

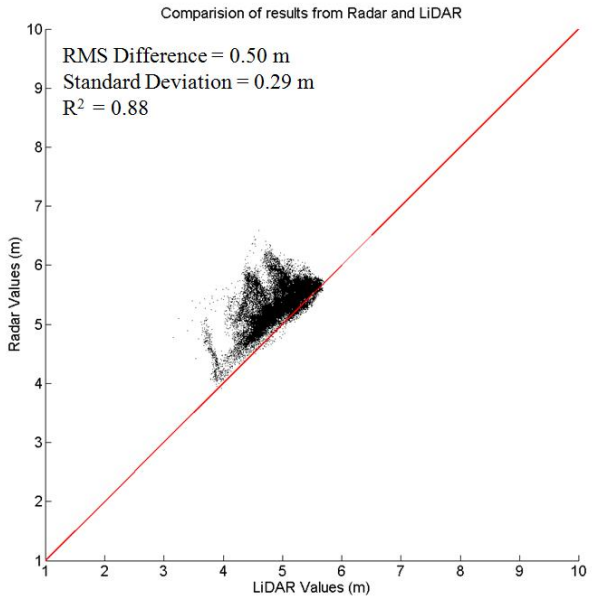

Figure 6.5: Comparison between radar-derived waterline elevations and LiDAR-observed bed elevations at West Hoyle sandbank.

It is important to reiterate that elevation values derived by the radar waterline method are indeed those of the water surface, not absolute bed elevations. However, these measurements can readily be considered as a proxy for bed elevation as water surface elevation intuitively changes depending on the underlying bed morphology. With this in mind the following sections illustrate changes in the inferred morphology of West Hoyle sandbank (Site A) and a large area of NW Wirral beach face (Site B) from March 2006 to December 2008.

6.4.2 Changing Sediment Volumes at Sites A (West Hoyle Sandbank) and B (NW Wirral Beach).

The radar survey technique provides the ability to estimate changing sediment volumes across large areas of the survey environment. The range resolution of the Cartesian grid onto which the radar data have been translated is 5 m; each point in this grid therefore not only represents elevation but can also be used to perform volumetric calculations. An estimate of sediment volume (relative to Admiralty Chart Datum) was made at each grid location and the total volume of the West Hoyle sandbank and the NW Wirral beach calculated every two weeks. **Error! Reference source not found.**a shows the estimated sediment volume over nearly three years at West Hoyle sandbank (site A), with gaps in the dataset filled using a third degree polynomial and the winter seasons (December- February) are marked as dashed red lines. **Error! Reference source not found.**b shows volumetric data from the NW Wirral Beach (site B). Wave data from a waverider buoy operated as part of the *CEFAS wavenet* in the Irish Sea off the coast of the Wirral Peninsula provided high temporal resolution (every 15 minutes) measurements of significant wave heights from 2006 - 2009 while the radar was deployed. The buoy was located

at 53°32'.01N, 003°21'.31W. Significant wave heights, periods and dominant directions from January 2006 to December 2008 are shown in Figure 6.6d a strong westerly dominance is evident.

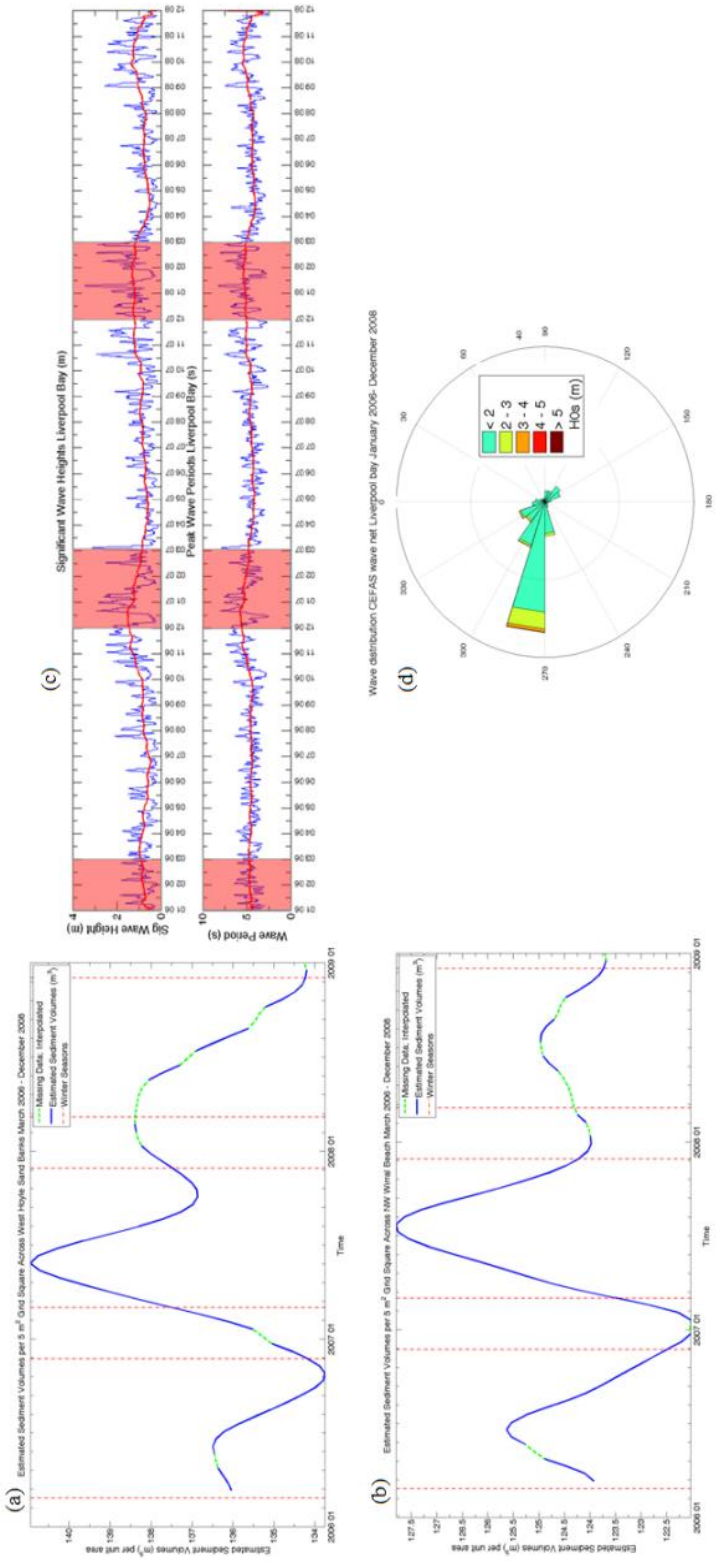
(a)
(b)
(c)
(d)
Missing Data, Interpolated
Estimated Sediment Volumes (m³)
Winter Seasons
Time
Significant Wave Heights Liverpool Bay (m)
Peak Wave Periods Liverpool Bay (s)
Sig Wave Height (m)
Wave Period (s)
Wave distribution CEFAS wave net Liverpool bay January 2006- December 2008
< 2
2 - 3
3 - 4
4 - 5
> 5
Hs (m)

Figure 6.6: (a) Estimated change in total sediment volume at Site A West Hoyle sandbank. The solid line represents values estimated using the radar waterline method, the dashed line shows interpolated missing data. (b) Estimated change in sediment volume at Site B NW Wirral beach. Solid line represents values estimated using the radar waterline method, dashed line the interpolated missing data, and dashed red vertical lines denote the winter seasons. (c) Wave statistics from CEFAS wavenet buoy in Liverpool Bay. Daily averaged significant wave heights and daily averaged peak wave periods. Red sections indicate winter seasons and red line represents monthly moving averaged values. (d) Wave directions and significant wave height distributions from wavenet buoy.

It has been noted that the Dee estuary is currently at or approaching stability at the equilibrium stage of its morphological evolution (Moore et al., 2009). Figure 6.6 broadly confirms this in that there is little net change over the analysis time period, but with large deviations over the course of a year, this does suggest a dynamic equilibrium state where the Dee estuarine system is constantly adapting to new boundary conditions and forcings (Dongeren and De Vriend, 1994). The signal of changing sediment volume at site A (Figure 6.6a) indicates lowest volumes towards the ends of the autumn season and early winter. In the UK this autumn period often experiences storms in October and November and throughout winter which contribute to the loss of sediment. It is interesting to note that the influx of sediment begins in winter and it may be that material is being transported from elsewhere in the local domain such as the outer areas of the East and West Hoyle sandbanks or the Point of Ayr to the west. Maximum sediment volumes are seen in spring and summer when wave conditions are generally

calmer (see Figure 6.6c**Error! Reference source not found.**). This seasonal cycle of changing volume is reflected well in the cycle of changing elevations shown later in Figure 6.9 suggesting both a removal of material and a flattening of bedforms during autumn and winter. Site B follows a similar pattern to that of Site A in terms of changing sediment volumes, as shown in Figure 6.6 (b). The key difference here however is that lowest sediment levels are seen in mid-winter. This lag in material loss could be indicative of changing wave angle and climate affecting the different locations in different ways or potentially some transfer of material from one site to the other. The record of daily averaged significant wave heights throughout 2006-2009 show that wave heights are generally high in autumn and winter, this is also reflected in the monthly averaged significant wave height values (red line in Figure 6.6c). This suggests that the seasonal cyclicity in sediment volume flux is somewhat independent of the regular macro-tidal processes in the Dee estuary, and is dominated by the change in wave climate throughout the year. The extent to which the changing wave climate influences the two sites analysed clearly varies significantly given the lag time in volume change.

The variation in susceptibility to wave action between the two sites is likely a result of their different geomorphological characteristics. The NW Wirral beach differs from West Hoyle sandbank in that sandbanks in a more central position in the estuary mouth are likely to be more exposed to waves than the tidal flats on the beach. They are also more difficult to survey using traditional manual techniques as the sandbank is isolated from the main beach area and only dry for a limited time. In addition, site A has a much shallower cross-shore gradient and a lower maximum elevation, this elevation difference will influence to some extent the duration and impact of nearshore processes effecting the area over the course of a given tidal cycle and the difference in gradient will

contribute to the determination of run up extents and wave breaking processes. It is clear from Figure 6.3 that the upper regions of site B are sheltered by Hilbre Island from westerly waves, potentially reducing erosion for the upper beachface during moderate conditions. Waves incoming from the north and northwest are likely to break and their energy be attenuated during the transition across East Hoyle bank to the North of site B.

6.4.3 Changing Intertidal Morphology at Site A (West Hoyle Sandbank)

At the temporal resolution outlined in Table 6.1, changes in the morphology of West Hoyle sandbank can be seen clearly. Figure 6.7 shows a sequence of radar waterline elevations described using surface plots with a 25 x vertical exaggeration to emphasise morphological features. These plots are generated initially using two weeks of data and a sample extracted every five months to illustrate changes in morphology across the sandbank. The movement of meso-scale bedforms can be seen across the sandbank and is representative of the sediment translation evident in Figure 6.7 It is much easier to see this movement in the video attached in supplementary material named WestHoyleBank_MorphologicalChange.mp4, which makes use of all available two-week surveys across the three-year deployment.

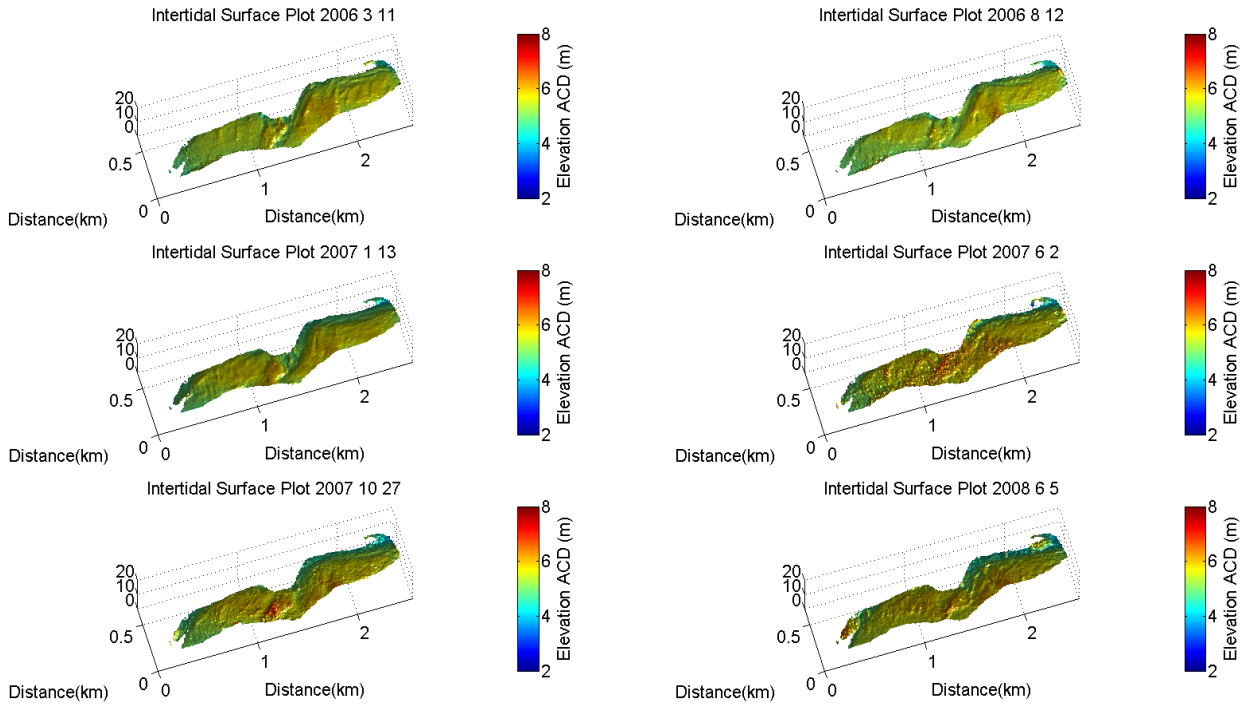

Figure 6.7: Surface plots illustrating morphological evolution at site A, West Hoyle sandbank. Plots shown were extracted every five months between March 2006 and December 2008.

Figure 6.8 shows the total residual change in waterline elevation between the start (March 2006) and the end (December 2008) of the three-year survey period, with the red regions indicating erosion and the blue areas indicating accretion. The northern section of the sandbank has suffered significant loss in elevation (~ 1 m) while the southern, central and western sections of the bank have accreted.

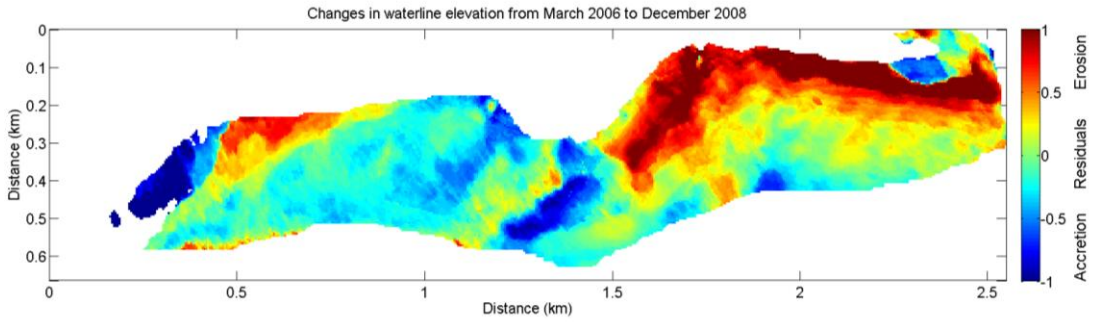

Figure 6.8: Long-term elevation change (March 2006 - December 2008) West Hoyle sandbank.

Estimations of sediment volume are not the only measure of beach state and shoreline health able to be resolved with this method. The variation of mean elevations of a given region gives an intuitive overview of the beach profile condition, higher mean elevations indicate the presence of significant bedforms while lower elevations reflect a levelling or destruction of bedforms, or of course their migration out of the study area. The pattern of these mean elevations follows a similar to those of the total sediment volume change over the three years. Figure 6.9 illustrates the change in mean waterline elevation (m) at Site A at each available two-week period from March 2006 to December 2008 and their deviation around the mean beach elevation (purple solid line). The red line describes 2006 elevations, the green line 2007 and the blue 2008. It is clear from Figure 6.9 that all lines follow a similar pattern where the sandbank elevations rise above the mean elevation in summer and drop below this in winter.

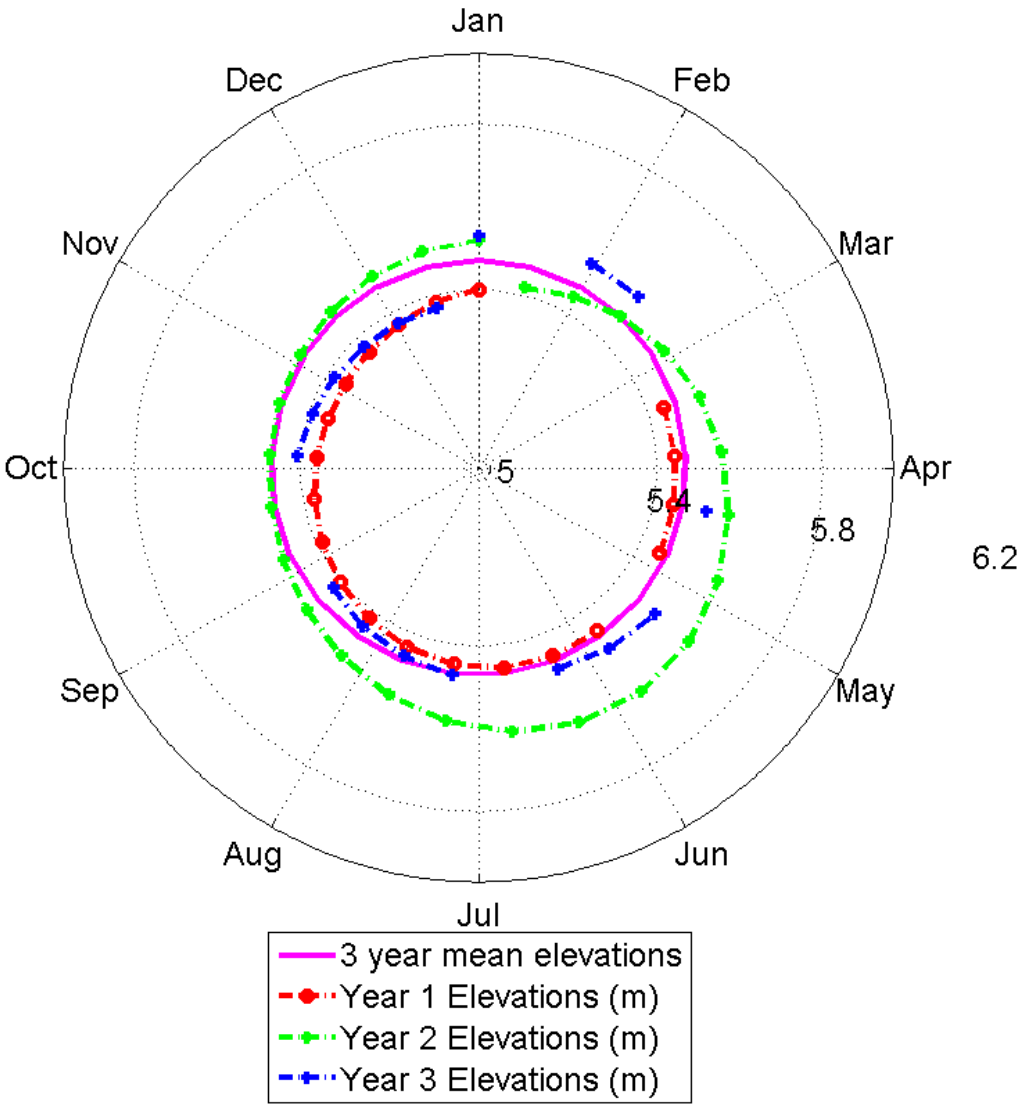

Figure 6.9: Variation in mean waterline elevations above Chart Datum for West Hoyle sandbank throughout 2006 (red line), 2007 (green line), 2008 (blue line) around the three-year mean elevation (purple solid line).

6.4.4 Morphological Change at Site B (NW Wirral beach).

Site B comprises the intertidal flat area immediately to the east of Hilbre Island where the radar is situated. Hilbre Island can only be accessed at low tide, and walkers visiting the Island are advised not to traverse this section of the intertidal area due to the speed at which the tide comes in at this location and the risk of being cut-off and stranded on one of the intertidal bars. Figure 6.3 shows the location of Site B in relation to the survey area and radar location. A similar exercise as that applied to Site A was performed in order to track the changing elevations at this site. The accuracy of results from this area compared to LiDAR elevations was explored in significant detail in Bell et al. (2016) and as such will not be reiterated here. It is however significant that shadowing is more of an issue here where there are many quasi-linear tidal channels and bedforms that give rise to a complex local morphology.

Figure 6.10 shows a series of surface plots constructed using radar waterline elevation data with a 25 x vertical exaggeration, showing the migration of linear sedimentary bedforms with wavelengths of the order of 200 m, it is likely these are intertidal bars that weld onto the beach during late 2007/early 2008. These surface plots are extracted from the three-year time series every five months in the interest of demonstrating this observation. The reader is also directed to the online supplementary material where a video showing the changing morphology, named EasternFlats_MorphologicalChange.mp4, is available.

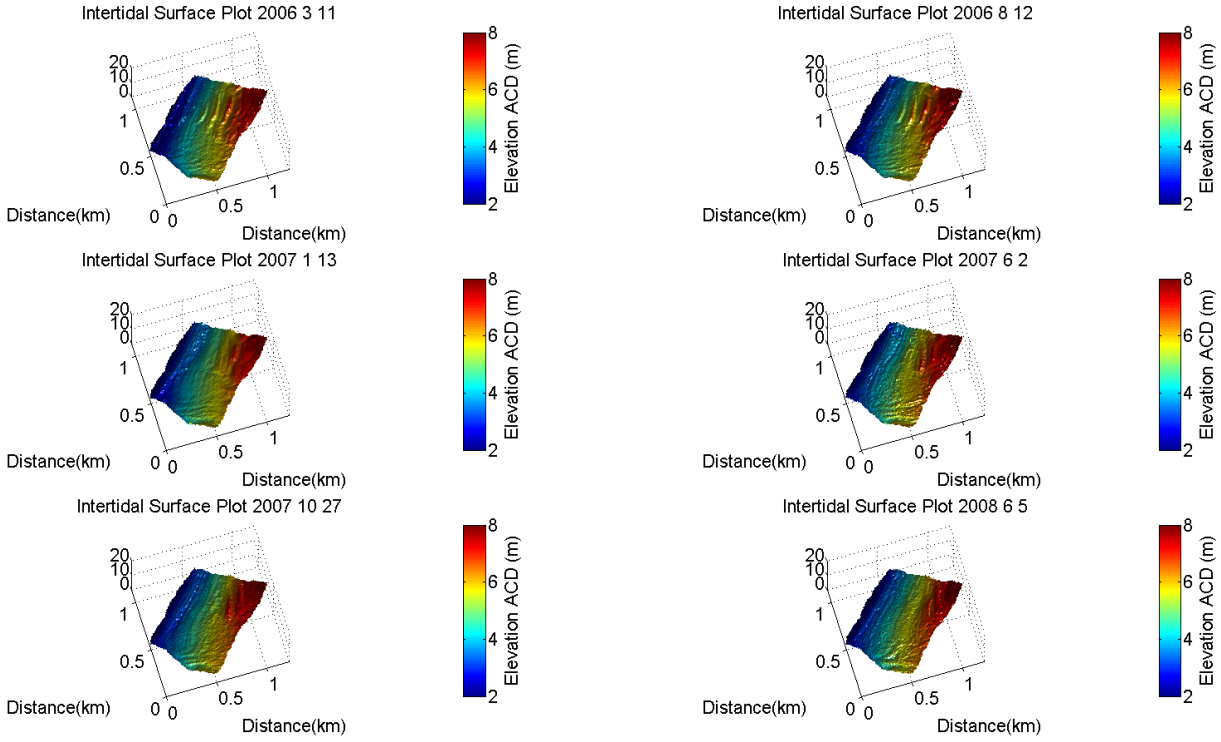

Figure 6.10: Sequence of surface plots illustrating morphological evolution of Site B, NW Wirral beach.

Figure 6.11 illustrates the change in mean waterline elevation at Site B, reflecting the changing sediment volume relatively well with elevations below the three-year average in winter and above in summer. Erosion and loss of material begins around one month later than at Site A but seems to follow a similar pattern suggesting an overarching forcing regime that is attenuated by local conditions.

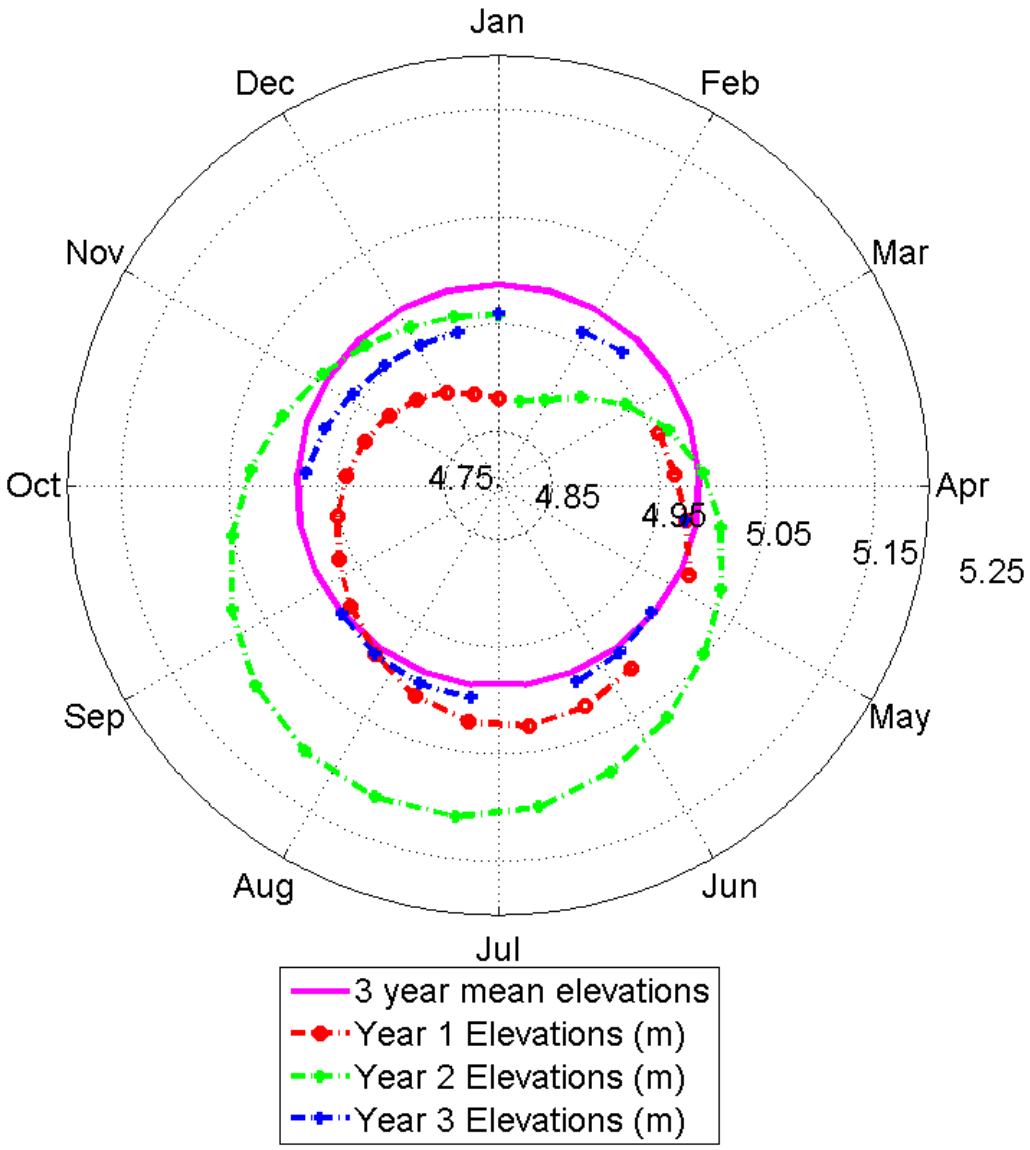

Figure 6.11: Variation in mean waterline elevations for Site B, NW Wirral beach throughout 2006 (red line), 2007 (green line), 2008 (blue line) around the three-year mean elevation (purple solid line).

6.5 MORPHOLOGICAL RESPONSE TO STORM EVENTS

In addition to long-term observations and snapshot surveys, this method can also be tuned to selectively survey waterline elevations over a given area leading up to and immediately following a storm event, this then allows for a customisable method for observing effects of high energy events.

The storm *Britta* in late October (29th) to early November (4th) 2006 was primarily a North Sea storm and contributed to gusts in the region of 170 km/h in many coastal areas across western Europe including Denmark, Norway and Scotland. As waves in the Irish Sea are predominantly fetch-limited (Dissanayake et al., 2015) it is reasonable to assume that similar (albeit much less dramatic) storm conditions contributed to the generation of the waves being measured by this buoy during this period.

Radar data were processed for two weeks up until the 29 October 2006 when significant wave heights began to increase up to a local maximum daily mean of 2.4 m. Peak significant wave height over the storm period was 3.4 m and peak wave period of 9 s on 31 October 2006 at 08:00. A survey was generated for this pre-storm period and another for the following two weeks. Figure 6.12 shows the residuals between the survey before and following storm *Britta* around Hilbre Island. Red areas indicate erosion, with maximum values suggesting around 1 m of relative (as the results indicate waterline elevations) sediment loss from the crests of bedforms .

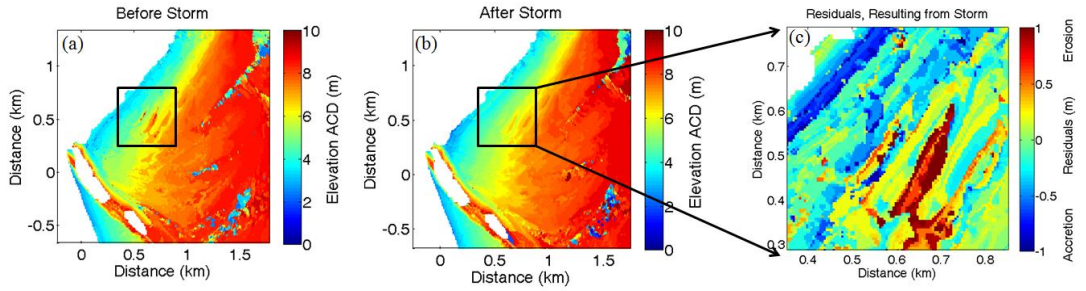

Figure 6.12: (a) Radar-derived waterline elevations from period before storm Britta (15-29 October). (b) Elevations from after the storm (31-14 November). (c) Sub-image showing radar-estimated residual waterline elevation changes (m) resulting from storm Britta (November 2006) around Hilbre Island.

A visual comparison between Figure 6.12a and b shows a clear overall reduction of elevation across the beachface. There are numerous linear features of erosion running from southwest to northeast along the beachface, these are likely the crests of bedforms being removed or being redistributed further offshore (as indicated by the areas of accretion indicated in blue concentrated close to the subtidal margins). The extracted sub-image marked by the black boundaries shows residual elevation change (c) between the pre- and post-storm radar-derived surveys. The current temporal resolution of two weeks is likely not sufficient to properly quantify the effects of a single storm, in this instance wave heights increase again only a week after the storm and thus some of the changes recorded may in fact be due to a separate storm event. Resolving this may be

achieved by using fewer data in the analysis, for example only one week before and after the storm event, though results will likely be less accurate, or by using a two-weekly moving window analysis.

6.6 RADAR-RETRIEVED CROSS-SHORE PROFILES

Beach profiles are an important form of input data to many nearshore morphological and hydrodynamic models, for example XBeach and XBeach-G (Roelvink et al., 2009; Masselink et al., 2014). Traditional methods of measuring beach profile evolution over time often involves the repeated sampling of a series of cross-shore profiles and measuring the differentials to determine erosion or accretion and track migration of observed bedforms (Pye and Smith, 1988). A clear disadvantage of relying on cross-shore profiles is the lack of 3-D monitoring that potentially causes the transition of a bedform to be missed if it migrates between two transects. This can also give the false impression of increased erosion from a transect when it is actually a case of migration. Many studies seek to address this by taking many profiles closely spaced along an area of the coast and often interpolating between profiles. However, the cost in manpower and time increases as more profiles are taken. The radar waterline technique allows the user to extract multiple profiles from a desired location and analyze their evolution over a long period of time or extract a single profile to use in further processing or as model input.

Figure 6.13a shows an area of the intertidal flats to the East of Hilbre Island that was extracted in order to sample several cross-shore profiles to demonstrate changes in these profiles over three years. Figure 6.13b shows this area rotated, such that each row

in the matrix is a cross-shore profile and each column is an alongshore profile, the locations of four transects (T 1-4) are also shown.

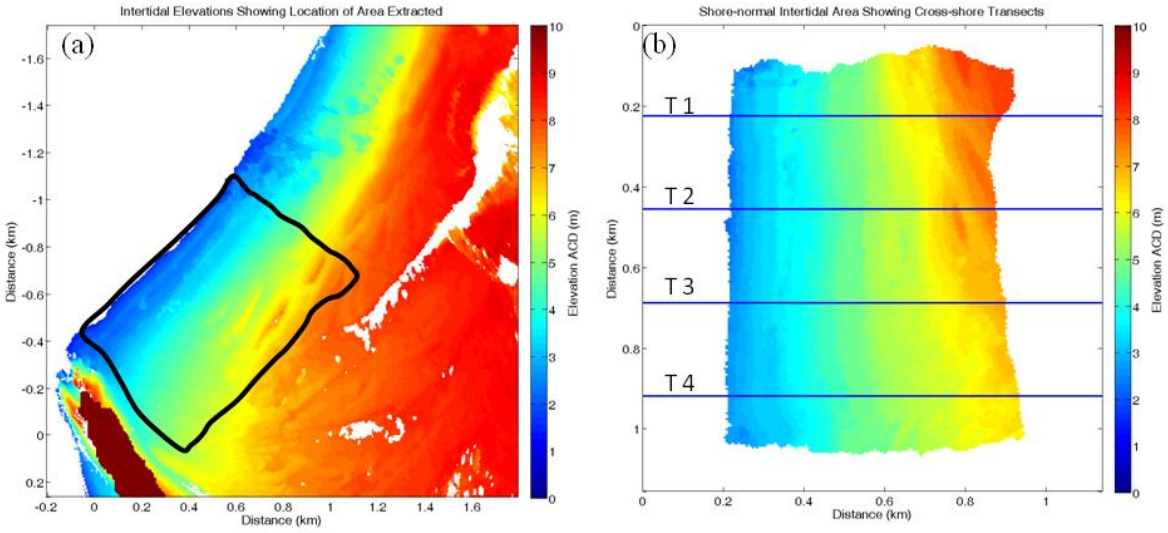

Figure 6.13: (a) Radar-estimated elevations with location of extracted section (b), extracted section rotated and the extracted cross-shore transect locations indicated.

In order to examine changes in transect elevation throughout the three-year study period, these transects were arranged into timestacks shown in Figure 6.14 with time on the y-axis, cross-shore distance on the x and elevation from ACD on the z-axis. Figure 6.14a shows these timestacks as a mesh and qualitatively shows the variations in elevation as bedforms migrate and erosion or accretion affects the profiles. The migration of these sedimentary features is more clearly seen in Figure 6.14b, particularly the linear migration of a bedform crest is evident in Transect 2. Two clear

crests are present in early 2006 and their progression in a shoreward direction captured. During winter 2007 it is clear that these crests are eroded and flattened to some extent. In the spring the crests build up again and resume shoreward migration before appearing to weld onto the beach during 2008. There is also a clear cyclicity to the erosion and accretion of these transects that is most evident in transects 3 and 4 demonstrating clear erosion in the upper, shoreward regions of the profiles during autumn and winter and subsequent accretion in the summer. This seems to support trends in sedimentary volume and elevation seen in earlier sections. The absence of linear bedform crests in transects 3 and 4 could be a result of their sheltered situation in lee of Hilbre Island reducing their exposure to wave action. Mean wave energy density figures are also calculated using data from the CEFAS Wavenet offshore buoy (details given above) these values are derived from the mean significant wave height over each two-week period corresponding to those of radar data collection. Intuitively, it is evident that the periods of highest wave energy correspond to those of greatest erosion on the cross-shore profiles.

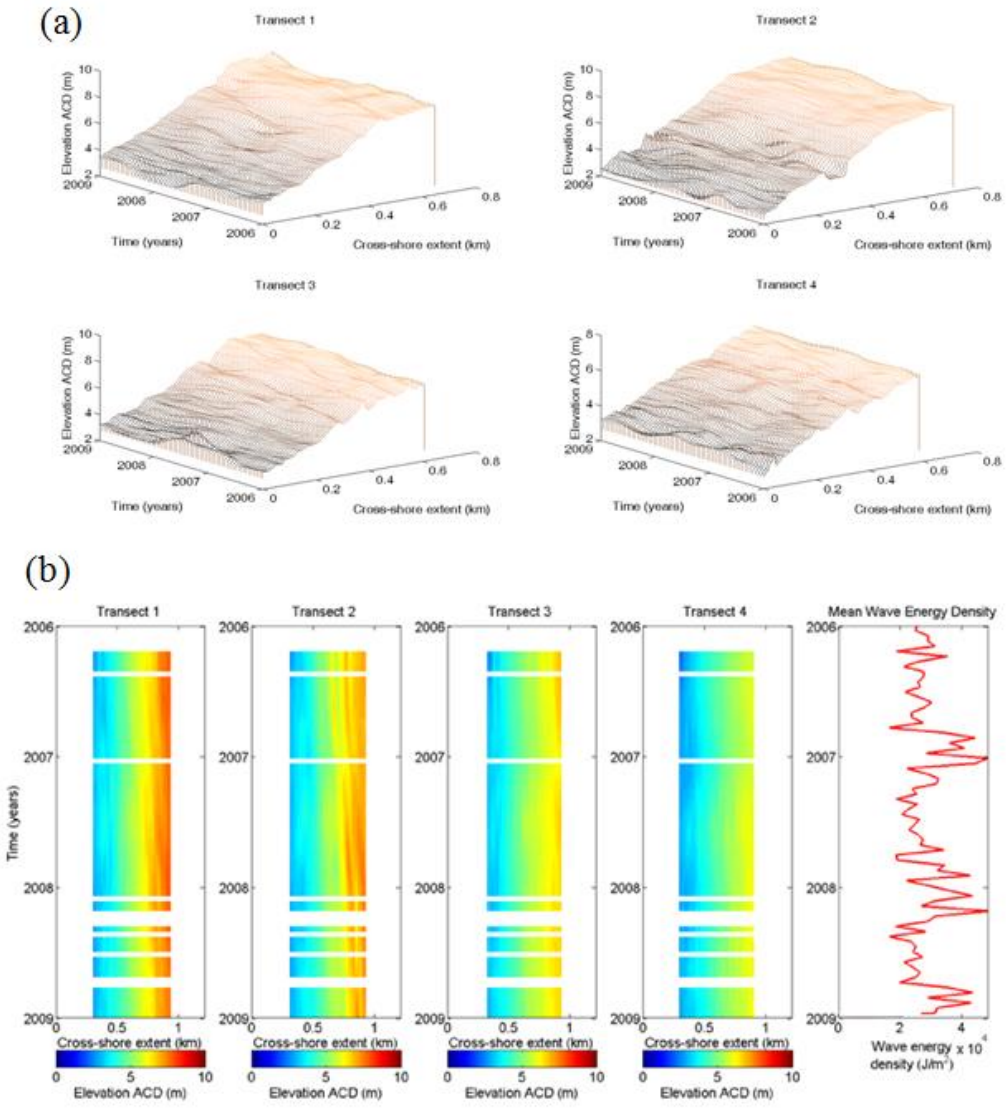

Figure 6.14: (a) Surface plot timestacks showing patterns of cross-shore profile evolution for the NW Wirral beach through 2006 - 2009. (b) Image timestacks colour-coded by elevation. Plots show cross-shore extent along the x-axis, time on the y-axis and elevations on the z-axis also shown are wave energy density figures for the corresponding time periods during the survey campaign.

Figure 6.15 shows two transects extracted from the above timestacks, April 2006 (red) and January 2007 (blue), these transects clearly illustrate the loss of material from the central regions of the profile and a corresponding shallowing of the beach towards the lower regions of the profile reflecting transfer of material offshore with increased wave energy in winter/autumn seasons. The boundary of the switch between erosion and accretion is marked on the figure below.

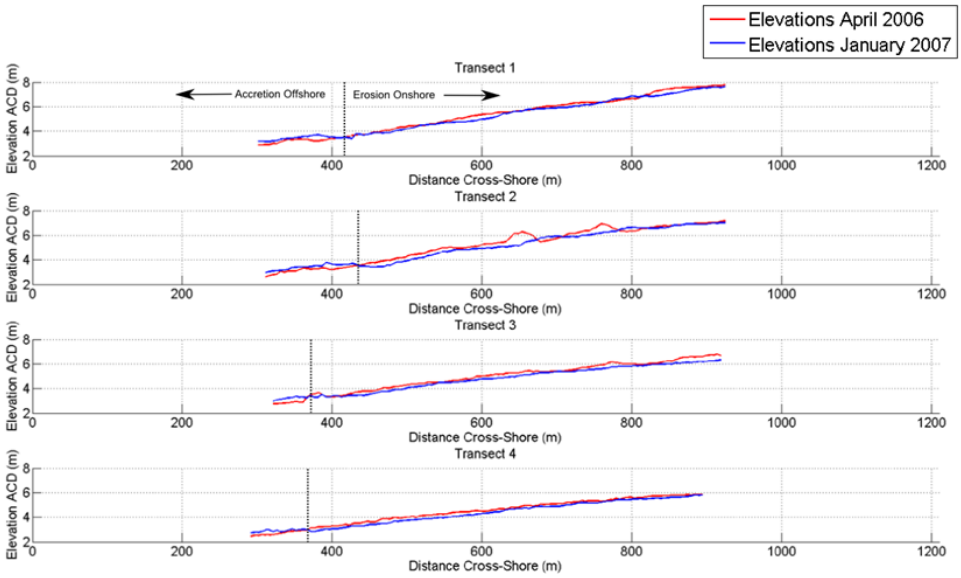

Figure 6.15: Cross shore profiles from April 2006 (red) and January 2007 (blue) illustrating net change in elevation from summer to winter seasons. Black dashed line indicates transition point between erosion and accretion along each transect.

6.7 DISCUSSION

6.7.1 Radar Remote Sensing Capabilities

The application of the radar waterline method developed by Bell et al. (2016) to the problem of intertidal morphological monitoring has been investigated in this contribution. Several sites within the intertidal area of the Dee estuary northwest UK were selected in order to explore their change in morphology in detail and with a resolution that would not have been possible using already established techniques. Significant changes in waterline (and therefore implied underlying bed elevation) were observed at both sites selected. At Site A, West Hoyle sandbank, large bedforms can be seen migrating across a relatively stable bank that is likely anchored by underlying geological structure. This is consistent with the theory that the Dee is an estuary approaching overall equilibrium, but with significant variations across an annual cycle the cyclicity of patterns of local sediment flux as evidenced in**Error! Reference source not found.** Figure 6.6a and Figure 6.6b.

The ability to monitor sediment movement, in addition to overall erosion or accretion of sandbanks in an estuarine setting, has a wide range of important applications in coastal management. In addition, sandbank systems often provide natural coastal defences attenuating incoming wave activity and, as such, often bear the brunt of high energy events, suffering degradation and erosion (Hanley et al., 2014). Many beach nourishment schemes aim to replenish material lost to erosion and, thus the presented

technique for monitoring intertidal areas could provide a cost effective and robust option for the long-term assessment of the effectiveness of these schemes.

Hard engineering at the coast and capital dredging for port and coastal infrastructure construction require detailed and comprehensive information on intertidal and nearshore bathymetry. Figure 6.16 shows a schematic of the remote sensing capabilities of marine radar remote sensing at this point in time, describing different physical phenomena that can now be observed and the different spatial and temporal scales these phenomena operate over. The nearshore and intertidal processes described in the central area of Figure 6.16 can be observed using a combination of the method used in this contribution and other bathymetric determination methods, chiefly a wave inversion technique (Hessner and Bell, 2009; Bell and Osler, 2011). This combination could allow a single marine radar to act as an integrated survey system providing sub- and intertidal bathymetry with good spatial and temporal resolution. In addition to bathymetric measurements, other marine radar data processing techniques are also capable of resolving surface currents (Bell et al., 2012), directional wave spectra and significant wave heights (e.g. Nieto-Borge and Guedes-Soares, 2000), and wind direction (Dankert, 2003; Dankert and Horstmann, 2006).

.

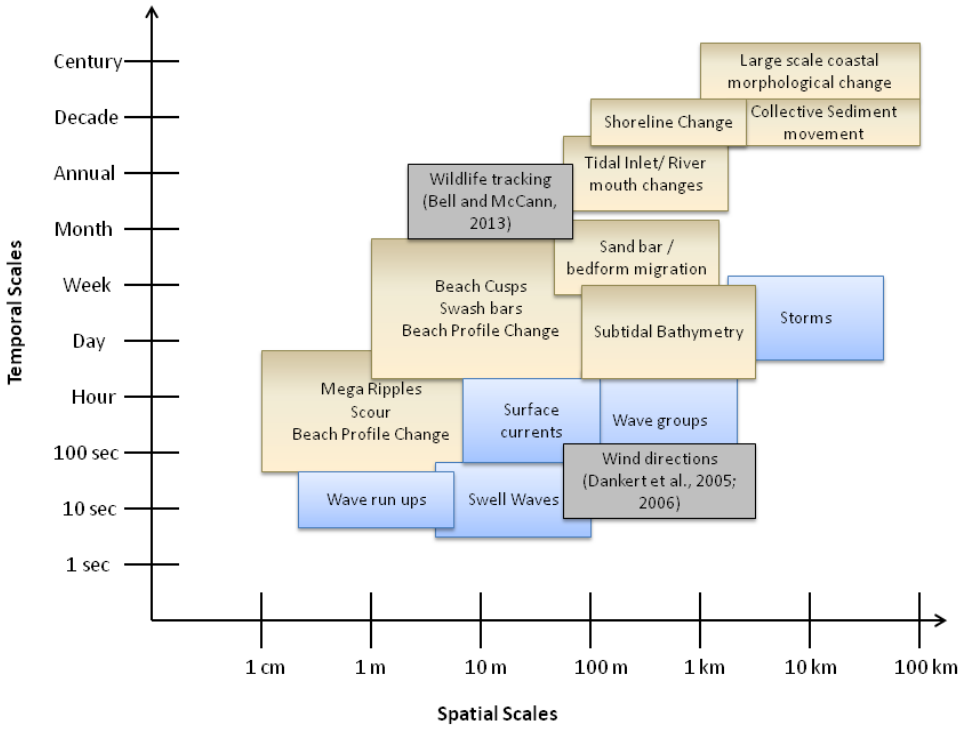

Figure 6.16: Schematic of current marine radar remote sensing capabilities showing the spatial (x-axis) and temporal (y-axis) scales over which these processes can be observed.

6.7.2 Integrated Data Source for Coastal Morphological Monitoring

It is clear the remote sensing capabilities of marine radar are diverse and extremely well suited to applications in areas that are difficult to survey with traditional methods, filling many required gaps in contemporary nearshore observation. A combination framework of the above-described monitoring techniques would provide a comprehensive and detailed dataset. These data would give an overview of environmental forcings, processes and impacts over a significant spatial scale. Currently it seems that monitoring

systems are deployed on an ad hoc basis, with the technique that is able to observe the phenomena best being deployed at scientifically significant, vulnerable and/or high value industrial/infrastructure areas, over relatively short timescales and short durations due to funding constraints.

The combination of data would be well suited to a long-term deployment with the aim of identifying shifts in the dominant regimes at a given coastal environment due to the efficient costs (low manpower and maintenance requirements) of marine radar as a remote sensing platform. With detailed information on erosion/accretion patterns and sediment migration trends (along with other information provided by marine radar), it may be possible to automate an observation system to provide advanced warning changes in morphology that would affect aspects of management. For example, highlighting critical vertical changes in beach elevation that may alert users to altered beach gradients or extents that, in turn, affect wave run-up characteristics and influence the robustness of flood defence structures. Another aspect that could be semi-automated is the tracking of sedimentary bedform movement, potentially providing advance warning on the compromise of navigation channels.

6.7.3 Coastal Infrastructure Analytics; Utilising Integrated Data

Analytics is a set of techniques that is commonly defined as a subset of business intelligence and is used effectively in large corporations to make 'data based' decisions rather than relying pure on instincts and past experiences, which often do not hold up well in dynamic environments. This practice has recently been applied to the

management of urban infrastructure, spatial and temporal analysis in urban planning is a well established discipline, however the use of "Big Data" combined with robust analytics have enabled city planners to better optimise the utilisation of existing infrastructure such as transport (Giffinger et al., 2007) and more effectively plan the inevitable expansion of urban infrastructure. Models and analytics using data such as transport loads and storage capacity, energy usage cycles, school and hospital population, housing levels in addition to detailed demographics of a given city or conurbation are being utilised to create "Smart Cities" (Caragliu et al., 2011). This system allows planners to cope with increasing demand on services and pressure on limited infrastructure in a more efficient manner than previously, due to the large amount of data support and the real time updates of critical data.

The authors believe that elements of this technique can be readily translated to the planning and management of both existing and future development of coastal infrastructure and use of resources. If the integrated coastal data can be treated in a similar manner to the extensive marketing data used in business analytics where the data can be fed into customised models and decision-support tools, delivering succinct and reliable information to coastal managers. The integrated and long-term nature of the collected data will give a better appreciation of the behaviour of the coastal system being observed, this is a clear advantage over the traditional short term surveys. Applying this technique to coastal management would require a set of standardised methodologies to be established, as outlined below in Table 6.2.

Sensing the coast
The initial consideration in any analytics campaign is the acquisition of a diverse and robust dataset. As already discussed, various remote sensing techniques provide ideal tools in gathering these data, with a marine radar deployment providing a good foundation. The data from these observations must be easily accessible to the relevant management organisations.
Visualising the coast
Visualisation is a vital first step in analysis, allowing interesting and dynamic areas to be identified and their vulnerability and impact of potential changes to be qualitatively assessed. At this point, there may be a need to more targeted surveying or data collection over a finer spatial resolution. These new data would feed into the integrated analysis framework.
Analysing the coast
At this stage detailed quantitative analysis can be performed on the dataset, deriving detailed hydrodynamics and morphodynamic information about a given region of coastline. These data can be collected and synthesized with relative ease when compared to disparate and uncoordinated survey campaigns.
Management and adaptation of the coast
The data gathered up to this point may be fed into decision support tools and distilled into reports and distributed to the relevant coastal stakeholders, authorities and management organizations. A web-based platform is the ideal dissemination method for this type of information.

Table 6.2: Theoretical high level methodological framework for coastal infrastructure analytics using integrated coastal data.

6.8 METHODOLOGICAL IMPROVEMENTS AND FURTHER WORK

The methodology presented shows itself to be aptly suited to long-term morphological monitoring. Significant improvements can potentially be made through several means, the first of which is an increase in the temporal resolution of the input time exposure images. Currently time-exposure images are processed hourly and, given the large tidal range in the Dee, the tidal elevation can change significantly within an hour. This could result in certain elevations being omitted from the analysis as the image sequence has insufficient temporal resolution to capture the whole transition of the tidal range. The issue could be alleviated by processing time-exposure images every 15 minutes, capturing more of the waterline progression through the image sequence. Future deployments at different sites will indeed feature this development.

Further improvement maybe made by the application of more advanced image processing and filtering techniques to the basic input image data. The objective of these techniques would be primarily two-fold: (i) to reduce over exposure and excessively high pixel intensities at short ranges (due to radar power saturation), (ii) to increase intensities at longer ranges, alleviating radar power drop off. In addition, reducing the noise of sea clutter in the subtidal area would serve to prevent many false waterline elevation acquisitions in these areas. Algorithms to accomplish these aims are currently under development. These techniques have been omitted from work so far due to their early stage of development and in order to demonstrate the inherent robustness and wide applicability of the radar waterline method at this relatively early stage of development.

In order to improve the method's application to tracking the changes resulting from instantaneous events, such as storms or other wave events, the temporal resolution must be increased. As discussed earlier it is possible to use a moving window type analysis to reduce the time between surveys. It is also possible to run an analysis over one week of data instead of two providing that the start and end times are synchronized with a spring and a neap tide correspondingly. This shorter analysis, however, gives the waterline matching algorithm less wet/dry transitions to lock onto and thus can reduce correlation coefficients and overall quality of results.

In order to directly increase the accuracy of waterline elevations derived with the radar method, the difference between absolute waterlevel and bed elevation must be either accounted for or directly identified. In areas of ebb tidal water pooling, little can be done to deterministically predict the difference in elevation without the use of full tidal propagation model with a high spatial and temporal resolution. Therefore the automated detection of areas where the phenomenon is likely to occur, and the highlighting of spurious elevation results in the these areas is necessary. In many areas where a moderate over-estimation of elevations by the radar method in the range of 20-50 cm is seen, this difference is likely a result of wave setup and run-up. If sufficient data on the local wave climate can be gathered through the radar, using a local in situ instrument, or modelled with SWAN, then an estimate of the wave setup and run-up contribution to absolute waterlevel can be made, and subtracted from the radar derived elevation.

6.9 CONCLUSIONS

A novel radar waterline survey method is applied to the difficult task of monitoring intertidal morphology over long periods of time. Data were collected using a standard marine radar operating at X-band (9.4 GHz) with a 3.83 km radial range from an installation on Hilbre Island. These data were used to create a series of time-exposure images and the pixel intensities from these images used as input to a matching algorithm along with a record of tidal elevations in order to estimate a waterline elevation above ACD for that individual pixel. Just under three years of data were processed, producing a survey of elevations every two weeks (where possible).

These assessments of morphological change exposed the dominant trends of volumetric change at both sites indicating a trend of sediment loss (Figure 6.6) in autumn and winter and subsequent accretion in spring and summer for West Hoyle sandbank and the NW Wirral beach respectively (Locations in Figure 6.3). These study sites also exhibit an increase in mean beach face elevations during the accretion periods and an overall flattening of the area during periods of erosion (Figure 6.9, Figure 6.11). This potentially indicates overall trends of sediment erosion by means of stronger wave events during winter; these wave events also serve to flatten bedforms. In the summer, wave conditions are more stable (indicated by records of daily significant wave heights from a nearby waverider buoy shown in Figure 6.6c) allowing the tides and currents to re-establish bedforms and rework sediment back onto the beaches.

Within the radar dataset there are several months of data where the radar was set to collect data to an extended range of 7.5 km with a spatial resolution of 10 m per pixel. These data are currently being processed to explore the wider patterns of erosion and accretion in the Dee estuary in support of the findings presented here.

The radar waterline method thus offers a tool for monitoring intertidal morphology over long periods of time and large areas. While vertical differences compared to a LiDAR are currently up to several decimetres, the good temporal resolution of the radar survey technique allows repeat surveys to quantify morphological change over large areas. The high temporal resolution potentially allows the technique to be applied to the tracking and measurement of sedimentary bedform migration. In addition to providing data to validate modelling efforts and to support other survey techniques in large-scale survey campaigns or act as a stand-alone sensor allowing other data processing methods . Routine collection of data such as these repeated wide area intertidal surveys was not previously possible with marine radar and is not possible using other remote sensing techniques. The application of this radar-based technique may significantly improve the situational awareness of coastal managers prior to large scale engineering project, and provide stakeholders with better long-term information on the overall 'health' of a given shoreline as conditions change or as maintenance projects progress.

6.10 ACKNOWLEDGEMENTS FOR CHAPTER 6

Thanks are due to many organizations and individuals for their contribution to this work. The author would like to extend gratitude firstly to the *Centre for Global Eco-Innovation (CGE)* through the *European Regional Development Fund (ERDF)* and *Marlan Maritime Technologies* for funding Cai Bird's PhD studies of which this work is a constituent part. The radar data used in this contribution were collected by the *National Oceanography Centre (NOC) Liverpool* under the umbrella of the *Liverpool Bay Coastal Observatory* and was funded by the *UK Natural Environment Research Council.* Thanks are also due to the Wirral Borough Council Ranger service, specifically the former Hilbre Island range Mr. David Cavanagh who assisted in deployment and maintenance of a remote system in a challenging environment.

7 LONG RANGE RADAR SURVEYS AND APPLICATION TO PORT ENVIRONMENTS

7.1 REQUIRMENT FOR LONG RANGE SURVEY

7.1.1 Radar Range Resolution

Current radar-derived intertidal surveys from the River Dee estuary have been shown to robustly derive waterline elevations with a radial range of ~4 km extending from the radar antenna. These radar data were collected by a radar system set to short pulse. As discussed in Chapter 3, the maximum effective range of a radar system can be estimated using the Radar Range Equation, however many systems operate at much shorter ranges. The range resolution determines the ability of a system to detect individual targets closely spaced along a given bearing, heavily affecting the possible spatial resolution of the final radar image grid and ultimately the topographical survey

produced. Range resolution S_r is largely dependent on pulse length τ and speed of light in air c_0 by:

$$\mathbf{S_r = \frac{c_0 \tau}{2}} \qquad \mathbf{(31)}$$

Marine radar systems frequently operate within ranges much less than their maximum range and use some measure of pulse compression in order to alter the radial range resolution of radar pulses. By changing the sampling frequency and thus the pulse length, the ability of a radar to resolve cross-range targets can be varied.

Data from the Hilbre Island radar installation were sampled at a sampling frequency (*fs*) of 40 MHz, giving a pulse length of 2.5×10^{-8} as $\tau = 1/fs$. The speed of light in air is used here (299.7×10^6 m/s) rather than the speed of light in a vacuum as using the value of c in a vacuum makes a difference of several metres at longer ranges and would introduce erros in further processing. This gives an S_r (pixel resolution) of ~3.75 m and a range of ~3.83 km with 1020 samples along the radial axis. These data were then sampled onto a 5 x 5 m grid during scan conversion.

Data collected from Hilbre from May 2007 through to December 2008 were also sampled at short pulse length but more cross-range samples were taken allowing data to be collected from longer ranges out to a maximum range of 7.5 km. These data were transformed onto a 10 x 10 m grid during scan conversion, effectively doubling the range over which radar image data were collected.

Figure 7.1a shows radar data collected in polar coordinates at short range and a single pulse extracted with a greater range resolution than the pulse taken at the same angle from long range data (see Figure 7.1b).

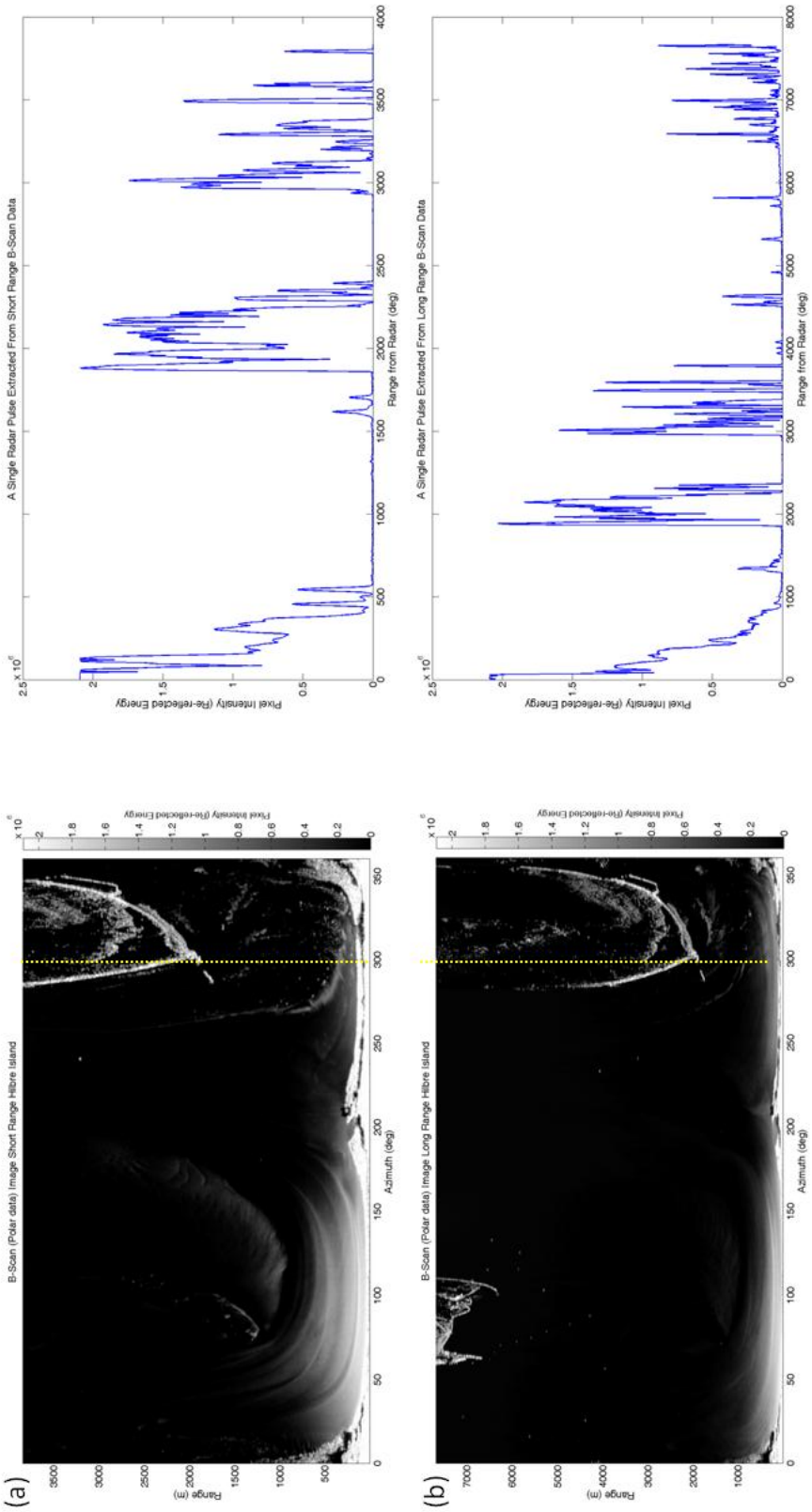
A Single Radar Pulse Extracted From Short Range B-Scan Data
Pixel Intensity (Re-reflected Energy
Range from Radar (deg)
A Single Radar Pulse Extracted From Long Range B-Scan Data
Pixel Intensity (Re-reflected Energy
Range from Radar (deg)
(a)
B-Scan (Polar data) Image Short Range Hilbre Island
Range (m)
Azimuth (deg)
(b)
B-Scan (Polar data) Image Long Range Hilbre Island
Range (m)
Azimuth (deg)

Figure 7.1: (a) Short-range polar image data with look angle (°) (Azimuth) on the x-axis and range from the range antenna (m) on the y-axis. The yellow dashed line indicates image pixel intensities (a function of re-radiated energy received by the antenna) along a single pulse from the radar with a range resolution of ~3.75 m. (b) Long-range image data with the same dimensions as (a), and a single pulse extracted along the same angle (300°) with a decreased cross-range resolution of ~7.5 m.

It is clear that in Figure 7.2a that the finer range resolution allows more detail to be resolved at short range while in Figure 7.2b more of the surrounding area is imaged but with decreased resolution. Figure 7.2a displays the short-range radar data scan converted onto a 5 x 5 m Cartesian grid, and Figure 7.2b illustrates the long-range data after scan conversion onto a larger Cartesian 10 x 10 m grid.

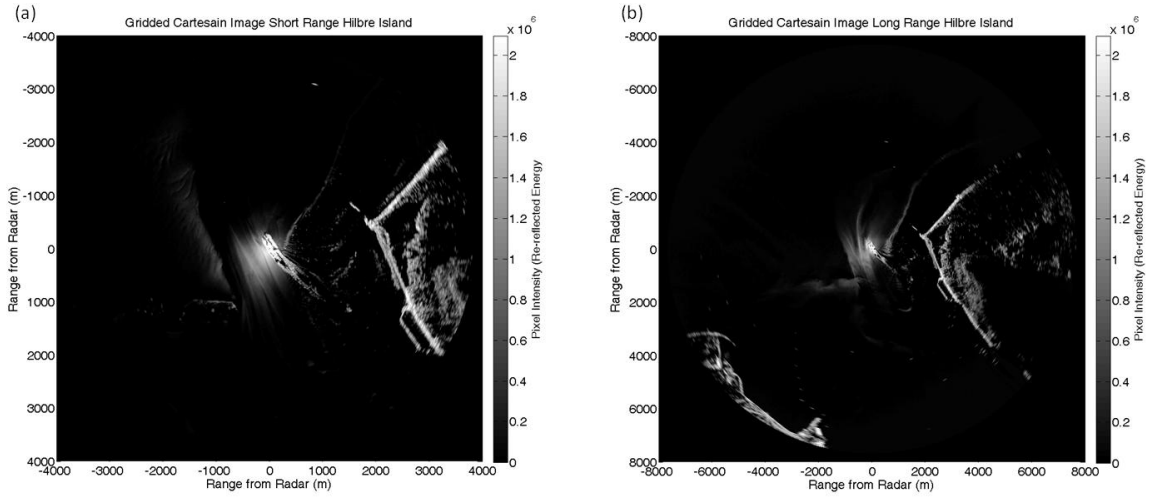

Figure 7.2: (a) Cartesian radar image with ~4 km max range and 5 m spatial resolution (b) Cartesian radar image with 10 m spatial resolution and ~7.5 km max range.

7.1.2 Motivation for Long-Range Waterline Survey Experiments.

While the short-range survey resolves a relatively large area by comparison to other survey techniques, in many locations, there are extensive intertidal areas lying further offshore than 4 km. In the Dee estuary (Figure 7.3) the short-range survey covers most of the West Hoyle sandbanks and much of the intertidal flats, and East Hoyle sandbank. However if the range is extended to 7.5 km, indicated by the second black concentric ring, a much larger area can be observed (albeit at a lower spatial resolution). The entirety of West Hoyle sandbank is observed by the radar, as is the offshore lobe of the East Hoyle sandbank to the north. In addition the survey extends to the Point of Ayr to the west, Salisbury Bank to the south along with Mostyn Port and the nearby mud banks to the southeast.

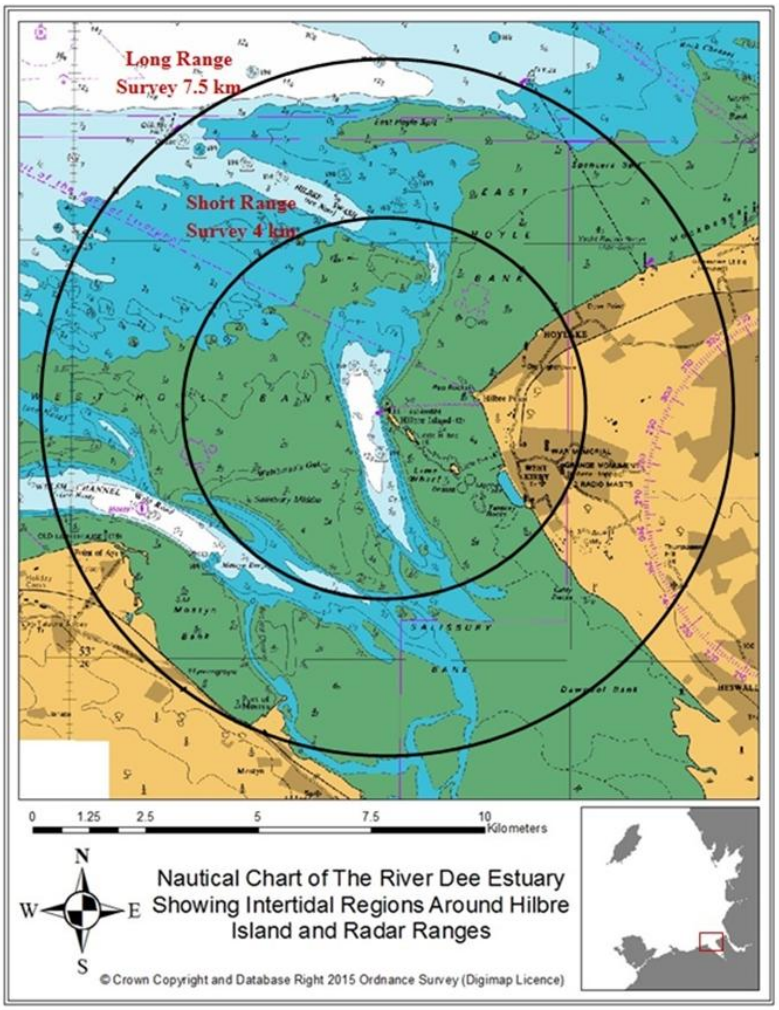

Figure 7.3: Nautical navigation chart of the Dee estuary showing radar survey range extents for both short and long-range surveys (black concentric rings) Chart data from SeaZone Solutions Ltd (2015).

It has been demonstrated that there is a trade-off between range resolution and survey range, in that distance between pixel samples is decreased at shorter ranges. This can be a significant issue if the data are used without further processing. However during the scan conversion process the desired Cartesian grid size is able to be explicitly defined

with a different size to the range resolution. For example the short-range data with a 3.75 m resolution are converted onto a 5 m grid using a degree of spatial averaging. It is also therefore simple enough to transform long-range data with a 7.5 m resolution onto a 5 m grid. Intuitively, target detection and object resolution will be less accurate when using this technique, but it does allow effective continuity between datasets sampled using a different pulse length or at different ranges, as is demonstrated in Chapter 6.

7.1.3 Extending the Range of the Radar Waterline Method

The methodology for surveying intertidal areas at longer ranges remains identical to that applied to the short range data, (see Chapter 5). The data, having been transformed onto 10 m Cartesian grids, were temporally averaged over ten minutes (256 images) forming time-exposure images (Figure 7.4). Key features of the Dee estuary are highlighted on Figure 7.4 including the location of Hilbre Island and the radar, morphological features, locations on land and landmarks within the Dee.

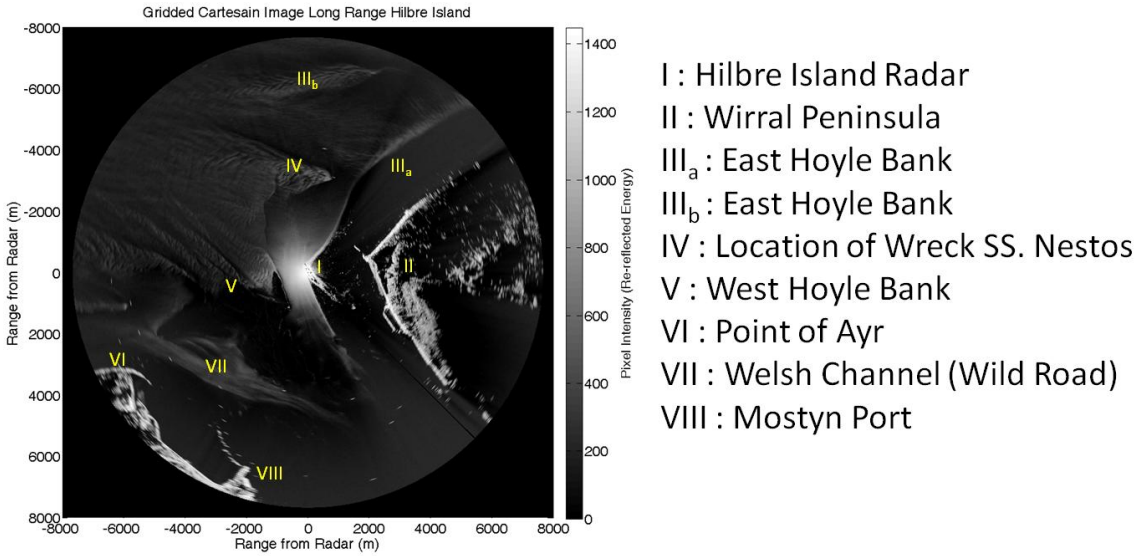

Figure 7.4: Time exposure image of long-range radar data within the Dee estuary with locations of interest marked.

7.1.4 Early Long-range Survey Attempts and Issues

The methodology described in Chapter 5 was applied to the long range data. Two weeks of data with time exposure images collected hourly from 28 October 2008 to 11 November 2008 were used to generate results shown in this section. Initial attempts to derive long-range survey elevations utilised the radar waterline technique with very few alterations. The unfiltered results are seen in Figure 7.5a, which displays maximum correlation coefficients between the recorded pixel intensity over two weeks and the gradient of a series of tidal pulses reflecting the pattern of wetting and drying at that pixel location. Stronger values of correlation coefficient reflect better confidence in the derived elevations seen in Figure 7.5b; these areas tend to be associated with stationary features such as rocks.

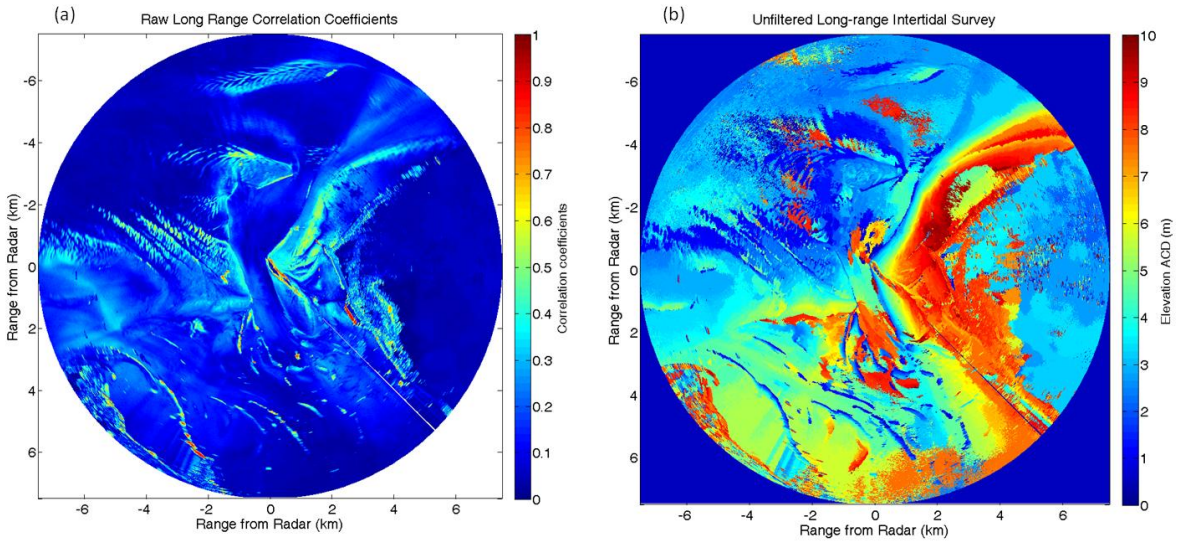

Figure 7.5: (a) Correlation coefficients indicating confidence of elevation estimate at each point based on matching between fluctuating pixel intensity and tidal gradients. (b) Raw unfiltered long range radar-derived elevation estimates.

Clearly, these results require significant filtering as the subtidal areas still see fluctuations in pixel intensity and therefore their maximum correlations are often still able to associate a waterline elevation with that location. These elevations should have weaker correlation coefficients due to their fluctuating pixel intensities not being caused by changing tidal levels, but more a function of changing wind direction relative to the radar, wave heights, wave angle and rain interference throughout the two-week analysis period. By defining a correlation threshold, below which elevation results are deemed unacceptable, most of these results in subtidal areas can be effectively filtered out. Figure 7.6a shows the correlation coefficients after having a threshold of 0.3 applied (as

described earlier this is an arbitrary threshold which subjectively filters the pixels in subtidal areas), the white regions indicate unused low coefficients and the corresponding elevations have been removed in Figure 7.6b.

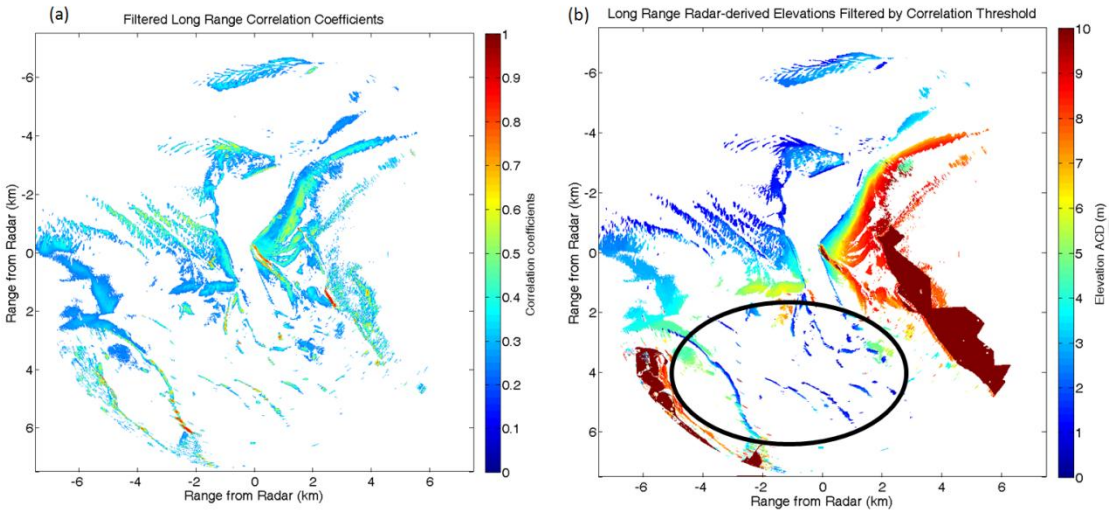

Figure 7.6: (a) Correlation coefficients with 0.3 threshold applied, (b) elevations filtered by correlation coefficient threshold. Black ring indicates a series of shallow features suggestive of channel margins.

There remain some elevation results in areas which are clearly subtidal and that show relatively high correlation coefficients. These spurious elevation results appear to be randomly distributed and are seen both at relatively short range, to the southwest of Hilbre Island, and at longer ranges, especially to the west within the Welsh Channel. Also, an interesting series of features can be seen to the south, these relatively linear features mark the edges of the navigation channels leading through Salisbury Bank in the centre of the estuary. These channels connect the canalised River Dee from Chester and Broughton to Mostyn Port and the Welsh Channel. A prominent arced ridge to the

southwest delineates the edge of Mostyn Bank. This bank is a relatively flat and stable mud bank in stark comparison to the topographically varied and dynamic sandbanks in the rest of the estuary. Mostyn Bank transitions into the Point of Ayr, a sandy headland feature to the west of Hilbre Island.

7.1.5 Refinements and Progression

In order to assess the performance of the initial long-range surveys, the radar-derived elevations from November 2008 were compared to a LiDAR survey carried out on 8 October 2006. There will be significant changes in elevations that have occurred between these two dates (as evidenced in Chapter 6) and therefore significant inaccuracies are expected. However, it is instructional to compare these two methods of surveying in order to determine problem areas where the difference in elevation is clearly due to more than annual variations or morphological processes. Elevations from LiDAR survey and the long-range radar survey are shown in Figure 7.7.

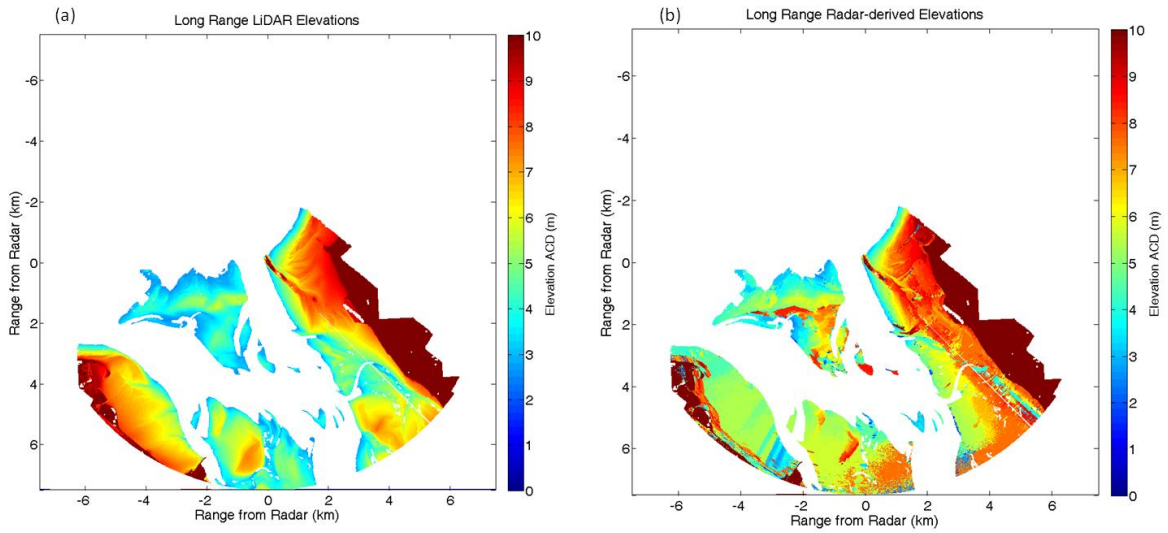

Figure 7.7: (a) Long-range LiDAR elevations above ACD surveyed on 8th October 2006 showing intertidal areas in the Dee estuary mouth. (b) Radar-derived elevations at available LiDAR survey points showing elevation above ACD.

From Figure 7.7 it is notable that the LiDAR survey does not extend to the north and the outer regions of the estuary mouth as the radar does, therefore many of the points derived by the radar cannot be validated using this comparison. This also highlights an advantage of the radar methodology, specifically that LiDAR surveys must fly along very strictly defined flight paths in order to capture the area of interest, and complete the flights within a predefined time window at low tide. This makes the surveying of nearshore intertidal areas and morphologically significant sedimentary features such as sandbanks more challenging due to the large distances involved.

A comparison between these two survey techniques yields residuals shown in Figure 7.8. The land areas to the east and west show large differences which can be ignored due

to the obvious lack of topographical elevations derived by the radar on terrestrial areas that do not experience wetting and drying. Broadly these residuals are indicative of a large degradation in radar-derived elevations at extreme ranges when compared to the LiDAR results. Mostyn Bank to the southwest shows significant >1 m under-estimations of elevation by the radar; the saltmarsh areas to the southeast are over-estimated in elevation significantly in addition to large parts of the central and south-central estuary that are also over-estimated.

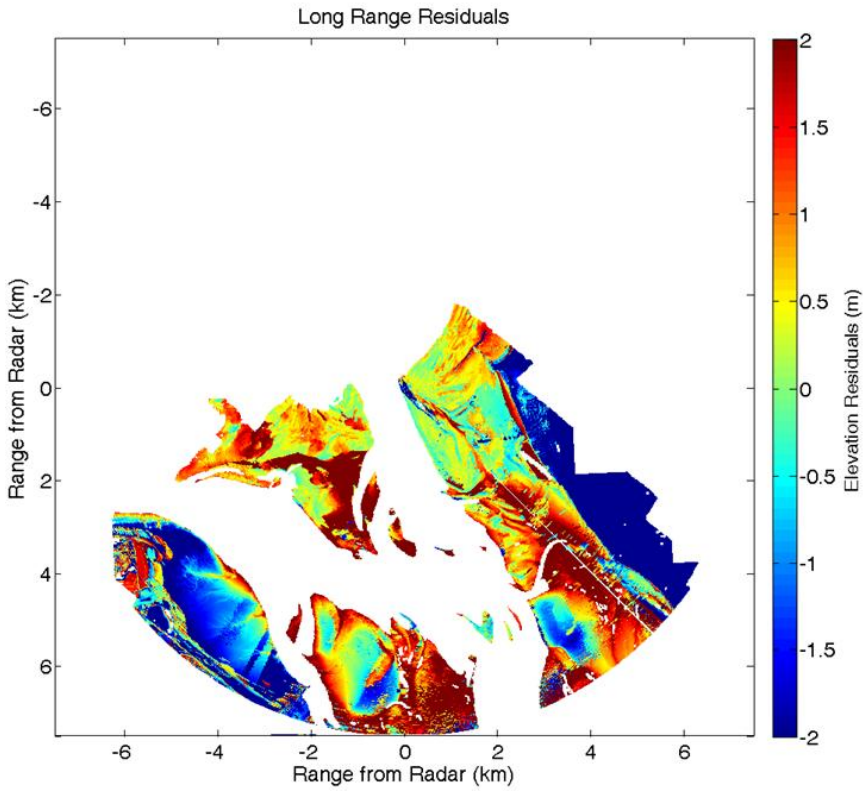

Figure 7.8: Residuals between radar-derived elevations from November 2008 at long range and LiDAR survey elevations from October 2006 in the Dee estuary.

The poor elevation estimates in these areas are likely an exacerbation of the pooling water effect described in Chapter 5, further planned work includes the development of methodologies able to discern areas subject to water pooling. The tidal record is measured by a tide gauge deployed on Hilbre Island. As the tide rises, the waterline elevation is accurately represented by the tidal curve in areas close to the Island; however further upstream into the estuary, the topography becomes more complex. As the tide turns and begins to ebb, the water can remain trapped behind, and pooled within large sandbanks and the varied topography of the intertidal area. In effect, this causes a large offset between the tidal waterline elevation measured at Hilbre and the actual real world waterline elevation which the radar continues to image, resulting in an over-estimation of elevations by the radar. This effect is also exaggerated by the phase lag in tidal propagation, that is, the difference in time it takes for the tide (and the associated waterline elevation) to travel 7.5 km (in this case) from the location at which it is measured on Hilbre Island to the point being sampled. Addressing this by incorporating a 2-D spatial water surface elevation model is a key part of planned future work. An alternative to using a model would be to deploy several in-situ elevation sensors at different points across the survey domain and use these to establish the differences in tidal elevation due to spatial variation.

A selection of techniques can be used to improve the accuracy of radar-derived elevations, some of these techniques were applied to data used in chapters 5 and 6. Instead of using correlations from a single two-week analysis period to filter unacceptably low correlation coefficients, an alternative is to use the mean correlations of several survey periods. This has the effect of reinforcing areas with consistently

strong correlations whilst suppressing sporadic high correlations that can occur in subtidal areas as demonstrated in Figure 7.9.

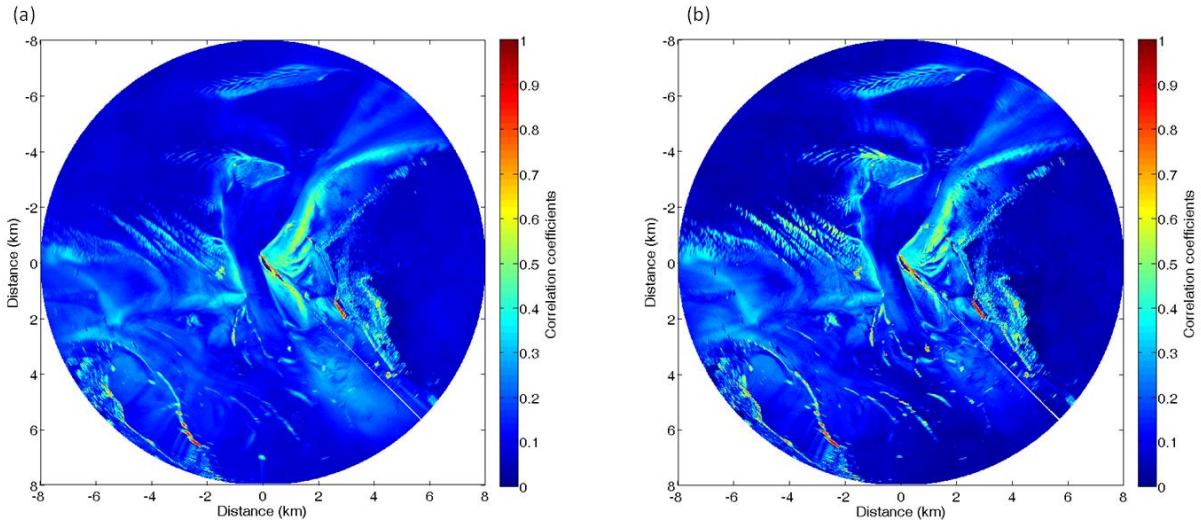

Figure 7.9: (a) Averaged correlations over long-range survey period and (b) raw correlation coefficients from a single two-week analysis period.

Spatial smoothing is an inappropriate technique to use in complex beach areas as the topography is rarely linear or predictable and assuming so can lead to significant errors during further processing (Holman and Bowen, 1979). An alternative to spatial smoothing is temporal smoothing, however this smoothing must be weighted by the correlation coefficients at each timestep. The robust smoothing technique developed by Garcia (2010) was applied to a vector made up of elevation values from each x , y coordinate and at each two week survey period t. The signal of extracted topographical elevations $\eta(_{x,y,t})$ is ideally relatively smooth reflecting gradual changes in elevation, or

indeed sharp changes from high energy erosive events. However the signal is often noisy as a result of low correlation coefficients which can give inaccurate elevation estimates (see Chapter 5 for examples). The robust smoothing algorithm applied to the elevation data uses the Discrete Cosine Transformation (DCT) weighted by the relative strengths of the correlation coefficients at each temporal sample point. The results of using this kind of smoothing can be seen in Figure 5.12 in Chapter 5, this technique was not applied to the data shown in this chapter.

The current two-week analysis period covers a full spring-neap tidal cycle. During this period, however there may be times when external conditions are not favourable to the collection of high quality radar image data. For example, very calm weather may result in smooth sea surface conditions which exhibit more specular reflection of radar energy and less energy returned to the antenna resulting in lower pixel intensities. Additionally very heavy rainfall can obscure the surface clutter, intensities of which are commonly lower at longer ranges such as those seen in the radar data used in this section. These gaps in data collection can cause pixel intensity records to omit or disassociate tidally-driven waterline transitions that are critical to providing an accurate assessment of intertidal elevations. In order to improve on this, longer periods of analysis may be used which will observe several tidal cycles, thereby increasing the number of observed instances where pixels transaction from wet to dry states. With the increased number of transitions available, it is more likely that the matching algorithm will be able to associate a more accurate waterline elevation.

These techniques were attempted on a series of long-range radar surveys but failed to improve results by any significant margin, highlighting underlying issues with this long-range data that are explored in the following sections.

7.1.6 Shadow Maps at Long Range

As radar range increases, the grazing angle between the projected electromagnetic energy from the radar antenna and the ground surface elevation decreases until reaching 0 at the horizon (if the range is long enough). With this decrease in grazing angle comes an increased amount of area shadowed from the radar line of sight, as even small variations in surface elevation can obscure large areas from sight at long range. It is useful to quantify the area that will be shadowed from the radar during the survey. The shadow map will change with the dynamic topography and, once validated, can be updated in response to the radar-derived elevation surveys. Initially, prior to a radar deployment, a shadow map can be constructed based on a previous topographical survey of the area or estimated from the areas with lower brightness in time exposure images. The shadow masks created in this work were generated based on a LiDAR survey from October 2006. Figure 7.10 shows a shadow mask of the study site around Hilbre Island. The map is constructed using a ray-tracing technique inspired by methods used to establish observer line of sight and collision detection in computer games (Bikker, 2007) and in modelling line of sight for wireless communications (McKown and Hamilton, 1991).

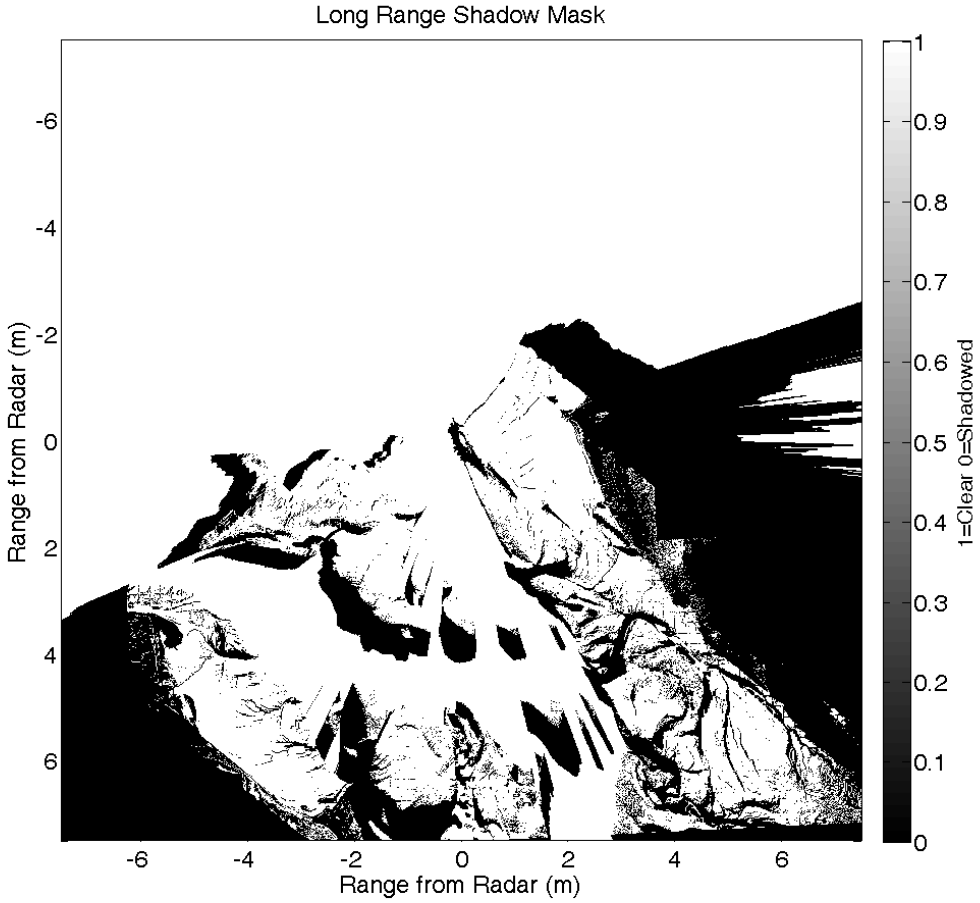

Figure 7.10: Shadow mask showing areas in clear line of sight of the radar antenna at 25m above ACD (1) and areas in shadow (0). Shadows are generated using a ray-tracing method based on topographical elevations observed by the LiDAR survey from October 2006.

This section describes the methodology used to create these shadow maps. It is worth noting that these shadow maps will not absolutely reflect the performance of a radar system as the ray-tracing technique assumes a linear projection of 'sight' which does not truly reflect the behaviour of radio frequency electromagnetic waves (described in

Chapter 2). It does however serve to give a good initial representation of areas which may not yield accurate results due to shadowing.

A line function can be used to represent re-radiated energy from a given point of the topography ($a,b,\eta(x,y)$) back to a radar antenna in a spatially fixed location given by (x_{Radar}, y_{Radar}, h) above the surface. The line of sight $L_{a,b}$ vector values describing the linear descent from the antenna to the surface point can be given by:

$$\frac{\boldsymbol{x}}{\boldsymbol{a}} = \frac{\boldsymbol{y}}{\boldsymbol{b}} = \frac{\boldsymbol{z}-\boldsymbol{h}}{\boldsymbol{\eta}\,(\boldsymbol{a},\boldsymbol{b})-\boldsymbol{h}} = \boldsymbol{p}$$

$$\boldsymbol{x} = \boldsymbol{ap}; \boldsymbol{y} = \boldsymbol{bp}; \boldsymbol{z} = (\,\boldsymbol{\eta}\,(\boldsymbol{a},\boldsymbol{b}) - \boldsymbol{h})\,\boldsymbol{p} + \boldsymbol{h} \qquad \textbf{(32)}$$

Surface elevations are sampled along the same spatial vector as L at a number of points on the surface η, the length N of which is calculated by:

$$\boldsymbol{N} = \sqrt{(\,\boldsymbol{x_{Radar}} - \boldsymbol{x_{\eta}})^2 + (\boldsymbol{y_{Radar}} - \boldsymbol{y_{\eta}})^2} \qquad \textbf{(33)}$$

Figure 7.11 illustrates the concept of retrieval of these vectors, one of which is in a region shadowed from the radar and the other which has clear line of sight. The vector of topographical surface elevations are extracted with i indices as $\eta_{a,b}(x_i, y_i)$ and compared to the values of the radar line of sight vector $L_{a,b}\,(x_i, y_i)$.

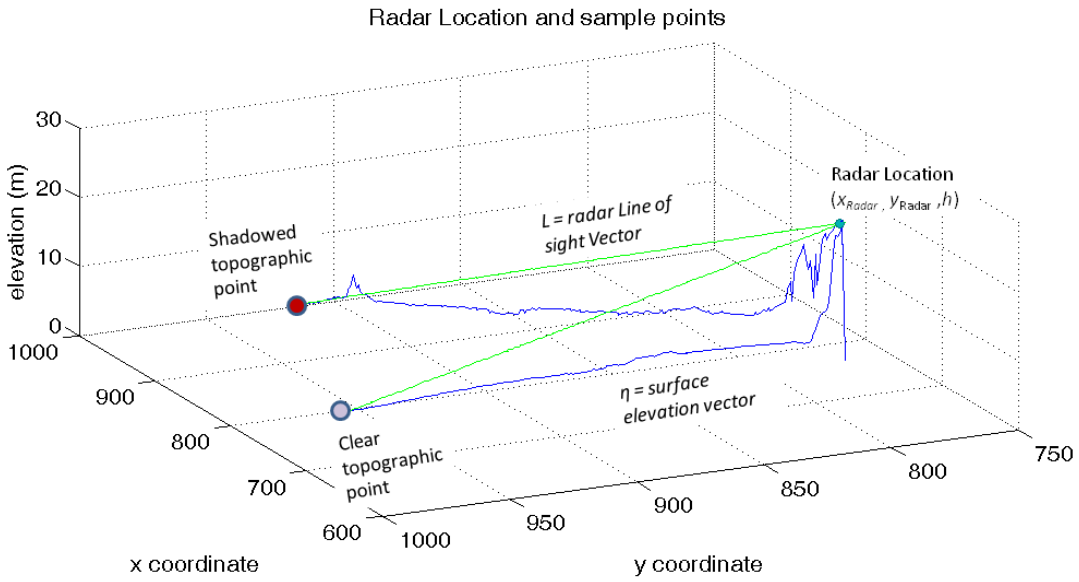

Figure 7.11: 3-D plot displaying representation of intertidal topography, and radar line of sight with several points illustrated, one that is shadowed and one clear.

In order to establish whether a point is shadowed or not, the surface elevation vector η is subtracted from the line of sight vector L. The residuals R can be negative or positive, if any value of R is negative then that point has been obstructed by an intervening feature and that area is potentially shadowed from the radar. Figure 7.12 shows an example of the line of sight and the surface elevations (Figure 7.12a) and the resulting residuals (Figure 7.12b), illustrating that this particular point has clear line of sight and is not shadowed. The point would then be given a binary value of 1 in the final shadow mask as seen in Figure 7.10.

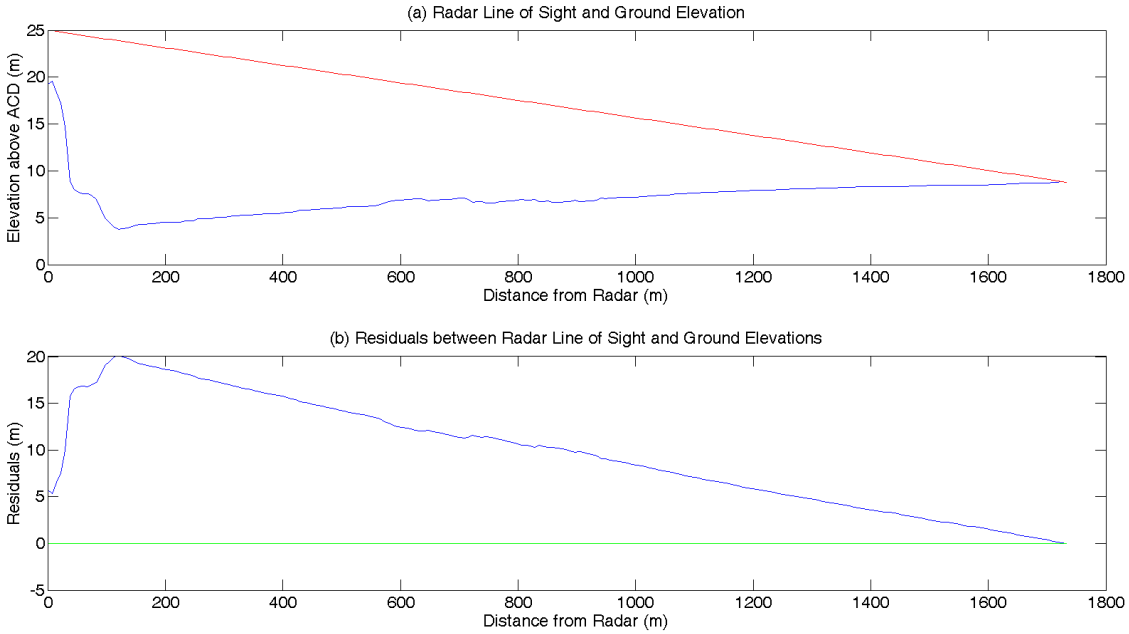

Figure 7.12: (a) Line of sight vector L (red) and surface elevation vector η (blue) showing a transect across a shallow beach gradient to a point around 1.7 km away from the radar. (b) Residuals R after η has been subtracted from L, in this case no value of R is negative (below the green line) and as such the point is not shadowed.

Shadow masks constructed using pre-surveyed topographical data are useful for establishing a generalised appreciation of areas that will likely not yield accurate elevation estimate. Once it is established which areas of a survey are not shadowed, then the shadow mask can then be generated and updated dynamically in response to changing intertidal topography. The area initially shadowed can potentially be analysed using video camera images from the same height and location as the radar antenna, or through detailed analysis of the raw radar data as part of the initial deployment of a radar survey platform, this will give an initial approximation of areas shadowed.

7.1.7 Limits of Operation and Conclusions on Viability of Long-range Survey

It is clear that the radar waterline technique is sufficiently robust to derive some elevations from long-range radar image data. However the accuracy of these elevations when compared to a LiDAR survey from 14 months earlier is far below tolerable values. Whilst there will some differences between the LiDAR and any radar-derived elevations due to the changing morphology (demonstrated in more detail in Chapter 6), these differences are clearly not sufficient to account for the large errors seen in the southeast, south and southwestern areas. In addition to the aforementioned factors of increased shadowing and inner-estuary, tidally-driven water pooling, there are some contributing effects that are a consequence of radar operation at this range. The first potential influence is the drop off in power projected at long range. As the long-range data were not sampled with a longer pulse length, more samples were simply taken along each azimuth, the amount of power returned to the radar is reduced by a factor of four with increasing range (as shown in the Radar Range Equations in Chapter 3). This means that the sea surface at long ranges yields very low image intensities and therefore the transitions between wet and dry (the detection of which are critical to deriving an accurate elevation estimate) may not be detected. This low power return can compromise image quality to a significant extent, as can the degrading azimuthal resolution, that is the increased distance between two adjacent pulses, which comes with increased range from the radar antenna. As range increases and the spatial resolution deteriorates, the cell averaging process, part of the method used to transform

the data from polar to Cartesian coordinates, can have the effect of 'smearing out' features on the surface. This smearing effect can homogenise the data at longer ranges and blur the spatial boundaries of the waterline resulting in the radar-derived elevations being assigned to the wrong location. The methods for improving elevation derivation, such as increasing the time over which the analyses run and implementing temporal smoothing algorithms seem unable to overcome the limitations of long-range data collected with a radar set to short pulse.

For these reasons it is likely that long-range analysis would not be carried out routinely using this technique. In particular the more inaccurate elevations that exhibit large under-estimations by the radar (most legitimate results tend to have a slight over-estimation due to wave setup/runup and differences in the physical location of the waterline image structure as described in Chapter 5) make the observation of long-term trends in erosion and accretion within the estuary very difficult to carry out effectively at long range.

It may be possible to perform long-range waterline surveys if the radar system is set to a longer pulse length, increasing the length of time over which power is projected along a given azimuth. This gives greater pixel intensity returns at these extreme ranges, increasing the chances of detecting a waterline transition and accurately associating an elevation with it. If this is done, however, then spatial resolution at shorter ranges will be compromised as the inter-sample distance would increase to 7.5 m, potentially removing the capability to perform accurate elevation surveys at short range. In

conclusion, these radar data in their current format are not conducive to performing long-range elevation surveys.

7.2 APPLICATION TO PORT ENVIRONMENTS

Many Port Authorities operate some type of radar system to work alongside simple AIS (Automatic Identification Systems) and pilotage services in the task of guiding vessels through navigation channels and into their assigned berths safely. AIS tracking systems make use of data from vessels, base stations and satellites. The IMO's international convention for the safety of lives at sea stipulates that all passenger ships and vessels over 300 gross tonnage (GT) to be equipped with an AIS transceiver. When combined with up-to-date Electronic Charts Display Systems (ECDIS), and competent pilotage, these systems are adequate in many cases. AIS alone however cannot detect small vessels such as pleasure craft, jet skis or, indeed, dangerous or illegally operated vessels that can compromise safety in port areas. Radar expands the situational awareness of a Port Authority allowing the detection of these vessels in bad weather conditions. If the required infrastructure is in place, the radar data can also be used to generate intertidal surveys using techniques as described in this thesis. For areas that do not have installed radar infrastructure, including smaller ports, residential or more remote stretches of coastline that require surveying or long-term morphological monitoring, a robust and highly mobile deployment option is required. The remainder of this chapter will detail the application of the radar waterline technique to port areas and describe the development of the Rapidar.

7.2.1 Requirements to Monitor Drying Areas within Port Operational Limits

Port Authorities have very little obligation to continuously survey the intertidal drying area, as the cost in both time and resources to perform regular manned intertidal surveys is often prohibitive. Manual surveys over isolated, mid-channel sandbanks or very muddy areas are potentially very dangerous. While even shallow-draught survey vessels can only access drying areas to perform surveys at high spring tides, which makes long-term regular monitoring of morphology impractical. The main navigation channel in most port areas is surveyed regularly to enable maintenance dredging and ensure safe navigation through the channels.

The installation of long-term, semi-autonomous intertidal elevation survey capabilities would enable the port to monitor the migration of navigation channel margins at their drying height. This information can be critical in gaining long-term strategic insight into the dynamics of the dominant morphological regimes which may greatly assist port and coastal management. In addition to channel margin monitoring, the movement, formation, and ultimate fate of large sedimentary bedforms across the intertidal area can be effectively tracked with the radar waterline method. The techniques for tracking bedforms have not been developed as part of work presented here but development of this capability is of high priority in future work.

7.3 DEVELOPMENT OF THE RAPIDAR

The Rapidar is a rapidly deployable, infrastructure independent self contained survey platform equipped with a marine radar and a PTZ (Pan, tilt and zoom) camera and is powered with several solar panels. The platform is contained in a secure 3 m ISO container and the radar tower is extendable from within, this makes it discrete, easily transportable and relatively vandal proof. Figure 7.13 shows the Rapidar in varying stages of deployment, the small size and self-contained nature of the product allows relatively inexpensive transport solutions and rapid deployment in order to minimise the time during which it is not gathering data. The fact that the Rapidar is not a permanent structure also alleviates many planning permission issues which would add large time and costs to a conventional scaffold tower deployment. In Figure 7.13a the radar, a *GEM Elettronica Supernet* with a horizontally polarized antenna, can be seen along with the PTZ camera that allows high resolution video and image data to be collected. These camera data can be potentially used to carry out other data processing techniques such as those described in Chapter 2, to derive useful coastal data at short range with finer spatial resolution to supplement the radar survey. The camera also has the capability to detect motion, track the moving object, and send .jpg images back to the user; this aids system security and acts as a deterrent to those who may potentially damage or remove the equipment. This capability was developed by *Marlan Maritime Technologies* and the construction of the Rapidar prototype was part funded by the *Centre for Global Eco-Innovation* as part of project 197 and by *Marlan Maritime Technologies*.

Figure 7.13: (a) Full Rapidar system deployed with mast extended to full, radar and camera system mounted, (b) Rapidar being deployed from flatbed truck, (c) Rapidar tower prior to mast extension.

The Rapidar will enable radar coverage to be extended to areas of the coast that would not normally have the required infrastructure to support a conventional deployment and is ideal not only for assisting port operations, but also as a preliminary wide-area morphological survey prior to or during large-scale engineering projects. Knowledge of beach morphology is critical in the planning of hard coastal defences in addition to the effective management and preservation of existing natural defences such as sand bars, saltmarshes or mud banks and soft defences including managed sand dunes or beach fill. These areas are often also critical habitats for flora and fauna and are often protected sites.

An example of this situation can be seen in the radar data presented in Chapters 5 and 6, to the east of Hilbre Island lies Red Rocks Nature Reserves on the north western tip of

the Wirral peninsula. This area consists of sand dunes, reed beds and saltmarsh and is a critical habitat for rare *Natterjack* Toads (*Bufo calamita*), and declining *Wheatear* bird populations. With the capability of the waterline method to differentiate between sand and saltmarsh and potentially sand and mudbank, due to the different morphological characteristics of their material composition, and material influence on water surface characteristics. The Rapidar presents an ideal tool in the monitoring of these vulnerable areas that are often far away from infrastructure that would normally be required to operate a radar system. Figure 7.14 shows the differentiation of landscape types by a radar waterline survey. It is clear to see how this technique could be potentially used to measure area change (habitat loss or gain) between two time periods.

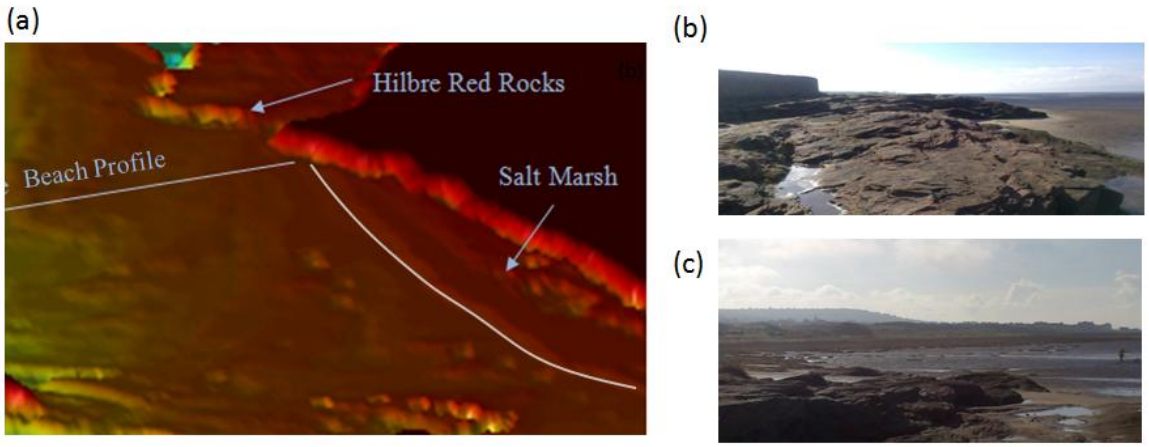

Figure 7.14: (a) Radar-derived elevation data presented as a surface plot with 25x vertical exaggeration. The difference in texture between the sand, the rocks (b) and the saltmarsh (demarked by the white line) can be seen clearly, the smoother texture of the saltmarsh (pictured in (c)) is likely due to breaking wave attenuation as a result of the robust saltmarsh vegetation roughness (Kobayashi et al., 1993; Möller et al., 1999).

Often in coastal management there are very complex phenomena interacting over a very wide range of spatial and temporal scales, and as a result it can be challenging to collect data with the required spatio-temporal resolution. Obtaining these data is especially important before, during and after construction of coastal defences. Coastal hydro and morphodynamic systems are highly interconnected and anthropogenic changes in the shoreline will have inevitable effects on both the immediate and wider coastal areas. The Rapidar system is ideal for monitoring a large stretch of intertidal coastal area during these construction periods which tend to be semi-permanent and last for a period of several years. During the construction period, the area will likely experience several significant stormy periods where erosive trends may be observed in near real-time using the Rapidar, and which may significantly change the morphology of the area.

Finally, the Rapidar presents an ideal tool for monitoring the impacts of beach nourishment or a sand engine scheme whereby large volumes of allochthonous sediment are essentially placed onto the beach and redistributed via environmental forcings, waves, tides and currents etc, with minimal human intervention. Regular elevation surveys of these areas would highlight patterns of redistribution and provide advance warning of adverse sediment movement and notifications of large-scale erosion due to a high energy event, that may require additional sediment to be deposited for the sand engine/nourishment to remain effective. The Rapidar may also have sufficient range to survey the areas surrounding a sand engine (provided shadowing is kept to a

minimum through elevation and unobstructed views), allowing for the collection of data on the fate of redistributed sediment.

7.3.1 Pilot Project Site Description

The Rapidar prototype began development in late 2014 and was fitted out, shot blasted, primed and painted to prevent rust and corrosion that could be caused by the potentially hostile coastal environments that it would primarily be deployed to. Salt water spray or flying gravel and pebbles propelled by wave overtopping are also serious considerations when deploying expensive equipment to the coast. The prototype system was completed during mid-2015 in preparation for the 2015 - 2016 winter storm season and was deployed in late November 2015 to a pilot project site in the Mersey estuary.

A northwest Port Authority expressed an interest in the radar survey technique as a method of monitoring extensive drying areas in the Mersey estuary. These areas are known to be very dynamic and impact the site at Eastham Locks, where a significant navigation channel links the Manchester Ship Canal with the Mersey river channel proper. It is therefore important to the local and national economy that this channel be maintained and the surrounding area monitored. Much effort is expended by the Port Authorities on maintenance dredging to keep the channel free of sediment. It is clear from the chart shown in Figure 7.15 that there are mobile sedimentary features on the sandbanks named Eastham Sands which potentially encroach on this channel (indicated by the 'caution, depths subject to change' label on Eastham Sands). If the radar survey

was able to monitor sediment movement and predict a point at which the sediment would be deposited, along with an estimate of conditions likely to force that movement, it would enable estimation of the time and volume of the sediment movement. This would provide a hitherto unprecedented level of situational awareness and potentially large cost/fuel savings through dredging optimisation.

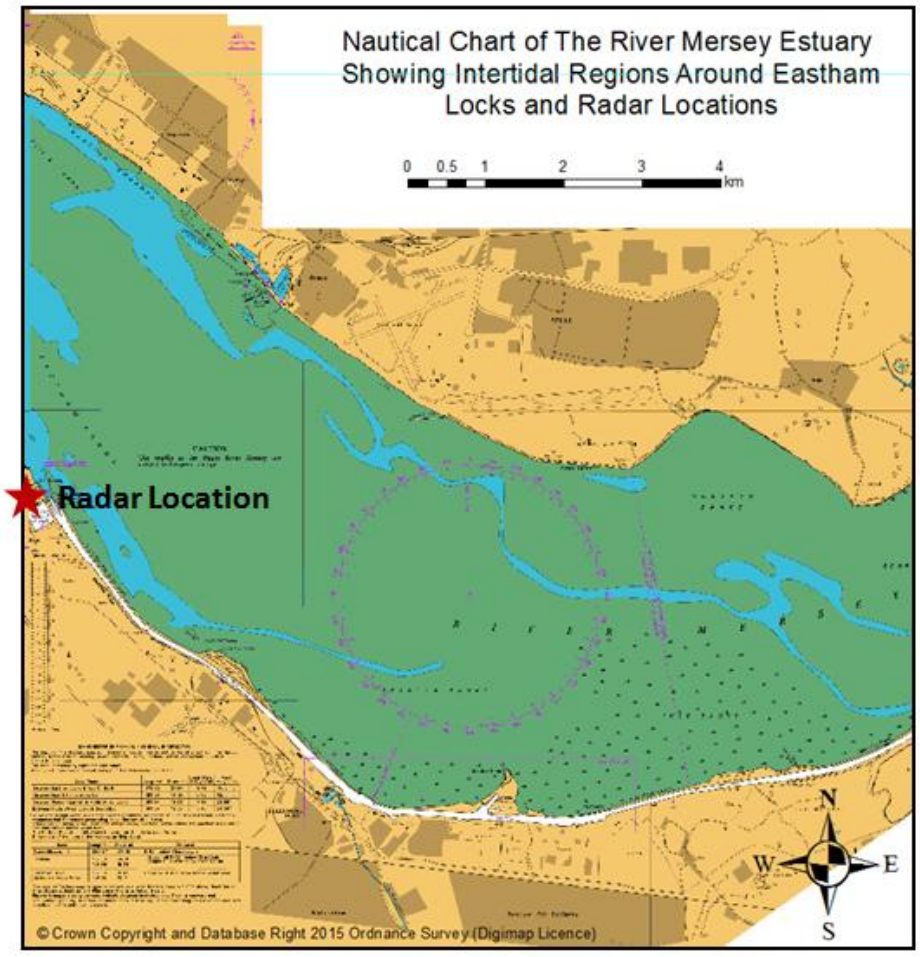

Figure 7.15: Chart data of River Mersey Eastham Locks, data from Sea Zone Solutions Ltd (2015);

The existing radar at this site shown to the left of the Rapidar in Figure 7.16a was taken out of commission by a lightning strike and therefore could not be used to perform the survey work. The Rapidar was an ideal solution as it provided a rapidly deployable replacement radar with limited infrastructure requirements, thus giving the port radar vessel traffic monitoring capability along with the ability to survey the intertidal area.

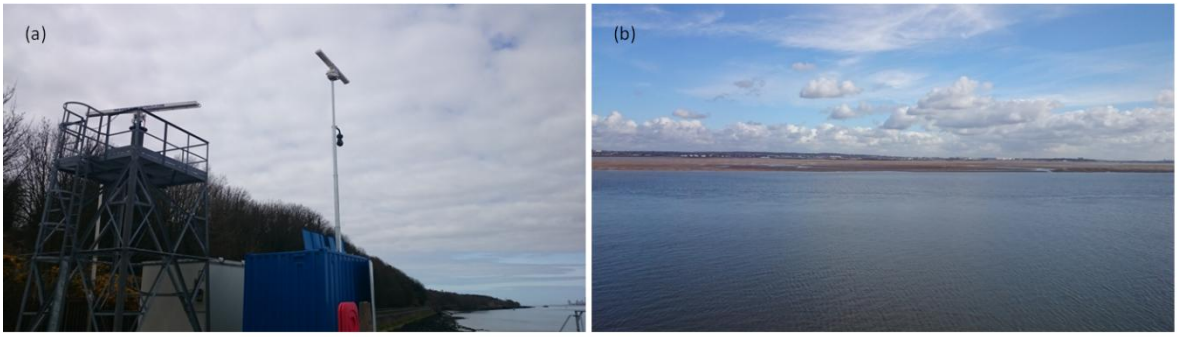

Figure 7.16: (a) Existing radar infrastructure (damaged) to the left and Rapidar replacement to the right deployed at Eastham Lock 2015; (b) view out into the Mersey estuary at mid-tide, the exposed sandbank of Eastham Sands is clearly visible.

7.3.2 Results from Data Collected During 2009

Coincidently, a limited set of data were collected from the original radar at the site during another project at the National Oceanography Centre during the summer and early autumn of 2009. These data were of limited use in the derivation of waterline

elevations, spanning only a short temporal period, with very calm waters providing minimal backscatter for the radar to detect, and very few breaking waves over the sandbanks and beaches. This area is 15 km upstream of the estuary mouth and is therefore very sheltered, however the Mersey is 4 km wide at this point and the fetch is considerable enough to generate a visible rough sea surface if wind speeds are above roughly 3 m/s. Figure 7.17 shows a snapshot of radar image data collected on 25 August 2009 at low-tide and shows minimal seas surface signatures over Eastham Sands.

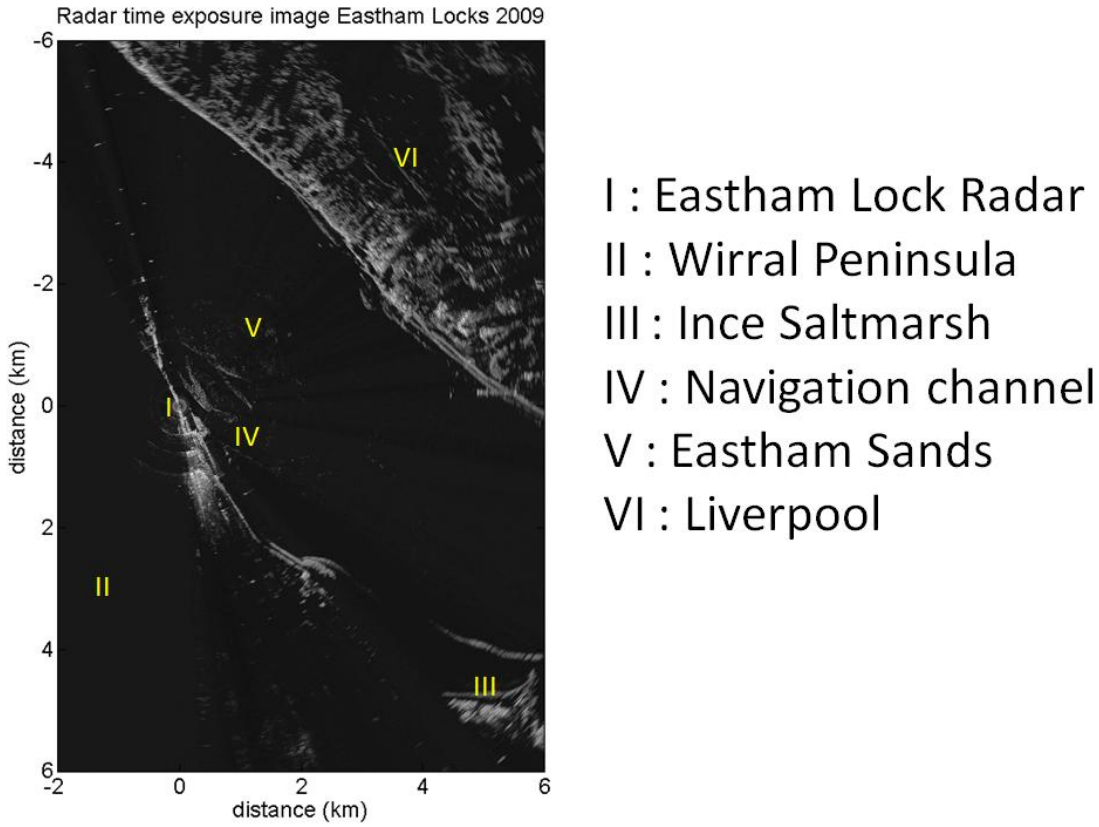

Figure 7.17: Time exposure radar data from 25 August 2009, showing locations of interest and radar location.

The height at which the radar was mounted for this experiment is far from ideal, the initial radar tower at Eastham was only 8 m high. This deployment height would result in a large amount of shadowing across the sandbanks in the estuary. It is also clear from Figure 7.17 that there is very little sea clutter present in these images but multiple waterline patterns can be made out most clearly close to the radar across Eastham Sands.

Two weeks of radar time exposure image data were used in conjunction with the record of tidal elevations measured at Eastham Lock only 100 m to the southeast of the radar site in order to derive a map of intertidal elevations above ACD for an extensive region of the Mersey estuary. Figure 7.18 shows the results after filtering with a correlation coefficient threshold (explained fully in Chapter 5). The pixel intensity normalisation process used in Chapter 5 was relaxed in this experiment as the intensity returns from the sea surface were often so low that data were unnecessarily removed. The narrow beach areas to the northeast are resolved well along with significant portions of the complex sandbank topography. The plot shows large amounts of noise to the southeast that persists despite correlation filtering, highlighting issues with the use of correlation filter as the primary method of filtering (these issues are described in more detail in Chapter 8). The major intertidal feature in this area is Eastham Sands and the results from this analysis shows the location and elevations of these sandbanks in the centre of the estuary. Figure 7.18b shows this location in more detail, the land areas have been masked out and set to an arbitrary supra-tidal elevation of 12 m to aid interpretation.

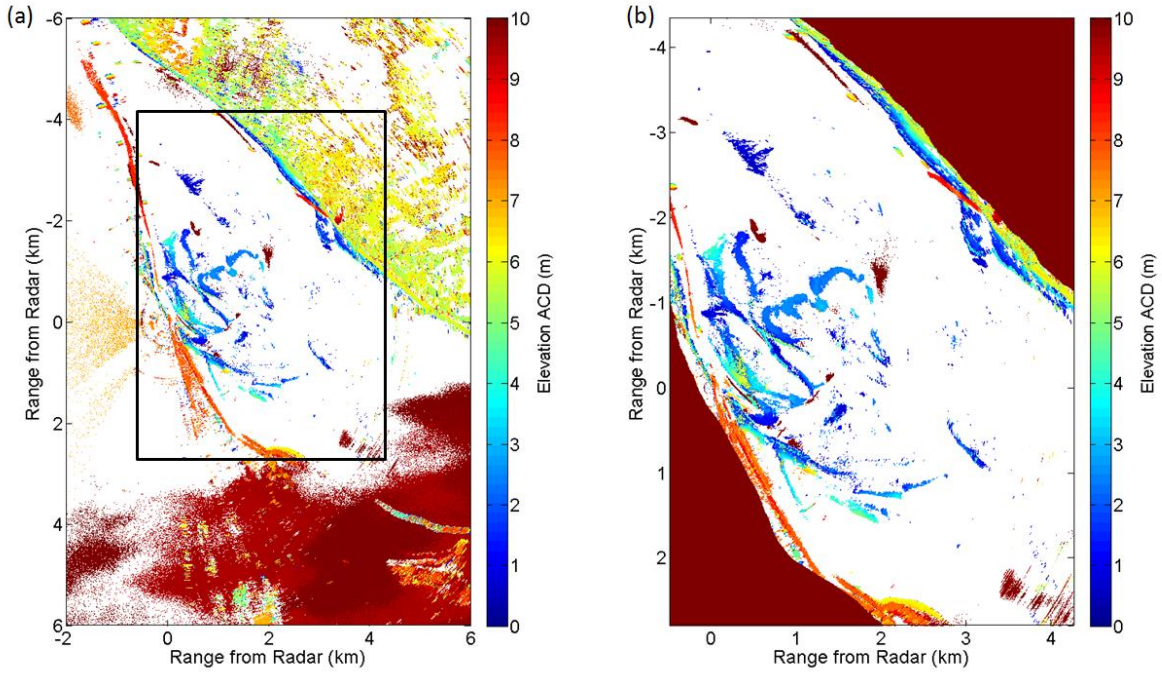

Figure 7.18: Elevation results filtered using correlation thresholds, derived using a tidal record from Eastham locks. Elevations represent the mean elevation over the period 11 August 2009 - 25 August 2009.

It must be noted that the data were collected in summer - autumn. While not so much of an issue on an open coast, the season clearly greatly effects the performance of the waterline algorithm in very sheltered regions. It is hoped that the data collected by the Rapidar system during winter 2015 - 2016 will be of much higher quality and better suited to waterline elevation surveys.

7.4 3-D Bathymetric Environment

With intertidal regions mapped, navigation channels surveyed and vessel traffic being monitored, the safety of shipping is much improved. When combined with up-to-date chart data the system can give vessels advance warning of entering shallow waters, potentially highlighting channels margins and areas best to avoid while navigating the channels. In order to better visualize this, a 3-D Bathymetric environment can be constructed as shown in Figure 7.19. These surface plots illustrate the key morphological features and, with a dynamic tidal watermark superimposed, a vessel in transit is able to locate itself with much better information about safe areas of navigation, depths to Chart Datum and distances across the channel.

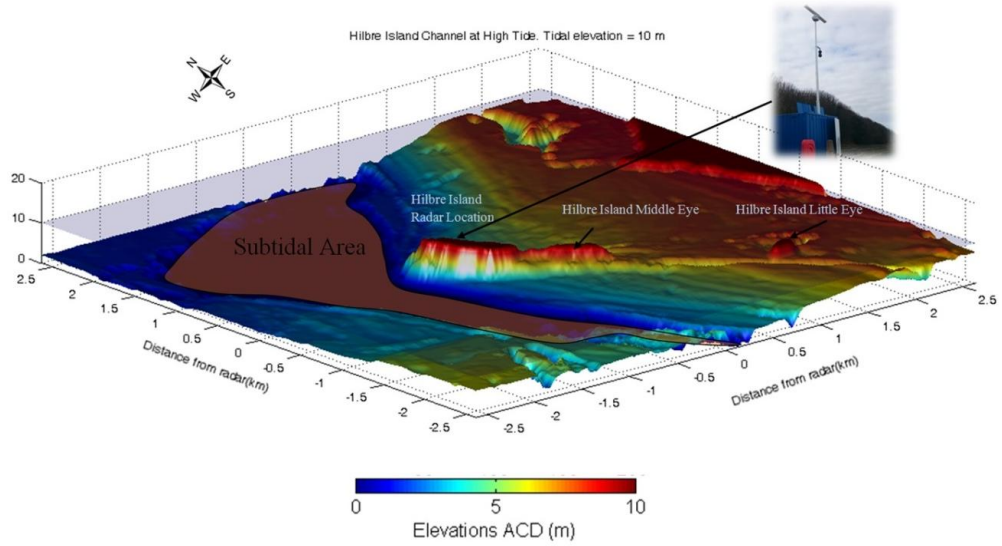

Figure 7.19: 3-D Bathymetric environment, showing the intertidal area and the channel outline, which operationally would be populated using the latest bathymetric surveys or radar-derived elevations retrieved through wave inversion techniques. The tidal elevation can also be superimposed and a ship located on the surface.

Through the use of data in this format it is possible to outline a series of alarm zones designating areas where the intertidal area is particularly mobile and may have compromised the subtidal regions in between bathymetric survey runs. This will increase the safety of shipping and reduce the chances of ships running aground, potentially spilling oil or hazardous substances.

7.5 Summary of Application of Radar Waterline Surveys.

This chapter has demonstrated the ability of radar to generate long-range survey information and drawn conclusions on the viability of survey generation using data collected at such extreme ranges using only short pulse length settings. In addition, the development of the innovative Rapidar survey platform was described in some detail. This is a potentially disruptive technology in the nearshore survey industry and in order to maximise the availability to customers, the mobile deployment option was required in order to facilitate surveying in areas of limited infrastructure. It was demonstrated that careful consideration must be given to location and elevation of the deployed radar system to minimise shadowing. It is also clear that the weather conditions, particularly wind speed and resulting sea state have a great impact on the waterline method when operating in sheltered estuaries. The robust and flexible Rapidar system can be outfitted with a variety of sensors, including varying polarizations and operating frequencies of radar antenna, extensive optical remote sensors, and weather monitoring equipment making it an ideal tool for coastal monitoring.

8 Discussion

This chapter will discuss the key findings presented so far in this thesis. These sections will expand on the requirement for further research and describe how the different research elements address current gaps in knowledge and capability, and build on previous techniques developed. The research is also linked back to the thesis title of developing the use of marine radar for intertidal area survey and monitoring coastal morphological change. The development of the Rapidar survey platform and its impacts on the coastal management industry are also reflected upon in this Chapter.

8.1 THE WATERLINE METHOD

Traditional methods of surveying intertidal regions, often rely on placing people or instruments in the potentially dangerous or damaging nearshore environment in order to obtain useful data. The cost of this process both monetary and temporal, combined with the difficulty in performing these surveys over long periods of time prompted

extensive research into more cost-effective remote sensing techniques. Remote sensing allows for longer range surveys and alleviates the issues involved in manual survey. Despite the considerable advances in remote sensing surveying technology over the last several decades, surveying large areas of the dynamic intertidal region remains very difficult. Cameras have limited range and are constrained by times during which data can be collected, and current radar bathymetric derivation methodologies have difficulty dealing with non-linear wave behaviour in very shallow complex areas.

Radar and tidal data collected throughout 2006 to 2009 are used in this thesis in the research and development of the radar waterline method, detailed in Bell et al. (2016). This method builds on a very basic idea of imaging a spatial location of the waterline and associating a recorded tidal elevation with that waterline contour based on the time at which the image was taken. First established by Bacon (1932) and built upon during WWII by Hart and Miskin (1945) and Williams (1947) through the use of aerial photography. A similar concept was applied to satellite images by Koopmans and Wang, (1994) (and others, see Chapter 2) but these techniques remain locked into spatial image analysis techniques in order to 'draw' the waterline contours onto an image and interpolate between them. This new technique moves the analysis into the temporal domain operating on a pixel by pixel basis making the process inherently more robust. The radar waterline method addresses several key gaps in the capabilities of marine radar-based surveying and provides a supplementary method to support other coastal monitoring techniques.

The results from Chapter 5 demonstrate the ability of the radar waterline method to derive relatively accurate estimates of elevation above Admiralty Chart Datum over a large area, with just under 4 km radial range; these elevations are shown in Figure 5.7. The ability to detect relatively small objects exposed at low tide such as the wreck of the *SS. Nestos*, demonstrates the good spatial resolution and precision of the method. One critical element is the difference between the radar-detected 'waterline' and that which is measured by the LiDAR survey, with which the radar-derived results are later compared. Figure 5.9 in Chapter 5 shows the differences in estimated waterline depending on the time-dependant tidal elevation selected over the course of the ten minute radar image record. In the analyses presented in this work, the start-record tidal elevation is selected as the elevation to be passed into the matching algorithm. In this situation the radar algorithm seems to select the peak intensity of the temporally averaged wave breaker line in the surfzone as the waterline location in space (consistent with results shown by Takewaka, (2005)) which is slightly offshore of the waterline as detected by the LiDAR. It may be that a better estimate of the real waterline would be the falling edge of the pixel intensity peak representing the maximum extent of the swashzone, including run-up. Verifying this and applying any possible developed correction has the potential to improve vertical elevation results and will be explored in future work, in order to develop the technique.

Given the early stage of development, the radar-derived results must be compared with the current industry standard in nearshore survey, in this case an airborne LiDAR survey. Details of the LiDAR survey carried out in October 2006 are given in Chapter 4. Elevations were compared in Figure 5.17 and the residuals shown in Figure 5.18. The radar was able to survey the topography of the beach around West Kirby Sands, the Red

Rocks nature reserve and the elevations of West Hoyle sandbanks accurately. Overall the comparisons between the radar and LiDAR showed good agreements of 0 - 50 cm between the two instruments in areas where little to no shadowing is effecting the radar data. Errors increase with range (Figure 5.21) primarily due to the increase in areas being shadowed with longer range; in the first 750 km of the survey, 97 % of radar-derived elevations lie within 1 m of the LiDAR elevations. It is to be expected that there are some small differences in derived elevations due to the different temporal range over which the techniques operate. The radar survey for instance represents the average elevations at these points over the two-week analysis period, whereas the LiDAR survey was performed over a single low-tide period, thus presenting a snapshot of elevations that may well have changed due to the Autumn storms occurring in October of 2006 (see Chapter 6). The area of poor elevations behind the West Hoyle sandbank further into the estuary highlights one of the critical deficiencies of the waterline method discovered throughout this work, i.e. the issue of tidal water pooling, whereby the ebb tide water becomes trapped behind sedimentary bedforms and takes longer to drain from the estuary. This causes the radar to continue imaging the retreating waterline and inadvertently assign a higher elevation to that location. While the effect may not be immediately obvious during a single semi-diurnal tidal cycle, the effect is clearly compounded over a full spring-neap cycle.

Another primary cause of poor elevation estimates, that of radar line of sight shadowing is also exposed during this comparison with the LiDAR data. The issue of radar shadowing is prevalent in the use of radar as a coastal monitoring instrument and indeed in the use of optical instruments for remote sensing. Shadow masks were

constructed based on the LiDAR survey, the process of which is described in Chapter 7. These shadow masks confirm the pattern of shadowing, exacerbating the over-estimation of elevations as shown in Figure 7.10.

It is clear that the use of radar as a data collection tool has some limitations including; shadowing, very heavy rainfall, low wind conditions and a resultant calm sea surface. However it has been shown that the waterline survey method developed in this work, provides a robust technique for mapping intertidal regions over a spatial and temporal range that was not previously possible using a single sensor platform. The elevations are currently not consistently accurate to industry standard (~20 cm vertical tolerance) across the entire imaged region. However, radar-derived elevations acquired over a large area, especially at close ranges and with clear line of sight, exhibit highly accurate results and with further research the vertical differences at longer ranges and in more complex areas are not insurmountable with the application of a combination of corrections for; tidal offsets, wave breaking, run up/set up and an estimation of the effect of pooling water. The value of long-term timeseries of elevation values can also not be overstated. It could be argued that the absolute accuracy of elevations derived over this range and timescale is less important than tracking patterns of bedform migration and overall beach condition.

8.1.1 Comparison of Radar Waterline Survey with Other Waterline Techniques

Radar is not the only sensor able to use waterline mapping techniques. As already covered in Chapter 2, the original waterline contour mapping research was conducted using aerial image data from airplanes and effectively used the sea as an altimeter (Bacon, 1932). It is useful to compare the method developed in this thesis with other waterline methods to establish the relative advantages and disadvantages between the radar waterline technique and primarily satellite-derived topography. Waterline techniques using satellite imagery allow the construction of DEMs over a very large area by interpolation between a set of heighted waterlines. The derived waterlines are more accurate on wide shallow/flat beaches and accuracy falls with increasing slope (Mason et al., 2001). Errors are between 20 - 30 cm (in flat, uniform regions) and have a spatial resolution of 10 - 50 m (Mason et al., 2000) depending on the type of sensor.

Satellites can be used to retrieve data from beaches and sandbanks which may be inaccessible to aircraft, vessel, or manual surveys, either due to their remote location or inhospitable weather/tidal patterns. When using SAR sensors mounted on satellites, images can be collected during day and night and under various adverse weather conditions, increasing the number of images available to perform the image analysis. The image data can also be used to analyse historical images to assess long-term macro-scale morphological changes (Mason and Garg, 2001). The use of satellite images for topographical mapping has several clear disadvantages, the first of which is the low spatial and temporal resolution, in comparison to other methods of remote sensing. The

lack of planimetric accuracy results in the smoothing out of smaller scale bedforms. This when combined with a low temporal resolution can curtail the ability of satellite waterline mapping being applied to the task of tracking and monitoring bedform migration and assessing event level morphological change. The low temporal frequency is a result of the low return period (time between satellite overpasses), leading to a small number of images that capture a limited extent of the intertidal area as the tide rises and falls.

Access to satellite image data can often be prohibitively expensive or restrictive to many organisations depending on the source of the image data. In a similar manner, a relatively advanced tide-surge model is required to generate elevations for the satellite waterline method. This is a considerable drawback of the use of satellite data for beach topographical mapping when compared to the radar which produces data independently of other organisations and (at least at this stage of development) does not require the use of hydrodynamic models to generate tidal elevation records; a single (or several in larger estuaries) in-situ tidal elevation sensor should be sufficient in most cases.

With the radar waterline technique, similar accuracies to the satellite method are seen in areas which are not shadowed or at extreme ranges. This is likely because similar problems are faced by the SAR satellites, such as the separation between the waterline detected and the underlying absolute bed elevation. The radar offers a primary advantage in increased spatial resolution and temporal frequency with 5 m grid squares in the final survey and a separate survey generated reliably every two weeks. The limitation in this situation is maximum survey range. While the radial range of 3.83 km

from the radar is large compared to other remote sensing techniques it is minimal when compared to the very large areas which can potentially be imaged by a satellite. The use of UAVs and imagery from drones has some potential to be applied to the waterline technique developed in this work, if flights can be run often enough over a spring neap cycle. This could alleviate some of the issues with standard photogrammetric techniques which often do not work particularly well on shallow sandy beaches. It is likely however, that the accuracy of photogrammetric techniques is likely to increase with the development of SfM techniques and new algorithms over the next few years, such that UAVs are able to map beach topography well with a single flight. Radar continues to retain some inherent advantages over UAVs however, the range of radar is much greater than that able to be observed by a UAV during a single low-tide period. Many flights of a drone would be needed to accurately map a very large intertidal area. Radar allows routine acquisition of very large topographical datasets while the UAVs still require manual data collection and significant processing, which is likely to be expensive if offered as a commercial service. Additionally, UAVs cannot operate currently in poor weather and light conditions. The data collected are also relatively limited in application, whereas the radar data can be applied to many tasks, including subtidal bathymetric measurement. There are also significant legal restrictions being placed on the use of drones/UAVs in many areas which may make routine survey of an area difficult.

The high temporal survey rate allows for the radar technique to be used to both monitor and track changing morphology as surveys can be produced with a high repeat period (potentially updating topographical elevations daily with sufficient processing capacity devoted to the task using a moving window type analysis). The radar waterline

technique is also able to observe morphological changes resulting from storms over relatively short time periods of observation when compared to the satellite images that are currently collected too infrequently.

The radar technique developed here is inherently more robust than those waterline techniques previously developed. This is a function of the pixel-by-pixel analysis and elevation estimations for each individual pixel rather than relying on (mostly) spatial image processing techniques, which can leave large gaps in a waterline survey and introduce interpolation errors as gaps were filled. Previous attempts at applying waterline analyses to radar image data have also relied on spatial analysis, thus requiring significant manual intervention and relied on continuous high quality data (Takewaka, 2005).

8.2 MORPHOLOGICAL ANALYSIS

Long-term monitoring of dynamic coastal areas has been an objective for coastal scientists for many years (Holman and Haller, 2013) but previous survey techniques were not easily applicable over the required ranges and resolutions. Manual surveys have difficulty covering the required area repeatedly and LiDAR flights quickly become prohibitively expensive, when weekly or even monthly surveys are required. This temporal resolution is essential in monitoring changing elevations, in response to storms and seasonal variations in morphology and the relevant driving forces. Remote sensing provides the opportunity to monitor changes over varying spatial and temporal scales. Video camera systems including Argus deployments, which can produce

topographic elevation maps of the immediate foreshore with very good resolution (albeit not in low light conditions) are common tools in coastal monitoring. Marine radar can now support other techniques or operate independently by providing wide-area topographic and subtidal bathymetric mapping with good temporal and reasonable spatial resolution. In addition, these methods have the potential to be automated to some extent so as to reduce end user cost significantly and allow for repeat sampling of the same data points, which would otherwise require meticulous and time-consuming planning in manual surveys.

The radar technique developed here allows for a survey to be generated every two weeks using a series of time-exposure images. In Chapter 6, a total of 62 such surveys were generated using data from March 2006 - December 2008, with some gaps in the dataset during periods of power outage and low quality data shown in Table 6.1. The aim of this experiment was to demonstrate the ability of a single marine radar sensor to independently monitor the morphological evolution of a large intertidal area over several years, a relevant timescale to coastal engineers and scientists. The sequence of surveys clearly demonstrated some interesting morphological behaviour around Hilbre Island. In order to quantify the changes over three years, two specific areas were selected from the survey. Site A, the West Hoyle sandbank exhibits mobile bed feature migration evident from Figure 6.7. While at Site B the NW Wirral beach an area located close to Hilbre Island, the on-shore migration of intertidal swash bars can be observed, which eventually become welded onto the foreshore.

Individual surveys sometimes exhibited gaps in the data where correlation coefficients between records of pixel intensity and pulses of tidal wet-dry transitions were too low to provide an accurate elevation estimate. In order to make use of the elevation information contained in the rest of the dataset the gaps were filled using the robust temporal smoothing technique described by Garcia (2010). This results in a robust timeseries of elevations for each individual pixel location reflecting the changing morphology at that point. It is assumed that the changing elevations reflect actual morphological change and not a result of artefacts in the image data. This assumption is validated by experiments performed in Chapter 5, where several 'unchanging' rock locations were selected and seen to be relatively stable over the course of ten months (Figure 5.16).

The results from Chapter 6 show the quantification of several measures of beach 'health'. The purpose of measuring beach health is to estimate a measure of beach stability and to identify areas suffering excessive erosion or adverse sedimentation. The first method sought to analyse the long-term (three year) pattern of total area volume change. For each of the two study sites described, the sum of sediment volume from Admiralty Chart Datum for all grid points was calculated for each two-week survey period. This gave a fluctuating timeseries of total estimated sediment volume for each site, (see Figure 6.6**Error! Reference source not found.**). These data demonstrated clear evidence of annual cyclicty showing erosion and accretion at varying times throughout the year. The West Hoyle sandbank exhibited lowest volumes in autumn and highest in spring, whilst the NW Wirral beach showed lower volumes in winter and highest volume in summer. These results are to be expected with generally stronger

wave conditions, combined with storms in autumn and winter and calmer periods in spring and summer facilitating sediment accretion.

To support this, another measure of beach health was assessed. This involved taking the average topographical elevation above ACD of a given region and tracking the changes throughout the months of the year. These values are compared to the three-year average elevation of that area in order to see when the major changes are occurring. These results are seen in Figure 6.9 and Figure 6.11, and they reinforce the previous sediment volume analyses very well, with elevations dropping during the same periods when sediment volumes are lowest and elevations are highest in the spring and summer. There appears to be an interesting phase lag between the times of erosion at the two sites, with the West Hoyle sandbank losing material and beginning its recovery earlier in the year than the NW Wirral beach. This could be a result of changing incoming wave directions throughout the year, a difference in sediment cohesiveness or stability between the two sites, or a transfer of material from Site B to Site A, contributing to the delayed recovery of Site A.

In addition to the passive monitoring of long-term morphological change, the technique is also well suited to assessing change resulting from the effects of a single high energy event. In Chapter 6 the daily average wave height record from January 2006 - January 2009 were retrieved from the *CEFAS* wavenet buoy several kilometres offshore from Hilbre Island. This wave height record shown in Figure 6.6c, illustrates the timing of several of the largest European storms during the period of data collection. A single

storm was selected to illustrate this capability; the storm *Britta* occurred from 29 October - 4 November 2006 with maximum daily averaged wave heights of 2.4 m (with maximum individual heights 3.4 m) seen on 31 October 2006. Two weeks of radar data were processed before the storm, capturing the full spring neap cycle up until 29 October and two weeks immediately after, thus including the spring neap cycle after 29 October 2006. This processing resulted in before and post-storm surveys which can then be used to calculate residuals giving an indication of the direct impacts of that particular storm on the morphology of the intertidal area around Hilbre Island. This process can potentially be automated in the future to detect conditions likely to be synonymous with storms and set a breakpoint to analyse before and after the event automatically. The results of this analysis (Figure 6.12) showed that storm *Britta* resulted in significant foreshore erosion of up to 1 m vertical material loss and helped to shift some of that material further offshore, indicated by the areas experiencing accretion. These differences can be shown to be indicative of actual material loss or gain, due to the evidence given by the stability analysis carried out in Chapter 5. Stable control points located at rocky locations throughout the domain were shown to only vary in elevation by ±10 cm and this offers confidence that changes of up to 1 m observed are not analysis artefacts or noise. It should be noted that at this point, this analysis reflects a relative change in elevation, not an absolute change as the waterline is still being used as a proxy for underling bed elevation.

The application of the radar waterline technique to the task of monitoring changing morphology over three years revealed the underlying morphological trends in sediment volume flux and mean elevations at two sites within the Dee estuary. Analysis of changing cross-shore profiles confirmed the remoal of material in the upper and middle

regions of the profile and a transfer of this eroded material to the lower regions of the profile during the summer-winter seasonal cycle. Changes resulting from a single storm event were also observed and again material was found to erode from the central and upper regions and accrete in the lower portions of the beach. This long-term, high temporal resolution monitoring over such a large area is currently not possible using other remote sensing techniques.

An experiment was conducted in Chapter 7 with the objective to expand the range of the radar survey technique developed in this project, in order to analyse the morphology of the wider Dee estuary. The radar pulse length settings were kept the same but more samples were taken along the radial transmit resulting in a range extension from $\sim$4 km to $\sim$7.5 km. This allowed the entire mouth of the Dee estuary to be imaged with the radar, the waterline method was applied to the long-range data. This resulted in a series of extensive surveys reaching some critical regions of the estuary including Mostyn Bank, which is the site of the Mostyn Port navigation channel and the eastern edge of the Point of Ayr a dynamic sandy headland in North Wales. These surveys again were generated every two weeks from May 2007 - December 2008, however the results of a comparison between these long-range surveys and the LiDAR survey of October 2006 (not an ideal comparison due to the difference in time between the surveys) found that large areas of the survey, particularly at long ranges were inaccurate (> 1 m differences) and therefore a full morphological analysis was impractical.

The influences of shadowing are exacerbated at longer ranges, due to the shallower grazing angle between the radar beam and the water (or land) surface being imaged. The process for estimating shadowed areas based on a prior topographical survey was fully explained in Chapter 7 and it was shown that these shadow masks (see Figure 7.10), will be an important part of the pre-deployment process of future radar deployments in order to broadly understand areas of survey which may give poor results.

In addition to shadowing, it was seen that radar image intensities at the longer ranges from the radar were extremely low. The EM waves projected from the radar spread over a wider area and are attenuated by the atmosphere and scattered from the surface along a radial path from the antenna. This resulted in lower energy returned to the radar receiver and poorer quality images being passed to the waterline algorithm. With poor quality image data at the longer ranges, only a small number of valid waterline transitions were detected which resulted in a much degraded estimate of elevation. Attempts were made to alleviate these issues through temporal smoothing and use of long term mean correlation coefficients in order to extract valid elevations at a set of points.

Another technique of improving results was also applied to the long-range data; this involved simply extending the length of time over which image data were sampled for use in the waterline algorithm. Standard practice is to use one full spring neap cycle so as to monitor the largest tidal range available and thus the most exposed topography. By extending the length of sampling to include two full spring neap cycles, the hypothesis

was that more waterline transitions would be detected and thus the accuracy of results would improve. Whilst this seemed to produce a survey with less gaps in the dataset it did not seem to improve results at long range significantly. It was therefore clear that data collected by a standard, horizontally polarized X-band radar set to short pulse length was not adequate for elevation survey duties at long ranges. It is very likely that data collected using a system set to longer pulse widths for example, sampling at 20 MHz, effectively doubling the time over which the radial pulse is transmitted would return data more suitable to this task. It would still present the trade-off between spatial resolution and extended range.

It is clear from these results that the radar is well suited to long-term morphological analysis of a given area. Potentially this plays a key role in the collection of "Big Data" for use in coastal science and a network of these sensors could be placed in strategic (or vulnerable) locations along the coast. The collected data could go a long way towards establishing a set of coastal infrastructure analytical techniques that allow data-based decisions to inform shoreline management plans and coastal defence strategies. Prior to the development of this technique, the provision of such a dataset was not possible using current technologies. It is however important to note that this radar waterline technique is a small part of a dedicated drive within the industry and the coastal survey community to expand the capabilities of marine radar and remote sensing. The true strength of radar as a platform is both the many diverse ways that the data can be used, and the wealth of information contained within the dataset. Not only can these data be used to derive hydrodynamics and bathymetry, they can also be used to continuously track vessels, people and wildlife. Marine radar is currently forming an integral part of

the marine renewable industry in providing cost effective measurements of tidal surface currents (Bell and McCann, 2013). It is also worth noting that the techniques developed in this thesis can also be applied to other remote sensing data. For example video camera data may prove extremely well suited to this waterline technique and would help to fill in the close range area with a better spatial resolution than the radar. Regular satellite imagery with sufficient temporal sampling rates over much larger areas may also provide very wide-area topographical mapping to support the radar-derived survey data.

8.2.1 Comparison of Radar Waterline Morphological Monitoring with Other Remote Sensing Techniques.

Many remote sensing techniques now exist for surveying beach and intertidal topography; see Mason et al. (2000) for a comparison of techniques that is still broadly current. However some of these techniques are better suited than others, to the specific task of monitoring morphological changes over various temporal and spatial scales.

Cameras and tower-mounted LiDAR systems (Masselink et al., 2010; 2015) are best suited to monitoring micro-scale morphological processes, such as those occurring in the swash zone over a single tidal cycle. Their suitability for this task is a function of their incredibly high spatial and temporal resolution; sampling frequencies of LiDAR and cameras are much high than those of radar for example. Video cameras, specifically Argus systems in combination with *cBathy* algorithms are also used to survey expansive

areas and monitor the evolution of intertidal bedforms (see Chapter 2). The camera data are however limited by both absolute range and lighting conditions.

Marine radar has also been used to monitor coastal morphology using techniques that differ from the wave inversion analyses described in Chapter 3 and the waterline technique developed in this work. For example, detailed analysis of radar timelapse image pixel intensities revealed the locations of nearshore bar crests (Ruessink et al., 2002). This relatively simple technique was used by Galal and Takewaka (2008) to monitor the longshore migration of mega cusps across a large intertidal beach area and by Esteves et al. (2007) to track nearshore bar movements during storms. This technique again relies on the patterns indicative of submerged bedforms modulating the sea surface conditions being reflected and therefore detected in the radar data being analysed.

The use of aerial UAVs and drones to monitor coastal morphology is still a relatively immature technology. Now that commercial unit costs for high quality quadcopters and optical equipment to be mounted on them has reduced significantly, attempts have been made to apply them to surveying (Mancini et al., 2013) and the monitoring of coastal areas (Benassai and Pugliano, 2015). There remain however, some significant systematic errors in topographic mapping with images collected with UAVs (James and Robson, 2014). UAVs have been used to assess erosion on terrestrial landscapes (Eltner et al., 2014), and for monitoring the condition of other coastal structures (González-jorge et al., 2011; Drummond et al., 2015). The use of UAVs commercially to map

intertidal areas has not yet been fully explored, but it is likely that they have the capability to monitor elevations in between storm events and on a seasonal basis. However, in a similar manner to aerial photogrammetry and airborne LiDAR, the weather conditions limit the times when surveys can be flown. It is likely difficult to cover a large extent of the drying area in a single flight and may require several repeat surveys. If a similar temporal resolution to the radar waterline method was required, costs will be higher using UAVs or aerial imagery due to the manual nature of data collection and processing. Much of this data collection and processing can be automated with the use of marine radar. It should be noted that the development of this radar waterline method is not intended to replace any other topographical mapping technology, it primarily adds another effective tool to the arsenal of coastal managers and coastal geomorphologists. It is envisioned that the Rapidar can supplement or support other survey techniques; or be deployed independently prior to the design of any costly, detailed survey campaign to identify areas of interest or morphological change that would require more detailed analysis.

8.3 COMMERCIAL APPLICATIONS

The coastal management industry has need of a robust and cost-effective coastal monitoring system for operation and data collection over inter-annual timescales. Current methods of surveying can be prohibitively expensive if long-term monitoring is needed as discussed throughout this thesis. Remote sensing in general and radar in particular can collect the required data. Advances in processing techniques can subsequently deliver the required end product; be that hydrodynamics, topography or

subtidal bathymetry over a wide area and long timescales. However the infrastructure required to mount a radar system for survey over long periods of time can often be quite prohibitive, as a steel scaffold tower and access to power infrastructure, along with facility for data collection and storage is usually required. A significant part of this project has been the development of the Rapidar in collaboration with *Marlan Maritime Technologies. T*he Rapidar is a self-contained survey platform powered by solar panels and houses the required data storage devices. The platform also features an extendable tower capable of mounting a standard 2.4 m radar antenna and turning unit weighing approximately 40 kg whilst withstanding wind stresses and minimizing the risk of vandalism. A more detailed description of the development of the Rapidar system are given in Chapter 7.

The development of the Rapidar allows for the intertidal survey and monitoring techniques developed in this thesis to be applied; along with other radar data processing techniques to remote or difficult to access areas. It is an effective cost-saving measure for the end user if the area to be surveyed does not have access to the required infrastructure, for example a small port which does not usually operate a marine radar as a navigational aid. A stretch of coastline where no suitable tower or power infrastructure is in place would also be an ideal location for a Rapidar deployment.

The radar waterline method has applications in several key areas of coastal management and science. In port management, the maintenance of navigation channels and the safety of vessel traffic is dependent on regular, accurate bathymetric surveys.

These surveys are commonly conducted using conventional multibeam echosounders which are well suited to the task of monitoring relatively linear subtidal channels such as those seen in ports. However, the intertidal area through which these channels transect is very dynamic and is rarely surveyed, due to the difficulties stressed in previous sections, namely time and cost limitations. As a result, these areas are frequently neglected as a survey target and important changes in the morphology of the surrounding area are missed. The very real consequence of this is that large sedimentary bedforms that are mobile in the intertidal area, may be encroaching on the navigation channel and lead to infilling. If the timings of these infilling events can be predicted by regular surveying of the intertidal area and potentially volumetric measurements of the sediment movement provided, then the efficiency of the required maintenance dredging operations may be greatly improved. With up-to-date information on both the sub and intertidal bathymetry, a 3-D reference environment can be created similar to that shown in Figure 7.19. This information provides a much greater situational awareness for port authorities along with information about the state of the intertidal area within a port's zone of control, allowing them to better respond to changing defence requirements or threats posed by erosion.

This point leads on to the application of the radar survey platform to the monitoring of large stretches of exposed coastline. As these areas are often extremely vulnerable to erosion, they are frequently the site of extensive hard engineering work, that have the capacity to significantly influence sediment dynamics and hydrodynamics at the point of construction and further along the shoreline. It is therefore of critical importance to monitor the effectiveness of these beach defences and monitor potential erosion of the beachface that could lead to undercutting and compromising of coastal defences if not

mitigated. The adaptability of coastal areas in response to sea-level rise and changing wave climate can be compromised when hard engineering is constructed along a coast. This is a significant part of the "Coastal Squeeze" effect where the intertidal area; which acts as a crucial buffer to erosive conditions and attenuates incoming wave energy is rapidly eroded (Pontee, 2013). In order to maintain these areas, the tactic of beach nourishment is employed. This involves deploying a significant amount of sediment at some point along the shoreline. Subsequently this material is allowed to be "naturally" redistributed with minimal anthropogenic interference post-deployment. It is vital that the redistribution of sediment from the deployments is monitored over the long time period that the deployment will be active. Current methods of surveying beach nourishment are limited. More involved, long-term projects are deployed such as 'Sandscaping' or 'Zandmotor/Sand engine' schemes, which are upscaled beach nourishment projects, require significant monitoring campaigns. The morphology of these schemes are currently being monitored with video camera systems (Wengrove and Henriquez, 2013). The disadvantages and advantages of video topographical monitoring have been discussed previously, but it is clear that the radar survey methods developed in this project would provide a good supporting technique to mapping large areas of these extensive schemes. Critically, the radar methodology would allow the tracking of the physical evolution of the scheme, in addition to highlighting resultant changes in morphology or a divergence in environmental forcings which can be driven by the deployment of the scheme itself. These monitoring efforts are required to assess the long-term effectiveness of the schemes and to justify the expense required to implement them.

Another crucial aspect of coastal management is the monitoring and maintenance of coastal habitats. In particular wetland habitats such as tidal saltmarshes and mud/sandbanks, that can be vulnerable to erosion over relatively short temporal scales. Current techniques include using aerial/satellite photography to assess inter-annual changes in area and limited DPGS surveys to monitor elevations. As demonstrated in Figure 7.14, the radar waterline method is able to discern variations in underlying surface texture due to the variations in wave propagation and breaking behaviour over mud, sand, or marshland. This can be potentially utilised to monitor changing area statistics and elevation changes.

From market research carried out in partnership with *The National Oceanography Centre* (*NOC*) and *Marlan Maritime technologies* it was discovered that commercial survey companies often have difficulty deriving topography in the intertidal zone, and their customers often have great need for these data. The use of the marine radar in this capacity would greatly assist the filling of the 'White Ribbon', the data gap prevalent in the coastal survey industry where offshore bathymetric data meets very shallow water and data collection is inhibited. Supporting traditional survey consultancy efforts is a significant potential application of this new technology.

Crucially, there is limited funding available for scientific monitoring of coastal regions. Therefore scientists and institutions applying for research funding must make the case that their results will have impact and that they can use the most cost-effective technology in order to achieve high impact results. The radar mapping techniques have been shown in Chapter 5 to be able to provide data of a similar quality to LiDAR, provide

cross and long-shore transects, along with a suite of unique abilities not currently provided by any other singular remote sensor. It is envisaged that the techniques developed here will be built upon considerably and will form a significant part of coastal monitoring infrastructure globally.

8.4 FUTURE WORK

The work presented in this thesis is still at a very early stage of development, as with any new technology, continued development is required to increase the technology readiness level (TRL). The techniques have currently been developed and demonstrated on a dataset that was not collected with this purpose in mind. Therefore a key next step is to collect a relevant, contemporary dataset with the purpose of applying the radar waterline technique to the data. The pilot deployment of the Rapidar system at Eastham Lock on the River Mersey estuary, will collect a dataset with a unique set of complications. A radar dataset from an exposed, relatively straight, wide sandy beach is required to fully demonstrate capabilities in an 'ideal' operating theatre. In addition to a new dataset, there are several key areas that have been identified as a result of this research, where potential improvements in the accuracy of derived elevations may be made. This section will summarise the potential areas for improvement and steps that can be taken to improve results.

During the current stage of analysis, ten minutes of radar data (256 images) are used to create a time-exposure image every hour over the course of the two-week analysis

period in order to cover the full spring-neap tidal cycle. As Figure 5.9 in Chapter 5 shows, the tidal elevation of the waterline can vary significantly over ten minutes of radar recording, 30 cm in the case of Figure 5.9, moving the spatial waterline location by around 25 m as the water rises (even more over one hour). It is clear from this section that the cyan line marking the waterline location derived by the LiDAR does not match the location of the radar-derived elevations. The line (green) corresponding to the mid-record 06:05 is close to the peak of mean radar backscatter associated with the breaking waves. This supports results from Takewaka (2005) defining the peak of breaker backscatter as the radar-defined waterline. However the location of the green line shows the radar-derived waterline to be offshore of the corresponding LiDAR waterline location and accounts for some of the over-estimation of elevations by the radar seen in Figure 5.18. There are two potential ways to address this issue. Firstly the results suggest that if the radar-defined waterline mark was attributed to a different point in the mean pixel intensity record, such as the shoreward falling edge of the wave breaker signal instead of the signal peak then the derived elevation should match the LiDAR elevations better. Alternatively, to achieve a similar effect, the tidal elevations to be matched to the pixel records can be changed. Currently the tidal elevation to be derived is sampled at the time when the radar record begins, e.g. a record beginning 6 October 2006 06:00 - 0610 attempt to match the tidal elevation at 6 October 2006 06:00 (2.97 m). Figure 5.9 shows that the tidal elevation at the end of the record 6 October 2006 06:10 (3.29 m) is the closest match to the LiDAR and if subsequent analyses sample tidal elevations at the end record time i.e. 06:10 instead of 06:00, then it may serve to improve elevations derived.

The fact that the radar images the physical waterline and that the elevations derived are waterline elevations, not absolute bed elevations as sampled by a LiDAR or other survey techniques, has been stressed throughout. At this stage of development there should almost always be an over-estimation of elevations by the radar due to the vertical separation between the bed and the water surface (this will be very small if there is limited separation). A significant contribution to this separation is the combination of wave setup and run-up. Strong winds can cause the cumulative 'piling' up of water at the coastal zone, and incoming waves can break and continue up the beach across the swash zone (Masselink et al., 2014). The radar continues to image this exaggerated water level above the elevation defined by the tidal curve. With the correct offshore wave data and prior beach profile survey, it is possible to use empirical formulae such as those developed by Stockdon et al. (2006) in order to derive an estimation of wave setup and run-up contributions to absolute water level elevation above ACD. Once an estimate has been made for each grid cell, the value can then be subtracted from the radar derived elevations, which should serve to reduce the elevation over-estimation by the radar. This solution is simple in the case of a simple beach profile transect, but becomes somewhat more complicated when dealing with an expansive 3-D survey where not all areas will exhibit the sample run-up and setup behaviour. For example, the sand banks and saltmarshes seen in the radar surveys, will likely show very different setup and run-up characteristics, so the above solution would not necessarily apply across the entire survey area. It should be reinforced that often the entire purpose of beach surveys is to measure elevations that can serve as data input to hydrodynamic models (such as X-Beach) that predict wave run-up and setup and/or wave overtopping in order to inform coastal defence. It is possible that with further quantification, quality control and

experimentation, the radar technique presented would be able to directly supply this information due to the fact that the radar images the absolute water surface.

In Chapter 5 the comparison between LiDAR and radar-derived elevations revealed a large discrepancy to the southwest where differences were in excess of 1 m. The hypothesised issue here was tidal pooling water being trapped behind significant morphological features. The radar continues to measure the water surface, which remains somewhat higher than the time-dependant tidal elevation recorded at Hilbre Island. A potential solution to this could be to separate the analysis out between the rising tide and the falling tide, with two separate surveys for each two-week period it could be possible to isolate this pooling effect and validate this hypothesis. It is likely that by separating out the analyses however, that the number of waterline transitions captured will be potentially halved and this may well impact the correlation coefficients of estimated elevations.

The area surveyed by the radar is quite large, with nearly 8 km^2 covered. Due to the large area covered, there is a significant phase lag as the tide propagates from one side of the domain to the other. This propagation is also attenuated by its translation over the complex topography of the Dee estuary mouth. The result of this is that actual tidal elevations at the long ranges from the radar will be different than the elevations measured at Hilbre Island. An ideal solution to this would be the use of a dynamic 3-D tidal model; with tidal elevation (and additional storm surge information) estimated at each grid point surveyed by the radar. This would enable the radar pixel intensity record

at each sample point to be analysed using a unique tidal elevation record from which to match elevations.

It is likely that a combination of the above techniques will be required in order to make the greatest use of the developed radar waterline method. However the overall robustness of the technique has been demonstrated in the work presented in this thesis. In many coastal areas, the accuracy of absolute elevations is less important than an overall appreciation of dominant erosion or accretion trends and a record of seasonal or inter-annual change.

In addition to the future work required to improve the algorithms developed so far, there is also potential improvement in results to be seen through the experimentation with other remote sensing hardware. The use of a vertically polarised (VV) radar, which is well known to observe and image sea clutter better than the horizontally polarised counterparts (Ward et al., 2013), will improve the quality of time exposure images created using the raw image data. More backscatter from the sea surface clutter will lead to stronger returns from areas at long ranges and more information on waterlines across the survey will be available. One of the primary drawbacks of relying on marine radar to image the sea surface is the lack of data availability during very calm sea states. If the sea surface does not exhibit a wind roughened surface then the traditional horizontally polarised (HH) radar will return very little information. Vertically polarised radar EM waves interact differently with the sea surface and will potentially provide more information at low sea states. The use of VV radar will cause difficulties in the

traditional radar role of vessel detection in poor weather (due to increased clutter levels), although the small range (relative to other radar ranges) of the X-band radar could alleviate this issue.

In tandem with improving elevation estimates, there must also be a focus on developing a suite of methods to monitor sediment bedforms dynamics. So far the waterline method provides a very useful qualitative view on morphological changes and the ability to quantitatively estimate relatively crude beach health parameters over very large areas; but there is so far limited ability to isolate and monitor individual bedform morphology. This process could be automated and the different stages of bedform morphology, identified and tracked over a wide area. With these mobile bedforms isolated from the more stable, underlying structure, then sediment volumes of these bedforms can be estimated which will be extremely useful information to coastal management and stakeholders.

An immediate next step in future work is the collection, processing and analysis of the marine radar data collected from new radar deployments, particularly the pilot deployment of the Rapidar at Eastham Locks which may also involve testing a vertically polarised antenna on the Rapidar platform. This area is critical for the local maritime economy, as the navigation channel connecting the Manchester Ship Canal and Stanlow oil refinery docks to the River Mersey estuary, cuts through the sandbanks close to the radar location. It is therefore of vital importance that the morphology of this area is monitored in order to optimise maintenance dredging and reduce risks to shipping. Further to this, the coupling of this intertidal survey technique with previously

developed wave inversion techniques to completely survey the nearshore area. This will certainly provide unprecedented information on morphology and give much greater situational awareness.

Table 8.1 outlines an overview of the recommended procedure for a Rapidar/radar deployment for the purpose of conducting coastal survey including site survey prior to deployment, installation and data analysis regime. This procedure is very site specific and as such details on logistics and timescales are omitted from this overview.

Stakeholder meeting
Assess the needs of the customer/partner. Meeting to discuss the area to be surveyed and particular morphological phenomena to be observed. Ensure that the radar is the most suitable technique and has the required horizontal and vertical resolution and accuracy to provide useful data to the stakeholder group. Decide on timings for the deployment and data delivery requirements.
Initial site survey
Identify potential locations to mount a radar system, ensure adequate power and communications infrastructures are available at the potential sites. If no suitable sites are identified, then a Rapidar deployment is required. Select sites with good line of sight to the area of coast to be surveyed stable foundation for Rapidar deployment i.e. not on sand dunes or mud. Potential sites for deployment of an in situ pressure transducer for measurement of tidal elevation are also assessed, in many cases there may already be a

tide gauge in place nearby, in which case assess to tidal data is arranged.
Site suitability assessment
Having inspected a number of potential deployment sites, each one must be assessed according to a variety of factors such as accessibility (for Rapidar transport), shadowing impact (which can be assessed using a previous topographical survey or camera images taken from the potential radar site) and power/communication infrastructure.
Radar deployment
Permission to work is secured from partner/customer, risk assessments and relevant health and safety measures are put in place. The Rapidar platform is prepared for deployment at the Marlan premises and logistics are planned to enable delivery of the survey platform. The Rapidar is deployed on-site and system checks are made, radar is engaged remotely. Tidal water level sensor is also deployed at a suitable location and transmission of water level data is confirmed. Mechanisms for data retrieval are put in place.
Warm up period
The initial period of the deployment is spent ensuring both image and tidal data are being collected effectively and radar is operating correctly. Preliminary analysis of snapshot radar images are used to estimate shadowed areas and identify potential problems with radar operation.
Data collection and analysis
Once the first dataset (two weeks) is retrieved, analysis of the data can proceed, tidal

data is collected remotely and feeds directly into the waterline analysis algorithm.
Data delivery
The customer/partner is sent the data product frequently according to their specified schedule. Includes processed xyz elevation survey, corresponding error estimates and confidence bounds along with a map of areas in shadow. These data products are provided for the duration of the project.
Withdrawal of installation
Following the successful provision of data throughout the duration of the project the stakeholders will reconvene and determine if continued monitoring is required, if so the system will continue to operate. If the service is no longer required, then the Rapidar platform will be removed from site along with any ancillary equipment.

Table 8.1: Recommended procedure for deployment of a Rapidar survey platform.

9 FINAL CONCLUSIONS

The extensive area of beach and sandbanks covered by the tidal range is notoriously difficult to monitor on a regular basis. Manual surveys are challenging due to the threat of the tides, the large expanse of area and the dynamic nature of the intertidal beach. These conditions present an ideal environment for a shore-based marine radar system capable of resolving the morphology of these areas accurately, cost-effectively and over long time periods. A novel methodology for surveying intertidal areas using standard X-band marine radar was developed in partnership with *Marlan Maritime Technologies* and the *National Oceanography Centre*. The methodology was developed using data from a previous radar deployment in the River Dee estuary

The robustness of the radar waterline technique was assessed by measuring the elevations of several points known to be stable rocks that are submerged at some point by the tide. These locations were measured over ten months and once temporal smoothing was applied, found to vary by only ±10 cm. This gave confidence that

elevation trends observed in sandy areas were reflective of actual processes of erosion or accretion, and not artefacts of data processing. Elevations derived using the radar were compared to those observed using an airborne LiDAR (details of survey given in Chapter 4) and were found to compare well (0 - 50 cm) over areas with clear line of sight and not liable to be subject to pooling tidal water. The results were seen to degrade with range, though this was mainly a function of an increase in area shadowed from the radar at longer ranges and decreased pixel intensity at extreme ranges.

The radar waterline survey was applied to a three year dataset from Hilbre Island resulting in a sequence of 62 bi-weekly elevation maps. This allowed the monitoring of changing morphology at several dynamic sites within the intertidal area. The results of this morphological analysis are presented in Chapter 6 where several measures of beach health were used to assess the morphological trends of the study site. The results derived indicate lowest sediment volumes during the autumn and winter, with highest volumes in spring and summer. A series of cross-shore profiles were also extracted and their changing morphology observed over three years, this enabled the observation of migrating bedform crests.

During the three year radar deployment at Hilbre Island, 18 months of data were also sampled out to a longer range of 7.5 km. When the radar waterline technique was applied to the long-range radar data, elevations were derived. However, a combination of factors including range induced radar power drop off, increased areas of shadow and

decreasing azimuthal resolution in the raw data make the results derived at longer ranges exhibit poor accuracy when compared to those derived by short-range surveys.

The value of a long-term, relatively low cost option for surveillance of vulnerable coastal areas is substantial, particularly to local authorities and coastal management professionals. Port Authorities can also make good use of the technology in order to improve their overall situational awareness during vessel navigation, especially when combined with subtidal bathymetric derivation techniques described in Chapter 3. Advance warning of sediment activity will likely lead to more focused dredging operations and a cost saving to the end user.

The development of the radar waterline method has highlighted several key areas of future research. These improvements focus primarily on developments to the methodology that improve vertical elevation estimates. The research presented here has prototyped the system well and identified the problem areas such as shadowing, tidal water pooling and wave run up which cause poor elevation estimates. These issues currently limit the effectiveness of the technique to carry out independent (i.e. without a LiDAR survey to provide ground truthing) and accurate instantaneous survey. However, at the current level of development it has been shown to be well suited to observing trends in intertidal morphology and tracking the migration of bedforms. Also identified were potential areas for increasing the quality of data retrieved using different hardware and supporting data. A combination of the prescribed future work will greatly increase the viability of the marine radar as a comprehensive survey and monitoring

platform, that will play a crucial role in management and defence of the ever-changing coastal zone.

10 BIBLIOGRAPHY

Aagaard, T., Nielsen, J., & Greenwood, B. (1998). Suspended sediment transport and nearshore bar formation on a shallow intermediate-state beach. *Marine Geology*, ***148***(3), 203-225.

Aarninkhof, S. G., Turner, I. L., Dronkers, T. D., Caljouw, M., & Nipius, L. (2003). A video-based technique for mapping intertidal beach bathymetry. *Coastal Engineering*, ***49***(4), 275-289.

Aarninkhof, S. G. J., Ruessink, B. G., & Roelvink, J. A. (2005). Nearshore subtidal bathymetry from time-exposure video images. *Journal of Geophysical Research: Oceans (1978–2012)*, ***110***(C6).

Admiralty, (2000). *Admiralty Tide Tables,* Volume 1, (2000) European Waters including Mediterranean Sea. Hydrographer of the Navy, *London*.

Airy, G. B. (1841). Tides and waves. *Encyclopedia Metropolitana*.

de Alegria Arzaburu, A. R., Ilic, S., & Gunawardena, Y. (2007). A study of intertidal bar dynamics using the Argus video system. In *Coastal Sediments' 07*. 1865-1876. ASCE.

Allan, J. C., & Komar, P. D. (2002). Extreme storms on the Pacific Northwest coast during the 1997-98 el niño and 1998-99 la niña. *Journal of coastal Research*, **18**(1), 175-193.

Allen, J. R. L. (1985). Principles of Physical Sedimentation.

Almar, R., Ranasinghe, R., Sénéchal, N., Bonneton, P., Roelvink, D., Bryan, K. R., & Parisot, J. P. (2012). Video-based detection of shorelines at complex meso-macro tidal beaches. *Journal of Coastal Research*, ***28***(5), 1040-1048.

Almeida, L. P., Masselink, G., Russell, P. E., Davidson, M., Poate, T., McCall, R., & Turner, I. L. (2013). Observations of the swash zone on a gravel beach during a storm using a laser-scanner (Lidar). *Journal of Coastal Research*, **65**, 636-641.

Almeida, L. P., Masselink, G., Russell, P. E., & Davidson, M. A. (2015). Observations of gravel beach dynamics during high energy wave conditions using a laser scanner. *Geomorphology*, ***228***, 15-27.

Alpers, W., & Hühnerfuss, H. (1988). Radar signatures of oil films floating on the sea surface and the Marangoni effect. *Journal of Geophysical Research: Oceans (1978–2012)*, ***93***(C4), 3642-3648.

Alpers, W. R., Ross, D. B., & Rufenach, C. L. (1981). On the detectability of ocean surface waves by real and synthetic aperture radar. *Journal of Geophysical Research*, ***86***(C7), 6481-6498.

Anderson, S., & Morris, J. (2010). Transitions in the polarimetric radar scattering properties of the sea surface. *IET radar, sonar & navigation*, ***4***(2), 251-264.

Annan, J. D. (2001). Hindcasting coastal sea levels in Morecambe Bay. *Estuarine, Coastal and Shelf Science*, ***53***(4), 459-466.

Askari, F., Donato, T. F., & Morrison, J. M. (1996). Detection of oceanic fronts at low grazing angles using an X band real aperture radar. *Journal of Geophysical Research: Oceans (1978–2012)*, ***101***(C9), 20883-20898.

Aubrey, D. G., & Speer, P. E. (1985). A study of non-linear tidal propagation in shallow inlet/estuarine systems Part I: Observations. *Estuarine, Coastal and Shelf Science*, ***21***(2), 185-205.

Austin, M. J., & Masselink, G. (2006). Observations of morphological change and sediment transport on a steep gravel beach. *Marine Geology*, ***229***(1), 59-77.

Axe, P., Ilic, S., & Chadwick, A. (1996). Evaluation of beach modelling techniques behind detached breakwaters. *Coastal Engineering Proceedings*, ***1***(25).

Bacon, R. (1932). *The Concise Story of the Dover Patrol*. Hutchinson & Company Limited.

Bailey, M. (2009). Report on the state of the navigation of the River Mersey, Department for Transport. Mersey conservancy. Port of Liverpool. Available at:, http://assets.dft.gov.uk/publications/report-on-navigation-of-river-mersey-2009/report.pdf (Date accessed: 08/08/14).

Barbier, E. B., Hacker, S. D., Kennedy, C., Koch, E. W., Stier, A. C., & Silliman, B. R. (2011). The value of estuarine and coastal ecosystem services. *Ecological Monographs*, ***81***(2), 169-193.

Barnard, P. L., Erikson, L. H., Rubin, D. M., Dartnell, P., & Kvitek, R. G. (2012). Analyzing bedforms mapped using multibeam sonar to determine regional bedload sediment transport patterns in the San Francisco Bay coastal system. *International Association of Sedimentologists' Special Publication Book on Shelf Sedimentology, Special Publication*, ***44***, 273-294.

Barnett, M. R., & Wang, H. (1988). Effects of a vertical seawall on profile response. *Coastal Engineering Proceedings*, ***1***(21).

Barrick, D.E., Fernandez, V., Ferrer, M. I., Whelan, C., & Breivik, Ø. (2012). A short-term predictive system for surface currents from a rapidly deployed coastal HF radar network. *Ocean Dynamics*, ***62***(5), 725-740.

Barrick, D. E. (1977). The ocean wave height nondirectional spectrum from inversion of the HF sea-echo Doppler spectrum. *Remote Sensing of Environment*, ***6***(3), 201-227.

Battjes, J. A. (1974). Surf similarity. *Coastal Engineering Proceedings*, ***1***(14).

Bell, F. C. (1971). The Mystery of Andrea Doria. *Journal of Navigation*, ***24***(02), 147-153.

Bell, P. S. (2001). Determination of bathymetry using marine radar images of waves. In: Proceedings of the 4th International Symposium on Ocean Wave Measurement and Analysis, San Francisco, California, **1**, 251-257.

Bell, P. S. (2008). Mapping shallow water coastal areas using a standard marine X-Band radar. In: Hydro8, Liverpool, 4th-6th November 2008. Liverpool, International Federation of Hydrographic Societies. 1–9.

Bell, P. S. (2009). Remote bathymetry and current mapping around shore-parallel breakwaters. *33rd IAHR Congress Water Engineering for a Sustainable Environment*.

Bell, P. S. (2010). Submerged dunes and breakwater embayments mapped using wave inversions of shore-mounted marine X-band radar data. In: *Geoscience and Remote Sensing Symposium (IGARSS), 2010 IEEE International*. 4334-4337. IEEE.

Bell, P. S., Lawrence, J., & Norris, J. V. (2012). Determining currents from marine radar data in an extreme current environment at a tidal energy test site. In: *Geoscience and Remote Sensing Symposium (IGARSS), 2012 IEEE International*. 7647-7650. IEEE.

Bell, P. S., Williams, J. J., Clark, S., Morris, B. D., & Vila-Concej, A. (2006). Nested radar systems for remote coastal observations. *Journal of Coastal Research*, *Special Issue* **39**, 483-487.

Bell, P. S. (2007). Mapping the bathymetry of the Dee estuary using wave inversions of marine radar image sequences. In: *Rapid Environmental Assessment (REA) Conference:*

Challenges for Monitoring and Prediction, Villa Marigola, Lerici, Italy, 25-27 September 2007. ITALY, N.U.R.C. NATO Research Centre, La Spezia, Italy.

Bell, P. S. (1999). Shallow water bathymetry derived from an analysis of X-band marine radar images of waves. *Coastal Engineering*, ***37***(3), 513-527.

Bell, P. S., Bird, C. O., & Plater, A. J. (2016). A temporal waterline approach to mapping intertidal areas using X-band marine radar. *Coastal Engineering*, ***107*,** 84-101.

Bell, P. S., & McCann, D. L. (2013). Hydrodynamics and Beastie Monitoring at UK Marine Renewable Energy Sites. *Unpublished Impact Summary*: Available at: http://nora.nerc.ac.uk/505438/ (Date accessed: 01/08/15).

Bell, P. S., & Osler, J. C. (2011). Mapping bathymetry using X-band marine radar data recorded from a moving vessel. *Ocean dynamics*, ***61***(12), 2141-2156.

Benassai, G., Pugliano, G., Di Paola, G., & Mucerino, L. (2015). UAV survey of a Thyrrenian micro-tidal beach for shoreline evolution update. In *EGU General Assembly Conference Abstracts.* **17**, 2676.

Benedet, L., Finkl, C. W., Campbell, T., & Klein, A. (2004). Predicting the effect of beach nourishment and cross-shore sediment variation on beach morphodynamic assessment. *Coastal Engineering*, ***51***(8), 839-861.

Benny, A. H., & Dawson, G. J. (1983). Satellite imagery as an aid to bathymetric charting in the Red Sea. *The Cartographic Journal*, ***20***(1), 5-16.

Bierwirth, P. N., Lee, T. J., & Burne, R. V. (1993). Shallow sea-floor reflectance and water depth derived by unmixing multispectral imagery. *Photogrammetric Engineering and Remote Sensing;(United States)*, ***59***(3).

Bikker, J. (2007). Real-time ray tracing through the eyes of a game developer. In *Interactive Ray Tracing, 2007. RT'07. IEEE Symposium on*. 1-10. IEEE.

Bird, E. (2011). Coastal geomorphology: an introduction. John Wiley & Sons.

Blackwell, M. S. A., Hogan, D. V., & Maltby, E. (2004). The short-term impact of managed realignment on soil environmental variables and hydrology. *Estuarine, Coastal and Shelf Science*, ***59***(4), 687-701.

Blanton, J. O., Lin, G., & Elston, S. A. (2002). Tidal current asymmetry in shallow estuaries and tidal creeks. *Continental Shelf Research*, ***22***(11), 1731-1743.

Blenkinsopp, C. E., Mole, M. A., Turner, I. L., & Peirson, W. L. (2010). Measurements of the time-varying free-surface profile across the swash zone obtained using an industrial LIDAR. *Coastal Engineering*, ***57***(11), 1059-1065.

Blenkinsopp, C. E., Turner, I. L., Masselink, G., & Russell, P. E. (2011). Swash zone sediment fluxes: Field observations. *Coastal engineering*, ***58***(1), 28-44.

Blott, S. J., & Pye, K. (2004). Morphological and sedimentological changes on an artificially nourished beach, Lincolnshire, UK. *Journal of Coastal Research*, **201**, 214-233.

Boczar-Karakiewicz, B., & Davidson-Arnott, R. G. (1987). Nearshore bar formation by non-linear wave processes—a comparison of model results and field data. *Marine Geology*, ***77***(3), 287-304.

Booij, N. (1981). *Gravity* waves on water with non-uniform depth and current (Doctoral dissertation, TU Delft, Delft University of Technology).

Booij, N., & Holthuijsen, L. H. (1987). Propagation of ocean waves in discrete spectral wave models. *Journal of Computational Physics*, ***68***(2), 307-326.

Bowen, A. J. (1980). In: McCann, S. B. (Eds.), The coastline of Canada. *Pap. Geol. Surv. Can.,* ***80***(*10)*, 439.

Boyd, R., Dalrymple, R., & Zaitlin, B. A. (1992). Classification of clastic coastal depositional environments. *Sedimentary Geology*, ***80***(3), 139-150.

Bray, M. J., & Hooke, J. M. (1997). Prediction of soft-cliff retreat with accelerating sea-level rise. *Journal of Coastal Research*, **13**(2), 453-467.

Briggs, J. N. (2004). *Target detection by marine radar* (Vol. 16). IET.

Brink-Kjær, O. (1984). Depth–current refraction of wave spectra. In *Proc. Symp. Description and Modelling of Directional Seas*, **12**. Tech. Univ. Denmark Copenhagen.

Brodie, K. L., Slocum, R. K., & McNinch, J. E. (2012). New insights into the physical drivers of wave runup from a continuously operating terrestrial laser scanner. In: *Oceans, 2012,* 1-8. IEEE.

Broussard, M. L. (Ed.). (1975). *Deltas: models for exploration*, **2**. Houston Geological Society.

Brown, J. M., & Davies, A. G. (2010). Flood/ebb tidal asymmetry in a shallow sandy estuary and the impact on net sand transport. *Geomorphology*, ***114***(3), 431-439.

Butt, T., & Russell, P. (2000). Hydrodynamics and cross-shore sediment transport in the swash-zone of natural beaches: a review. *Journal of Coastal Research*, **16**, 255-268.

Caragliu, A., Del Bo, C., & Nijkamp, P. (2011). Smart cities in Europe. *Journal of urban technology*, ***18***(2), 65-82.

Carter, R. W. G., & Woodroffe, C. D., (Eds.) (1997). (Eds) Coastal evolution - Late Quaternary shoreline morpholodynamics: Cambridge, UK: Cambridge University Press.

Castelle, B., Marieu, V., Bujan, S., Splinter, K. D., Robinet, A., Sénéchal, N., & Ferreira, S. (2015). Impact of the winter 2013–2014 series of severe Western Europe storms on a double-barred sandy coast: Beach and dune erosion and megacusp embayments. *Geomorphology*, ***238***, 135-148.

Catalan, P. A., & Haller, M. C. (2005). Nonlinear Phase Speeds And Depth inversions. In *Proc. 5th Coastal Dynamics conf., ASCE*.

Chang, L., Tang, Z. S., Chang, S. H., & Chang, Y. L. (2008). A region-based GLRT detection of oil spills in SAR images. *Pattern Recognition Letters*, ***29***(14), 1915-1923.

Chust, G., Galparsoro, I., Borja, A., Franco, J., & Uriarte, A. (2008). Coastal and estuarine habitat mapping, using LIDAR height and intensity and multi-spectral imagery. *Estuarine, Coastal and Shelf Science*, ***78***(4), 633-643.

Chust, G., Grande, M., Galparsoro, I., Uriarte, A., & Borja, Á. (2010). Capabilities of the bathymetric Hawk Eye LiDAR for coastal habitat mapping: a case study within a Basque estuary. *Estuarine, Coastal and Shelf Science*, ***89***(3), 200-213.

Coakley, D. B., Haldeman, P. M., Morgan, D. G., Nicolas, K. R., Penndorf, D. R., Wetzel, L. B., & Weller, C. S. (2001). Electromagnetic scattering from large steady breaking waves. *Experiments in fluids*, ***30***(5), 479-487.

Coco, G., Huntley, D. A., & O'Hare, T. J. (2000). Investigation of a self-organization model for beach cusp formation and development. *Journal of Geophysical Research: Oceans (1978–2012)*, ***105***(C9), 21991-22002.

Cooper, J. A. G., & McKenna, J. (2008). Working with natural processes: the challenge for coastal protection strategies. *The Geographical Journal*, ***174***(4), 315-331.

Cowell, P. J., Roy, P. S., & Jones, R. A. (1995). Simulation of large-scale coastal change using a morphological behaviour model. *Marine Geology*, ***126***(1), 45-61.

Cowell, P. J., & Thom, B. G. (1994). *Morphodynamics of coastal evolution*. Cambridge University Press, Cambridge, United Kingdom and New York, NY, USA.

Crombie, D. D. (1955). Doppler spectrum of sea echo at 13.56 Mc./s *Nature*, **175**(4459), 681–682.

Dally, W. R. (1990). Random breaking waves: a closed-form solution for planar beaches. *Coastal Engineering*, ***14***(3), 233-263.

Dally, W.R., Dean, R.G., (1984) Suspended sediment transport and beach profile evolution. Journal Waterway, Port, Coastal and Ocean Engineering, **10**, 15-33.

Dally, W. R., Dean, R. G., & Dalrymple, R. A. (1985). Wave height variation across beaches of arbitrary profile. *Journal of Geophysical Research: Oceans (1978–2012)*, ***90***(C6), 11917-11927.

Dalrymple, R. W., Zaitlin, B. A., & Boyd, R. (1992). Estuarine facies models: conceptual basis and stratigraphic implications: perspective. *Journal of Sedimentary Research*, ***62***(6).

Dalrymple, R. A. (1988). Model for refraction of water waves. *Journal of Waterway, Port, Coastal, and Ocean Engineering*, ***114***(4), 423-435.

Dalrymple, R. A., Kirby, J. T., & Hwang, P. A. (1984). Wave diffraction due to areas of energy dissipation. *Journal of Waterway, Port, Coastal, and Ocean Engineering*, ***110***(1), 67-79.

Dalrymple, R. W. (1984). Morphology and internal structure of sandwaves in the Bay of Fundy. *Sedimentology*, ***31***(3), 365-382.

Dankert, H., Horstmann, J., & Rosenthal, W. (2003). Ocean wind fields retrieved from radar-image sequences. *Journal of Geophysical Research: Oceans (1978–2012)*, ***108***(C11).

Dankert, H., & Horstmann, J. (2006). A marine-radar wind sensor. In: *IEEE International Symposium on Geoscience and Remote Sensing, 2006. IGARSS 2006,* 1296-1299. IEEE.

Dankert, H., & Rosenthal, W. (2004). Ocean surface determination from X-band radar-image sequences. *Journal of Geophysical Research: Oceans (1978–2012)*, ***109***(C4).

Darwin, N., Ahmad, A., & Zainon, O. (2014). The potential of unmanned aerial vehicle for large scale mapping of coastal area. In *IOP Conference Series: Earth and Environmental Science*, **18**(1). IOP Publishing.

Davidson, M., Van Koningsveld, M., de Kruif, A., Rawson, J., Holman, R., Lamberti, A., & Aarninkhof, S. (2007). The CoastView project: Developing video-derived Coastal State Indicators in support of coastal zone management. *Coastal Engineering*, ***54***(6), 463-475.

Davis Jr, R., & Fitzgerald, D. (2009). *Beaches and coasts*. John Wiley & Sons.

Dawson, A. G. (1994). Geomorphological effects of tsunami run-up and backwash. *Geomorphology*, ***10***(1), 83-94.

Dean, R. G. (1986). Coastal armoring: effects, principles and mitigation. *Coastal Engineering Proceedings*, ***1***(20).

Dean, R. G., & Dalrymple, R. A. (2004). *Coastal processes with engineering applications*. Cambridge University Press.

Dalrymple, R. A., & Dean, R. G. (1991). *Water wave mechanics for engineers and scientists*. Prentice-Hall.

Dellepiane, S., De Laurentiis, R., & Giordano, F. (2004). Coastline extraction from SAR images and a method for the evaluation of the coastline precision. *Pattern Recognition Letters*, ***25***(13), 1461-1470.

Demirbilek, Z., & Sargent, F. (1999). Deep-draft coastal navigation entrance channel practice (No. CHETN-IX-1). Engineering Research and Development Center, Vicksburg MS Coastal and Hydraulics Lab.

Dingler, J. R., & Reiss, T. E. (2002). Changes to Monterey Bay beaches from the end of the 1982–83 El Nino through the 1997–98 El Nino. *Marine Geology*, ***181***(1), 249-263.

Diop, S., Barusseau, J. P., & Descamps, C. (Eds.). (2014). The Land/ocean Interactions in the Coastal Zone of West and Central Africa. Springer.

Dissanayake, P., Brown, J., & Karunarathna, H. (2015). Impacts of storm chronology on the morphological changes of the Formby beach and dune system, UK. *Natural Hazards and Earth System Sciences Discussions*, ***3***(4), 2565-2597.

Van Dongeren, A., Plant, N., Cohen, A., Roelvink, D., Haller, M. C., & Catalán, P. (2008). Beach Wizard: Nearshore bathymetry estimation through assimilation of model computations and remote observations. *Coastal engineering*, ***55***(12), 1016-1027.

Van Dongeren, A. R., & De Vriend, H. J. (1994). A model of morphological behaviour of tidal basins. *Coastal Engineering*, ***22***(3), 287-310.

Draper, L. (1966). 'Freak' ocean waves. *Weather*, ***21***(1), 2-4.

Dronkers, J. (1986). Tidal asymmetry and estuarine morphology. *Netherlands Journal of Sea Research*, ***20***(2), 117-131.

Drummond, C. D., Harley, M. D., Turner, I. L., Matheen, A. N. A., & Glamore, W. C. (2015). UAV Applications to Coastal Engineering. *Coast and Ports 2015*. 1-6.

Duffy, G. P., & Clarke, J. H. (2012). Measurement of bedload transport in a coastal sea using repeat swath bathymetry surveys: assessing bedload formulae using sand dune migration. *Sediments, Morphology and Sedimentary Processes on Continental Shelves: Advances in Technologies, Research and Applications. International Association of Sedimentology, Wiley–Blackwell, Oxford*, 249-272.

Dugan, J. P., & Piotrowski, C. C. (2003). Surface current measurements using airborne visible image time series. *Remote sensing of environment*, ***84***(2), 309-319.

Dugan, J. P., Piotrowski, C. C., & Williams, J. Z. (2001). Water depth and surface current retrievals from airborne optical measurements of surface gravity wave dispersion. *Journal of Geophysical Research: Oceans (1978–2012)*,***106***(C8), 16903-16915.

Elfrink, B., & Baldock, T. (2002). Hydrodynamics and sediment transport in the swash zone: a review and perspectives. *Coastal Engineering*, ***45***(3), 149-167.

El-Magd, I. A., & Hillman, P. F. (2009). Geomorphological monitoring of a highly dynamic estuary using oblique aerial photographs. *International Journal of Digital Earth*, ***2***(2), 109-121.

Eltner, A., Baumgart, P., Maas, H. G., & Faust, D. (2015). Multi-temporal UAV data for automatic measurement of rill and interrill erosion on loess soil. *Earth Surface Processes and Landforms*, ***40***(6), 741-755.

Emerson, S. D., & Nadeau, J. (2003). A coastal perspective on security. *Journal of hazardous materials*, ***104***(1), 1-13.

Emmerson, R. H. C., Birkett, J. W., Scrimshaw, M., & Lester, J. N. (2000). Solid phase partitioning of metals in managed retreat soils: field changes over the first year of tidal inundation. *Science of the Total Environment*, ***254***(1), 75-92.

van Enckevort, I. V., & Ruessink, B. G. (2001). Effect of hydrodynamics and bathymetry on video estimates of nearshore sandbar position. *Journal of Geophysical Research: Oceans (1978–2012)*, ***106(***C8), 16969-16979.

Enfield, D. B., Mestas-Nunez, A. M., & Trimble, P. J. (2001). The Atlantic multidecadal oscillation and its relation to rainfall and river flows in the continental U. S. *Geophysical Research Letters*, ***28***(10), 2077-2080.

Esteves, L. S., Williams, J. J., & Bell, P. S. (2007). Assessing nearshore bar movements during storms using time-averaged X-band radar images. *Proc. Coastal Sediments' 07, ASCE*, 1886-1899.

Fernandes, R. D., Vinzon, S. B., & de Oliveira, F. A. (2007). Navigation at the Amazon River Mouth: sand bank migration and depth surveying. In: *Ports, **3**,* 1977-2007.

Fingas, M., & Brown, C. (2014). Review of oil spill remote sensing. *Marine pollution bulletin*, ***83***(1), 9-23.

FitzGerald, D. M., Kraus, N. C., & Hands, E. B. (2000). *Natural mechanisms of sediment bypassing at tidal inlets* (No. ERDC/CHL-CHETN-IV-30). Engineering Research and Development Center, Vicksburg MS Coastal and Hydraulics Lab.

Flampouris, S., Seemann, J., & Ziemer, F. (2009). Sharing our experience using wave theories inversion for the determination of the local depth. In *OCEANS 2009-EUROPE*, 1-7. IEEE.

Flather, R. A., & McCartney, B. S. (1995). Construction of an inter-tidal digital elevation model by the 'water-line' method. *Geophysical Research Letters*, ***22***(23), 3187-3190.

French, P. W. (2001). Coastal defences: processes, problems and solutions. Psychology Press.

French, P. W. (2004). The changing nature of, and approaches to, UK coastal management at the start of the twenty-first century. *The Geographical Journal*, ***170***(2), 116-125.

French, P. W. (2006). Managed realignment–the developing story of a comparatively new approach to soft engineering. *Estuarine, Coastal and Shelf Science*, ***67***(3), 409-423.

Friedrichs, C. T., & Aubrey, D. G. (1988). Non-linear tidal distortion in shallow well-mixed estuaries: a synthesis. *Estuarine, Coastal and Shelf Science*, ***27***(5), 521-545.

Friedrichs, C., & Madsen, O., (1992). Nonlinear diffusion of the tidal signal in frictionally dominated embayments. *Journal of Geophysical Research*, ***97***(N3C4), 5637-5650.

Fuchs, J., Regas, D., Waseda, T., Welch, S., & Tulin, M. P. (1999). Correlation of hydrodynamic features with LGA radar backscatter from breaking waves. *Geoscience and Remote Sensing, IEEE Transactions on*, ***37***(5), 2442-2460.

Füssel, H. M., & Jol, A. (2012). Climate change, impacts and vulnerability in Europe 2012 an indicator-based report. *European Environment Agency.*

Galal, E. M., & Takewaka, S. (2008). Longshore migration of shoreline mega-cusps observed with X-band radar. *Coastal engineering journal*, ***50***(03), 247-276.

Gallop, S. L., Woodward, E., Brander, R. W., & Pitman, S. J. (2016). Perceptions of rip current myths from the central south coast of England. *Ocean & Coastal Management*, ***119***, 14-20.

Gao, J. (2009). Bathymetric mapping by means of remote sensing: methods, accuracy and limitations. *Progress in Physical Geography*, ***33***(1), 103-116.

Garcia, D. (2010). Robust smoothing of gridded data in one and higher dimensions with missing values. *Computational statistics & data analysis*, ***54***(4), 1167-1178.

Gaudin, D., Delacourt, C., Allemand, P., Jaud, M., Ammann, J., Tisseau, C., & Cuq, V. (2009). High resolution DEM derived from thermal infrared images: Example of Aber Benoit (France). In *Geoscience and Remote Sensing Symposium, 2009 IEEE International, IGARSS 2009*, **4**, IEEE.

Geyer, W. R., & Signell, R. (1990). Measurements of tidal flow around a headland with a shipboard acoustic Doppler current profiler. *Journal of Geophysical Research: Oceans (1978–2012)*, ***95***(C3), 3189-3197.

Ghermandi, A., & Nunes, P. A. (2013). A global map of coastal recreation values: Results from a spatially explicit meta-analysis. *Ecological economics*, ***86***, 1-15.

Giffinger, R., Fertner, C., Kramar, H., Kalasek, R., Pichler-Milanovic, N., & Meijers, E. (2007). *Smart cities-Ranking of European medium-sized cities*. Vienna University of Technology.

Goff, J. A., Swift, D. J., Duncan, C. S., Mayer, L. A., & Hughes-Clarke, J. (1999). High-resolution swath sonar investigation of sand ridge, dune and ribbon morphology in the offshore environment of the New Jersey margin. *Marine Geology*, ***161***(2), 307-337.

González-Jorge, H., Puente, I., Roca, D., Martínez-Sánchez, J., Conde, B., & Arias, P. (2014). UAV Photogrammetry Application to the Monitoring of Rubble Mound Breakwaters. *Journal of Performance of Constructed Facilities*, **6**, 1-8.

Greenwood, B., & Davidson-Arnott, R. G. (1979). Sedimentation and equilibrium in wave-formed bars: a review and case study. *Canadian Journal of Earth Sciences*, ***16***(2), 312-332.

Greidanus, H. (1997). The use of radar for bathymetry in shallow seas. *Oceanographic Literature Review*, ***6***(44), 650.

Griggs, G. B., Tait, J. F., Scott, K., & Plant, N. (1991). The interaction of seawalls and beaches: Four years of field monitoring, Monterey Bay, California. In *Coastal Sediments (1991),* 1871-1885. ASCE.

Guenther, G. C., Brooks, M. W., & LaRocque, P. E. (2000). New capabilities of the "SHOALS" airborne lidar bathymeter. *Remote Sensing of Environment*, ***73***(2), 247-255.

Hale, P. B., & McCann, S. B. (1982). Rhythmic topography in a mesotidal, low-wave-energy environment. *Journal of Sedimentary Research*, ***52***(2).

Hands, E. B. (1991). Unprecedented migration of a submerged mound off the Alabama Coast. In: Proceedings of the 12th Annual Conference for the Western Dredging Association and 24th Annual Texas A & M Dredging Seminar.

Hanley, M. E., Hoggart, S. P. G., Simmonds, D. J., Bichot, A., Colangelo, M. A., Bozzeda, F., & Thompson, R. C. (2014). Shifting sands? Coastal protection by sand banks, beaches and dunes. *Coastal Engineering*, ***87***, 136-146.

Hanson, H., Brampton, A., Capobianco, M., Dette, H. H., Hamm, L., Laustrup, C., & Spanhoff, R. (2002). Beach nourishment projects, practices, and objectives - a European overview. *Coastal Engineering*, ***47***(2), 81-111.

Hapke, C. J., Himmelstoss, E. A., Kratzmann, M. G., List, J. H., & Thieler, E. R. (2011). National assessment of shoreline change; historical shoreline change along the New England and Mid-Atlantic coasts, 2010-1118. US Geological Survey.

Harris, P. T., & Collins, M. B. (1984). Bedform distributions and sediment transport paths in the Bristol Channel and Severn Estuary, UK. *Marine Geology*, ***62***(1), 153-166.

Hart, C. A., & Miskin, E. A. (1945). Developments in the method of determination of beach gradients by wave velocities. *Air survey research paper no. 15, Directorate of Military Survey, UK War Office*.

Harwin, S., & Lucieer, A. (2012). An accuracy assessment of georeferenced point clouds produced via multi-view stereo techniques applied to imagery acquired via unmanned aerial vehicle. *ISPRS International Archives of the Photogrammetry, Remote Sensing and Spatial Information Sciences*, ***39***, B7.

Hasan, G. J., & Takewaka, S. (2007). Observation of a stormy wave field with X-band radar and its linear aspects. *Coastal engineering journal*, ***49***(02), 149-171.

Hayes, M. O., & Boothroyd, J. C. (1969). Storms as modifying agents in the coastal environment. *Coastal Environments. NE Massachusetts, Department of Geology, University of Massachusetts, Amherst*, 290-315.

Haykin, S. (1994). *Remote sensing of sea ice and icebergs.* **13**. John Wiley & Sons.

Headrick, J. M., & Skolnik, M. I. (1974). Over-the-horizon radar in the HF band. *Proceedings of the IEEE*, ***62***(6), 664-673.

Heathershaw, A. D., Blackley, M. W. L., & Hardcastle, P. J. (1980). Wave direction estimates in coastal waters using radar. *Coastal Engineering*, ***3***, 249-267.

Hedges, T. S. (1976). Technical Note. an Empirical Modification To Linear Wave Theory. In *ICE Proceedings, **61**(3), 575-579.* Thomas Telford.

Heiss, W. H., McGrew, D. L., & Sirmans, D. (1990). NEXRAD-Next generation weather radar (WSR-88D). *Microwave Journal*, ***33***, 79.

Hessner, K., Reichert, K., Borge, J. C. N., Stevens, C. L., & Smith, M. J. (2014). High-resolution X-band radar measurements of currents, bathymetry and sea state in highly inhomogeneous coastal areas. *Ocean Dynamics*, ***64***(7), 989-998.

Hessner, K., & Bell, P. S. (2009). High resolution current & bathymetry determined by nautical X-Band radar in shallow waters. In *OCEANS 2009-EUROPE*. 1-5. IEEE.

Hessner, K., Nieto-Borge, J. C., & Bell, P. S. (2008). Nautical radar measurements in Europe: applications of WaMoS II as a sensor for sea state, current and bathymetry. In *Remote Sensing of the European Seas*. 435-446. Springer Netherlands.

Hessner, K., Reichert, K., & Rosenthal, W. (1999). Mapping of sea bottom topography in shallow seas by using a nautical radar. In *2nd Symposium on Operationalization of Remote Sensing*.

Heygster, G., Dannenberg, J., & Notholt, J. (2010). Topographic mapping of the German tidal flats analyzing SAR images with the waterline method. *IEEE Transactions on Geoscience and Remote Sensing,* ***48***(3), 1019-1030.

Holland, K. T., Raubenheimer, B., Guza, R. T., & Holman, R. A. (1995). Runup kinematics on a natural beach. *Journal of Geophysical Research: Oceans (1978–2012)*, ***100***(C3), 4985-4993.

Holland, K. T., & Holman, R. A. (1999). Wavenumber-frequency structure of infragravity swash motions. *Journal of Geophysical Research: Oceans (1978–2012)*, ***104***(C6), 13479-13488.

Holland, T. K., Holman, R., Lippmann, T. C., Stanley, J., & Plant, N. (1997). Practical use of video imagery in nearshore oceanographic field studies. *IEEE Journal of Oceanic Engineering*, ***22***(1), 81-92.

Holman, R. A., & Bowen, A. J. (1979). Edge waves on complex beach profiles. *Journal of Geophysical Research: Oceans (1978–2012)*, ***84***(C10), 6339-6346.

Holman, R. A., & Stanley, J. (2007). The history and technical capabilities of Argus. *Coastal engineering*, ***54***(6), 477-491.

Holman, R. A., & Bowen, A. J. (1982). Bars, bumps, and holes: models for the generation of complex beach topography. *Journal of Geophysical Research: Oceans (1978–2012)*, ***87***(C1), 457-468.

Holman, R., & Haller, M. C. (2013). Remote sensing of the nearshore. *Annual review of marine science*, ***5***, 95-113.

Holman, R., & Stanley, J. (2013). cBathy Bathymetry Estimation in the Mixed Wave-Current Domain of a Tidal Estuary. *Journal of Coastal Research, Special Issue,* **65**.

Holman, R. A., Lippmann, T. C., O'neill, P. V., & Hathaway, K. (1991). Video estimation of subaerial beach profiles. *Marine Geology*, ***97***(1), 225-231.

Holman, R. A., & Guza, R. T. (1984). Measuring run-up on a natural beach. *Coastal Engineering*, ***8***(2), 129-140.

Holman, R., & Stanley, J. (2013). cBathy Bathymetry Estimation in the Mixed Wave-Current Domain of a Tidal Estuary. *Journal of Coastal Research*, ***2***(65), 1391.

Holt, J. T., & Proctor, R. (2003). The role of advection in determining the temperature structure of the Irish Sea. *Journal of Physical Oceanography*, ***33***(11), 2288-2306.

Holthuijsen, L. H., Booij, N., & Ris, R. C. (1993). A spectral wave model for the coastal zone. In *Ocean Wave Measurement and Analysis (1993)* 630-641. ASCE.

Houwelingen, S. V., Masselink, G., & Bullard, J. (2008). Dynamics of multiple intertidal bars over semi-diurnal and lunar tidal cycles, North Lincolnshire, England. *Earth Surface Processes and Landforms*, ***33***(10), 1473-1490.

Hsu, K. J. (2004). Physics of sedimentology. *Springer.*

Hughes, M. G., Masselink, G., & Brander, R. W. (1997). Flow velocity and sediment transport in the swash zone of a steep beach. *Marine Geology*, ***138***(1), 91-103.

Hughes, M. G., & Turner, I. (1999). The beachface. Handbook of Beach and Shoreface Morphodynamics. Wiley, Chichester, 119-144.

Hunter, R. E., Clifton, H. E., & Phillips, R. L. (1979). Depositional processes, sedimentary structures, and predicted vertical sequences in barred nearshore systems, southern Oregon coast. *Journal of Sedimentary Research*, ***49***(3).

IEEE, 2003. IEEE Standard for letter designations for radar frequency bands, New York.

Ilić, S., & Ružić, I. (2007). Evolution of the Beach in Front of a New Seawall: Cleveleys, UK. In *Coastal Structures 2007*. Hrvatska znanstvena bibliografija i MZOS-Svibor.

Ilic, S., Van der Westhuysen, A. J., Roelvink, J. A., & Chadwick, A. J. (2007). Multidirectional wave transformation around detached breakwaters. *Coastal engineering*, ***54***(10), 775-789.

Ilic, S., & Ruiz de Alegria, A. (2006). Study of the impact of a seawall during storm events using Argus video images: Cleveleys, UK. In: *Proceedings 2nd International Short Course and Workshop in Coastal Processes and Engineering, ASCE.*.

Inoue, H. Y., Kusunoki, K., Kato, W., Suzuki, H., Imai, T., Takemi, T., & Suzuki, O. (2011). Finescale Doppler radar observation of a tornado and low-level misocyclones within a winter storm in the Japan Sea coastal region. *Monthly Weather Review*, ***139***(2), 351-369.

Irish, J. L., & Lillycrop, W. J. (1999). Scanning laser mapping of the coastal zone: the SHOALS system. *ISPRS Journal of Photogrammetry and Remote Sensing*, ***54***(2), 123-129.

Ja, S. J., West, J. C., Qiao, H., & Duncan, J. H. (2001). Mechanisms of low-grazing-angle scattering from spilling breaker water waves. *Radio Science*, ***36***(5), 981-998.

James, M. R., & Robson, S. (2014). Mitigating systematic error in topographic models derived from UAV and ground-based image networks. *Earth Surface Processes and Landforms*, ***39***(10), 1413-1420.

Jessup, A. T., Zappa, C. J., Loewen, M. R., & Hesany, V. (1997). Infrared remote sensing of breaking waves. *Nature*, **385**(6611), 52-55.

Jones, J. E., & Davies, A. M. (1996). A high-resolution, three-dimensional model of the M 2, M 4 M 6, S 2, N 2, K 1 and O 1 tides in the Eastern Irish Sea. *Estuarine, Coastal and Shelf Science*, ***42***(3), 311-346.

Kamphuis, J. W. (1991). Alongshore sediment transport rate. *Journal of Waterway, Port, Coastal, and Ocean Engineering*, ***117***(6), 624-640.

Kang, Y. Y., Ding, X. R., & Ge, X. P. (2015). Construction of a historical digital elevation model of tidal flats in Jiangsu coast using satellite data. *Remote Sensing and Smart City*, ***64***, 285.

Katoh, K. (1981). Analysis of edge waves by means of empirical eigenfunctions. *Report of the Port and Harbour Research Institute*, ***20***(3).

Kennedy, J. F. (1969). The formation of sediment ripples, dunes, and antidunes. *Annual Review of Fluid Mechanics*, ***1***(1), 147-168.

King, C. A. M. (1972). Beaches and coasts.

King, C. A. M., & Barnes, F. A. (1964). Changes in the configuration of the inter-tidal beach zone of part of the Lincolnshire coast since 1951.

King, C. A. M., & Williams, W. W. (1949). The formation and movement of sand bars by wave action. *Geographical Journal*, 70-85.

Kirby, J. T., & Dalrymple, R. A. (1986). An approximate model for nonlinear dispersion in monochromatic wave propagation models. *Coastal Engineering*, ***9***(6), 545-561.

Kirshen, P., Wake, C., Huber, M., Knuuti, K., Stampone, M. (2014). Sea-level Rise, Storm Surges, and Extreme Precipitation in Coastal New Hampshire: Analysis of Past and Projected Future Trends. *Science and Technical Advisory Panel New Hampshire Coastal Risks and Hazards Commission (RSA 483-E).*

Knaapen, M. A., Hulscher, S., Vriend, H. J., & Stolk, A. (2001). A new type of sea bed waves. *Geophysical Research Letters*, ***28***(7), 1323-1326.

Knight, P., Prime, T., Brown, J. M., Morrissey, K., & Plater, A. J. (2015). Application of flood risk modelling in a web-based geospatial decision support tool for coastal adaptation to climate change. *Natural Hazards and Earth System Sciences Discussions*, ***3***, 1615-1642.

Kobayashi, N., Raichle, A. W., & Asano, T. (1993). Wave attenuation by vegetation. *Journal of Waterway, Port, Coastal, and Ocean Engineering*, *119* **(1)**, 30-48.

Komar, P. D., & McDougal, W. G. (1988). Coastal erosion and engineering structures: the Oregon experience. *Journal of Coastal Research, Special Issue*, ***4***, 77-92.

Koopmans, B. N., & Wang, Y. (1994). Satellite radar data for topographic mapping of the tidal flats in the Wadden Sea, The Netherlands. In: *Proceedings of the 2nd Thematic Conference on Remote Sensing for Marine and Coastal Environments*. 25-35.

Kraus, N. C. (1988). The effects of seawalls on the beach: an extended literature review. *Journal of coastal Research*, *Special Issue,* **4**, 1-28.

Krivtsov, V., Howarth, M. J., Jones, S. E., Souza, A. J., & Jago, C. F. (2008). Monitoring and modelling of the Irish Sea and Liverpool Bay: An overview and an SPM case study. *ecological modelling*, ***212***(1), 37-52.

Kroon, A., & De Boer, A. (2001). Horizontal flow circulation on a mixed energy beach. In *Proceedings Coastal Dynamics*, **1**, 548-557.

Kroon, A., & Masselink, G. (2002). Morphodynamics of intertidal bar morphology on a macrotidal beach under low-energy wave conditions, North Lincolnshire, England. *Marine geology*, ***190***(3), 591-608.

Kubicki, A. (2008). Large and very large subaqueous dunes on the continental shelf off southern Vietnam, South China Sea. *Geo-Marine Letters*, ***28***(4), 229-238.

Lambiase, J. J. (1980). Sediment dynamics in the macrotidal Avon river estuary, bay of Fundy, Nova Scotia. *Canadian Journal of Earth Sciences*, ***17***(12), 1628-1641.

Van Landeghem, K. J., Uehara, K., Wheeler, A. J., Mitchell, N. C., & Scourse, J. D. (2009). Post-glacial sediment dynamics in the Irish Sea and sediment wave morphology: data–model comparisons. *Continental Shelf Research*, ***29***(14), 1723-1736.

Larson, M., & Kraus, N. C. (1992). *Analysis of cross-shore movement of natural longshore bars and material placed to create longshore bars* (No. CERC-DRP-92-5). Coastal Engineer Research and Development Center Vicksburg.

Leafe, R. (1992). Northey Island–an experimental setback. *Earth Science Conservation*, ***31***, 21-2.

Leewis, L., van Bodegom, P. M., Rozema, J., & Janssen, G. M. (2012). Does beach nourishment have long-term effects on intertidal macroinvertebrate species abundance?. *Estuarine, Coastal and Shelf Science*, ***113***, 172-181.

Leu, L. G., Kuo, Y. Y., & Liu, C. T. (1999). Coastal bathymetry from the wave spectrum of SPOT images. *Coastal Engineering Journal*, ***41***(01), 21-41.

Lippmann, T. C., & Holman, R. A. (1990). The spatial and temporal variability of sand bar morphology. *Journal of Geophysical Research: Oceans (1978–2012)*, ***95***(C7), 11575-11590.

Lippmann, T. C., Holman, R. A., & Hathaway, K. K. (1993). Episodic, nonstationary behavior of a double bar system at Duck, North Carolina, USA, 1986–1991. *Journal of Coastal Research*, *Special Issue,* **15**, 49-75.

Liu, Y., Li, M., Mao, L., Cheng, L., & Chen, K. (2013a). Seasonal pattern of tidal-flat topography along the Jiangsu middle coast, China, using HJ-1 optical images. *Wetlands*, ***33***(5), 871-886.

Liu, Y., Li, M., Zhou, M., Yang, K., & Mao, L. (2013b). Quantitative Analysis of the Waterline Method for Topographical Mapping of Tidal Flats: A Case Study in the Dongsha Sandbank, China. *Remote Sensing*, ***5***(11), 6138-6158.

Long, M. W. (1975). Radar reflectivity of land and sea. *Lexington, Mass., DC Heath and Co., 1975. 390 1*.

Longuet-Higgins, M. S., & Stewart, R. W. (1962). Radiation stress and mass transport in gravity waves, with application to 'surf beats'. *Journal of Fluid Mechanics*, *13*(04), 481-504.

Lynch, P. J., & Wagner, R. J. (1970). Rough-Surface Scattering: Shadowing, Multiple Scatter, and Energy Conservation. *Journal of Mathematical Physics*, ***11***(10), 3032-3042.

Lyzenga, D. R. (1985). Shallow-water bathymetry using combined lidar and passive multispectral scanner data. *International Journal of Remote Sensing*,***6***(1), 115-125.

Maillet, G. M., Vella, C., Berné, S., Friend, P. L., Amos, C. L., Fleury, T. J., & Normand, A. (2006). Morphological changes and sedimentary processes induced by the December 2003 flood event at the present mouth of the Grand Rhône River (southern France). *Marine Geology*, ***234***(1), 159-177.

Mancini, F., Dubbini, M., Gattelli, M., Stecchi, F., Fabbri, S., & Gabbianelli, G. (2013). Using Unmanned Aerial Vehicles (UAV) for high-resolution reconstruction of topography: The structure from motion approach on coastal environments. *Remote Sensing*, ***5***(12), 6880-6898.

de Sainte Marc, S. (1954). MG and Vincent MG: Transport Littoral Formation de Fleches et de Tombolos. In: *Proc. 5th Conference Coasial Engg*. 296-326.

Maresca, J. W., & Seibel, E. (1976). Terrestrial photogrammetric measurements of breaking waves and longshore currents in the nearshore zone. *Coastal Engineering Proceedings*, ***1***(15).

Marker, M. E. (1967). The Dee estuary: its progressive silting and salt marsh development. *Transactions of the Institute of British Geographers*, **41**, 65-71.

Mason, D. C., Davenport, I. J., Robinson, G. J., Flather, R. A., & McCartney, B. S. (1996). Construction of an inter-tidal digital elevation model by the water-line method. *Oceanographic Literature Review*, ***8***(43), 785.

Mason, D. C., & Garg, P. K. (2001). Morphodynamic modelling of intertidal sediment transport in Morecambe Bay. *Estuarine, Coastal and Shelf Science*, ***53***(1), 79-92.

Mason, D. C., Davenport, I. J., Flather, R. A., Gurney, C., Robinson, G. J., & Smith, J. A. (2001). A sensitivity analysis of the waterline method of constructing a digital elevation model for intertidal areas in ERS SAR scene of eastern England. *Estuarine, Coastal and Shelf Science*, ***53***(6), 759-778.

Mason, D. C., Amin, M., Davenport, I. J., Flather, R. A., Robinson, G. J., & Smith, J. A. (1999). Measurement of recent intertidal sediment transport in Morecambe Bay using the waterline method. *Estuarine, Coastal and Shelf Science*, ***49***(3), 427-456.

Mason, D. C., Gurney, C., & Kennett, M. (2000). Beach topography mapping—a comparison of techniques. *Journal of Coastal Conservation*, ***6***(1), 113-124.

Masselink, G. (2004). Formation and evolution of multiple intertidal bars on macrotidal beaches: application of a morphodynamic model. *Coastal Engineering*, ***51***(8), 713-730.

Masselink, G., & Anthony, E. J. (2001). Location and height of intertidal bars on macrotidal ridge and runnel beaches. *Earth Surface Processes and Landforms*, ***26***(7), 759-774.

Masselink, G., Austin, M., Scott, T., Poate, T., & Russell, P. (2014). Role of wave forcing, storms and NAO in outer bar dynamics on a high-energy, macro-tidal beach. *Geomorphology*, ***226***, 76-93.

Masselink, G., Hegge, B. J., & Pattiaratchi, C. B. (1997). Beach cusp morphodynamics. *Earth surface processes and landforms*, *22*(12), 1139-1155.

Masselink, G., Hughes, M., & Knight, J. (2014). *Introduction to coastal processes and geomorphology*. Routledge.

Masselink, G., Kroon, A., & Davidson-Arnott, R. G. D. (2006). Morphodynamics of intertidal bars in wave-dominated coastal settings—a review. *Geomorphology*, ***73***(1), 33-49.

Masselink, G., McCall, R., Poate, T., & van Geer, P. (2014). Modelling storm response on gravel beaches using XBeach-G. *Proceedings of the ICE-Maritime Engineering*, ***167***(4), 173-191.

Masselink, G., Russell, P., Blenkinsopp, C., & Turner, I. (2010). Swash zone sediment transport, step dynamics and morphological response on a gravel beach. *Marine Geology*, ***274***(1), 50-68.

Masselink, G., & Short, A. D. (1993). The effect of tide range on beach morphodynamics and morphology: a conceptual beach model. *Journal of Coastal Research*, **9**(3), 785-800.

Masselink, G., & Turner, I. L. (1999). The effect of tides on beach morphodynamics. In: *Handbook of beach and shoreface morphodynamics. Wiley, Chichester*, 204-229.

Mattie, M. G., & Harris, D. L. (1978). The use of imaging radar in studying ocean waves. *Coastal Engineering Proceedings*, ***1***(16).

McKown, J. W., & Hamilton, R. L. (1991). Ray tracing as a design tool for radio networks. *Network, IEEE*, ***5***(6), 27-30.

McCann, D. L., (2007). Dune tracking in the Dee with X-band radar: a new remote sensing technique for quantifying bedload transport. *Bangor University.* MSc. Thesis.

Mei, C. C. (1989). The applied dynamics of ocean surface waves (Vol. 1). World scientific.

Mohanty, P. K., Patra, S. K., Bramha, S., Seth, B., Pradhan, U., Behera, B., & Panda, U. S. (2012). Impact of groins on beach morphology: a case study near Gopalpur Port, east coast of India. *Journal of Coastal Research*, ***28***(1), 132-142.

Miles, A., Ilic, S., James, M., & Whyatt, D. (2013). Morphological evolution around a groyne structure at Cleveleys beach, northwest England, during a range of wave conditions. *Coastal Dynamics* 2013. 1195-1206.

Misra, S. K., Kennedy, A. B., & Kirby, J. T. (2003). An approach to determining nearshore bathymetry using remotely sensed ocean surface dynamics. *Coastal Engineering*, ***47***(3), 265-293.

Möller, I., Spencer, T., French, J. R., Leggett, D. J., & Dixon, M. (1999). Wave transformation over salt marshes: a field and numerical modelling study from North Norfolk, England. *Estuarine, Coastal and Shelf Science*, ***49***(3), 411-426.

Moore, R. D., Wolf, J., Souza, A. J., & Flint, S. S. (2009). Morphological evolution of the Dee Estuary, Eastern Irish Sea, UK: a tidal asymmetry approach. *Geomorphology*, ***103***(4), 588-596.

Morris, J. C. (2013). Estimation of the Nearshore Bathymetry using Remote Sensing Techniques: Combining Beach Wizard and cBathy (Doctoral dissertation, TU Delft, Delft University of Technology).

De Moustier, C., & Matsumoto, H. (1993). Seafloor acoustic remote sensing with multibeam echo-sounders and bathymetric sidescan sonar systems. *Marine Geophysical Researches*, ***15***(1), 27-42.

Muirhead, K., & Cracknell, A. P. (1986). Airborne lidar bathymetry. *International Journal of Remote Sensing*, ***7***(5), 597-614.

Mulder, J. P. M., & Stive, M. J. (2011). Zandmotor (sand motor): building with nature. In 25th ICID European Regional Conference, Integrated Water Management for Multiple Land Use in Flat Coastal Areas, Groningen, The Netherlands, 16-20 May 2011.

Németh, A. A., Hulscher, S. J., & de Vriend, H. J. (2002). Modelling sand wave migration in shallow shelf seas. *Continental Shelf Research*, ***22***(18), 2795-2806.

Nicholson, K. J., & Wang, C. H. (2009). Improved near-field radar cross-section measurement technique. *IEEE Antennas and Wireless Propagation Letters*, **8**, 1103-1106.

Niedermeier, A., Borge, J. C. N., Lehner, S., & Schultz-Stellenfleth, J. (2005). A wavelet-based algorithm to estimate ocean wave group parameters from radar images. *Geoscience and Remote Sensing, IEEE Transactions on*, ***43***(2), 327-336.

Niedermeier, A., Hoja, D., & Lehner, S. (2005). Topography and morphodynamics in the German Bight using SAR and optical remote sensing data. *Ocean Dynamics*, ***55***(2), 100-109.

Nieto-Borge, J. C., RodrÍguez, G. R., Hessner, K., & González, P. I. (2004). Inversion of marine radar images for surface wave analysis. *Journal of Atmospheric and Oceanic Technology*, ***21***(8), 1291-1300.

Nieto-Borge, J. C., Hessner, K., Jarabo-Amores, P., & de La Mata-Moya, D. (2008a). Signal-to-noise ratio analysis to estimate ocean wave heights from X-band marine radar image time series. *IET Radar, Sonar & Navigation*, ***2***(1), 35-41.

Nieto-Borge, J. C., Estal-Fernández, V. D., Jarabo-Amores, P., & Reichert, K. (2008b). Moving ship detection in presence of sea clutter from temporal sequences of marine radar images. In *Radar, 2008 International Conference on*, 88-93. IEEE.

Nieto-Borge ,J. C., & Guedes Soares, C. (2000). Analysis of directional wave fields using X-band navigation radar. *Coastal Engineering*, ***40***(4), 375-391.

Nieto-Borge ,J. C., Reichert, K., & Dittmer, J. (1999). Use of nautical radar as a wave monitoring instrument. *Coastal Engineering*, ***37***(3), 331-342.

NOC (2014) The coastal observatory project, COBS. Available from :http://cobs.noc.ac.uk/ (Date Accessed: 10/12/14).

Noda, E. K. (1974). Wave-induced nearshore circulation. *Journal of Geophysical Research*, ***79***(27), 4097-4106.

Nordstrom, K. F. (1980). Cyclic and seasonal beach response: a comparison of oceanside and bayside beaches. *Physical Geography*, ***1***(2), 177-196.

Nordstrom, K. F. (2014). Living with shore protection structures: A review. *Estuarine, Coastal and Shelf Science*, ***150***, 11-23.

O'Reilly, W. C., Herbers, T. H. C., Seymour, R. J., & Guza, R. T. (1996). A comparison of directional buoy and fixed platform measurements of Pacific swell. *Journal of Atmospheric and Oceanic Technology*, ***13***(1), 231-238.

Ohlmann, C., White, P., Washburn, L., Emery, B., Terrill, E., & Otero, M. (2007). Interpretation of coastal HF radar-derived surface currents with high-resolution drifter data. *Journal of Atmospheric and Oceanic Technology*, ***24***(4), 666-680.

Osorio, A. F., Medina, R., & Gonzalez, M. (2012). An algorithm for the measurement of shoreline and intertidal beach profiles using video imagery: PSDM. *Computers & Geosciences*, ***46*****,** 196-207.

Otay, E. N. (1994). Long-Term Evolution of Disposal Berms. University of Florida, Gainesville, Florida. Ph. D. thesis.

Parker, W. R. (1975). Sediment mobility and erosion on a multibarred foreshore (southwest Lancashire, UK). *Nearshore Sediment Dynamics and Sedimentation. Wiley and Sons, London*, 151-179.

Parsa, A., & Hansen, N. H. (2012). Comparison of vertically and horizontally polarized radar antennas for target detection in sea clutter—An experimental study. In *Radar Conference (RADAR), 2012 IEEE*. 0653-0658.

Patsch, K., & Griggs, G. (2008). A sand budget for the Santa Barbara littoral cell, California. *Marine Geology*, ***252***(1), 50-61.

Pérez-Alberti, A., & Trenhaile, A. S. (2015). An initial evaluation of drone-based monitoring of boulder beaches in Galicia, north-western Spain. *Earth Surface Processes and Landforms*, ***40***(1), 105-111.

Perry, A. (2000). The North Atlantic Oscillation: an enigmatic see-saw. *Progress in Physical Geography*, ***24***(2), 289-294.

Pethick, J. (1994). Estuary and wetlands: function and form. In: *International Conference on Wetland Management* 2-3.

Philander, S. G. (1999). El Nino and La Nina predictable climate fluctuations. *Reports on Progress in Physics*, ***62***(2), 123.

Phillips, O. M. (1980). Dynamics of the Upper Layer of the Ocean. *Gidrometeoizdat, Leningrad*.

Plant, N. G., & Holman, R. A. (1997). Intertidal beach profile estimation using video images. *Marine Geology*, ***140***(1), 1-24.

Plant, W. J., & Keller, W. C. (1990). Evidence of Bragg scattering in microwave Doppler spectra of sea return. *Journal of Geophysical Research: Oceans (1978–2012)*, ***95***(C9), 16299-16310.

Plater, A.J. & Grenvillle, J., (2010). Liverpool Bay: Linking the eastern Irish Sea to the Sefton Coast. In *Proceedings of the conference on coastal geomorphology and management 2008.* Sefton MBS Technical Services Department.

Poate, T., Masselink, G., Russell, P., & Austin, M. (2014). Morphodynamic variability of high-energy macrotidal beaches, Cornwall, UK. *Marine Geology*, ***350***, 97-111.

Pontee, N. (2013). Defining coastal squeeze: a discussion. *Ocean & Coastal Management*, ***84***, 204-207.

Postma, G. (1990). Depositional architecture and facies of river and fan deltas: a synthesis. *Coarse-grained deltas*, ***10***, 13-27.

Prime, T., Brown, J. M., Knight, P., & Plater, A. J. (2015). Sandscaping for mitigating coastal flood and erosion risk to energy infrastructure on gravel shorelines: Dungeness flood risk assessment. National Oceanography Centre Research and Consultancy Report, 49.

Pye, K. (1990). Physical and human influences on coastal dune development between the Ribble and Mersey estuaries, northwest England. *Coastal Dunes: Form and Process. Wiley, Chichester*, 339-359.

Pye, K. (1994). Properties of sediment particles. *Sediment Transport and Depositional Processes*, 1-24.

Pye, K., & Blott, S. J. (2006). Coastal processes and morphological change in the Dunwich-Sizewell area, Suffolk, UK. *Journal of Coastal Research*, **22**(3) ,453-473.

Pye, K., & Smith, A. J. (1988). Beach and dune erosion and accretion on the Sefton coast, northwest England. *Journal of coastal research Special Issue*, **3**, 33-36.

Quater, P. B., Grimaccia, F., & Masini, A. (2014). Airborne Unmanned Monitoring System for Coastal Erosion Assessment. In: *Engineering Geology for Society and Territory-Volume **4***, 115-120. Springer International Publishing.

Reichert, K., Nieto-Borge, J.C., & Dittmer, J. (1997). WaMoS II: an operational wave monitoring system. In *Ocean Wave Measurement and Analysis (1997)*. 370-381. ASCE.

Reichert, K., Hessner, K., Nieto-Borge, J. C., & Dittmer, J. (1999). WaMoS II: A radar based wave and current monitoring system. In *The Ninth International Offshore and Polar Engineering Conference*. International Society of Offshore and Polar Engineers.

Reineck, H. E., & Singh, I. B. (1980). Tidal flats. In *Depositional Sedimentary Environments*, 430-456. Springer Berlin Heidelberg.

Richards, M. A. (2005). *Fundamentals of radar signal processing*. McGraw-Hill Education.

Rijn, L. C. V. (1986). Sedimentation of dredged channels by currents and waves. *Journal of Waterway, Port, Coastal, and Ocean Engineering*, ***112***(5), 541-559.

Roelvink, D., Reniers, A., van Dongeren, A. P., de Vries, J. V. T., McCall, R., & Lescinski, J. (2009). Modelling storm impacts on beaches, dunes and barrier islands. *Coastal engineering*, ***56***(11), 1133-1152.

Roelvink, J. A., & Stive, M. J. F. (1989). Bar-generating cross-shore flow mechanisms on a beach. *Journal of Geophysical Research: Oceans (1978–2012)*, ***94***(C4), 4785-4800.

Rosati, J. D., & Kraus, N. C. (1999). *Shoal-reduction strategies for entrance channels*. Coastal Engineering Research and Development Center Vicksburg MS Coastal and Hydraulics Lab.

Rosenberg, L. (2013). Sea-spike detection in high grazing angle X-band sea-clutter. *Geoscience and Remote Sensing, IEEE Transactions on*, ***51***(8), 4556-4562.

Rovere, A., Casella, E., Vacchi, M., Mucerino, L., Pedroncini, A., Ferrari, M., & Firpo, M. (2014). Monitoring beach evolution using low-altitude aerial photogrammetry and UAV drones. In *EGU General Assembly Conference Abstracts* **16**. 8341.

Roy, P. S., Cowell, P. J., Ferland, M. A., & Thom, B. G. (1994). Wave-dominated coasts. *Coastal evolution: Late quaternary shoreline morphodynamics*, 121-186.

Ruessink, B. G., Kleinhans, M. G., & den Beukel, P. G. L. (1998). Observations of swash under highly dissipative conditions. *Journal of Geophysical Research: Oceans (1978–2012)*, ***103***(C2), 3111-3118.

Ruessink, B. G., & Kroon, A. (1994). The behaviour of a multiple bar system in the nearshore zone of Terschelling, the Netherlands: 1965–1993. *Marine Geology*, ***121***(3), 187-197.

Ruessink, B. G., Bell, P. S., Van Enckevort, I. M. J., & Aarninkhof, S. G. J. (2002). Nearshore bar crest location quantified from time-averaged X-band radar images. *Coastal Engineering*, ***45***(1), 19-32.

de Alegria-Arzaburu, A. R., & Masselink, G. (2010). Storm response and beach rotation on a gravel beach, Slapton Sands, UK. *Marine Geology*, ***278***(1), 77-99.

Russell, P. E., & Huntley, D. A. (1999). A cross-shore transport" shape function" for high energy beaches. *Journal of Coastal Research*, **15**(1),198-205.

Ryu, J. H., Won, J. S., & Min, K. D. (2002). Waterline extraction from Landsat TM data in a tidal flat: a case study in Gomso Bay, Korea. *Remote Sensing of Environment*, ***83***(3), 442-456.

Ryu, J. H., Kim, C. H., Lee, Y. K., Won, J. S., Chun, S. S., & Lee, S. (2008). Detecting the intertidal morphologic change using satellite data. *Estuarine, Coastal and Shelf Science*, ***78***(4), 623-632.

De Santiago, I., Morichon, D., Abadie, S., Castelle, B., Liria, P., & Epelde, I. (2013). Video monitoring nearshore sandbar morphodynamics on a partially engineered embayed beach. *Journal of Coastal Research Special Issue*, **65** 458-463.

Sasaki, T., Horikawa, K., & Hotta, S. (1976). Nearshore current on a gently sloping beach. *Coastal Engineering Proceedings*, ***1***(15).

Schanz, A., & Asmus, H. (2003). Impact of hydrodynamics on development and morphology of intertidal seagrasses in the Wadden Sea. *Marine Ecology Progress Series*, ***261***(1), 123-134.

Scharf, L. L. (1991). Statistical Signal Processing, Detection, Estimation, and Time Series Analysis. Addison.

Schmidt, A., & Soergel, U. (2013). Monitoring and change detection of Wadden Sea areas using Lidar data. *ISPRS-International Archives of the Photogrammetry, Remote Sensing and Spatial Information Sciences*, ***1***(2), 219-224.

SeaZone Solutions ltd, (2015). River Dee Navigational Chart, Scale: 1:200,000. Using: : EDINA Marine Digimap Service, Available from: http://edina.ac.uk/digimap, UK. (Date Accessed: 10/09/15).

Seiji, M., Uda, T., & Tanaka, S. (1987). Statistical study on the effect and stability of detached breakwaters. *Coastal Engineering in Japan*, ***30***(1), 131-141.

Senechal, N., Coco, G., Castelle, B., & Marieu, V. (2015). Storm impact on the seasonal shoreline dynamics of a meso-to macrotidal open sandy beach (Biscarrosse, France). *Geomorphology*, ***228***, 448-461.

Senet, C. M., Seemann, J., Flampouris, S., & Ziemer, F. (2008). Determination of bathymetric and current maps by the method DiSC based on the analysis of nautical X-band radar image sequences of the sea surface. *IEEE Transactions on Geoscience and Remote Sensing*, ***46***(8), 2267-2279.

Senet, C. M., Seemann, J., & Ziemer, F. (2001). The near-surface current velocity determined from image sequences of the sea surface. *IEEE Transactions on*, *Geoscience and Remote Sensing*, ***39***(3), 492-505.

Serafino, F., Ludeno, G., Flampouris, S., & Soldovieri, F. (2012a). Analysis of nautical X-band radar images for the generation of bathymetric map by the NSP method. In: *Geoscience and Remote Sensing Symposium (IGARSS), 2012 IEEE International*, 2829-2832. IEEE.

Serafino, F., Lugni, C., Ludeno, G., Arturi, D., Uttieri, M., Buonocore, B., & Soldovieri, F. (2012b). REMOCEAN: A flexible X-band radar system for sea-state monitoring and surface current estimation. *Geoscience and Remote Sensing Letters, IEEE*, ***9***(5), 822-826.

Serafino, F., Lugni, C., Nieto-Borge, J. C., Zamparelli, V., & Soldovieri, F. (2010a). Bathymetry determination via X-band radar data: A new strategy and numerical results. *Sensors*, ***10***(7), 6522-6534.

Serafino, F., Lugni, C., & Soldovieri, F. (2010b). A novel strategy for the surface current determination from marine X-band radar data. *Geoscience and Remote Sensing Letters, IEEE*, ***7***(2), 231-235.

Shepard, F. P. (1963). Submarine geology.

Shi, Z. (1991). Tidal bedding and tidal cyclicities within the intertidal sediments of a microtidal estuary, Dyfi River Estuary, west Wales, UK. *Sedimentary Geology*, ***73***(1), 43-58.

Short, A. D. (1975). Offshore bars along the Alaskan Arctic coast. *The Journal of Geology*, **83**(2), 209-221.

Short, A. D., & Aagaard, T. (1993). Single and multi-bar beach change models. *Journal of Coastal Research*, *Special Issue.* **15**, 141-157.

Short, A. D., & Hesp, P. A. (1982). Wave, beach and dune interactions in southeastern Australia. *Marine Geology*, ***48***(3), 259-284.

Skolnik, M. I (2008). Radar Handbook, Electronics electrical engineering.

Skolnik, M. l (1980). Introduction to RADAR systems. 2nd ed. McGraw-Hill, ed., Singapore

Sly, P. G. (1966). Marine geological studies in the eastern Irish Sea and adjacent estuaries, with special reference to sedimentation in Liverpool Bay and River Mersey (Doctoral dissertation, University of Liverpool).

Snoussi, M., Haïda, S., & Imassi, S. (2002). Effects of the construction of dams on the water and sediment fluxes of the Moulouya and the Sebou Rivers, Morocco. *Regional Environmental Change*, ***3***(1-3), 5-12.

Sobral, F., Pereira, P., Cavalcanti, P., Guedes, R., & Calliari, L. (2013). Intertidal Bathymetry Estimation Using Video Images on a Dissipative Beach. *Journal of coastal research, Special Issue*. **65**, 1439-1444.

Sonu, C. J. (1972). Field observation of nearshore circulation and meandering currents. *Journal of Geophysical Research*, ***77***(18), 3232-3247.

Soulsby, R. (1997). Dynamics of marine sands: a manual for practical applications. Thomas Telford.

Stanev, E. V., Flöser, G., & Wolff, J. O. (2003). First-and higher-order dynamical controls on water exchanges between tidal basins and the open ocean. A case study for the East Frisian Wadden Sea. *Ocean Dynamics*, ***53***(3), 146-165.

Stive, M. J., Nicholls, R. J., & de Vriend, H. J. (1991). Sea-level rise and shore nourishment: a discussion. *Coastal Engineering*, ***16***(1), 147-163.

Stive, M. J., de Schipper, M. A., Luijendijk, A. P., Aarninkhof, S. G., van Gelder-Maas, C., van Thiel de Vries, J. S., & Ranasinghe, R. (2013). A new alternative to saving our beaches from sea-level rise: The sand engine. *Journal of Coastal Research*, ***29***(5), 1001-1008.

Stockdon, H. F., Holman, R. A., Howd, P. A., & Sallenger, A. H. (2006). Empirical parameterization of setup, swash, and runup. *Coastal engineering*, ***53***(7), 573-588.

Stockdon, H. F., & Holman, R. A. (2000). Estimation of wave phase speed and nearshore bathymetry from video imagery. *Journal of Geophysical Research.* **105**(C9), 22015-22033.

Storlazzi, C. D., & Griggs, G. B. (2000). Influence of El Niño–Southern Oscillation (ENSO) events on the evolution of central California's shoreline. *Geological Society of America Bulletin*, ***112***(2), 236-249.

Strine, M. A., & Dalrymple, R. A. (1989). *Beach Fill at Fenwick Island, Delaware*. Center for Applied Coastal Research, University of Delaware.

Suh, K., & Dalrymple, R. A. (1987). Offshore breakwaters in laboratory and field. *Journal of Waterway, Port, Coastal, and Ocean Engineering*, ***113***(2), 105-121.

Sunamura, T., & Takeda, I. (1984). Landward migration of inner bars. *Marine Geology*, ***60***(1), 63-78.

Takewaka, S. (2005). Measurements of shoreline positions and intertidal foreshore slopes with X-band marine radar system. *Coastal Engineering Journal*, ***47***(03), 91-107.

Tanaka, H., Tinh, N. X., Umeda, M., Hirao, R., Pradjoko, E., Mano, A., & Udo, K. (2012). Coastal and estuarine morphology changes induced by the 2011 Great East Japan Earthquake Tsunami. *Coastal Engineering Journal*, ***54***(01), 1250010.

Tătui, F., Vespremeanu-Stroe, A., & Preoteasa, L. (2014). Alongshore variations in beach-dune system response to major storm events on the Danube Delta coast. *Journal of Coastal Research, Special Issue.* **70**.

Tennyson, E. (1991). Recent results from oil spill response research. In: *International Oil Spill Conference*. American Petroleum Institute. **1**, 673-676.

Tennyson, E. J. (1988). Shipboard navigational radar as an oil spill tracking tool-a preliminary assessment. In *OCEANS'88. A Partnership of Marine Interests. Proceedings* 857-859. IEEE.

Thom, B. G., & Hall, W. (1991). Behaviour of beach profiles during accretion and erosion dominated periods. *Earth Surface Processes and Landforms*, ***16***(2), 113-127.

Thomas, C. G., Spearman, J. R., & Turnbull, M. J. (2002). Historical morphological change in the Mersey Estuary. *Continental Shelf Research*, ***22***(11), 1775-1794.

Thomas, T. J., & Dwarakish, G. S. (2015). Numerical Wave Modelling–A Review. *Aquatic Procedia*, ***4***, 443-448.

Trizna, D. B., Hansen, J. P., Hwang, P., & Wu, J. (1991). Laboratory studies of radar sea spikes at low grazing angles. *Journal of Geophysical Research: Oceans (1978–2012)*, ***96***(C7), 12529-12537.

Tucker, M.E., (1995). Sedimentary Petrology: An Introduction to the Origin of Sedimentary Rocks. Blackwell Science, Oxford.

Uchiyama, Y. (2007). Hydrodynamics and associated morphological variations on an estuarine intertidal sand flat. *Journal of Coastal Research*, **23**(4), 1015-1027.

Us Army Corps of Engineers (1984). Shore protection manual. *Army Engineer Waterways Experiment Station, Vicksburg*, 37-53.

Uunk, L. (2008). Automated collection of intertidal beach bathymetries from Argus video images. M.Sc. Thesis.

Valenzuela, G. R. (1978). Theories for the interaction of electromagnetic and oceanic waves—A review. *Boundary-Layer Meteorology*, ***13***(1-4), 61-85.

Verhagen, H. J. (1996). Analysis of beach nourishment schemes. *Journal of Coastal Research*, **12**(1), 179-185.

Verhagen, H. J. (1992). Method for artificial beach nourishment. *Coastal Engineering Proceedings*, ***1***(23).

Viles, H. A., & Goudie, A. S. (2003). Interannual, decadal and multidecadal scale climatic variability and geomorphology. *Earth-Science Reviews*, ***61***(1), 105-131.

Vogt, P. R., & Tucholke, B. E. (1986). Imaging the ocean floor: History and state of the art. *The Geology of North America*, ***1000***, 19-44.

De Vriend, H. J., Wang, Z. B., Ysebaert, T., Herman, P. M., & Ding, P. (2011). Eco-morphological problems in the Yangtze Estuary and the Western Scheldt. *Wetlands*, ***31***(6), 1033-1042.

De Vroeg, J. H. (1987). *Schematisering brandingsruggen met behulp van jaarlijkse kustmetingen* (Doctoral dissertation, TU Delft, Delft University of Technology).

Way, O., (2013) The migration of large scale bed forms in the Dee Estuary. PhD Thesis, University of Bangor.

Wadey, M. P., Haigh, I. D., & Brown, J. M. (2014). A century of sea level data and the UK's 2013/14 storm surges: an assessment of extremes and clustering using the Newlyn tide gauge record. *Ocean Science*, ***10***(6), 1031-1045.

Wahl, T., Jensen, J., Frank, T., & Haigh, I. D. (2011). Improved estimates of mean sea level changes in the German Bight over the last 166 years. *Ocean Dynamics*, ***61***(5), 701-715.

van der Wal, D., Forster, R. M., Rossi, F., Hummel, H., Ysebaert, T., Roose, F., & Herman, P. M. (2011). Ecological evaluation of an experimental beneficial use scheme for dredged sediment disposal in shallow tidal waters. *Marine pollution bulletin*, ***62***(1), 99-108.

van der Wal, D., Pye, K., & Neal, A. (2002). Long-term morphological change in the Ribble Estuary, northwest England. *Marine Geology*, ***189***(3), 249-266.

Walton, T. L., & Sensabaugh, W. (1979). Seawall design on the open coast. Florida Sea Grant College. Technical Report, 29.

Wan, H., Wang, Q., Jiang, D., Fu, J., Yang, Y., & Liu, X. (2014). Monitoring the invasion of Spartina alterniflora using very high resolution unmanned aerial vehicle imagery in Beihai, Guangxi (China). *The Scientific World Journal*, *2014*.

Wang, H. J., Zhang, R. H., Cole, J., & Chavez, F. (1999). El Niño and the related phenomenon Southern Oscillation (ENSO): the largest signal in interannual climate variation. *Proceedings of the National Academy of Sciences*, ***96***(20), 11071-11072.

Wang, Z. B., Jeuken, M. C. J. L., Gerritsen, H., De Vriend, H. J., & Kornman, B. A. (2002). Morphology and asymmetry of the vertical tide in the Westerschelde estuary. *Continental Shelf Research*, ***22***(17), 2599-2609.

Ward, K. D., Watts, S., & Tough, R. J. (2013). Sea clutter: scattering, the K distribution and radar performance 2nd Edition. IET.

Watanabe, Y., & Mori, N. (2008). Infrared measurements of surface renewal and subsurface vortices in nearshore breaking waves. *Journal of Geophysical Research: Oceans (1978–2012)*, ***113***(C7).

Watts, S., & Gordon, A. J. (1997). The Searchwater family of radars. In *Proc. IEE Int. Conf. Radar* **97**, 334-338.

Wengrove, M. E., Henriquez, M., De Schipper, M. A., Holman, R., & Stive, M. J. F. (2013). Monitoring morphology of the sand engine leeside using Argus' cBathy. In *Coastal Dynamics 2013: 7th International Conference on Coastal Dynamics, Arcachon, France, 24-28 June 2013*. Bordeaux University.

Werner, B. T., & Fink, T. M. (1993). Beach cusps as self-organized patterns. *Science*, ***260***(5110), 968-971.

Wetzel, L. B. (1990). Electromagnetic scattering from the sea at low grazing angles. In *Surface waves and fluxes,* 109-171. Springer Netherlands.

White, K., & El Asmar, H. M. (1999). Monitoring changing position of coastlines using Thematic Mapper imagery, an example from the Nile Delta. *Geomorphology*, ***29***(1), 93-105.

Wiegel, R. L. (1964). Water wave equivalent of Mach-reflection. *Coastal Engineering Proceedings*, ***1***(9).

Wiehle, S., Lehner, S., & Pleskachevsky, A. (2015). Waterline Detection and Monitoring in the German Wadden Sea Using High Resolution Satellite-Based Radar Measurements.

International Archives of the Photogrammetry, Remote Sensing & Spatial Information Sciences. **40**(3).

Wijnberg, K. M., & Kroon, A. (2002). Barred beaches. *Geomorphology*, ***48***(1), 103-120.

Williams, W. W. (1947). The determination of gradients on enemy-held beaches. *Geographical Journal*, **109**(1), 76-90.

Wolf, J., Brown, J. M., & Howarth, M. J. (2011). The wave climate of Liverpool Bay—observations and modelling. *Ocean Dynamics*, ***61***(5), 639-655.

Wright, L. D., & Short, A. D. (1984). Morphodynamic variability of surf zones and beaches: a synthesis. *Marine geology*, ***56***(1), 93-118.

Wright, P. (1976). A cine-camera technique for process measurement on a ridge and runnel beach. *Sedimentology*, ***23***(5), 705-712.

Wyatt, L. R., Thompson, S. P., & Burton, R. R. (1999). Evaluation of high frequency radar wave measurement. *Coastal Engineering*, ***37***(3), 259-282.

Xiqing, C., Erfeng, Z., Hongqiang, M., & Zong, Y. (2005). A preliminary analysis of human impacts on sediment discharges from the Yangtze, China, into the sea. *Journal of Coastal Research*, **21**(3), 515-521.

Young, I. R., Rosenthal, W., & Ziemer, F. (1985). A three-dimensional analysis of marine radar images for the determination of ocean wave directionality and surface currents. *Journal of Geophysical Research: Oceans (1978–2012)*, ***90***(C1), 1049-1059.

Yoder, N., (2011). PeakFinder (Matlab program). Available at http://www.mathworks.com-/matlabcentral/fileexchange/25500. (Date Accessed: 01/05/2013).

Zenkovich, V.P. (1967) Processes of Coastal Development. Oliver and Boyd, Edinburgh.

Zhang, Y., Lin, H., Liu, Q., Hu, J., Li, X., & Yeung, K. (2012). Oil-spill monitoring in the coastal waters of Hong Kong and vicinity. *Marine Geodesy*, ***35***(1), 93-106.

11 APPENDIX - EXTERNAL MATLAB FUNCTIONS USED.

11.1 PEAKFINDER FUNCTION.

This section details two of the functions used in this work that were developed by the scientific community and made available for use online by their respective authors. The first of which is a 'peakfinder' algorithm used in Chapter 5 to analyse the noisy signal of pixel intensities over a two-week period, pick out the peaks which are assumed to be the transition of the breaking waves at the waterline i.e. a pixel moving from a wet to a dry state. There are numerous smaller peaks in this signal that could be wrongly interpreted as waterline transitions, this function features a selectivity index which can be changed to pick out smaller peaks in a noisy signal. This value was left as default during the analysis in this work. This function was not applied to analysis of data at long-range in Chapter 7 as the pixel intensity returns at long range were so low that this function often did not detect valid peaks, leading to data being removed.

The function is displayed below:

Yoder, N., (2011). PeakFinder (Matlab program). Available at http://www.mathworks.com-/matlabcentral/fileexchange/25500. (Date Accessed: 01/05/2013).

```
function varargout = peakfinder(x0, sel, thresh, extrema, includeEndpoints, interpolate)
%PEAKFINDER Noise tolerant fast peak finding algorithm
%  INPUTS:
%     x0 - A real vector from the maxima will be found (required)
%     sel - The amount above surrounding data for a peak to be,
%        identified (default = (max(x0)-min(x0))/4). Larger values mean
%        the algorithm is more selective in finding peaks.
%     thresh - A threshold value which peaks must be larger than to be
%        maxima or smaller than to be minima.
%     extrema - 1 if maxima are desired, -1 if minima are desired
%        (default = maxima, 1)
%     includeEndpoints - If true the endpoints will be included as
%        possible extrema otherwise they will not be included
%        (default = true)
%     interpolate - If true quadratic interpolation will be performed
%        around each extrema to estimate the magnitude and the
%        position of the peak in terms of fractional indicies. Note that
%        unlike the rest of this function interpolation assumes the
%        input is equally spaced. To recover the x_values of the input
%        rather than the fractional indicies you can do:
%        peakX = x0 + (peakLoc - 1) * dx
%        where x0 is the first x value and dx is the spacing of the
%        vector. Output peakMag to recover interpolated magnitudes.
%        See example 2 for more information.
%        (default = false)
%
%  OUTPUTS:
%     peakLoc - The indicies of the identified peaks in x0
%     peakMag - The magnitude of the identified peaks
%
%  [peakLoc] = peakfinder(x0) returns the indicies of local maxima that
%     are at least 1/4 the range of the data above surrounding data.
%
%  [peakLoc] = peakfinder(x0,sel) returns the indicies of local maxima
%     that are at least sel above surrounding data.
%
%  [peakLoc] = peakfinder(x0,sel,thresh) returns the indicies of local
```

```
%      maxima that are at least sel above surrounding data and larger
%      (smaller) than thresh if you are finding maxima (minima).
%
%   [peakLoc] = peakfinder(x0,sel,thresh,extrema) returns the maxima of the
%      data if extrema > 0 and the minima of the data if extrema < 0
%
%   [peakLoc] = peakfinder(x0,sel,thresh,extrema, includeEndpoints)
%      returns the endpoints as possible extrema if includeEndpoints is
%      considered true in a boolean sense
%
%   [peakLoc, peakMag] = peakfinder(x0,sel,thresh,extrema,interpolate)
%      returns the results of results of quadratic interpolate around each
%      extrema if interpolate is considered to be true in a boolean sense
%
%   [peakLoc, peakMag] = peakfinder(x0,...) returns the indicies of the
%      local maxima as well as the magnitudes of those maxima
%
%   If called with no output the identified maxima will be plotted along
%      with the input data.
%
%   Note: If repeated values are found the first is identified as the peak
%
% Example 1:
% t = 0:.0001:10;
% x = 12*sin(10*2*pi*t)-3*sin(.1*2*pi*t)+randn(1,numel(t));
% x(1250:1255) = max(x);
% peakfinder(x)
%
% Example 2:
% ds = 100;  % Downsample factor
% dt = .001; % Time step
% ds_dt = ds*dt; % Time delta after downsampling
% t0 = 1;
% t = t0:dt:5 + t0;
% x = 0.2-sin(0.01*2*pi*t)+3*cos(7/13*2*pi*t+.1)-2*cos((1+pi/10)*2*pi*t+0.2)-0.2*t;
% x(end) = min(x);
% x_ds = x(1:ds:end); % Downsample to test interpolation
% [minLoc, minMag] = peakfinder(x_ds, .8, 0, -1, false, true);
% minT = t0 + (minLoc - 1) * ds_dt; % Take into account 1 based indexing
% p = plot(t,x,'-',t(1:ds:end),x_ds,'o',minT,minMag,'rv');
% set(p(2:end), 'linewidth', 2); % Show the markers more clearly
% legend('Actual Data', 'Input Data', 'Estimated Peaks');
% Copyright Nathanael C. Yoder 2015 (nyoder@gmail.com)

% Perform error checking and set defaults if not passed in
error(nargchk(1,6,nargin,'struct'));
error(nargoutchk(0,2,nargout,'struct'));
```

```
s = size(x0);
flipData =  s(1) < s(2);
len0 = numel(x0);
if len0 ~= s(1) && len0 ~= s(2)
   error('PEAKFINDER:Input','The input data must be a vector')
elseif isempty(x0)
   varargout = {[],[]};
   return;
end
if ~isreal(x0)
   warning('PEAKFINDER:NotReal','Absolute value of data will be used')
   x0 = abs(x0);
end

if nargin < 2 || isempty(sel)
   sel = (max(x0)-min(x0))/4;
elseif ~isnumeric(sel) || ~isreal(sel)
   sel = (max(x0)-min(x0))/4;
   warning('PEAKFINDER:InvalidSel',...
      'The selectivity must be a real scalar.  A selectivity of %.4g will be used',sel)
elseif numel(sel) > 1
   warning('PEAKFINDER:InvalidSel',...
      'The selectivity must be a scalar.  The first selectivity value in the vector will be
used.')
   sel = sel(1);
end

if nargin < 3 || isempty(thresh)
   thresh = [];
elseif ~isnumeric(thresh) || ~isreal(thresh)
   thresh = [];
   warning('PEAKFINDER:InvalidThreshold',...
      'The threshold must be a real scalar. No threshold will be used.')
elseif numel(thresh) > 1
   thresh = thresh(1);
   warning('PEAKFINDER:InvalidThreshold',...
      'The threshold must be a scalar.  The first threshold value in the vector will be
used.')
end

if nargin < 4 || isempty(extrema)
   extrema = 1;
else
   extrema = sign(extrema(1)); % Should only be 1 or -1 but make sure
   if extrema == 0
      error('PEAKFINDER:ZeroMaxima','Either 1 (for maxima) or -1 (for minima) must be
input for extrema');
   end
end
```

```
if nargin < 5 || isempty(includeEndpoints)
   includeEndpoints = true;
else
   includeEndpoints = boolean(includeEndpoints);
end

if nargin < 5 || isempty(interpolate)
   interpolate = false;
else
   interpolate = boolean(interpolate);
end

x0 = extrema*x0(:); % Make it so we are finding maxima regardless
thresh = thresh*extrema; % Adjust threshold according to extrema.
dx0 = diff(x0); % Find derivative
dx0(dx0 == 0) = -eps; % This is so we find the first of repeated values
ind = find(dx0(1:end-1).*dx0(2:end) < 0)+1; % Find where the derivative changes sign

% Include endpoints in potential peaks and valleys as desired
if includeEndpoints
   x = [x0(1);x0(ind);x0(end)];
   ind = [1;ind;len0];
   minMag = min(x);
   leftMin = minMag;
else
   x = x0(ind);
   minMag = min(x);
   leftMin = min(x(1), x0(1));
end

% x only has the peaks, valleys, and possibly endpoints
len = numel(x);

if len > 2 % Function with peaks and valleys
   % Set initial parameters for loop
   tempMag = minMag;
   foundPeak = false;

   if includeEndpoints
      % Deal with first point a little differently since tacked it on
      % Calculate the sign of the derivative since we tacked the first
      %  point on it does not neccessarily alternate like the rest.
      signDx = sign(diff(x(1:3)));
      if signDx(1) <= 0 % The first point is larger or equal to the second
         if signDx(1) == signDx(2) % Want alternating signs
            x(2) = [];
            ind(2) = [];
            len = len-1;
```

```
    end
  else % First point is smaller than the second
    if signDx(1) == signDx(2) % Want alternating signs
      x(1) = [];
      ind(1) = [];
      len = len-1;
    end
  end
end

% Skip the first point if it is smaller so we always start on a
%  maxima
if x(1) >= x(2)
  ii = 0;
else
  ii = 1;
end

% Preallocate max number of maxima
maxPeaks = ceil(len/2);
peakLoc = zeros(maxPeaks,1);
peakMag = zeros(maxPeaks,1);
cInd = 1;
% Loop through extrema which should be peaks and then valleys
while ii < len
  ii = ii+1; % This is a peak
  % Reset peak finding if we had a peak and the next peak is bigger
  %  than the last or the left min was small enough to reset.
  if foundPeak
    tempMag = minMag;
    foundPeak = false;
  end

  % Found new peak that was lager than temp mag and selectivity larger
  %  than the minimum to its left.
  if x(ii) > tempMag && x(ii) > leftMin + sel
    tempLoc = ii;
    tempMag = x(ii);
  end

  % Make sure we don't iterate past the length of our vector
  if ii == len
    break; % We assign the last point differently out of the loop
  end

  ii = ii+1; % Move onto the valley
  % Come down at least sel from peak
  if ~foundPeak && tempMag > sel + x(ii)
    foundPeak = true; % We have found a peak
    leftMin = x(ii);
```

```
        peakLoc(cInd) = tempLoc; % Add peak to index
        peakMag(cInd) = tempMag;
        cInd = cInd+1;
      elseif x(ii) < leftMin % New left minima
        leftMin = x(ii);
      end
    end

    % Check end point
    if includeEndpoints
      if x(end) > tempMag && x(end) > leftMin + sel
        peakLoc(cInd) = len;
        peakMag(cInd) = x(end);
        cInd = cInd + 1;
      elseif ~foundPeak && tempMag > minMag % Check if we still need to add the last
point
        peakLoc(cInd) = tempLoc;
        peakMag(cInd) = tempMag;
        cInd = cInd + 1;
      end
    elseif ~foundPeak
      if x(end) > tempMag && x(end) > leftMin + sel
        peakLoc(cInd) = len;
        peakMag(cInd) = x(end);
        cInd = cInd + 1;
      elseif tempMag > min(x0(end), x(end)) + sel
        peakLoc(cInd) = tempLoc;
        peakMag(cInd) = tempMag;
        cInd = cInd + 1;
      end
    end

    % Create output
    peakInds = ind(peakLoc(1:cInd-1));
    peakMags = peakMag(1:cInd-1);
else % This is a monotone function where an endpoint is the only peak
    [peakMags,xInd] = max(x);
    if includeEndpoints && peakMags > minMag + sel
      peakInds = ind(xInd);
    else
      peakMags = [];
      peakInds = [];
    end
end

% Apply threshold value.  Since always finding maxima it will always be
%   larger than the thresh.
if ~isempty(thresh)
```

```
   m = peakMags>thresh;
   peakInds = peakInds(m);
   peakMags = peakMags(m);
end

if interpolate && ~isempty(peakMags)
   middleMask = (peakInds > 1) & (peakInds < len0);
   noEnds = peakInds(middleMask);

   magDiff = x0(noEnds + 1) - x0(noEnds - 1);
   magSum = x0(noEnds - 1) + x0(noEnds + 1)  - 2 * x0(noEnds);
   magRatio = magDiff ./ magSum;

   peakInds(middleMask) = peakInds(middleMask) - magRatio/2;
   peakMags(middleMask) = peakMags(middleMask) - magRatio .* magDiff/8;
end

% Rotate data if needed
if flipData
   peakMags = peakMags.';
   peakInds = peakInds.';
end

% Change sign of data if was finding minima
if extrema < 0
   peakMags = -peakMags;
   x0 = -x0;
end

% Plot if no output desired
if nargout == 0
   if isempty(peakInds)
      disp('No significant peaks found')
   else
      figure;
      plot(1:len0,x0,'.-',peakInds,peakMags,'ro','linewidth',2);
   end
else
   varargout = {peakInds,peakMags};
end
```

11.2 ROBUST TEMPORAL SOOTHING

The second external function used in this work is a method of fast and robust data smoothing for one-dimensional and multi-dimensional data analysis. The function SMOOTHN is sued to smooth a timeseries of topographical elevation estimates derived using the radar waterline technique. These elevation estimates have varying confidences defined by the correlation coefficient (explained fully in Chapter5) and these correlation coefficients are used as a vector of weightings to the smoothing process. That is to say that elevations with stronger correlations are given greater precedence during smoothing such that these points do not adversely effect the smoothed results as would be the case if a linear or cubic smoothing was used.

Garcia, D. (2010). Robust smoothing of gridded data in one and higher dimensions with missing values. *Computational statistics & data analysis*, ***54***(4), 1167-1178.

The full function is displayed below:

```
function [z,s,exitflag,Wtot] = smoothn(varargin)

%SMOOTHN Robust spline smoothing for 1-D to N-D data.
%   SMOOTHN provides a fast, automatized and robust discretized smoothing
%   spline for data of any dimension.
%
%   Z = SMOOTHN(Y) automatically smoothes the uniformly-sampled array Y. Y
%   can be any N-D noisy array (time series, images, 3D data,...). Non
%   finite data (NaN or Inf) are treated as missing values.
%
%   Z = SMOOTHN(Y,S) smoothes the array Y using the smoothing parameter S.
%   S must be a real positive scalar. The larger S is, the smoother the
```

```
%  output will be. If the smoothing parameter S is omitted (see previous
%  option) or empty (i.e. S = []), it is automatically determined using
%  the generalized cross-validation (GCV) method.
%
%  Z = SMOOTHN(Y,W) or Z = SMOOTHN(Y,W,S) specifies a weighting array W of
%  real positive values, that must have the same size as Y. Note that a
%  nil weight corresponds to a missing value.
%
%  Robust smoothing
%  ----------------
%  Z = SMOOTHN(...,'robust') carries out a robust smoothing that minimizes
%  the influence of outlying data.
%
%  [Z,S] = SMOOTHN(...) also returns the calculated value for S so that
%  you can fine-tune the smoothing subsequently if needed.
%
%  An iteration process is used in the presence of weighted and/or missing
%  values. Z = SMOOTHN(...,OPTION_NAME,OPTION_VALUE) smoothes with the
%  termination parameters specified by OPTION_NAME and OPTION_VALUE. They
%  can contain the following criteria:
%    -----------------
%    TolZ:      Termination tolerance on Z (default = 1e-3)
%               TolZ must be in ]0,1[
%    MaxIter:   Maximum number of iterations allowed (default = 100)
%    Initial:   Initial value for the iterative process (default =
%               original data)
%    -----------------
%  Syntax: [Z,...] = SMOOTHN(...,'MaxIter',500,'TolZ',1e-4,'Initial',Z0);
%
%  [Z,S,EXITFLAG] = SMOOTHN(...) returns a boolean value EXITFLAG that
%  describes the exit condition of SMOOTHN:
%    1     SMOOTHN converged.
%    0     Maximum number of iterations was reached.
%
```

```
%  Class Support
%  -------------
%  Input array can be numeric or logical. The returned array is of class
%  double.
%
%  Notes
%  -----
%  The N-D (inverse) discrete cosine transform functions <a
%  href="matlab:web('http://www.biomecardio.com/matlab/dctn.html')"
%  >DCTN</a> and <a
%  href="matlab:web('http://www.biomecardio.com/matlab/idctn.html')"
%  >IDCTN</a> are required.
%
%  To be made
%  ----------
%  Estimate the confidence bands (see Wahba 1983, Nychka 1988).
%
%  Reference
%  ---------
%  Garcia D, Robust smoothing of gridded data in one and higher dimensions
%  with missing values. Computational Statistics & Data Analysis, 2010.
%  <a
%
href="matlab:web('http://www.biomecardio.com/pageshtm/publi/csda10.pdf')">PDF
download</a>
%
%  Examples:
%  --------
%  % 1-D example
%  x = linspace(0,100,2^8);
%  y = cos(x/10)+(x/50).^2 + randn(size(x))/10;
%  y([70 75 80]) = [5.5 5 6];
%  z = smoothn(y); % Regular smoothing
```

```
%   zr = smoothn(y,'robust'); % Robust smoothing
%   subplot(121), plot(x,y,'r.',x,z,'k','LineWidth',2)
%   axis square, title('Regular smoothing')
%   subplot(122), plot(x,y,'r.',x,zr,'k','LineWidth',2)
%   axis square, title('Robust smoothing')
%
%   % 2-D example
%   xp = 0:.02:1;
%   [x,y] = meshgrid(xp);
%   f = exp(x+y) + sin((x-2*y)*3);
%   fn = f + randn(size(f))*0.5;
%   fs = smoothn(fn);
%   subplot(121), surf(xp,xp,fn), zlim([0 8]), axis square
%   subplot(122), surf(xp,xp,fs), zlim([0 8]), axis square
%
%   % 2-D example with missing data
%   n = 256;
%   y0 = peaks(n);
%   y = y0 + rand(size(y0))*2;
%   I = randperm(n^2);
%   y(I(1:n^2*0.5)) = NaN; % lose 1/2 of data
%   y(40:90,140:190) = NaN; % create a hole
%   z = smoothn(y); % smooth data
%   subplot(2,2,1:2), imagesc(y), axis equal off
%   title('Noisy corrupt data')
%   subplot(223), imagesc(z), axis equal off
%   title('Recovered data ...')
%   subplot(224), imagesc(y0), axis equal off
%   title('... compared with original data')
%
%   % 3-D example
%   [x,y,z] = meshgrid(-2:.2:2);
%   xslice = [-0.8,1]; yslice = 2; zslice = [-2,0];
%   vn = x.*exp(-x.^2-y.^2-z.^2) + randn(size(x))*0.06;
```

```
%   subplot(121), slice(x,y,z,vn,xslice,yslice,zslice,'cubic')
%   title('Noisy data')
%   v = smoothn(vn);
%   subplot(122), slice(x,y,z,v,xslice,yslice,zslice,'cubic')
%   title('Smoothed data')
%
%   % Cardioid
%   t = linspace(0,2*pi,1000);
%   x = 2*cos(t).*(1-cos(t)) + randn(size(t))*0.1;
%   y = 2*sin(t).*(1-cos(t)) + randn(size(t))*0.1;
%   z = smoothn(complex(x,y));
%   plot(x,y,'r.',real(z),imag(z),'k','linewidth',2)
%   axis equal tight
%
%   % Cellular vortical flow
%   [x,y] = meshgrid(linspace(0,1,24));
%   Vx = cos(2*pi*x+pi/2).*cos(2*pi*y);
%   Vy = sin(2*pi*x+pi/2).*sin(2*pi*y);
%   Vx = Vx + sqrt(0.05)*randn(24,24); % adding Gaussian noise
%   Vy = Vy + sqrt(0.05)*randn(24,24); % adding Gaussian noise
%   I = randperm(numel(Vx));
%   Vx(I(1:30)) = (rand(30,1)-0.5)*5; % adding outliers
%   Vy(I(1:30)) = (rand(30,1)-0.5)*5; % adding outliers
%   Vx(I(31:60)) = NaN; % missing values
%   Vy(I(31:60)) = NaN; % missing values
%   Vs = smoothn(complex(Vx,Vy),'robust'); % automatic smoothing
%   subplot(121), quiver(x,y,Vx,Vy,2.5), axis square
%   title('Noisy velocity field')
%   subplot(122), quiver(x,y,real(Vs),imag(Vs)), axis square
%   title('Smoothed velocity field')
%
%   See also SMOOTH, SMOOTH3, DCTN, IDCTN.
%
```

```
%   -- Damien Garcia -- 2009/03, revised 2010/11
%   Visit my <a
%
href="matlab:web('http://www.biomecardio.com/matlab/smoothn.html')">website</a
> for more details about SMOOTHN


% Check input arguments
error(nargchk(1,12,nargin));


% Test & prepare the variables
%---
k = 0;
while k<nargin && ~ischar(varargin{k+1}), k = k+1; end
%---
% y = array to be smoothed
y = double(varargin{1});
sizy = size(y);
noe = prod(sizy); % number of elements
if noe<2, z = y; return, end
%---
% Smoothness parameter and weights
W = ones(sizy);
s = [];
if k==2
   if isempty(varargin{2}) || isscalar(varargin{2}) % smoothn(y,s)
      s = varargin{2}; % smoothness parameter
   else % smoothn(y,W)
      W = varargin{2}; % weight array
   end
elseif k==3 % smoothn(y,W,s)
      W = varargin{2}; % weight array
      s = varargin{3}; % smoothness parameter
end
if ~isequal(size(W),sizy)
      error('MATLAB:smoothn:SizeMismatch',...
```

```
        'Arrays for data and weights must have same size.')
elseif ~isempty(s) && (~isscalar(s) || s<0)
   error('MATLAB:smoothn:IncorrectSmoothingParameter',...
      'The smoothing parameter must be a scalar >=0')
end
%---
% "Maximal number of iterations" criterion
I = find(strcmpi(varargin,'MaxIter'),1);
if isempty(I)
   MaxIter = 100; % default value for MaxIter
else
   try
      MaxIter = varargin{I+1};
   catch ME
      error('MATLAB:smoothn:IncorrectMaxIter',...
         'MaxIter must be an integer >=1')
   end
   if ~isnumeric(MaxIter) || ~isscalar(MaxIter) ||...
         MaxIter<1 || MaxIter~=round(MaxIter)
      error('MATLAB:smoothn:IncorrectMaxIter',...
         'MaxIter must be an integer >=1')
   end
end
%---
% "Tolerance on smoothed output" criterion
I = find(strcmpi(varargin,'TolZ'),1);
if isempty(I)
   TolZ = 1e-3; % default value for TolZ
else
   try
      TolZ = varargin{I+1};
   catch ME
      error('MATLAB:smoothn:IncorrectTolZ',...
```

```
        'TolZ must be in ]0,1[')
    end
    if ~isnumeric(TolZ) || ~isscalar(TolZ) || TolZ<=0 || TolZ>=1
        error('MATLAB:smoothn:IncorrectTolZ',...
            'TolZ must be in ]0,1[')
    end
end
%---
% "Initial Guess" criterion
I = find(strcmpi(varargin,'Initial'),1);
if isempty(I)
    isinitial = false; % default value for TolZ
else
    isinitial = true;
    try
        z0 = varargin{I+1};
    catch ME
        error('MATLAB:smoothn:IncorrectInitialGuess',...
            'Z0 must be a valid initial guess for Z')
    end
    if ~isnumeric(z0) || ~isequal(size(z0),sizy)
        error('MATLAB:smoothn:IncorrectTolZ',...
            'Z0 must be a valid initial guess for Z')
    end
end
%---
% "Weighting function" criterion
I = find(strcmpi(varargin,'Weights'),1);
if isempty(I)
    weightstr = 'bisquare'; % default weighting function
else
    try
        weightstr = lower(varargin{I+1});
    catch ME
```

```
    error('MATLAB:smoothn:IncorrectWeights',...
      'A valid weighting function must be chosen')
  end
  if ~ischar(weightstr)
    error('MATLAB:smoothn:IncorrectWeights',...
      'A valid weighting function must be chosen')
  end
end
%---
% Weights. Zero weights are assigned to not finite values (Inf or NaN),
% (Inf/NaN values = missing data).
IsFinite = isfinite(y);
nof = nnz(IsFinite); % number of finite elements
W = W.*IsFinite;
if any(W<0)
  error('MATLAB:smoothn:NegativeWeights',...
    'Weights must all be >=0')
else
  W = W/max(W(:));
end
%---
% Weighted or missing data?
isweighted = any(W(:)<1);
%---
% Robust smoothing?
isrobust = any(strcmpi(varargin,'robust'));
%---
% Automatic smoothing?
isauto = isempty(s);
%---
% DCTN and IDCTN are required
test4DCTNandIDCTN
```

```
% Creation of the Lambda tensor
%---
% Lambda contains the eingenvalues of the difference matrix used in this
% penalized least squares process.
d = ndims(y);
Lambda = zeros(sizy);
for i = 1:d
   siz0 = ones(1,d);
   siz0(i) = sizy(i);
   Lambda = bsxfun(@plus,Lambda,...
      cos(pi*(reshape(1:sizy(i),siz0)-1)/sizy(i)));
end
Lambda = -2*(d-Lambda);
if ~isauto, Gamma = 1./(1+s*Lambda.^2); end

% Upper and lower bound for the smoothness parameter
% The average leverage (h) is by definition in [0 1]. Weak smoothing occurs
% if h is close to 1, while over-smoothing appears when h is near 0. Upper
% and lower bounds for h are given to avoid under- or over-smoothing. See
% equation relating h to the smoothness parameter (Equation #12 in the
% referenced CSDA paper).
N = sum(sizy~=1); % tensor rank of the y-array
hMin = 1e-6; hMax = 0.99;
sMinBnd = (((1+sqrt(1+8*hMax.^(2/N)))/4./hMax.^(2/N)).^2-1)/16;
sMaxBnd = (((1+sqrt(1+8*hMin.^(2/N)))/4./hMin.^(2/N)).^2-1)/16;

% Initialize before iterating
%---
Wtot = W;
%--- Initial conditions for z
if isweighted
   %--- With weighted/missing data
   % An initial guess is provided to ensure faster convergence. For that
   % purpose, a nearest neighbor interpolation followed by a coarse
```

```
  % smoothing are performed.
  %---
  if isinitial % an initial guess (z0) has been provided
    z = z0;
  else
    z = InitialGuess(y,IsFinite);
  end
else
  z = zeros(sizy);
end
%---
z0 = z;
y(~IsFinite) = 0; % arbitrary values for missing y-data
%---
tol = 1;
RobustIterativeProcess = true;
RobustStep = 1;
nit = 0;
%--- Error on p. Smoothness parameter s = 10^p
errp = 0.1;
opt = optimset('TolX',errp);
%--- Relaxation factor RF: to speedup convergence
RF = 1 + 0.75*isweighted;

% Main iterative process
%---
while RobustIterativeProcess
  %--- "amount" of weights (see the function GCVscore)
  aow = sum(Wtot(:))/noe; % 0 < aow <= 1
  %---
  while tol>TolZ && nit<MaxIter
    nit = nit+1;
    DCTy = dctn(Wtot.*(y-z)+z);
```

```
    if isauto && ~rem(log2(nit),1)
      %---
      % The generalized cross-validation (GCV) method is used.
      % We seek the smoothing parameter s that minimizes the GCV
      % score i.e. s = Argmin(GCVscore).
      % Because this process is time-consuming, it is performed from
      % time to time (when nit is a power of 2)
      %---
      fminbnd(@gcv,log10(sMinBnd),log10(sMaxBnd),opt);
    end
    z = RF*idctn(Gamma.*DCTy) + (1-RF)*z;

    % if no weighted/missing data => tol=0 (no iteration)
    tol = isweighted*norm(z0(:)-z(:))/norm(z(:));

    z0 = z; % re-initialization
  end
  exitflag = nit<MaxIter;

  if isrobust %-- Robust Smoothing: iteratively re-weighted process
    %--- average leverage
    h = sqrt(1+16*s); h = sqrt(1+h)/sqrt(2)/h; h = h^N;
    %--- take robust weights into account
    Wtot = W.*RobustWeights(y-z,IsFinite,h,weightstr);
    %--- re-initialize for another iterative weighted process
    isweighted = true; tol = 1; nit = 0;
    %---
    RobustStep = RobustStep+1;
    RobustIterativeProcess = RobustStep<4; % 3 robust steps are enough.
  else
    RobustIterativeProcess = false; % stop the whole process
  end
end
```

```
% Warning messages
%---
if isauto
  if abs(log10(s)-log10(sMinBnd))<errp
    warning('MATLAB:smoothn:SLowerBound',...
      ['s = ' num2str(s,'%.3e') ': the lower bound for s ',...
      'has been reached. Put s as an input variable if required.'])
  elseif abs(log10(s)-log10(sMaxBnd))<errp
    warning('MATLAB:smoothn:SUpperBound',...
      ['s = ' num2str(s,'%.3e') ': the upper bound for s ',...
      'has been reached. Put s as an input variable if required.'])
  end
end
if nargout<3 && ~exitflag
  warning('MATLAB:smoothn:MaxIter',...
    ['Maximum number of iterations (' int2str(MaxIter) ') has ',...
    'been exceeded. Increase MaxIter option or decrease TolZ value.'])
end


% GCV score
%---
function GCVscore = gcv(p)
  % Search the smoothing parameter s that minimizes the GCV score
  %---
  s = 10^p;
  Gamma = 1./(1+s*Lambda.^2);
  %--- RSS = Residual sum-of-squares
  if aow>0.9 % aow = 1 means that all of the data are equally weighted
    % very much faster: does not require any inverse DCT
    RSS = norm(DCTy(:).*(Gamma(:)-1))^2;
  else
    % take account of the weights to calculate RSS:
```

```
    yhat = idctn(Gamma.*DCTy);
    RSS = norm(sqrt(Wtot(IsFinite)).*(y(IsFinite)-yhat(IsFinite)))^2;
  end
  %---
  TrH = sum(Gamma(:));
  GCVscore = RSS/nof/(1-TrH/noe)^2;
end

end

% Robust weights
function W = RobustWeights(r,I,h,wstr)
  % weights for robust smoothing.
  MAD = median(abs(r(I)-median(r(I)))); % median absolute deviation
  u = abs(r/(1.4826*MAD)/sqrt(1-h)); % studentized residuals
  if strcmp(wstr,'cauchy')
    c = 2.385; W = 1./(1+(u/c).^2); % Cauchy weights
  elseif strcmp(wstr,'talworth')
    c = 2.795; W = u<c; % Talworth weights
  else
    c = 4.685; W = (1-(u/c).^2).^2.*((u/c)<1); % bisquare weights
  end
  W(isnan(W)) = 0;
end

% Test for DCTN and IDCTN
function test4DCTNandIDCTN
  if ~exist('dctn','file')
    error('MATLAB:smoothn:MissingFunction',...
      ['DCTN and IDCTN are required. Download DCTN <a href="matlab:web('''',...
      'http://www.biomecardio.com/matlab/dctn.html'')">here</a>.'])
  elseif ~exist('idctn','file')
    error('MATLAB:smoothn:MissingFunction',...
      ['DCTN and IDCTN are required. Download IDCTN <a href="matlab:web('''',...
```

```
        'http://www.biomecardio.com/matlab/idctn.html'')">here</a>.'])
    end
end

%  Initial Guess with weighted/missing data
function z = InitialGuess(y,I)
    %-- nearest neighbor interpolation (in case of missing values)
    if any(~I(:))
        if license('test','image_toolbox')
            [z,L] = bwdist(I);
            z = y;
            z(~I) = y(L(~I));
        else
        % If BWDIST does not exist, NaN values are all replaced with the
        % same scalar. The initial guess is not optimal and a warning
        % message thus appears.
            z = y;
            z(~I) = mean(y(I));
            warning('MATLAB:smoothn:InitialGuess',...
                ['BWDIST (Image Processing Toolbox) does not exist. ',...
                'The initial guess may not be optimal; additional',...
                ' iterations can thus be required to ensure complete',...
                ' convergence. Increase ''MaxIter'' criterion if necessary.'])
        end
    else
        z = y;
    end
    %-- coarse fast smoothing using one-tenth of the DCT coefficients
    siz = size(z);
    z = dctn(z);
    for k = 1:ndims(z)
        z(ceil(siz(k)/10)+1:end,:) = 0;
        z = reshape(z,circshift(siz,[0 1-k]));
```

```
    z = shiftdim(z,1);
end
z = idctn(z);
```

12 END